



<https://theses.gla.ac.uk/>

Theses Digitisation:

<https://www.gla.ac.uk/myglasgow/research/enlighten/theses/digitisation/>

This is a digitised version of the original print thesis.

Copyright and moral rights for this work are retained by the author

A copy can be downloaded for personal non-commercial research or study, without prior permission or charge

This work cannot be reproduced or quoted extensively from without first obtaining permission in writing from the author

The content must not be changed in any way or sold commercially in any format or medium without the formal permission of the author

When referring to this work, full bibliographic details including the author, title, awarding institution and date of the thesis must be given

Enlighten: Theses

<https://theses.gla.ac.uk/>  
[research-enlighten@glasgow.ac.uk](mailto:research-enlighten@glasgow.ac.uk)

**Spontaneous Ca<sup>2+</sup> Waves in rabbit cardiac myocytes: a  
modelling study**

**By  
Niall MacQuaide**

**Submitted in fulfilment of the degree  
Doctor of Philosophy**

**to**

**University of Glasgow  
Faculty of Biomedical & Life Sciences**

**December 2004**

ProQuest Number: 10390852

All rights reserved

INFORMATION TO ALL USERS

The quality of this reproduction is dependent upon the quality of the copy submitted.

In the unlikely event that the author did not send a complete manuscript and there are missing pages, these will be noted. Also, if material had to be removed, a note will indicate the deletion.



ProQuest 10390852

Published by ProQuest LLC (2017). Copyright of the Dissertation is held by the Author.

All rights reserved.

This work is protected against unauthorized copying under Title 17, United States Code  
Microform Edition © ProQuest LLC.

ProQuest LLC.  
789 East Eisenhower Parkway  
P.O. Box 1346  
Ann Arbor, MI 48106 – 1346

GLASGOW  
UNIVERSITY  
LIBRARY:

## Declaration

The material contained within this thesis is my own work, except where stated.

This material has not been submitted for the fulfilment of any other degree.

Some of the results obtained have been published in paper and abstract form and are detailed below:

Zhang, H., D. Noble, M. Cannell, C. Orchard, M Lancaster, M. R. Boyett, A.V. Holden, M. Saleet Jafri, E.A. Sobie, W.J. Lederer, S.S. Demir, A. Michailova, F. DelPrincipe, M. Egger, E. Niggli, G.L. Smith, C.M. Loughrey, N. MacQuaide, J. Dempster, and A.T. Trafford. 2003. Dynamics of cardiac intracellular  $Ca^{2+}$  handling – from experiments to virtual cells. *International Journal of Bifurcation and Chaos* 13:3535-3560.

Niall MacQuaide, John Dempster, and Godfrey Smith: The effect of cytosolic Ca on spontaneous Ca wave characteristics in permeabilised cardiomyocytes from the rabbit. Abstract – Biophysical Meeting, Baltimore, *Biophys J* 2004; Vol.84; No.1.

N. MacQuaide, J. Dempster, C.M. Loughrey and G.L. Smith. Modelling of  $Ca^{2+}$  wave characteristics in cardiac muscle over a range of cytoplasmic  $[Ca^{2+}]$ . Abstract – Physiological Society meeting Manchester, *J Physiol* 2003.

Propagating intracellular  $\text{Ca}^{2+}$  waves in cardiac myocytes occur as a consequence of the overloaded state of the sarcoplasmic reticulum (SR).

To examine these events in detail, ventricular cardiomyocytes were isolated from rabbit hearts and permeabilised with  $\beta$ -escin. Cytosolic  $\text{Ca}^{2+}$  signals were monitored using Fluo-5F ( $10\mu\text{M}$ ) in combination with laser-scanning confocal microscopy. Through careful calibration of the intracellular  $\text{Ca}^{2+}$  signals and construction of analysis programs, the fluxes which underlie the  $\text{Ca}^{2+}$  wave were derived and subsequently incorporated into a mathematical model.

The decline in cytosolic  $\text{Ca}^{2+}$  subsequent to rapid application of caffeine was used to quantify cellular  $\text{Ca}^{2+}$  diffusional loss (diffusional constant =  $31.2\pm 0.9\text{ s}^{-1}$ ).  $\text{Ca}^{2+}$  binding to cellular proteins was then calculated and the sum of the free  $\text{Ca}^{2+}$ , bound  $\text{Ca}^{2+}$  and  $\text{Ca}^{2+}$  lost by diffusion was used as the integral of the  $\text{Ca}^{2+}$  flux across the SR. The first derivative of this was taken as the trans-SR flux rate.

From the analysis of these signals it was apparent that the  $\text{Ca}^{2+}$  released from the SR during a wave was not significantly different from that released on application of 10mM caffeine ( $0.149\pm 0.10\text{ mM}$  vs.  $0.154\pm 0.10\text{ mM}$ ). This information, coupled with values of intra-SR buffering allowed calculation of intra-SR  $[\text{Ca}^{2+}]$ . This in turn allowed the trans SR  $[\text{Ca}^{2+}]$  gradient to be estimated and the subsequent calculation of RyR and SERCA mediated  $\text{Ca}^{2+}$  flux.

These measurements were used to derive parameters for construction of a 3-compartment model of  $\text{Ca}^{2+}$  flux using existing models of  $\text{Ca}^{2+}$  buffering, SERCA activity and leak.

Three experimental interventions were used to study changes in  $\text{Ca}^{2+}$  wave properties and assess the effectiveness of the model in predicting wave frequency,

minimum and maximum  $[Ca^{2+}]$ . These were: (i) changing extracellular  $Ca^{2+}$ , (ii) inhibiting the RyR using tetracaine and (iii) inhibiting SERCA using 2',5'-di(tert-butyl)-1,4-benzohydroquinone (TBQ).

As cytosolic  $Ca^{2+}$  was increased from 300 to 900nM, so frequency and systolic  $Ca^{2+}$  were shown to increase nonlinearly, whilst diastolic  $[Ca^{2+}]$  increased linearly. Calculated SR release threshold was found not to change. SERCA  $V_{max}$  and  $K_D$  both increased, with  $V_{max}$  rising from 160 to 380  $\mu Ms^{-1}$  and  $K_D$  rising from  $239 \pm 48$  to  $354 \pm 18$  nM as extracellular  $[Ca^{2+}]$  was increased from 300nM to 900nM. The calculated peak permeability of RyR mediated flux also increased from  $41.1 \pm 6.5$  to  $61.2 \pm 3.6$   $s^{-1}$  over this range.

These changes, when included in the model, subsequently provided acceptable predictions of experimental results.

Tetracaine caused frequency of the  $Ca^{2+}$  waves to decrease from  $0.59 \pm 0.03$  Hz to  $0.35 \pm 0.02$  Hz, systolic  $[Ca^{2+}]$  to increase from  $2.06 \pm 0.11$   $\mu M$  to  $3.16 \pm 0.24$   $\mu M$  and diastolic  $[Ca^{2+}]$  to decrease from  $185 \pm 9$  nM to  $157 \pm 10$  nM. Flux analysis indicated that these changes were associated with an increase in the SR release threshold from  $1.16 \pm 0.04$  mM to  $1.58 \pm 0.08$  mM ( $n=6$ ). Implementation of this threshold change in the computational model predicted a decrease in  $Ca^{2+}$  wave frequency to a similar value to that observed experimentally. The increased systolic  $[Ca^{2+}]$  was comparable to but greater than that observed experimentally. In contrast, the model predicted diastolic  $[Ca^{2+}]$  to increase while a decrease diastolic was observed experimentally. Application of the SERCA inhibitor TBQ (1 $\mu M$ ) decreased SR  $Ca^{2+}$  content, the amplitude and frequency of  $Ca^{2+}$  waves. Analysis of the underlying fluxes suggested that TBQ caused a 43% reduction in SERCA  $V_{max}$ ,

with no significant change in  $K_{dp}$ . Analysis also suggested that this reduction in  $V_{max}$  was accompanied by a 25% reduction in SR release threshold. While the reduced SERCA  $V_{max}$  is consistent with TBQ's known action on SERCA, the effect on  $Ca^{2+}$  wave amplitude was unexpected and cannot be easily explained with the current  $Ca^{2+}$  wave model.

Declaration .....	i
Figures .....	ix
Tables .....	xiv
Abbreviations .....	xv
Chapter 1 Introduction.....	1
1.1 Overview of E-C Coupling.....	2
1.1.1 VSRM.....	3
1.1.2 CICR.....	4
1.1.3 Problems with CICR .....	8
1.1.4 Local control of CICR.....	8
1.2 The Sarcoplasmic Reticulum.....	9
1.2.1 Calsequestrin .....	10
1.2.2 The ryanodine receptor.....	11
1.2.3 SERCA .....	12
1.3 Spontaneous $\text{Ca}^{2+}$ oscillations in cardiomyocytes- a historical perspective .....	13
1.3.1 Transient inward Current.....	14
1.3.2 Fabiato's disrupted membrane study.....	15
1.3.3 SLIFs .....	16
1.3.4 Early $\text{Ca}^{2+}$ measurements.....	17
1.3.5 Improved $\text{Ca}^{2+}$ indicators.....	17
1.3.6 Subcellular resolution achieved by confocal microscopy .....	18
1.3.7 Deconvolution of the $\text{Ca}^{2+}$ wave.....	21
1.3.8 Spontaneous release –role in afterdepolarisations.....	22
1.4 Modelling spontaneous $\text{Ca}^{2+}$ release .....	22
1.4.1 Modelling $\text{Ca}^{2+}$ wave velocity .....	23
1.4.2 Saltatory $\text{Ca}^{2+}$ Propagation .....	23
1.4.3 Luminal control of $\text{Ca}^{2+}$ release.....	26
1.5 Current theory for mechanisms underlying spontaneous waves .....	27
1.5.1 Why do sparks not always trigger propagated release?.....	29
1.5.2 Is there a refractory period for $\text{Ca}^{2+}$ release in $\text{Ca}^{2+}$ waves?.....	29
1.6 Aims of the project .....	32
Chapter 2 Experimental Methods.....	34
2.1 Solutions Used.....	35
2.2 Cell Isolation .....	36
2.2.1 Isolation of ventricular cardiomyocytes from the rat .....	36

2.2.2 Isolation of ventricular cardiomyocytes from the rabbit .....	37
2.3 Cell permeabilisation.....	38
2.3.1 Rationale behind permeabilisation .....	38
2.3.2 Methods of permeabilisation .....	38
2.3.3 Permeabilisation Protocol.....	40
2.4 Microscopy.....	40
2.4.1 Confocal Laser-scanning microscopy .....	41
2.4.2 CLSM data collection.....	43
2.4.3 Problems associated with confocal microscopy.....	44
2.5 Experimental protocols for $[Ca^{2+}]$ measurement in cardiomyocytes.....	45
2.5.1 Introduction to single wavelength $Ca^{2+}$ measurement.....	45
2.5.2 Protocol for production and calibration of Spontaneous $Ca^{2+}$ Waves.....	46
2.5.3 Methods for conversion of fluorescence to $[Ca^{2+}]$ .....	47
2.5.4 Fast switching perfusion system.....	49
2.5.5 Possible problems resolving $[Ca^{2+}]$ at the peak of a $Ca^{2+}$ wave.....	50
2.6 Measuring the intrinsic $Ca^{2+}$ buffering capacity of permeabilised cells from the rat.....	55
2.6.1 Introduction .....	55
2.6.2 Preparation of cells for buffer capacity measurement.....	56
2.6.3 System for studying calcium dynamics on populations of cells.....	56
2.6.4 Protocol for measuring $[Ca^{2+}]$ buffering.....	58
2.6.5 Results .....	58
<b>Chapter 3 Computational methods used to analyse wave properties in permeabilised cardiomyocytes.....</b>	<b>60</b>
3.1 Analysing the cardiac $Ca^{2+}$ release event.....	61
3.1.1 Intrinsic Cellular $Ca^{2+}$ Buffering .....	63
3.1.2 $Ca^{2+}$ Diffusion.....	65
3.1.3 Quantification of SERCA activity.....	71
3.1.4 Calculation of $[Ca^{2+}]_{SR}$ .....	72
3.1.5 Extraction of RyR flux .....	75
3.2 Extraction of wave velocity.....	77
3.2.1 Introduction .....	77
3.2.2 Why measure the velocity of the $Ca^{2+}$ wave?.....	78
3.2.3 Why correct for velocity?.....	78
3.2.4 Signal vs. noise.....	80
3.2.5 Finding the velocity of a $Ca^{2+}$ Wave .....	83
3.2.6 Cross-correlation method and its use in estimation of $Ca^{2+}$ wave velocity. ....	84
3.2.7 CrossCorr Program.....	86

3.2.8 Testing the cross-correlation method .....	90
3.2.9 Optimising the program.....	92
3.2.10 Effect of noise .....	96
<b>Chapter 4 Experimental manipulations used to alter wave characteristics in permeabilised cardiomyocytes.....</b>	<b>99</b>
4.1 Introduction .....	100
4.2 Previous work.....	100
4.2.1 The effect of increased mean $[Ca^{2+}]_i$ on $Ca^{2+}$ waves .....	100
4.2.2 The effect of tetracaine on spontaneous release from the SR.....	102
4.2.3 The effect of SERCA inhibition on $Ca^{2+}$ waves .....	104
4.3 Experimental results .....	107
4.3.1 Cytosolic $Ca^{2+}$ study.....	107
4.3.2 Tetracaine study .....	119
4.3.3 TBQ study .....	124
4.4 Discussion .....	130
4.4.1 Cytosolic $[Ca^{2+}]$ study .....	130
4.4.2 Tetracaine study .....	135
4.4.3 TBQ study .....	137
<b>Chapter 5 <math>Ca^{2+}</math> wave model: Construction and comparison with experimental results .....</b>	<b>141</b>
5.1 Model description.....	142
5.2 Program implementation .....	145
5.2.1 Calculating free from total.....	146
5.3 Model verification .....	147
5.4 Error analysis of model parameters.....	149
5.4.1 Diffusion constant .....	149
5.4.2 RyR Permeability .....	151
5.4.3 SERCA $K_D$ .....	153
5.4.4 SERCA $V_{max}$ .....	154
5.4.5 SR $Ca^{2+}$ threshold .....	156
5.5 Model Results.....	158
5.5.1 The effect of changing $[Ca^{2+}]_{bath}$ on parameters of spontaneous release.....	158
5.5.2 The effects of tetracaine on parameters of spontaneous waves.....	166
5.5.3 The effects of TBQ on parameters of spontaneous waves. ....	170
5.6 Discussion .....	173
5.6.1 The effects of changing $[Ca^{2+}]_{bath}$ .....	173
5.6.2 The effects of tetracaine .....	174
5.6.3 The effects of TBQ.....	182

Chapter 6 General Discussion .....	184
Chapter 7 Appendices .....	188
7.1 Description of WaveModel Program.....	189
7.1.1 Purpose of program .....	189
7.1.2 Setting up simulation variables. ....	189
7.1.3 To run a single simulation .....	190
7.1.4 To run a batch of simulations for a range of one variable.....	191
7.1.5 To run a batch of simulations for a range of two variables .....	192
7.1.6 Exploring the output.....	192
7.2 Description of Flo2Ca program.....	198
7.2.1 Purpose of program .....	198
7.2.2 How to use:.....	198
7.3 Description of PolySmooth program.....	206
7.3.1 Purpose of program .....	206
7.3.2 Import data .....	206
7.3.3 Polynomial smooth.....	207
7.3.4 Polynomial extension .....	208
7.3.5 Joining Polynomials.....	208
7.3.6 Calculating the first derivative.....	210
7.3.7 Exporting Data .....	211
7.3.8 Possible artefacts of method.....	211
7.4 Description of CellFlux program.....	215
7.4.1 Purpose of program .....	215
7.4.2 Importing data .....	215
7.4.3 Calculating SR $[Ca^{2+}]$ .....	216
7.4.4 Fitting parameters of SERCA.....	216
7.4.5 Calculating RyR flux rate.....	218
7.4.6 Calculating permeability .....	219
7.4.7 Exporting data and results.....	220
References .....	221

## Figures

Figure 1-1 $\text{Ca}^{2+}$ transport in cardiomyocytes.....	2
Figure 1-2 Inactivation of the $\text{Ca}^{2+}$ -induced release of $\text{Ca}^{2+}$ from the SR by a supraoptimal increase of $[\text{free Ca}^{2+}]$ during the $\text{Ca}^{2+}$ release induced by a suboptimal $[\text{free Ca}^{2+}]$ .....	5
Figure 1-3 Relation between bulk solution pCa used as a trigger and amplitude of the contraction resulting from CICR from the SR.....	6
Figure 1-4 The effect of varying L-Type current on $\text{Ca}^{2+}$ release from the SR.....	7
Figure 1-5 Diagram showing the structure of the t-tubules, mitochondria and sarcoplasmic reticulum. (From Fawcett & McNutt, 1969).....	10
Figure 1-6 Three-dimensional reconstruction of the cardiac ryanodine receptor.....	11
Figure 1-7 The transient depolarization (TD) and the TI: a comparison of.....	15
Figure 1-8 Figures showing spontaneous $\text{Ca}^{2+}$ release events in ventricular cardiomyocytes.....	20
Figure 1-9 Abortive $\text{Ca}^{2+}$ wave.....	21
Figure 1-10 Geometry of the Subramanian et al., model.....	25
Figure 1-11 E-C coupling gain vs. total SR $[\text{Ca}^{2+}]/([\text{Ca}^{2+}]_{\text{SR}})$ .....	28
Figure 1-12 Recovery of action potential and caffeine evoked transients following a $\text{Ca}^{2+}$ wave in a rat ventricular myocyte.....	31
Figure 2-1 Illustration of confocal microscopy.....	41
Figure 2-2 Example of a waterfall plot from the confocal microscope.....	43
Figure 2-3 Example of typical protocol for studying $[\text{Ca}^{2+}]$ waves in permeabilised cardiomyocytes from the rabbit.....	47
Figure 2-4 Apparatus for perfusion of isolated cardiomyocytes.....	49
Figure 2-5 Graphs showing differences in $\text{Ca}^{2+}$ affinities of Fluo 3 and Fluo 5F and the subsequent increases in error above $1\mu\text{M}$ .....	51
Figure 2-6 Linescan images of $\text{Ca}^{2+}$ waves in permeabilised rat (left) and rabbit (right) cardiomyocytes.....	52
Figure 2-7 $\text{Ca}^{2+}$ waves from the rat before and after application of BDM.....	53
Figure 2-8 Graphs showing effects of Cytochalasin D on wave frequency and cell shortening.....	54
Figure 2-9 Linescan images of $\text{Ca}^{2+}$ waves in permeabilised rat (left) and rabbit (right) cardiomyocytes.....	55
Figure 2-10 Diagram showing apparatus used for measuring intrinsic cellular $\text{Ca}^{2+}$ buffering.....	57
Figure 2-11 Graph showing 2-site binding properties for $\text{Ca}^{2+}$ of permeabilised cardiomyocytes.....	58

Figure 3-1 Typical  $[Ca^{2+}]_i$  trace of  $Ca^{2+}$  waves from a spontaneously oscillating permeabilised myocyte..... 61

Figure 3-2 Compartmental Flux Diagram..... 62

Figure 3-3 Averaged wave profile from 5 typical  $Ca^{2+}$  waves..... 63

Figure 3-4 Buffer curve derived from Hove-Madsen & Bers study..... 64

Figure 3-5 Time course of total cytosolic  $[Ca^{2+}]$  converted from free cytosolic  $[Ca^{2+}]$  from Figure 3-3..... 65

Figure 3-6 Calculation of diffusion constant (k) from decline of caffeine induced  $Ca^{2+}$  release in permeabilised cardiomyocyte..... 67

Figure 3-7 Diffusion added to  $[Ca^{2+}]_{total}$ ..... 68

Figure 3-8 Reconstructed polynomial smoothed trace of SR Ca flux integral..... 69

Figure 3-9 First derivative of polynomial smoothed  $Ca^{2+}$  wave plot (black)..... 70

Figure 3-10 Graphs to demonstrate fitting of SERCA activity..... 71

Figure 3-11 Intra-SR  $[Ca^{2+}]_i$  calculated from cytosolic  $[Ca^{2+}]_{total}$ ..... 73

Figure 3-12 Graph showing calculated net flux from experiment (black line) and SERCA flux (grey line) calculated by fitting the region between 300 and 500 nM  $[Ca^{2+}]$ ..... 74

Figure 3-13 SR  $Ca^{2+}$  flux due to SERCA vs.  $[Ca^{2+}]_i$  when SR  $Ca^{2+}$  is clamped at  $1\mu M$ .  $V_{max}$  and  $k_m$  used to construct the curve are illustrated..... 75

Figure 3-14 Graph of the change in  $Ca^{2+}$  efflux during a wave..... 76

Figure 3-15 Typical RyR permeability calculated from previous RyR flux..... 77

Figure 3-16 Example of typical  $Ca^{2+}$  Wave..... 78

Figure 3-17 Resultant fluorescence signal from averaged 4-pixel and 80-pixel bands..... 79

Figure 3-18 Graph showing change in variance with increasing signal amplitude..... 81

Figure 3-19 Histogram of pixel intensity..... 82

Figure 3-20 Manual estimation of wavefront position using LaserPix program..... 83

Figure 3-21 Figure shows correlation result (upper) when dashed shape is moved in x direction (lower)..... 85

Figure 3-22 Graphical display from cross correlation program..... 89

Figure 3-23 Examples of simulated linescan images with more (left) and less (right) noise..... 91

Figure 3-24 Graph showing variability on correlation plots from bands of varying pixel width..... 93

Figure 3-25 Graph showing the effect of increasing the width of band for averaging fluorescence on the estimated velocity using the correlation program..... 94

Figure 3-26 Graph showing the effect of increasing number of bands on velocity estimation..... 95

Figure 3-27 Noise dependency of velocity estimation..... 97

Figure 4-1. The effects of tetracaine on spontaneous  $Ca^{2+}$  waves in intact rat myocytes..... 103

Figure 4-2 Calculated fluctuations in SR $Ca^{2+}$ content during $Ca^{2+}$ waves with and without tetracaine (100 $\mu$ M).....	104
Figure 4-3 Effect of TBQ on time course of spontaneous wave of $Ca^{2+}$ release.....	106
Figure 4-4 $Ca^{2+}$ waves from cardiomyocytes with increasing $[Ca^{2+}]_i^{mean}$ .....	108
Figure 4-5 Wave parameters over a range of mean $[Ca^{2+}]$ .....	110
Figure 4-6 Calcium efflux in waves and SR content over a range of $[Ca^{2+}]_i^{mean}$ .....	112
Figure 4-7 Conversion of free to total bound + free allowing estimation of SR efflux during $Ca^{2+}$ wave.....	113
Figure 4-8 Average $[Ca^{2+}]_i$ from cells in Figure 4-4, with calculated total $[Ca^{2+}]$ , and SR fluxes due to SERCA uptake and RyR release.....	115
Figure 4-9 Plot of $V_{max}$ vs. $[Ca^{2+}]_{cytosol}$ .....	116
Figure 4-10 Changes in SERCA parameters over a range of $[Ca^{2+}]_i^{mean}$ .....	117
Figure 4-11 Effect of increasing $[Ca^{2+}]_i^{mean}$ on RyR opening during a $Ca^{2+}$ wave.....	118
Figure 4-12 Effect of tetracaine (50 $\mu$ M) on $Ca^{2+}$ waves in permeabilised cardiomyocytes from the rabbit.....	119
Figure 4-13 Comparison of Caffeine and spontaneously evoked transients from after application of tetracaine.....	120
Figure 4-14 Effect of tetracaine on parameters of spontaneous $Ca^{2+}$ waves.....	121
Figure 4-15 Calculated RyR permeability and SR content before (i) and after (ii) tetracaine (50 $\mu$ M) application.....	122
Figure 4-16 Effect of tetracaine on SR $[Ca^{2+}]_i$ .....	122
Figure 4-17 Changes in RyR opening characteristics after application of tetracaine (50 $\mu$ M).....	123
Figure 4-18 Effect of tetracaine on SERCA $V_{max}$ and $K_D$ .....	124
Figure 4-19 Effect of TBQ on $Ca^{2+}$ release in $Ca^{2+}$ waves and caffeine.....	125
Figure 4-20 Mean changes in minimum, maximum $[Ca^{2+}]_i$ and frequency after TBQ application for approx. 1 Minute.....	126
Figure 4-21 Analysis of changes seen in SR fluxes from control (i) and after application of TBQ (5 $\mu$ M) (ii).....	127
Figure 4-22 Mean peak $[Ca^{2+}]_{SR}$ during $Ca^{2+}$ waves before and after application of TBQ (5 $\mu$ M) (n=5).....	128
Figure 4-23 Mean behaviour of SERCA with and without TBQ (5 $\mu$ M).....	128
Figure 4-24 Mean behaviour of RyR with and without TBQ.....	129
Figure 4-25 The effect of TBQ on $Ca^{2+}$ wave velocity.....	130
Figure 5-1 Diagram of fluxes occurring between compartments in model.....	142
Figure 5-2 Average permeability profile.....	144

Figure 5-3 Comparison of modelled and experimental  $[Ca^{2+}]$  profile from wave. .... 148

Figure 5-4 Error analysis of diffusion  $k$  parameter. .... 150

Figure 5-5 Error analysis of peak RyR permeability profile. .... 152

Figure 5-6 Error analysis of SERCA forward mode  $K_D$ . .... 153

Figure 5-7 Error analysis of SERCA  $V_{max}$ . .... 155

Figure 5-8 Error analysis of SR  $Ca^{2+}$  threshold for release. .... 157

Figure 5-9 Linear fit of SERCA  $V_{max}$  from experimental results. .... 159

Figure 5-10 Linear fit of SERCA  $K_D$  from experimental results. .... 160

Figure 5-11 Linear fit of RyR peak permeability from experimental results. .... 160

Figure 5-12 Plot of changes in  $[Ca^{2+}]_i$  from cytosol (upper panel) and SR (lower panel) compartments of model. .... 161

Figure 5-13 The effect of a transient rise in external  $Ca^{2+}$  on  $Ca^{2+}$  release in the model. .... 162

Figure 5-14 Modelling results over 300 to 900nM bath  $[Ca^{2+}]$  range, with modulation of model variables seen in experiment. .... 163

Figure 5-15 Graph showing simulation results when SERCA  $K_D$  and  $V_{max}$  are changed to the values found experimentally at 300 and 900 nM  $[Ca^{2+}]_{bath}$ . .... 165

Figure 5-16 Plot showing changes in cytosolic  $[Ca^{2+}]$  and frequency when threshold is suddenly increased, then decreased. .... 167

Figure 5-17 Effect of modulating SR release threshold in model to mimic effect on tetracaine (50 $\mu$ M) on 3 parameters of  $Ca^{2+}$  waves. .... 169

Figure 5-18 An example of changes observed when  $V_{max}$  is transiently lowered by 40% in the  $Ca^{2+}$  release model. .... 171

Figure 5-19 Effect of modulating SERCA  $V_{max}$  in model to mimic effect on TBQ (1 $\mu$ M) on 3 parameters of  $Ca^{2+}$  waves. .... 172

Figure 5-20 Plots of changes in wave systolic (peak)  $Ca^{2+}$ , diastolic (min)  $Ca^{2+}$  and frequency with increases in leak  $k$  in the model. .... 177

Figure 5-21 Diagram of  $Ca^{2+}$  leak effects on  $Ca^{2+}$  uptake. .... 178

Figure 5-22 Effect of varying leak  $k$  parameter in estimation of  $V_{max}$  and  $K_D$  using the CellFlux program. .... 180

Figure 5-23 Hypothetical simulation of tetracaine's effect on SR leak and threshold. .... 181

Figure 7-1 Screenshot of program when first initialised. .... 193

Figure 7-2 Screenshot showing imported RyR permeability profile (red) and cubic-interpolation of plot (blue). .... 194

Figure 7-3 Screenshot of Ca Cytosol plot. .... 194

Figure 7-4 Screenshot of Ca Lumen plot (i.e. SR  $[Ca^{2+}]$ ). .... 195

Figure 7-5 Screenshot of RyR flux plot. .... 195

Figure 7-6 Screenshot of SERCA Flux plot. .... 196

Figure 7-7 Screenshot of Net Flux plot (i.e.) net flux between SR and cytosol compartments. ....196

Figure 7-8 Screenshot of Bath Flux .....197

Figure 7-9 Imported intracellular and extracellular fluorescence trace from typical protocol.....202

Figure 7-10 Imported traces after applying filter. ....203

Figure 7-11 Resultant  $[Ca^{2+}]_i$  trace after conversion of fluorescence. ....203

Figure 7-12 Screen used to select waves for averaging. ....204

Figure 7-13 Average  $[Ca^{2+}]_i$  transient from region selected in figure 4. ....205

Figure 7-14 Screenshot of program after importing data. ....207

Figure 7-15 Example of cubic spline fitted to span region of two joining polynomials. ....209

Figure 7-16 First derivative before joining method was applied.....209

Figure 7-17 Plot of first derivative after joining method has been applied. ....210

Figure 7-18 Plot of flux rate vs.  $[Ca^{2+}]_i$  after polynomial smoothing. ....211

Figure 7-19 Examples of glitches in the  $Ca^{2+}$  and  $dCa/dt$  .....211

Figure 7-20 Plot of first derivative vs. time from manual zoom tab. ....212

Figure 7-21 Average  $[Ca^{2+}]_{total}$  calculated from previous figure.....213

Figure 7-22 Plot shows section where caffeine was applied. ....213

Figure 7-23 Adjusted trace, after allowing for quench.....214

Figure 7-24 Screenshot of plot displayed after inputting data from PolySmooth program.....216

Figure 7-25 Screenshot showing experimental flux (red line) and calculated flux (blue line), plotted against cytosolic  $[Ca^{2+}]$ .....218

Figure 7-26 Plot showing goodness of fit of experimental (black) and calculated (red) fluxes. ....219

Figure 7-27 RyR permeability constant profile.....220

**Tables**

Table 1 Table showing the effect of averaging on the rate of rise of the upstroke of the $\text{Ca}^{2+}$ wave and % change in noise.....	79
Table 2 Table showing the effect of changing the number of pixels averaged before correlation on both noise and variance of correlation. ....	93
Table 3 Relative volumes of compartments as used in model. ....	145
Table 4 Simulation Parameters: .....	161

## Abbreviations

°C	degrees Celsius, temperature
a.u.	arbitrary units
AIP	autocamtide-2-related inhibitory peptide
ATP	adenosine 5' triphosphate
BDM	2,3-butanedione monoxime, contraction inhibitor
B <sub>max</sub>	maximal buffer capacity
bpm	beats per. minute
Ca <sup>2+</sup>	calcium ion (s)
Ca <sub>Bath</sub>	Free bath calcium concentration
CaCl <sub>2</sub>	calcium chloride
[Ca <sup>2+</sup> ] <sub>cyt</sub>	free cytosolic calcium ion concentration
[Ca <sup>2+</sup> ] <sub>i</sub> <sup>mean</sup>	mean intracellular calcium ion concentration
CaMKII	Ca <sup>2+</sup> /calmodulin-dependent kinase
cAMP	adenosine-3',5'-cyclic monophosphate
[Ca <sup>2+</sup> ] <sub>SR</sub>	free intra-SR calcium concentration
[Ca <sup>2+</sup> ] <sub>total</sub>	total calcium concentration
CCCP	meta-chloro carbonyl cyanide phenylhydrazone, mitochondrial transport inhibitor
CICR	calcium-induced calcium release
CPA	cyclopiazonic acid
CRU	calcium release unit
CSQ	calsequestrin
D	diffusion coefficient

DAD	delayed after-depolarisation
EAD	early after-depolarisation
EC	extracellular
E-C	excitation-contraction
EGTA	ethylene glycol bis(2-aminoethyl ether)-N,N,N',N'-tetraacetic acid
F	fluorescence
FKBP	FK506-binding protein
Fluo-3	fluorescent calcium probe
Fluo-5F	fluorescent calcium probe
F <sub>max</sub>	maximum fluorescence
F <sub>min</sub>	minimum fluorescence
F <sub>0</sub>	baseline fluorescence
H	Hill coefficient
HEPES	4-(2-hydroxyethyl)-1-piperazineethanesulfonic acid, hydrogen ion buffer
HRC	histidine-rich, calcium-binding protein
Hz	Hertz, frequency
IC	intracellular
I <sub>ti</sub>	transient inward current
J <sub>Diff</sub>	flux due to diffusion
J <sub>Leak</sub>	flux due to SR leak
J <sub>Net</sub>	sum of SR fluxes
J <sub>RyR</sub>	flux due to RyR
J <sub>SERCA</sub>	flux due to SERCA
JSR	junctional sarcoplasmic reticulum

kb	binding association constant $= 1/K_D$
KCl	potassium chloride
$K_D$	ligand dissociation constant
kDa	kilodaltons, atomic mass unit
$K_m$	dissociation constant in the Michaelis-Menten equation
min	minute, time
ms	milliseconds, time
mV	millivolts, electric potential
MW	molecular weight
nA	nanoamperes, current
NA	numerical aperture
$\text{NaCl}_2$	sodium chloride
$\text{NaH}_2\text{PO}_4$	Sodium dihydrogen orthophosphate
NCX	sodium/calcium exchanger
$\text{Ni}^{2+}$	nickel
NJSR	non-junctional sarcoplasmic reticulum
nM	nanomoles, concentration
pCa	logarithmic calcium concentration
pH	logarithmic hydrogen ion concentration
PLB	phospholamban
PMT	photon-multiplier tube
PP1	protein phosphatase-1
RV	right ventricle
RyR	ryanodine receptor

S	siemens, conductance
S.E.M.	standard error of measurement
SERCA	sarco/endoplasmic reticulum calcium ATPase
SLIF	scattered light intensity fluctuation
SNR	signal-to-noise ratio
SR	sarcoplasmic reticulum
TBQ	2',5'-di(tert-butyl)-1,4-benzohydroquinone
t-tubule	transverse tubule
V <sub>max</sub>	maximum enzyme velocity
VSRM	voltage-sensitive release mechanism
μg	micrograms, weight
μs	microseconds, time
σ	standard deviation

## Chapter 1 Introduction

$\text{Ca}^{2+}$  (the  $\text{Ca}^{2+}$  ion) is a highly versatile intracellular signal employed by numerous cell types to regulate cellular function (Berridge *et al.*, 2000). In the cardiomyocyte,  $\text{Ca}^{2+}$  is the intermediate between electrical activity and cell contraction and relaxation. This process is called excitation-contraction (E-C) coupling and alterations in E-C coupling occur in a number of pathological situations including heart failure. A greater knowledge of the mechanisms contributing to pathophysiological modes of E-C coupling is needed in order for these alterations to be treated appropriately. This thesis examines the spontaneous activity of cardiac SR which generates  $\text{Ca}^{2+}$  waves within heart cells and has been associated with electrical arrhythmias. Clarification of current theories that underlie these spontaneous events through experimental and mathematical modelling techniques was the basis of these studies.

### 1.1 Overview of E-C Coupling

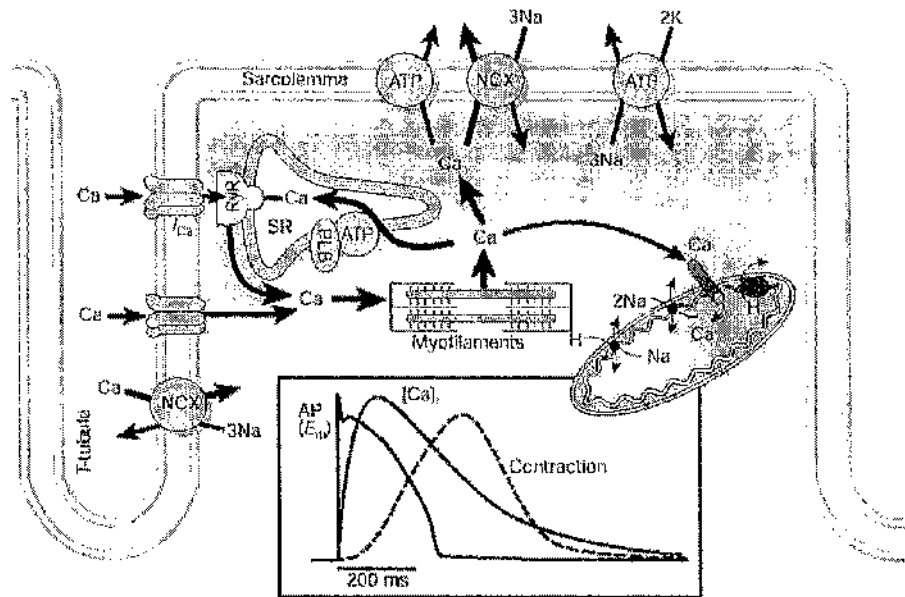


**Figure 1-1  $\text{Ca}^{2+}$  transport in cardiomyocytes.** Inset shows the time course of an action potential,  $\text{Ca}^{2+}$  transient and contraction measured in a rabbit ventricular myocyte at  $37^\circ\text{C}$  (Bers, 2002).

In E-C coupling, an action potential propagates along the sarcolemmal membrane, and into the t-tubules (See Fig 1-1). The subsequent membrane depolarisation activates L-type  $\text{Ca}^{2+}$  channels to open and allows a relatively small entry of  $\text{Ca}^{2+}$  ions into the cytosol, elevating  $[\text{Ca}^{2+}]$  local to the sarcolemma. This rise of  $\text{Ca}^{2+}$  triggers ryanodine receptors (RyRs) on the sarcoplasmic reticulum (SR) to open, releasing stored  $\text{Ca}^{2+}$  ions. This much larger release of  $\text{Ca}^{2+}$  elevates  $[\text{Ca}^{2+}]$  globally within the cell. This process is termed  $\text{Ca}^{2+}$ -induced  $\text{Ca}^{2+}$  release (CICR). Released  $\text{Ca}^{2+}$  binds to regulatory proteins on the myofilaments, causing them to contract. Relaxation of the cell is facilitated by removal of  $[\text{Ca}^{2+}]$  from the cytosol. Most (70%) is sequestered by the SR via the Sarco(end)plasmic reticulum calcium-ATPase (SERCA). A smaller proportion (~29%) is extruded to the extracellular space, via the Na/ $\text{Ca}^{2+}$  exchanger (NCX) and sarcolemmal  $\text{Ca}^{2+}$  ATPase. The remainder of the  $\text{Ca}^{2+}$  is taken up by the mitochondria.

Other sarcolemmal influx pathways may also trigger CICR.  $\text{Ca}^{2+}$  can enter the cell via reverse NCX on the depolarising phase of the action potential (Nuss & Houser, 1992) and T-type  $\text{Ca}^{2+}$  channels allow entry of  $\text{Ca}^{2+}$  (Vassort & Alvarez, 1994) (Sipido *et al.*, 1998). Both these mechanisms contribute minimally to E-C coupling under normal conditions (Sipido *et al.*, 1998; Sipido *et al.*, 1997).

The mechanisms underlying depolarisation induced  $\text{Ca}^{2+}$  release for the SR are still under debate. Current evidence suggests CICR is the dominant mechanism for RyR activation (Bers, 2002). A voltage-induced  $\text{Ca}^{2+}$  release, as is seen in skeletal muscle has also been proposed (Ferrier & Howlett, 1995), but is less well accepted.

### 1.1.1 VSRM

A voltage-sensitive release mechanism (VSRM) was first proposed in 1995 (Ferrier & Howlett, 1995). The paper describes how cell depolarisations insufficient to

fully activate L-type channels, (from  $-65$  to  $-40$ mV) nevertheless activated contraction in guinea-pig cardiomyocytes. It was proposed that the RyR was activated by a mechanism similar to the voltage-coupled opening seen in skeletal muscle. This theory has yet to receive wide acceptance. The paper was criticized for the need for the presence of extracellular  $\text{Ca}^{2+}$  for the process to occur, suggesting that Ca influx actually was involved. Criticism also arose from the high concentration of cAMP used. It has been hypothesized that high [cAMP] sensitised L-type channels (McDonald *et al.*, 1994), lowering activation voltages thresholds. High [cAMP] also leads to increased SR load, sensitising the RyR allowing activation by very small amounts of  $\text{Ca}^{2+}$  entry through the L-type channel. A recent paper, (Trafford & Eisner, 2003) showed that blocking the L-type channel with high ( $500\mu\text{M}$ )  $\text{Cd}^{2+}$  caused smaller transients. These transients were abolished when  $\text{Ni}^{2+}$  blocked the NCX. This suggested the transients were due to  $\text{Ca}^{2+}$  entry via NCX and found no role for VSRM.

### 1.1.2 CICR

First described in skeletal muscle fibres (Ford & Podolsky, 1970; Endo *et al.*, 1970), this process describes the regenerative process whereby a small  $\text{Ca}^{2+}$  signal elicits a larger  $\text{Ca}^{2+}$  efflux from the SR. In their landmark papers using mechanically skinned cardiac myocytes, Fabiato and Fabiato demonstrated the mechanism of  $\text{Ca}^{2+}$  activation of SR stored  $\text{Ca}^{2+}$  release, (Fabiato & Fabiato, 1972; Fabiato & Fabiato, 1975; Fabiato, 1985c; Fabiato, 1985a). The experiments were technically difficult, as the membrane had to be mechanically removed from the cell with microtweezers and very rapid ( $\sim 5$ msec) solution changes were needed. Due to these difficulties, these experiments have never been repeated. The studies showed *graded* SR calcium release in proportion to the size of the trigger  $\text{Ca}^{2+}$ .

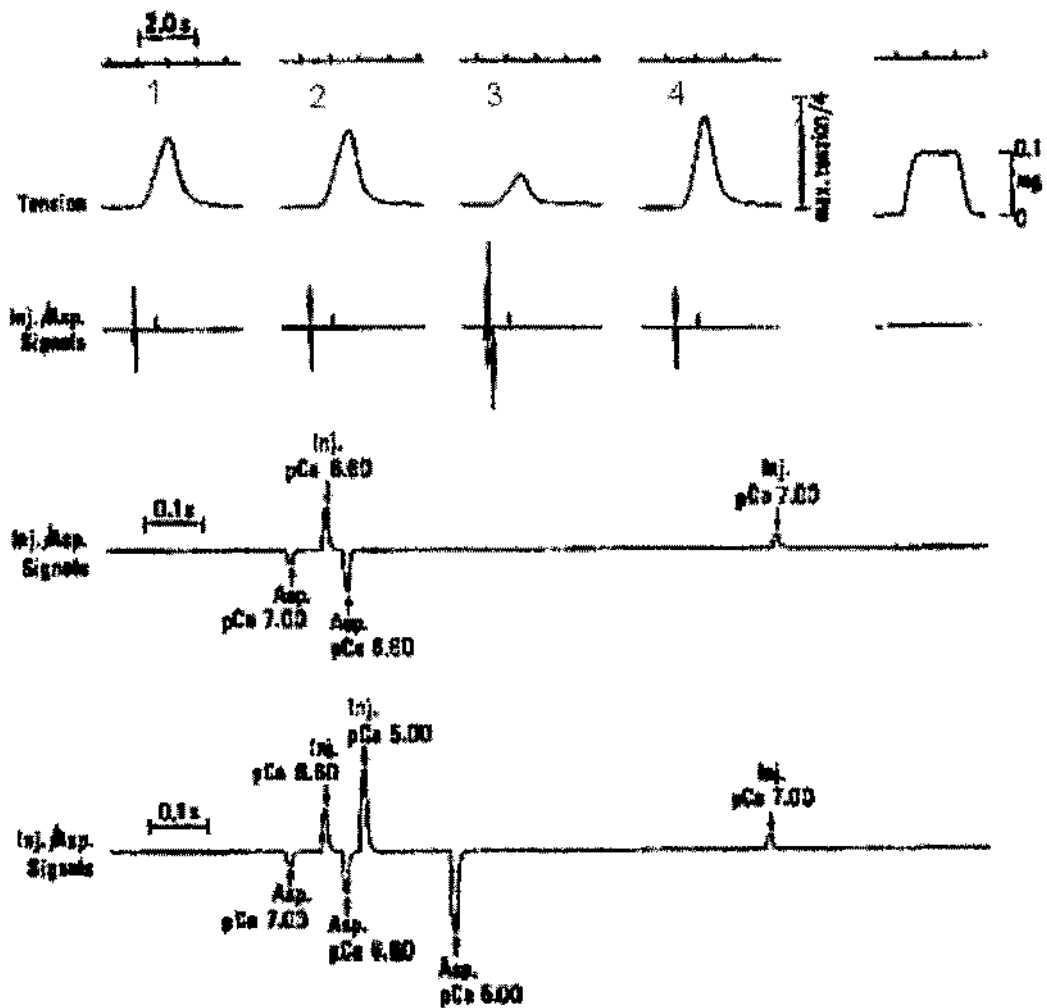


**Figure 1-2** Inactivation of the  $\text{Ca}^{2+}$ -induced release of  $\text{Ca}^{2+}$  from the SR by a supraoptimal increase of  $[\text{free Ca}^{2+}]$  during the  $\text{Ca}^{2+}$  release induced by a suboptimal  $[\text{free Ca}^{2+}]$ .

The experiment was performed on a skinned canine cardiac Purkinje cell at  $22^\circ\text{C}$ . The preparation was stimulated by microinjection-aspirations at regular intervals of 25 msec. The upper high-speed recording corresponds to the injection-aspiration signals for the first, second, and fourth tension transients. The lower high-speed recording corresponds to the injection-aspiration signals for the third tension transient. (Fabiato, 1985c)

Figure 1-2 shows the experimental protocol Fabiato used. The cells were first loaded in pCa7 (100nM), then a pCa of 6.6 (25nM) was applied, then removed after ~25msec. This caused a CICR and subsequent contraction (upper contractions 1,2 and 4). When a pCa of 5.0 (10 $\mu\text{M}$ ) was used, a diminished contraction occurred (upper contraction 3). This demonstrated a  $[\text{Ca}^{2+}]$  dependent

CICR inactivating at higher  $[Ca^{2+}]$ . This was further investigated and a bell shaped relationship between pCa and CICR was found, with an additional effect of triggering  $Ca^{2+}$  exposure time. This is shown below.

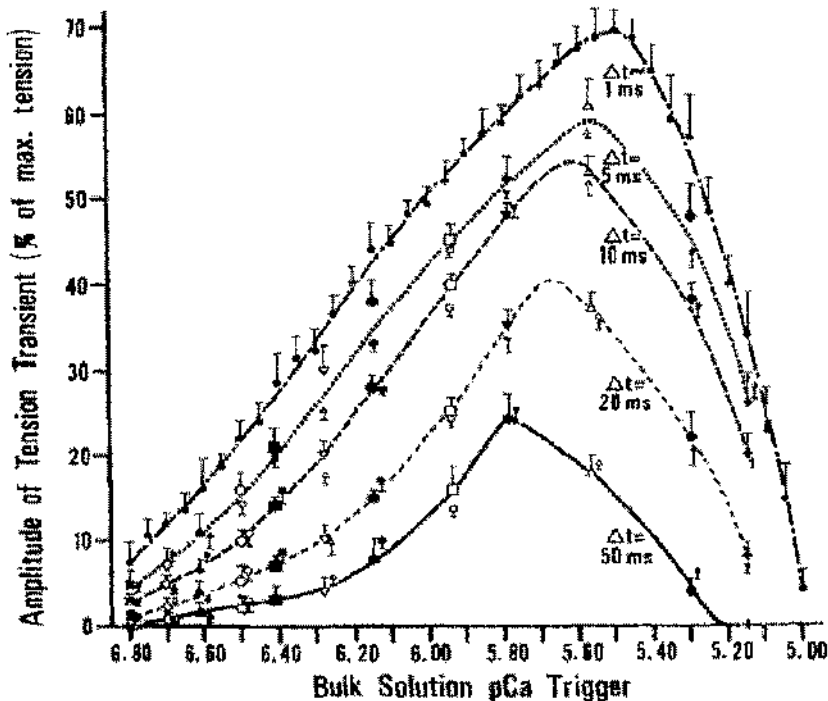


**Figure 1-3 Relation between bulk solution pCa used as a trigger and amplitude of the contraction resulting from CICR from the SR.**

Triggering  $Ca^{2+}$  injections were applied for 1-50 msec durations. The data are from skinned canine cardiac Purkinje cells at 22 ° C. Figure taken from (Fabiato, 1985c).

This shows a peak response when trigger  $pCa^{2+}$  is between 5.8-5.3 (1.6 – 5  $\mu M$ ), depending on the trigger exposure time, with inactivation at higher  $[Ca^{2+}]$ . The study has been criticized because of the unphysiological state of the tissue, having been mechanically skinned. Subsequent studies have been carried out on intact cells to investigate these observations.

Voltage clamp studies have shown the graded effect of  $Ca^{2+}$  entry through L-type  $Ca^{2+}$  channels (Beuckelmann & Wier, 1988; Barceñas-Ruiz & Wier, 1987; Cleemann & Morad, 1991; London & Krueger, 1986). See Figure below.

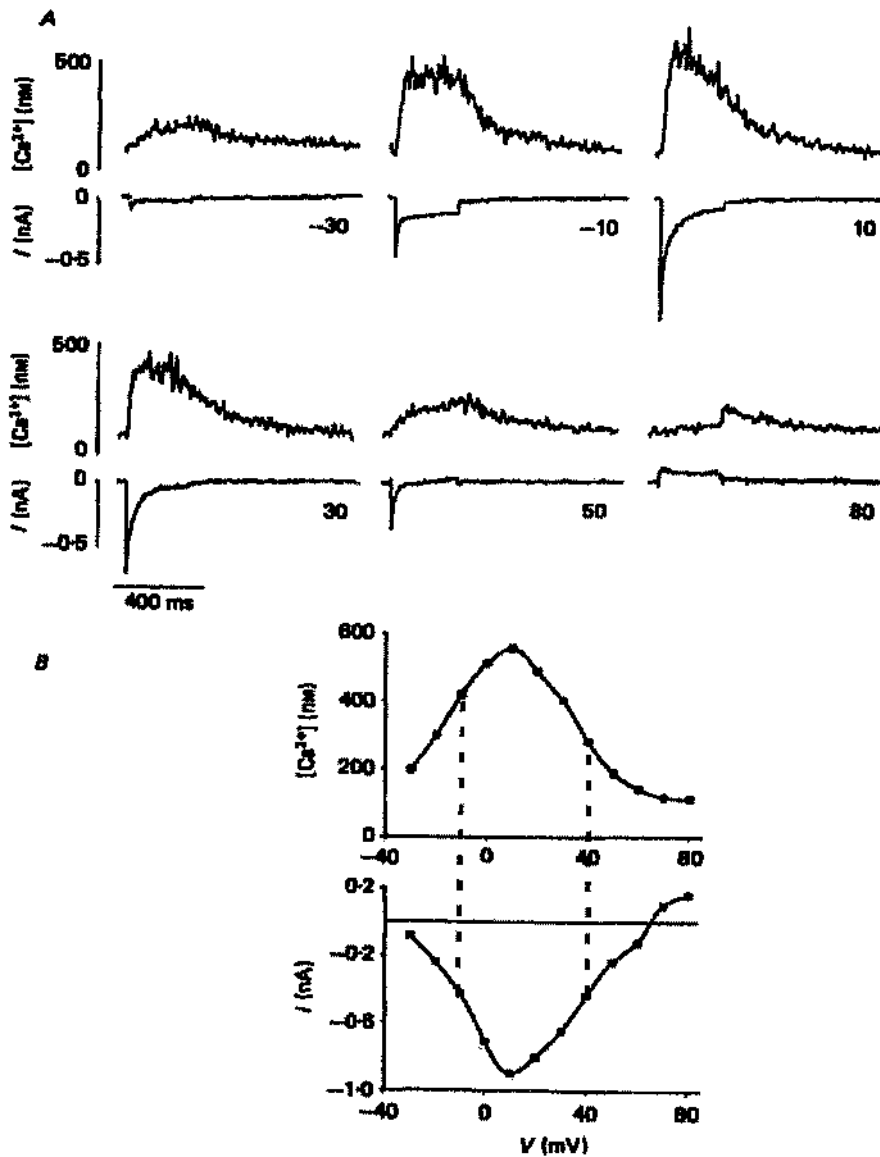


**Figure 1-4** The effect of varying L-Type current on  $Ca^{2+}$  release from the SR. **A.** Depolarising to -30, -10, 10, 30, 50 and 80 mV. Changing  $I_{Ca}$  and resultant  $Ca^{2+}$  transient. **B.** Bell shaped relationship between voltage and  $I_{Ca}$ . Increasing current evoked larger  $Ca^{2+}$  transients. (Beuckelmann & Wier, 1988)

These studies showed how increasing  $Ca^{2+}$  entry via L-type channels increased  $Ca^{2+}$  release from the SR. An asymmetry in the L-type current magnitude and subsequent  $[Ca^{2+}]$  release was observed. As voltage became more positive, the CICR seemed to become less effective. At -10 mV the -0.5nA current elicited a larger transient than the -0.5nA at +40mV. This was later concluded to be due to

the increased electrochemical gradient at  $-10\text{mV}$  increasing the current through single L-type channels, subsequently activating RyR's more effectively.

"Caged"  $\text{Ca}^{2+}$  studies carried out in intact cells (Niggli & Lederer, 1990; Valdeolmillos *et al.*, 1989) also found this graded release. Photolysis of the caged  $\text{Ca}^{2+}$  moderately elevated cytosolic  $\text{Ca}^{2+}$  initiating a larger release via CICR. Increasing the caged  $\text{Ca}^{2+}$  release caused larger SR  $\text{Ca}^{2+}$  release.

Neither the voltage nor the caged  $\text{Ca}^{2+}$  studies have demonstrated an inactivation of the RyR at higher  $[\text{Ca}^{2+}]$ . Single channel lipid bilayer studies have shown a bell shaped dependence of  $[\text{Ca}^{2+}]$  sensitivity, but inactivation does not occur until  $[\text{Ca}^{2+}]$  reaches  $1\text{mM}$ , which is presently believed to be unphysiological (Chen *et al.*, 1997; Copello *et al.*, 1997; Jeyakumar *et al.*, 1998).

### 1.1.3 Problems with CICR

CICR as a stand alone theory is inherently unstable. Once triggered, the RyR releases  $\text{Ca}^{2+}$ , which leads to further activation, generating a positive feedback loop. This leaves no mechanism for the closure of the RyR seen experimentally. Another problem with the theory is the gradedness of the release seen by Fabiato. This is difficult to reconcile with an "all-or-nothing" regenerative process. An additional, overriding process is required to explain both paradigms.

### 1.1.4 Local control of CICR

The theories of graded release and regenerative release could not be explained using a simple "common pool" model. It was generally believed that the part of the cytosolic pool in which calcium release and activation of Ca release from the SR occurred were continuous. A new theory of "local control" was proposed by Stern (Stern, 1992). This proposed that the majority of  $\text{Ca}^{2+}$  was released into the

surrounding cytosol, as opposed to the pool involved in activation. This overcame the regenerative positive feedback loop, by preventing re-activation of RyRs by released  $\text{Ca}^{2+}$ . Stern also concluded that the  $\text{Ca}^{2+}$  fluxes through individual release channels required to create a transient would be unfeasibly large. He therefore proposed RyR's were arranged in arrays (or "clusters"). This reconciled the graded aspect of CICR, as larger  $\text{Ca}^{2+}$  influx recruited clusters of ryanodine receptors, hence less  $\text{Ca}^{2+}$  flux was required though each receptor. Their opening was gated by "stochastic" processes, where the probability that a cluster would fire was increased by the cytosolic  $[\text{Ca}^{2+}]$ . In electron micrograph studies (Franzini-Armstrong *et al.*, 1999a) RyR clusters have since been observed, with an estimated 100-200 RyRs present in each. Stern proposed less than 10 channels gave the graded response and stopped instability. This is in disagreement with the numbers found by Franzini-Armstrong's group. Currently the number of RyR's that constitute a cluster is still to be resolved.

## 1.2 The Sarcoplasmic Reticulum

The SR is the main  $\text{Ca}^{2+}$  store in skeletal and cardiac muscle cells. The structure is analogous to the endoplasmic reticulum present in other types of cell, with a more regular structure, specialised for the efficient release of  $\text{Ca}^{2+}$  required for CICR.

The SR has a complex geometry, which can be divided into junctional SR (JSR) and non-junctional SR (NJSR). The non-junctional SR is distributed throughout the myoplasm and is thought to be mostly concerned with  $\text{Ca}^{2+}$  sequestration. The junctional SR exists as a foot-like structure in close proximity to the T-tubule. This foot like structure is also called the terminal cisternae (referred to as the subsarcolemmal cisternae in Figure 1-5). This region has a high density of RyRs and functions as a release unit.

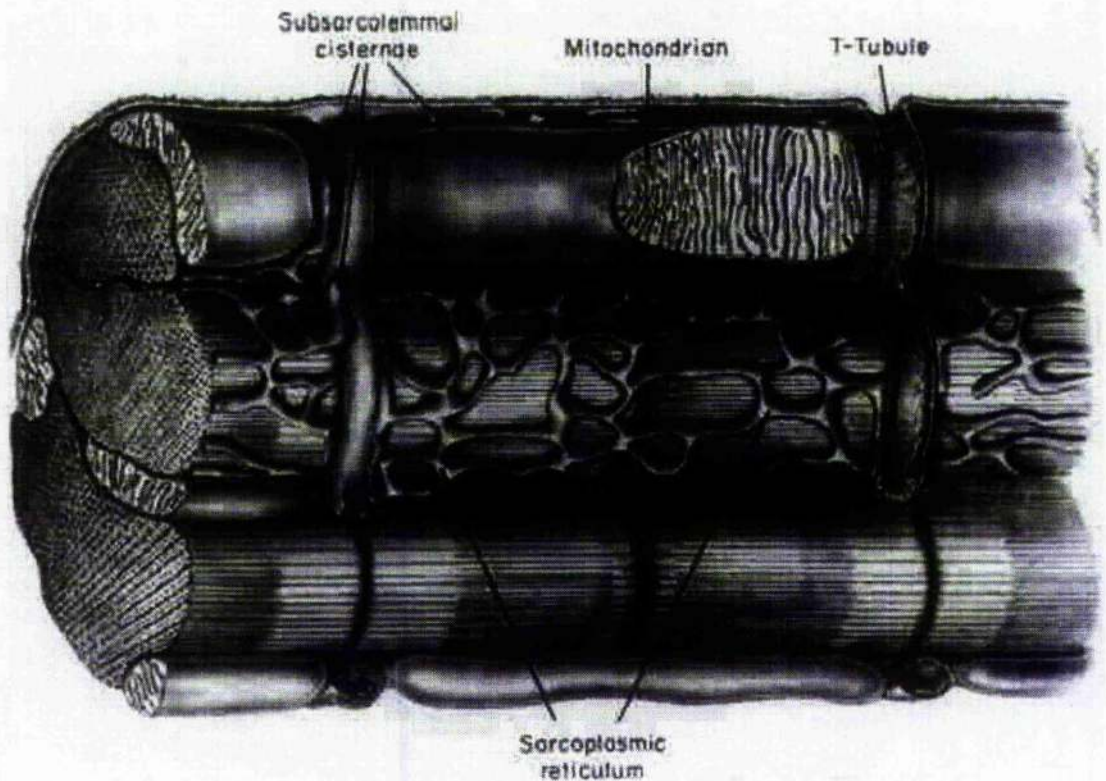


**Figure 1-5** Diagram showing the structure of the t-tubules, mitochondria and sarcoplasmic reticulum. (From Fawcett & McNutt, 1969).

Three known  $\text{Ca}^{2+}$  binding proteins exist within the SR. Calsequestrin is thought to bind the majority of  $\text{Ca}^{2+}$  in the SR and is localised to the junctional SR. Other proteins in the SR bind  $\text{Ca}^{2+}$ . Histidine-rich  $\text{Ca}^{2+}$ -binding protein (HRC) and sarcalumenin are distributed throughout the SR (Leberer *et al.*, 1990) suggesting a role in non-junctional  $\text{Ca}^{2+}$  buffering.

### 1.2.1 Calsequestrin

Calsequestrin (CSQ) is a 60kDa protein found within the terminal cisternae of the SR. Its major functional role is to buffer transported  $\text{Ca}^{2+}$  by serving as an intraluminal sink, facilitating active transport (Ikemoto *et al.*, 1989) of  $\text{Ca}^{2+}$  by serving as an intravesicular sink. It has a moderate affinity ( $K_D \approx 1 \text{ mM}$ ) and high capacity (40–50 molecules  $\text{Ca}^{2+}$  per molecule calsequestrin) for  $\text{Ca}^{2+}$  (Cozens and

Reithmeier, 1984; Ikemoto et al., 1972; MacLennan and Wong, 1971). It is thought to be functionally linked to the RyR via junctin and triadin to form a macromolecular complex.

RyRs may be functionally altered by  $\text{Ca}^{2+}$  binding to CSQ. Lipid bilayer studies have shown increasing  $[\text{Ca}^{2+}]$  on the luminal face increases the open probability ( $P_o$ ) of the RyR (Gyorke & Gyorke, 1998; Beard *et al.*, 2002). This action is proposed to be mediated by junctin and triadin (Gyorke *et al.*, 2004).

### 1.2.2 The ryanodine receptor

The RyR receptor is a homotetramer, with a total molecular mass of  $\sim 2.3$  Mda, so named because it reacts specifically with ryanodine, a highly toxic alkaloid (Campbell *et al.*, 1987; Fleischer *et al.*, 1985). The 3-d structure has recently been reconstructed from cryoelectron microscopy (see Figure 1-6)(Liu *et al.*, 2002).

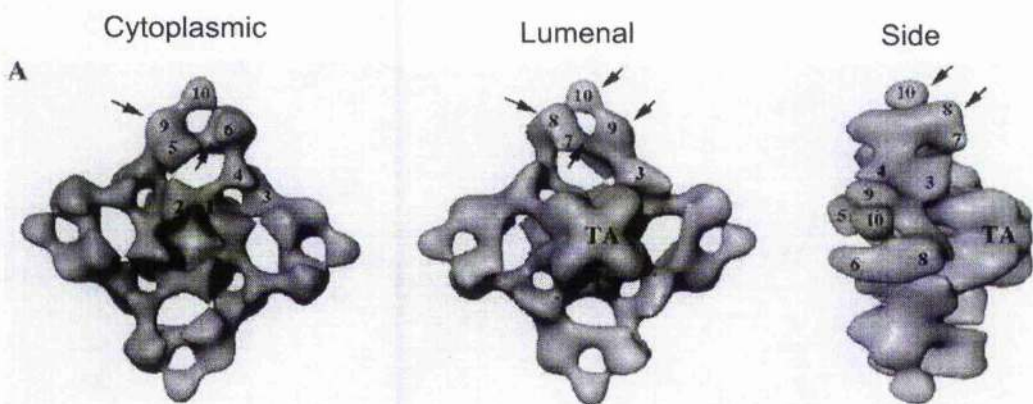


**Figure 1-6 Three-dimensional reconstruction of the cardiac ryanodine receptor. Three views from cytoplasmic, luminal and side. Figure from Liu et al., (Liu *et al.*, 2002).**

It serves as a high conductance  $\text{Ca}^{2+}$  channel ( $\sim 100\text{pS}$ ), active in various cell types. Type 1 RyR (RyR1) is primarily expressed in skeletal muscle, Type 2 (RyR2) is the primary isoform in heart involved in the E-C coupling in cardiac muscle and

Type 3 (RyR3) is expressed predominantly in non-muscle tissues (Murayama *et al.*, 1999). Physiologically, the channels serve to release stored  $\text{Ca}^{2+}$  in response to a cytosolic  $\text{Ca}^{2+}$  trigger. RyR  $\text{Ca}^{2+}$  sensitivity can be decreased by various agents ( $\text{Mg}^{2+}$ , tetracaine, ruthenium red) and increased by others ( $\text{Ca}^{2+}$ , ATP, caffeine).

In cardiac tissue it is thought to exist in arrays of clusters, each cluster regularly spaced along the cell. The minimum spacing has recently been found to be  $\sim 0.5\mu\text{m}$  in the transverse direction and  $\sim 1.8\mu\text{m}$  in the longitudinal direction (Franzini-Armstrong *et al.*, 1999b).

RyRs within each cluster are functionally coupled. One candidate for coupling is thought to be FKBP (FK506 Binding Protein) 12.6 (Marx *et al.*, 1998). This is proposed to allow communication between channels within a cluster, facilitating synchronisation of release.

### 1.2.3 SERCA

$\text{Ca}^{2+}$  sequestration by the SR is mediated by Sarcoplasmic/Endoplasmic Reticulum  $\text{Ca}^{2+}$ -ATPase (SERCA). Two calcium ions are transported by SERCA for each ATP molecule consumed (Tada & Katz, 1982). At least three species of SERCA exist. SERCA 1 is expressed in fast twitch skeletal muscle, while the SERCA 2 gene encodes two alternatively spliced products, SERCA 2a and 2b. SERCA 2a is expressed in cardiac and slow-twitch skeletal muscles (Brandl *et al.*, 1986); SERCA 2b in smooth muscle and non-muscle tissues (Tada & Toyofuku, 1996).

The rate of  $\text{Ca}^{2+}$  uptake by SERCA is regulated by cytosolic and lumenal  $[\text{Ca}^{2+}]$ . Its cytosolic pumping rate is stimulated by increased cytosolic  $\text{Ca}^{2+}$ , described by a Michaelis-Menten type enzyme kinetic scheme. Recently a dependence on

luminal  $\text{Ca}^{2+}$  has been proposed (Shannon *et al.*, 2000). The study demonstrates SERCA working in “reverse mode”, resulting in ATP production and  $\text{Ca}^{2+}$  pumping from luminal to cytosolic compartments. This increases energetic efficiency during the diastolic period, as ATP is produced by the reverse mode ATPase activity during the diastolic period.

SERCA is also regulated by the regulatory protein phospholamban (PLB). PLB association to SERCA inhibits the pump by increasing its  $\text{Ca}^{2+}$  dissociation constant ( $K_D$ ), with no effect on maximal pumping rate ( $V_{\text{max}}$ ). Tonic inhibition of the pump is thought to be relieved on stimulation by  $\beta$ -adrenergic agonists activating the cAMP second messenger system which activates PKA-dependent phosphorylation of PLB. PLB may also dissociate from SERCA in response to high cytosolic  $\text{Ca}^{2+}$  (Asahi *et al.*, 2000). This would lead to increased pumping rates at higher intracellular  $[\text{Ca}^{2+}]$ .

### **1.3 Spontaneous $\text{Ca}^{2+}$ oscillations in cardiomyocytes- a historical perspective**

$\text{Ca}^{2+}$  release from the SR is normally facilitated by  $\text{Ca}^{2+}$  entry through the L-type  $\text{Ca}^{2+}$  channel via CICR. In the absence of L-type  $\text{Ca}^{2+}$  activity, local spontaneous openings of RyR clusters occurs which generates a very localised release of  $\text{Ca}^{2+}$  termed  $\text{Ca}^{2+}$  sparks. If the SR  $[\text{Ca}^{2+}]$  is increased above a certain level, periodic spontaneous  $\text{Ca}^{2+}$  release occurs that significantly increases cytoplasmic  $[\text{Ca}^{2+}]$ . If the SR is sufficiently loaded with  $\text{Ca}^{2+}$ , the  $\text{Ca}^{2+}$  release propagates along the length of the cell. This is called a  $\text{Ca}^{2+}$  wave. This phenomenon has been known about for over 50 years in skeletal muscle (Natori, 1954; Marco & Nastuk, 1968; Takahashi, 1942). These early studies showed propagating contractions in

skinned myofibrils, usually exposed to a RyR sensitising agent such as caffeine or quinine chloride.

These were first described in cardiomyocytes as “after-contractions” or “nachkontraktionen” by Reiter (REITER, 1962).

### 1.3.1 Transient inward Current

With the advent of voltage clamp techniques developed for cardiac muscle, these after-contractions were recorded in Purkinje fibres on exposure to acetylstrophanthidin, and seen closely related in time to “transient depolarisations” (Ferrier, 1976). The electrophysiological attributes of the events was investigated further by Lederer and Tsien (Lederer & Tsien, 1976).

Strophanthidin is a cardioactive steroid, which works by inhibiting the sarcolemmal Na/K ATPase. This elevates intracellular  $\text{Na}^+$ , which in turn increases  $\text{Na}^+$  extrusion and  $\text{Ca}^{2+}$  entry on the NCX.

Lederer and Tsien found that after exposure to strophanthidin ( $1\mu\text{M}$ ), an action potential was followed by a transient depolarisation, that was insufficient to cause arrhythmia. These transient depolarisations were associated with transient inward current ( $I_{ti}$ ) when under voltage-clamp. This is shown in Figure 1-7

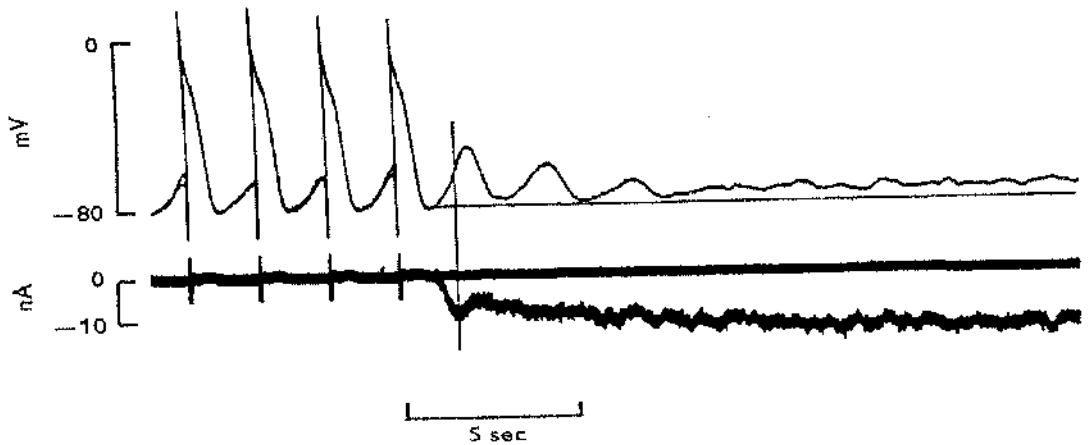


**Figure 1-7** The transient depolarization (TD) and the TI: a comparison of timing and magnitude.

The two superimposed records are from the same experiment. The upper panel shows the two records of membrane potential, while the lower panel shows the two corresponding current records. After the tenth action potential of the first run, external stimulation was discontinued and voltage-clamp control was not imposed, allowing the development of transient depolarizations. Following the tenth action potential in the next series, the membrane potential was clamped at the maximum diastolic potential. The vertical bar runs through the peak of the TI and shows its relationship to the TD. The magnitude of the TI is 10 nA and the maximum rate of rise of the TD is 0.06 V/sec. (from Lederer and Tsien, 1976).

The link with SR  $\text{Ca}^{2+}$  release was made 2 years later, by Kass et al., (Kass *et al.*, 1978). This study showed inhibition of the  $I_{\text{ti}}$  when the “slow inward current” (i.e. the L-type calcium channel) was blocked. They also showed the occurrence of  $I_{\text{ti}}$  when external  $\text{Ca}^{2+}$  was elevated. They concluded the  $I_{\text{ti}}$  was caused by  $\text{Ca}^{2+}$  release from a  $\text{Ca}^{2+}$  overloaded SR as seen earlier by Fabiato and Fabiato (Fabiato & Fabiato, 1972).

### 1.3.2 Fabiato's disrupted membrane study

Alexandre Fabiato produced a series of papers investigating the behaviour of the SR in isolated cells with disrupted membranes. The cells showed spontaneous oscillations, with contractions propagating at 50-100 $\mu\text{m}/\text{sec}$ .

When free  $[Ca^{2+}]$  in the bathing solution was increased from 316 nM to 3160 nM, the oscillations were shown to increase in frequency and amplitude. The study concluded that the cyclic contractions were caused by a regenerative release from a “ $Ca^{2+}$  sink” within the cell, induced by filling above a threshold. Propagation of the oscillations was explained by proposing that the initial  $Ca^{2+}$  release from one storage site triggers release from an adjacent storage site. The study proposed 3 possible release sites:- the SR, the mitochondria and sub-sarcolemmal vesicles, which were probably the junctional SR (JSR). No conclusion was drawn as to which played the key role in the release.

### 1.3.3 SLIFs

A new method was developed, which allowed measurement of scattered light intensity fluctuations (SLIF) in resting rat papillary muscles (Lappe & Lakatta, 1980). This technique used phase-contrast microscopy under coherent illumination. The emitted light was scattered due to diffraction by the sarcomere pattern. When sarcomeres contracted, the scattered light pattern changed. In intact rat trabeculae, Lakatta and his group showed spontaneous changes in the SLIFs, while the preparation was unstimulated. They identified the SR as the source of  $Ca^{2+}$ , which generated this form of spontaneous activity. At the time, they put forward the argument that the underlying spontaneous  $Ca^{2+}$  release and uptake for the SR was part of the normal activity of heart muscle.

This method was used to investigate SLIFs until the early 90's (Lappe & Lakatta, 1980; Stern *et al.*, 1983; Kort & Lakatta, 1984; Walford *et al.*, 1984; Kort *et al.*, 1985; Capogrossi *et al.*, 1986; Sutko *et al.*, 1986; Orchard *et al.*, 1987; Kort & Lakatta, 1988b; Kort & Lakatta, 1988a; Stern *et al.*, 1989; Weiss *et al.*, 1990).

Whilst this method could be used to monitor movement in isolated papillary and

whole heart preparations, no additional information of subcellular  $\text{Ca}^{2+}$  release was found.

#### 1.3.4 Early $\text{Ca}^{2+}$ measurements.

The first  $\text{Ca}^{2+}$  measurement from a cardiac cell was made by Allen & Blinks in 1978 and the first measurements from a mammalian cell were made by Wier in 1979 (Allen & Blinks, 1978; Wier, 1979). In their 1983 paper Orchard *et al.*, (Orchard *et al.*, 1983) measured spontaneous intracellular  $\text{Ca}^{2+}$  oscillations with aequorin luminescence (Orchard *et al.*, 1983). Strophanthidin ( $10\mu\text{M}$ ) was used to produce  $\text{Ca}^{2+}$  overload and hence induce  $\text{Ca}^{2+}$  waves. Previous studies had inferred these fluctuations from changes in tension or observation of the propagated contraction. This was the first paper to directly measure a rise of intracellular free  $[\text{Ca}^{2+}]_i$  due to spontaneous release of  $\text{Ca}^{2+}$  from the SR. Due to the low levels of light emitted by aequorin, measurements were typically made using multicellular preparations ~80 cells injected with aequorin. One study restricted injection to one cell in a papillary muscle (Allen *et al.*, 1985). This facilitated the study of spontaneous  $\text{Ca}^{2+}$  oscillations at the cellular level.

#### 1.3.5 Improved $\text{Ca}^{2+}$ indicators

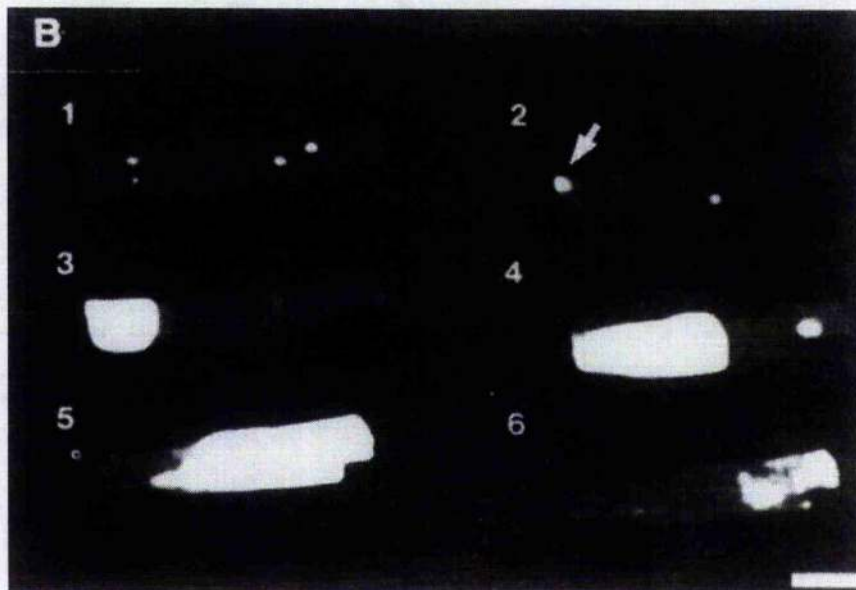
The next technological advancement was the development of fluorescent indicators (Tsien *et al.*, 1985; Grynkiewicz *et al.*, 1985). These allowed measurement of  $[\text{Ca}^{2+}]_i$  and could be loaded into cardiomyocytes to allow subcellular measurements (Tsien *et al.*, 1985). Wier *et al.* (Wier *et al.*, 1987) were the first to use this technique in isolated ventricular cardiomyocytes. They found spontaneous  $\text{Ca}^{2+}$  release events propagating as "waves" along the cell with a velocity of  $\sim 100\mu\text{m}/\text{sec}$ . The temporal and spatial resolution was limited, so quantification of the time course of the wave was not possible.

### 1.3.6 Subcellular resolution achieved by confocal microscopy

With the advent of commercially available confocal microscopes, the time course of the wave could be examined more thoroughly. The confocal microscope was invented by Marvin Minsky in 1953 but did not become feasible as a biological tool until the late eighties/early nineties. Investigators studying  $\text{Ca}^{2+}$  signals in cardiomyocytes used the single wavelength dye Fluo 3 (Minta *et al.*, 1989). This was capable of accurately observing  $\text{Ca}^{2+}$  changes in the 0.1 to 1.5  $\mu\text{M}$  range, which was ideal for the  $\text{Ca}^{2+}$  release events taking place in cardiac cells. The first paper to use this technique was published in 1992 (Williams *et al.*, 1992). This was a preliminary paper, which examined the possibilities of studying the properties of  $\text{Ca}^{2+}$  waves. Initial estimates showed rise times of the release seen in waves and electrically evoked transients were different. Waves reached a peak after 84 msec, whilst transients rose more quickly, reaching their peak after 36msec. Wave velocities were also estimated at between 50 and 150  $\mu\text{ms}^{-1}$ .

The study was repeated the following year, with emphasis on the initiation of the wave (Cheng *et al.*, 1993). Their method allowed resolution of small spontaneous release events which were confined to a small volume of the cell. This they named the “ $\text{Ca}^{2+}$  spark” (Figure 1-8 A). Early studies using single RyRs reconstituted into lipid bilayers showed the flux of  $\text{Ca}^{2+}$  ions through the RyR was  $\sim 3$  pA (Fill & Coronado, 1988). The sparks study showed fluxes of  $\sim 4$  pA. They therefore concluded the fluxes they saw in a spark were due to either one RyR or a cluster of channels acting in concert. Other groups later revised these RyR flux amplitude estimations using more physiological conditions. These are currently believed to be 0.2 pA for single channels (Mejia-Alvarez *et al.*, 1999) and 7-12 pA for the flux due to a spark (Soeller & Cannell, 2002).

The study also showed propagating releases ( $\text{Ca}^{2+}$  waves)(Figure 1-8 B and C). Waves were commonly seen to follow what they termed “macrosparks”. These were concluded to be summation of adjacent release sites. This summation of sparks was proposed to initiate the propagating events. Waves were seen when external  $\text{Ca}^{2+}$  was raised from 1mM to 10 mM. This induced  $\text{Ca}^{2+}$  “overload leading to production of propagating events.



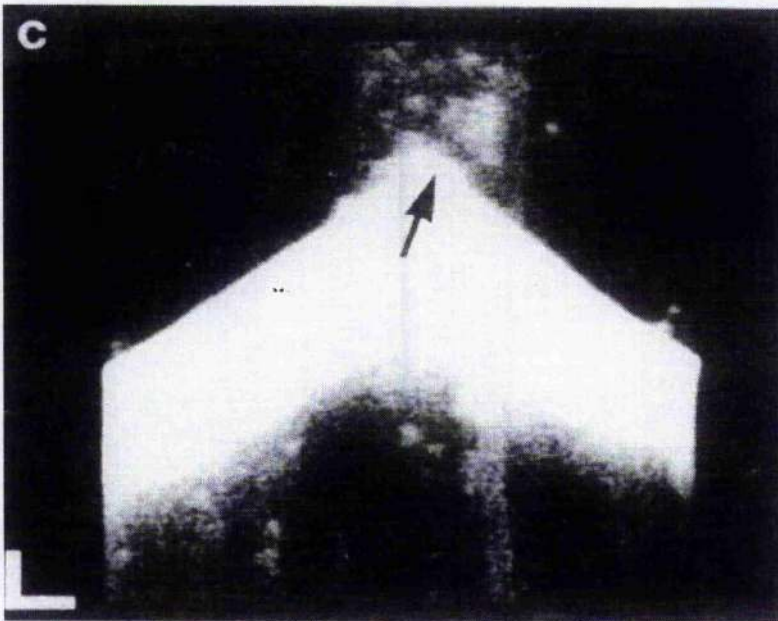


**Figure 1-8** Figures showing spontaneous  $\text{Ca}^{2+}$  release events in ventricular cardiomyocytes.

Scale bar in A and B represents  $20\mu\text{m}$ ; In C horizontal represents  $10\mu\text{m}$ , vertical  $200\text{ms}$ .

**A-** Fluo 3 loaded ventricular cardiomyocyte. Extracellular  $\text{Ca}^{2+}$  is elevated causing  $\text{Ca}^{2+}$  overload. Spontaneous localized releases are seen as bright “sparks”. The arrow shows the summation of adjacent release sites in a “macrospark”.

**B-** Sequential images from the same cell. The arrow points to a macrospark site, which initiates a propagating  $\text{Ca}^{2+}$  release event.

**C-** A linescan image of a  $\text{Ca}^{2+}$  wave. One line within the cell is scanned repeatedly every 2 ms. Consecutive lines are appended to the bottom of the image. Hence time displaced downwards and the distance along the cell is displaced horizontally. The arrow shows a macrospark which activates the wave. The wave propagates from the centre outwards. (Cheng *et al.*, 1993).

The group revisited the subject 3 years later, with a more quantitative approach (Cheng *et al.*, 1996a). Extensive image analysis allowed the resolution of some unanswered questions. After linescans were adjusted for optical artefacts, the wave and depolarisation evoked transient were found to have the same time course, suggesting the same underlying kinetics of release and reuptake. This view directly contradicts the earlier studies (Williams *et al.*, 1992; Takamatsu & Wier, 1990).

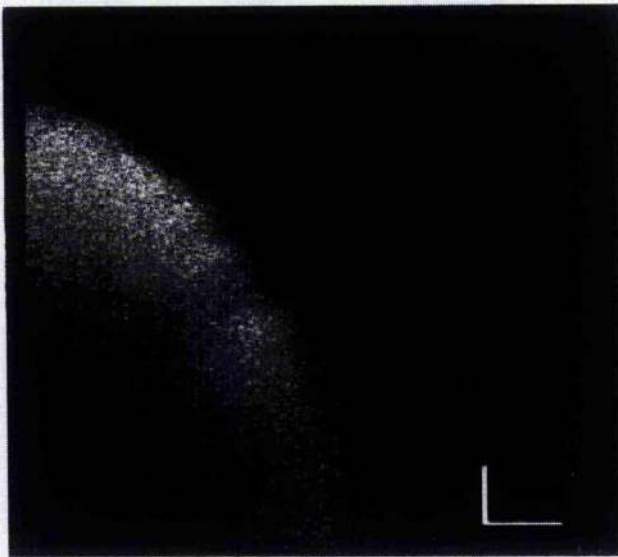


**Figure 1-9 Abortive  $\text{Ca}^{2+}$  wave.**

**A decrease in velocity and amplitude is observed as the wave moves left to right. Scale bars: 5  $\mu\text{m}$  horizontally and 100 ms vertically.**

### **1.3.7 Deconvolution of the $\text{Ca}^{2+}$ wave**

The study used deconvolution of the wave to correct for velocity. This corrected for the underestimation of time course and amplitude of the wave when averaging the wavefront.

The study therefore concluded that the underlying mechanism behind CICR seen in waves and transients was the same and that both were due to the summation of  $\text{Ca}^{2+}$  sparks. The other important conclusion they made concerned wave velocity. They used a cross-correlation method to measure wave velocity. This allowed them to draw the conclusion that wave velocity change with wave amplitude. As  $\text{Ca}^{2+}$  wave events aborted, their velocity and amplitude was shown to fall concomitantly. The reason for this was thought to be a decrease in open probability of the RyR combined with a decrease in SR  $[\text{Ca}^{2+}]$  (Cheng *et al.*, 1996a).

### 1.3.8 Spontaneous release –role in afterdepolarisations

The transient inward current ( $I_{ti}$ ) and spontaneous contractions as observed in the overload experiments of the studies by Reiter and later Lederer were revisited by Volders et al (Volders *et al.*, 1997). This study induced  $Ca^{2+}$  overload by application of isoproterenol and varying pacing frequencies in isolated canine cardiomyocytes. They observed early afterdepolarizations (EAD's) and delayed afterdepolarizations (DAD's) accompanying spontaneous cell contraction. They concluded both EAD's and DAD's were caused by the same mechanism i.e. spontaneous  $Ca^{2+}$  release similar to that seen by Cheng et al in 1996, Blocking NCX stopped initiation of EAD's and DAD's, but did not stop spontaneous contractions. It was therefore concluded that EAD's and DAD's were initiated by  $Ca^{2+}$  efflux via NCX.

Recent advances in understanding the mechanisms underlying  $Ca^{2+}$  waves have used mathematical modelling. This is discussed below.

### 1.4 Modelling spontaneous $Ca^{2+}$ release

Over the years, uncertainties raised by experimental procedures have necessitated the mathematical models to increase understanding of the mechanisms proposed to explain CICR. Models generally address:

$Ca^{2+}$  release as part of E-C coupling

$Ca^{2+}$  sparks

$Ca^{2+}$  waves

No models exist which incorporate all three phenomena.

With increasing computing power, models have increased in complexity, modelling release, uptake and diffusion in both 2 and 3 dimensions.

### 1.4.1 Modelling $\text{Ca}^{2+}$ wave velocity

An early model of propagating CICR, by Backx et al., (Backx *et al.*, 1989) described a cytosol where  $\text{Ca}^{2+}$  release units (CRUs) were distributed uniformly throughout the cell. This model showed velocity to increase when diastolic  $[\text{Ca}^{2+}]$ , rate of rise of the release and the amplitude of release were increased. With a homogeneous distribution of CRUs, this model predicted unrealistic velocities (up to  $15 \text{ mms}^{-1}$ ). In a real cell, CRUs are typically  $2\mu\text{m}$  apart. However leaving aside this quantitative discrepancy, the basic behaviour was similar to experimental results, with higher levels of loading resulting in higher propagation velocity.

### 1.4.2 Saltatory $\text{Ca}^{2+}$ Propagation

Keizer and Smith (Keizer & Smith, 1998) created a model with more realistic CRU separation. CRUs were  $2\mu\text{m}$  apart and were triggered by increased cytosolic  $[\text{Ca}^{2+}]$ . The CRUs included a 2-state gating scheme, which was shown to have similar release characteristics to other 4-state gating models (Smith, 1996). The RyRs existed as either refractory or non-refractory sites, such that when refractory, CRUs could not be activated until a set period of time had passed. With this scheme, the study showed realistic “saltatory” propagation of  $\text{Ca}^{2+}$  waves, with realistic velocities. It was also noted that the velocity increased linearly with the diffusion coefficient ( $D$ ), unlike the homogeneously distributed release site model, where velocity increased linearly with  $\sqrt{D}$  (where  $D$  = diffusion coefficient for  $\text{Ca}^{2+}$ ). This model had significant simplifications to shorten time required to run the simulation, these are listed below:

True stochastic behaviour of the RyR channels was simplified to approximate the underlying processes, with opening occurring after a threshold cytoplasmic  $[\text{Ca}^{2+}]$  was reached.

Cytosolic buffering of  $\text{Ca}^{2+}$  was approximated by modifying the diffusion coefficient (D).

The model was extended by Subramanian et al., (Subramanian *et al.*, 2001), to include cellular buffering and propagation in 2 dimensions. The model focused on the geometry of the  $\text{Ca}^{2+}$  wave. They modified RyR spacing to produce circular as opposed to elliptically propagating  $\text{Ca}^{2+}$  waves. The sarcomere was modelled as a cylinder, with RyRs spaced  $2\mu\text{m}$  apart longitudinally and  $0.5\mu\text{m}$  transversely (see Figure 1-10). Evidence for this geometry comes from Franzini-Armstrong's group (Franzini-Armstrong *et al.*, 1999b), where electron microscopy was used to discover RyR spacing  $\geq 412\text{nm}$ . Subramanian et al., concluded that with this arrangement, waves would propagate in an elliptical fashion (Franzini-Armstrong *et al.*, 1999b). This caused them to speculate that diffusion was anisotropic. A similar conclusion was made when elliptically shaped sparks were observed by Cheng et al.,(Cheng *et al.*, 1996c). This group surmised that this anisotropic diffusion was due to cellular diffusion barriers e.g. mitochondria.

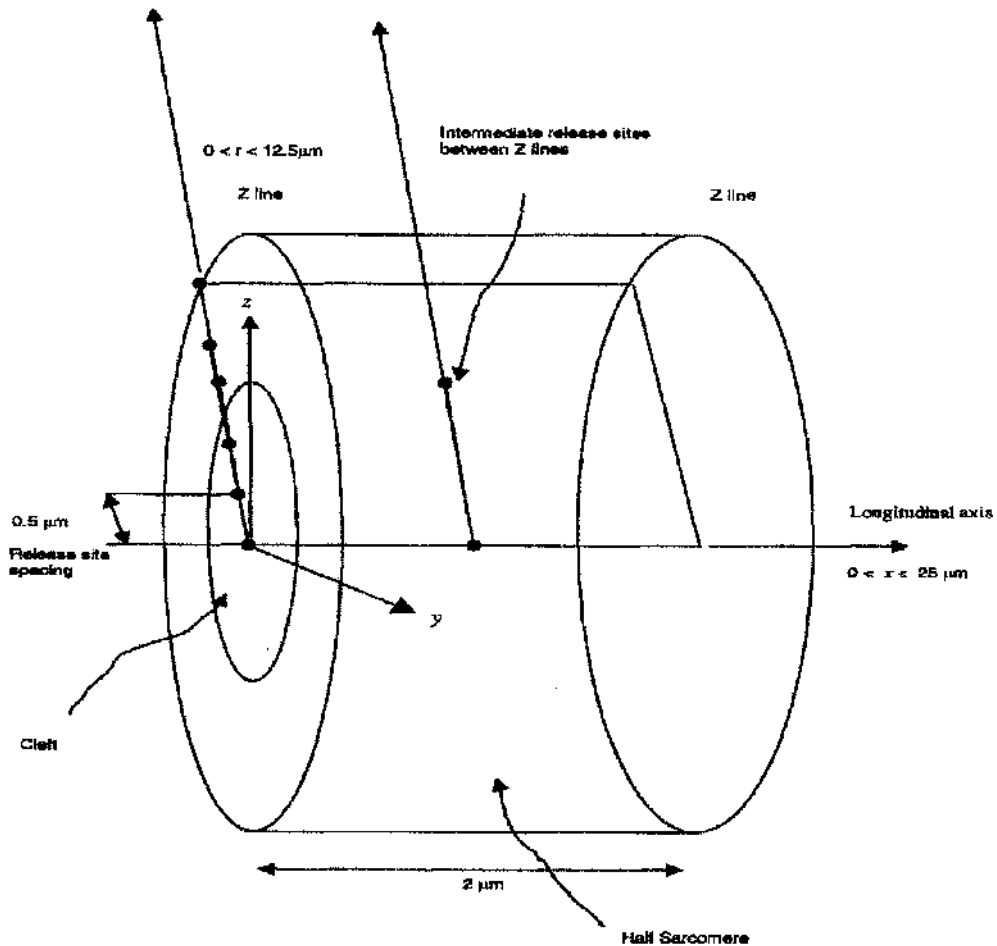


Figure 1-10 Geometry of the Subramanian et al., model.

The area labelled cleft refers to the dyadic cleft, which is the space just under the extracellular membrane, where  $\text{Ca}^{2+}$  enters the cell when the I-type channel is opened). The half-sarcomere is modelled in cylindrical coordinates ( $r, x$ ). The simulation was conducted over a domain spanning a distance of  $25 \mu\text{m}$  in both the  $r$  and  $x$  directions. Discrete release sites of identical source strength are placed at a distance of  $0.5 \mu\text{m}$  from each other in the  $r$  direction, at each Z-line. The Z-lines are spaced  $2 \mu\text{m}$  apart in the longitudinal direction. Intermediate release sites are placed (one intermediate site for every five release sites at Z-lines) between Z-lines in some of the simulations to study their effect of wave symmetry and velocity. Distribution of Ca:dye at various times in this simulation domain was collected in the form of  $r$ - $x$  images. (Subramanian *et al.*, 2001).

Published, with an accompanying paper by Izu et al. (Izu *et al.*, 2001), this paper proposed a model capable of generating  $\text{Ca}^{2+}$  sparks and waves.

This also used cytosolic  $\text{Ca}^{2+}$  as a trigger for  $\text{Ca}^{2+}$  waves. Once triggered, the release was terminated after a set time. The flux amplitude through the release site

and the cytosolic  $\text{Ca}^{2+}$  release threshold were varied as required to assess changes in  $\text{Ca}^{2+}$  wave velocity and amplitude.

From this scheme, the prime determinant of wave velocity was found to be the sensitivity of the CRU to cytosolic Ca. The trigger threshold was set relatively high (15 $\mu\text{M}$ ), in order to recreate velocities found experimentally. The currents required in this model, (20pA) were unrealistically high. In-depth spark analysis has been carried out and the current through the RyR was estimated as  $\sim 6$  pA (Soeller & Cannell, 2002). The discrepancy between the Izu et al. model and those measured experimentally may either highlight experimental limitations or limitations of the model. Possibly such large fluxes are necessary to compensate for the exclusion of additional aspects of the release event. For instance, neither luminal control of release nor inactivation of the release were dealt with. This may point to the fact that this is necessary for a complete description of the model.

#### **1.4.3 Luminal control of $\text{Ca}^{2+}$ release**

The aspect of luminal control was focused on by Lukyanenko et al., (Lukyanenko *et al.*, 1999) in their model of propagating  $\text{Ca}^{2+}$  release. This paper, which included this model, stressed the concept that increasing luminal  $\text{Ca}^{2+}$  leads to increased sensitivity of the cytosolic  $\text{Ca}^{2+}$  sensor. Regulation by luminal  $\text{Ca}^{2+}$  was modelled indirectly in this study by changing the threshold cytosolic  $[\text{Ca}^{2+}]$  required for release. They found that decreasing cytosolic  $\text{Ca}^{2+}$  sensor sensitivity lead to increased wave velocity. This fitted well with their experimental results, which showed increased wave velocity when low concentrations of caffeine were applied, thus increasing RyR sensitivity. Surprisingly, changes in luminal  $[\text{Ca}^{2+}]$  were not modelled. SR  $[\text{Ca}^{2+}]$  was modelled as a fixed value in the simulation and was unchanged by SR fluxes.

### 1.5 Current theory for mechanisms underlying spontaneous waves

$\text{Ca}^{2+}$  waves as observed in the cardiac ventricular myocyte are a phenomenon associated with overload of the SR (Fabiato & Fabiato, 1972; Cheng *et al.*, 1993; Cheng *et al.*, 1996a; Lukyanenko *et al.*, 1999).

$[\text{Ca}^{2+}]$  in the SR reaches a threshold value; a cluster of RyRs opens, releasing  $\text{Ca}^{2+}$ , which causes a regenerative wave of CICR, propagating along the cell. The event begins with the release from an initial site causing a macrospark. This macrospark causes a release of sufficient amplitude to spread to neighbouring release sites. Since the SR is overloaded in these neighbouring sites, they are rendered more sensitive to cytosolic  $\text{Ca}^{2+}$ . The  $\text{Ca}^{2+}$  diffusing from the macrospark is sufficient to cause the neighbouring site to fire by CICR. The macrospark site has elevated  $\text{Ca}^{2+}$  locally, so the majority of newly released  $\text{Ca}^{2+}$  from the CICR site will tend to move to the region of cytoplasm where release has not occurred.

The release secondary to diffusion from the macrospark has 3 possible triggers:

- (1) A rise in cytosolic  $\text{Ca}^{2+}$  triggers RyR opening via CICR.
- (2)  $\text{Ca}^{2+}$  is taken up by neighbouring SR uptake units, increasing lumenal  $\text{Ca}^{2+}$ , sensitising the RyR to cytosolic  $\text{Ca}^{2+}$  causing it to open.
- (3) A combination of both mechanisms, whereby SR  $\text{Ca}^{2+}$  load sensitises the cytosolic  $\text{Ca}^{2+}$  sensor to initiate release.

A recent study used thapsigargin to inhibit SERCA, thus reducing uptake (Lukyanenko *et al.*, 1999). This was found to potentiate propagation, thus contradicting the second mechanism. However, it could still play a minor role in propagation.

The relationship between luminal  $\text{Ca}^{2+}$  and RyR sensitivity is best illustrated by examining the gain of E-C coupling. Gain used in the context of E-C coupling means the ability of the L-type channel to elicit a release from the SR.

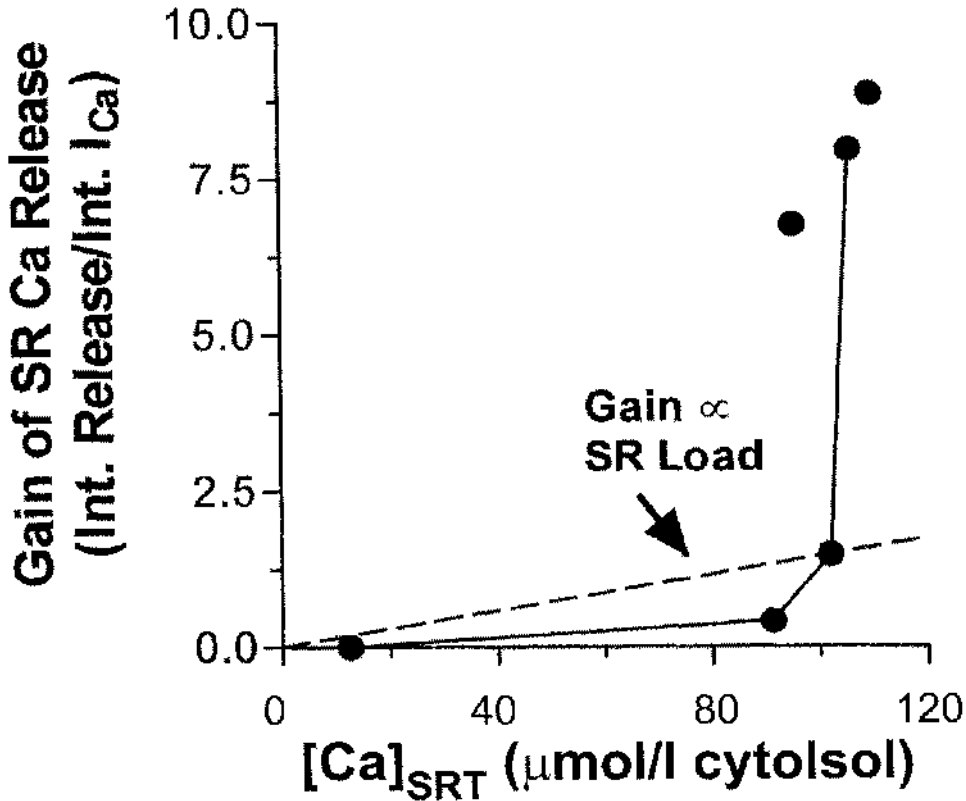


Figure 1-11 E-C coupling gain vs. total SR  $[\text{Ca}^{2+}]$  ( $[\text{Ca}^{2+}]_{\text{SRT}}$ ). After a threshold value is passed, gain increases sharply.

The data suggests a sharp increase in gain once  $[\text{Ca}^{2+}]_{\text{SRT}}$  (Total  $[\text{Ca}^{2+}]$  within the SR) passes a threshold value. This indicates that luminal  $\text{Ca}^{2+}$  can act as an effective “switch” triggering the opening of RyRs above a threshold level. This threshold has also been alluded to by Diaz *et al.*, where spontaneous waves were studied, with increasing external  $\text{Ca}^{2+}$  (Diaz *et al.*, 1997). This caused increased wave frequency, but assessment of SR  $\text{Ca}^{2+}$  by caffeine application showed no increase in load. They therefore determined that the SR calcium load reached a limit, after which a spontaneous release was triggered.

### 1.5.1 Why do sparks not always trigger propagated release?

Under conditions of low cytosolic  $\text{Ca}^{2+}$ , sparks occur without propagation and experimental evidence exists to show that the SR is unable to support regenerative waves (Trafford *et al.*, 1995). As lumenal  $\text{Ca}^{2+}$  is increased, sparks increase in amplitude and frequency and become initiation sites for propagating  $\text{Ca}^{2+}$  waves (Cheng *et al.*, 1993; Lukyanenko *et al.*, 1996; Satoh *et al.*, 1997). Waves are not seen at low cytosolic  $[\text{Ca}^{2+}]$  because  $\text{Ca}^{2+}$  release and RyR sensitivity are lower due to lower  $[\text{Ca}^{2+}]_{\text{SR}}$ .

### 1.5.2 Is there a refractory period for $\text{Ca}^{2+}$ release in $\text{Ca}^{2+}$ waves?

The mechanism behind the termination of  $\text{Ca}^{2+}$  transients, sparks and waves is the subject of debate. Conflicting studies have shown inactivation due to lumenal depletion (Terentyev *et al.*, 2002; Sitsapesan & Williams, 1997) and adaptation/inactivation due to high cytosolic  $\text{Ca}^{2+}$  (Laver *et al.*, 1995; Laver & Lamb, 1998).

#### 1.5.2.1 Theories of Refractoriness

**Adaptation** was first proposed by Fabiato (Fabiato, 1985c). This describes the process whereby release from the RyR increases locally, causing a decrease in sensitivity of the channel. This has been supported by lipid bilayer studies (Gyorke & Fill, 1993), but is thought to act too slowly to play a major physiological role (Sham *et al.*, 1998; Bers, 2002).

**Inactivation** of the ryanodine receptor is a description of true refractoriness. This process describes a mechanism whereby  $\text{Ca}^{2+}$  release through a RyR prevents further release through that channel until a refractory period is ended. This was elegantly described in the study by Sham *et al.* (Sham *et al.*, 1998). The study was criticised for its use of high [EGTA] (5mM) to investigate release. This may

impede full activation of RyR clusters by preventing local diffusion of  $\text{Ca}^{2+}$ , reduce inactivation/adaptation by decreasing local cytosolic  $[\text{Ca}^{2+}]$  subsequent to release and might decrease uptake by SERCA, leading to luminal depletion.

**Luminal depletion** of SR  $\text{Ca}^{2+}$  may cause an inactivation of the RyR.

Termination of  $\text{Ca}^{2+}$  sparks and transients cannot be accounted for by a passive mechanism such as depletion (Sham *et al.*, 1998; Lukyanenko *et al.*, 1998). An additional, extinguishing mechanism is required. This was initially investigated in mice overexpressing calsequestrin, which exhibited decreased  $\text{Ca}^{2+}$  transients. Increased buffer should have caused larger, prolonged transients, but the opposite was seen. This discrepancy may have been caused by compensatory changes in expression of other proteins involved in CICR.

A subsequent study on luminal buffering was carried out by Terentyev *et al.* (Terentyev *et al.*, 2002). This study mimicked increased calsequestrin by adding exogenous  $\text{Ca}^{2+}$  buffers, which were loaded into the SR. This study showed increased RyR opening time and amplitude of transients, and concluded RyR openings were extinguished by intra SR regulation of RyRs.

#### 1.5.2.2 Is there evidence for this in the $\text{Ca}^{2+}$ wave?

When  $\text{Ca}^{2+}$  waves collide, the propagation is annihilated (Cheng *et al.*, 1996a; Williams *et al.*, 1992; Lipp & Niggli, 1993). This annihilation may be due to depletion of SR stores, or a desensitisation of the RyRs. When a propagating  $\text{Ca}^{2+}$  wave is closely followed by a depolarisation induced  $\text{Ca}^{2+}$  transient, the release is attenuated depending on how recently the region has released  $\text{Ca}^{2+}$ . This is shown in Figure 1-12. The depolarising action potential releases less  $\text{Ca}^{2+}$  when a  $\text{Ca}^{2+}$  wave has recently occurred in that region. This refractoriness was not observed when caffeine was applied (Lukyanenko *et al.*, 1996). This is difficult to reconcile

with depletion-inactivation theories. Caffeine seems to overcome the mechanism responsible for the refractoriness seen in the depolarisation evoked release.

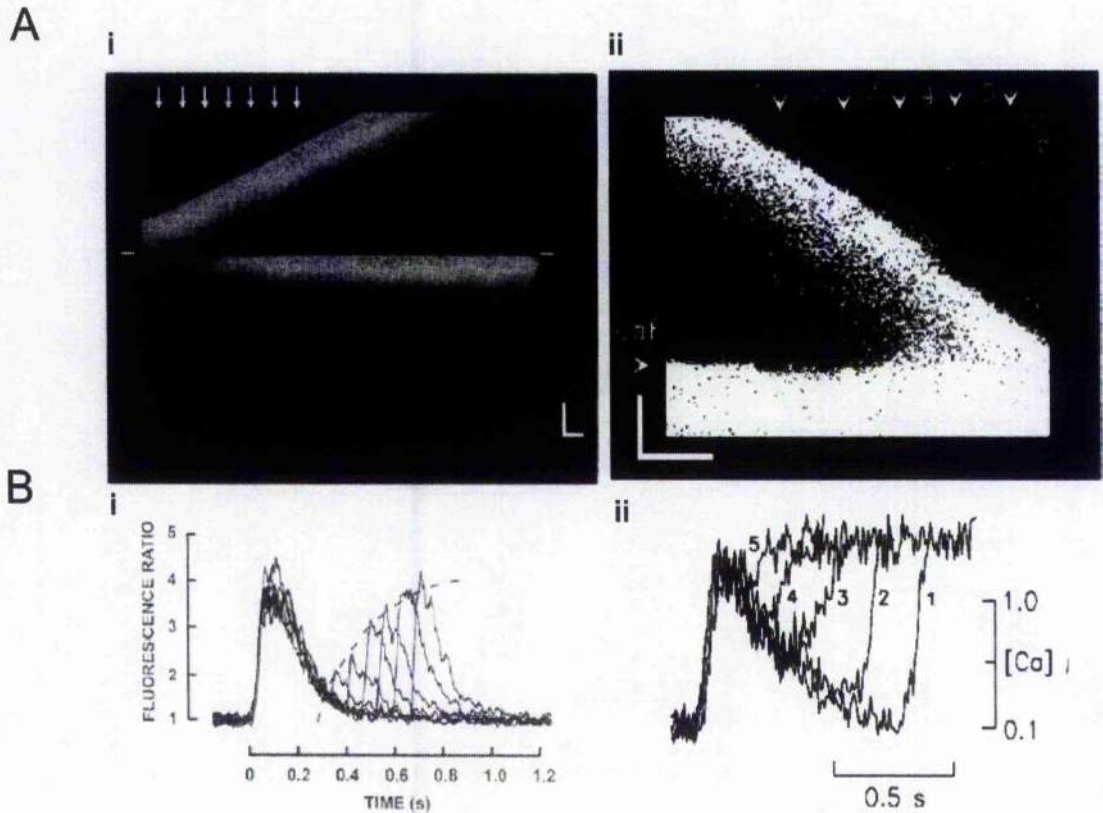


**Figure 1-12 Recovery of action potential and caffeine evoked transients following a  $\text{Ca}^{2+}$  wave in a rat ventricular myocyte.**

**A.** Linescan showing action potential (i) and caffeine evoked transient (ii) following  $\text{Ca}^{2+}$  wave. i) Image shows  $\text{Ca}^{2+}$  wave propagating from right to left. White bar at either side of image shows time of depolarization. Subsequent transient show less release where  $\text{Ca}^{2+}$  wave has recently occurred. **B i)**  $\text{Ca}$  wave (measured with Fluo-3) amplitude taken from bands indicated by arrows above image, after offsetting temporally for velocity of wave. Evoked transients are displaced relative to the preceding wave.

**Ai.** Depolarization evoked transient following a  $\text{Ca}^{2+}$  wave. **ii.** Same as Bi, only with caffeine evoked transient. Amplitude of transient is not diminished by release from preceding wave.

Data on left from Cheng et al. (1996) and Lukyanenko et al. (1996) on the right.

To investigate whether refractoriness is dependent on SR [ $\text{Ca}^{2+}$ ], a reliable measure of SR [ $\text{Ca}^{2+}$ ] is required. Recently, it has been shown that it is possible to load the SR with the  $\text{Ca}^{2+}$  fluorophore Fluo-5N (Shannon *et al.*, 2003). A “useful” signal was acquired by averaging whole cell behaviour, as signal-to-noise ratio was very

low. This allowed estimation of SR depletion during 1Hz stimulation (~50%). They discovered the SR filled with a time constant of 100ms compared to previous measures of the time constant of refractoriness measured as ~300 ms (Niggli, 1999). No studies on refractoriness of measuring SR  $[Ca^{2+}]$  changes during  $Ca^{2+}$  waves exist, so no conclusions can be drawn to explain the annihilation of colliding waves.

### **1.6 Aims of the project.**

The overall aim of this project is to first quantify the fluxes involved in the regenerative  $Ca^{2+}$  release seen in the wave, then to incorporate these in a realistic 3-compartmental model of a permeabilised cardiomyocyte.

Confocal microscopy will be employed to quantify the changes in  $[Ca^{2+}]_i$  during  $Ca^{2+}$  waves in permeabilised cardiomyocytes. Methods will be employed to ensure cell contraction is minimised and intracellular dyes are calibrated to allow accurate conversion of fluorescence to  $[Ca^{2+}]$ .

$Ca^{2+}$  fluxes between the SR and cytosol will be quantified by accounting for  $Ca^{2+}$  binding to cellular proteins,  $Ca^{2+}$  loss/gain due to diffusion. The resultant derived SR  $Ca^{2+}$  flux will then be quantified in terms of SR uptake and release.

Cellular  $Ca^{2+}$  binding will be quantified using a novel multicellular cell assay system.  $Ca^{2+}$  diffusion will be assessed using rapid application of Caffeine. Caffeine will also be used to assess the percentage of SR  $Ca^{2+}$  released during a wave.

A method of deriving the changing SR  $[Ca^{2+}]$  will also be devised.

An existing model of SERCA will be utilised to quantify its maximal pumping rate ( $V_{max}$ ) and affinity constant ( $K_m$ ). Once this is done, it will allow derivation of RyR fluxes and permeability.

Changes in wave frequency, Systolic (peak) and Diastolic (min)  $[Ca^{2+}]_i$  will be assessed under three experimental conditions:

- 1) Over a range of external  $Ca^{2+}$ .
- 2) In the presence of a SERCA inhibitor.
- 3) In the presence of a RyR inhibitor.

Changes in properties of uptake and release will be quantified.

A 3-compartment computational model will be constructed, which replicates the  $Ca^{2+}$  release behaviour observed experimentally. The model will be extensively validated and its success in replicating the three experimental situations mentioned above will be assessed.

## **Chapter 2**

# **Experimental Methods**

## 2.1 Solutions Used

Where physiological extracellular solutions are required, i.e. in cell isolation, Krebs solution was used as stated below. All chemicals were from Sigma unless otherwise stated.

### Krebs Solution

120 NaCl, 20 HEPES, 5.4 KCl, 0.52 NaH<sub>2</sub>PO<sub>4</sub>, 3.5 MgCl<sub>2</sub>·6H<sub>2</sub>O, 20 Taurine, 10 Creatine, 11.1 Glucose, pH 7.4 (Concentrations in mM).

Where physiological/mock intracellular solutions were required i.e. when perfusing permeabilised cells, 0.05R was used with as stated below.

### 0.05R Solution

0.05 EGTA, 5 K<sub>2</sub>ATP, 5 phosphocreatine (Fluka), 25 HEPES, 100 KCl, 5.5 MgCl<sub>2</sub>, pH 7.0 (concentrations in mM).

Mean cytosolic [Ca<sup>2+</sup>]<sub>i</sub> was manipulated by varying the [Ca<sup>2+</sup>] in this solution. Free [Ca<sup>2+</sup>] was calculated from the amount of 1M CaCl<sub>2</sub> added using the react computer program (React, Smith, G.L.) and metal affinity constants for EGTA (Smith & Miller, 1985) and ATP and phosphocreatine (Fabiato, 1983). It was determined that contaminating [Ca<sup>2+</sup>] from, the water supply, glassware and chemical reagents was ~ 6μM. To get solutions of ~300, 600 and 900nM free [Ca<sup>2+</sup>] it was therefore necessary to add 2, 3 and 3.9 μl/ml of 10mM CaCl<sub>2</sub> respectively to the 0.05R solution. The contaminating [Ca<sup>2+</sup>] was monitored and these amounts were adjusted as necessary.

## Calibration Solutions

Where calibration of fluorescent solutions is mentioned, the solution resembled the 0.05R solution, containing with ratios of 10mM EGTA/CaEGTA. 100 mM stock solutions were made up and appropriate ratios were added to give the required  $[Ca^{2+}]$ . In permeabilised cell calibration, 1:1 ratio represents  $\sim 370nM$ .

## 2.2 Cell Isolation

### 2.2.1 Isolation of ventricular cardiomyocytes from the rat

White Wistar male rats were stunned by a blow to the head and killed by cervical dislocation. The thoracic cavity was opened, the heart quickly excised and placed into a beaker containing ice-cold Krebs' solution. The excised heart was quickly mounted and tied via the aorta onto the cannula of a Langendorff retrograde perfusion system. Fat and connective tissues were trimmed away. 50mL of  $Ca^{2+}$  free Krebs' solution, maintained at  $37^{\circ}C$  was perfused through the heart at a rate of 13mL/min to wash out blood and  $Ca^{2+}$ . The heart was then perfused with Collagenase/Protease solution (3mg Protease (Sigma) and 50mg Collagenase (Worthington) dissolved in 25ml  $Ca^{2+}$  free, sterile Krebs' solution). The enzyme solution was collected as it passed through the heart and re-circulated after the initial volume of the solution had passed through. Re-circulation of the enzyme solution and hence the digestion, was continued for approximately 16 minutes until the heart felt soft to the touch. The enzyme solution was washed out of the heart by perfusion with 50mL sterile Krebs' solution containing 1mM EGTA. The heart was excised and placed into Krebs' solution containing 1mM EGTA. The tissue was then finely chopped. The myocytes were dissociated by lightly titrating the

solution using a plastic Pasteur pipette. The dissociated cardiac myocytes were filtered through gauze mesh to remove undigested ventricle and other cells. The cells were then counted using a haemocytometer and the concentration adjusted to  $1 \times 10^5$  cells/ml. The two sub-populations of cells rod-shaped and ball shaped were deemed 'live' and 'dead' respectively. Dead cells being cells having undergone hyper-contraction.

### **2.2.2 Isolation of ventricular cardiomyocytes from the rabbit.**

White New Zealand male rabbits were given a lethal intravenous injection of 500 U Heparin together with an overdose of Sodium Pentobarbitone (100mg/kg) via the left marginal ear vein. Terminal anaesthesia was confirmed when both stretch and corneal reflex were absent. The thoracic cavity was opened, the heart quickly excised and placed into a sterile beaker containing sterile, Krebs' solution, which had been cooled to just above 0°.

The heart was then quickly mounted and tied via the aorta onto the cannula of a Langendorff retrograde perfusion system. Fat and connective tissues were trimmed away. 200mL of  $\text{Ca}^{2+}$  free Krebs' solution, maintained at 37°C was perfused through the heart at a rate of 25ml./min to wash out blood and  $\text{Ca}^{2+}$ . The heart was then perfused with Collagenase/Protease solution (3mg Protease and 50mg Collagenase dissolved in 75ml  $\text{Ca}^{2+}$  free, sterile Krebs' solution).

The enzyme solution was collected from heart and re-circulated after the initial volume of the solution had passed through. Re-circulation of the enzyme solution and hence the digestion, was continued for 5-6 minutes until the right ventricular (RV) tissue felt softened to the touch. The enzyme solution was washed out of the heart by perfusion with 100mL Sterile Krebs' solution containing 1%(w/v) Bovine Serum Albumin (BSA).

The RV was excised and immersed in Krebs' solution containing 1mM EGTA- to reduce contaminating  $\text{Ca}^{2+}$ . The tissue was then finely chopped. The myocytes were dissociated by lightly titrating the solution using a plastic Pasteur pipette. The dissociated cardiac myocytes were filtered through gauze mesh to remove undigested and other tissues. The cells concentration was then adjusted so ~ 5 cells filled the objective field on the 60x lens fitted to the confocal microscope (see 2.4.2).

## **2.3 Cell permeabilisation**

### **2.3.1 Rationale behind permeabilisation**

Cell permeabilisation is the process of using treatments to render the membrane hyperpermeable to allow free diffusion of substances between intra- and extracellular environments. Once this has taken place, intracellular ions and metabolites are dictated by the solution the cell is bathed by. This also allows introduction of cell impermeable dyes such as Fluo-3 and Fluo 5F (molecular probes, Oregon, USA). Through this technique, mean intracellular  $[\text{Ca}^{2+}]$  can be effectively "clamped" to that of the perfusing solution. This also allows accurate calibration for conversion of cellular fluorescence signals to  $[\text{Ca}^{2+}]$ .

### **2.3.2 Methods of permeabilisation**

Past studies have accomplished "skinning" of the cardiac cell by various methods:

- 1) Mechanical skinning of cardiac Purkinje was successfully used in the CICR studies of Fabiato (Fabiato, 1985a;Fabiato, 1985b;Fabiato, 1985c). This involves removing the sarcolemma with microelectrodes. No one has been able to replicate this technically challenging technique since and it has yet to be accomplished on the ventricular myocyte.

- 2) Chemical detergents such as Triton x100 have been used in the past to permeabilise cell membranes. This is not selective for the sarcolemma, and has the undesirable effect of disrupting all membranes it comes into contact with, so is not suitable for study of cardiac SR function.
- 3) Electroporation of cardiac cell membranes has been successfully used for the introduction of genes into isolated cells. This method has many drawbacks. For instance only small holes, (allowing permeation of molecules of ~MW 1000) are formed in the membrane, and the process reverses with time (Escande-Geraud *et al.*, 1988). This makes it unsuitable for the experiments described in this thesis.
- 4) Pore forming toxins such as saponin and its derivative  $\beta$ -Escin have been used successfully in our lab for the purposes of irreversible permeabilisation of cardiac myocytes (Orchard *et al.*, 1998). This offers many benefits over the other methods mentioned. It provides irreversible, specific permeabilisation of the sarcolemmal membrane.

The latter method acts by formation of complexes with sterols/cholesterol located on the sarcolemma and subsequent lateral displacement with the formation of aqueous pores ~8nm (BANGHAM *et al.*, 1962). The agents are not thought to disrupt the SR since the relative content of cholesterol on this organelle membrane is very low (<2% of SR lipid content). Adverse effects of permeabilisation with these agents have been observed. Effects on the RyR and subsequent reductions in the ability of the SR to load  $\text{Ca}^{2+}$  have been seen after 30 min exposures (Launikonis & Stephenson, 1999). In all the experiments in this thesis, exposure is limited to <1 min, therefore adverse effects on RyR activity are minimal. The large pores formed by these agents allow free diffusion of the fluorescent dyes and drugs

used (e.g. thapsigargin, TBQ, tetracaine) in our experiments.  $\beta$ -Escin offers a slight advantage over saponin, as its time course of action is longer. This allows a larger window where the cell is permeabilised, yet effects on the RyR are not yet evident (Elliot, 2002).

### 2.3.3 Permeabilisation Protocol

Isolated myocytes were allowed to settle on a coverslip, which served as the base of the perfusion bath (Fig.1). The cells were then superfused with a mock intracellular solution (see solutions) containing Fluo-5F (molecular probes) and  $\sim 300\text{nM}$   $[\text{Ca}^{2+}]$ . Perfusion was then stopped and  $\beta$ -Escin (Sigma) was added to give a final concentration of  $\sim 15\mu\text{g/ml}$ . The bath solution was then agitated gently with a p10 Gilson pipette. To minimize overexposure to  $\beta$ -Escin, the cell was visualized on the confocal microscope. Permeabilisation was achieved when fluorophore was observed crossing the cell membrane. Perfusion was immediately resumed subsequent to permeabilisation.

## 2.4 Microscopy

Before the advent of confocal microscopy, whole cell, epifluorescence microscopy was the mainstay for study changes in intracellular  $[\text{Ca}^{2+}]$ . This was usually coupled with use of ratiometric dyes and changes in fluorescence ratio were used to follow global  $\text{Ca}^{2+}$  signals. Most of the experimental results described in this thesis have been acquired through the use of confocal laser scanning microscopy (CLSM). The high temporal and spatial resolution yielded from this technique has allowed better understanding of the rapid changes in cytosolic  $\text{Ca}^{2+}$  seen in *local*  $\text{Ca}^{2+}$  release processes. Before the experimental data can be fully understood, an understanding of the underlying principles of confocal microscopy is needed. This is described below.

### 2.4.1 Confocal Laser-scanning microscopy.

In the context of the experiments carried out in this thesis, CLSM is a method used to optically section the cardiac cell (Figure 2-1). The cell cytosol is perfused with a solution containing a  $\text{Ca}^{2+}$  sensitive dye, which fluoresces when excited by a specific wavelength (488nm) of light emitted by a laser light source. The emitted fluorescent light,  $>500\text{nm}$  is then collected by a Photo Multiplier Tube (PMT). Confocal in the context of the microscope means that both the illumination focal volume and the detection focal volume are coincident.

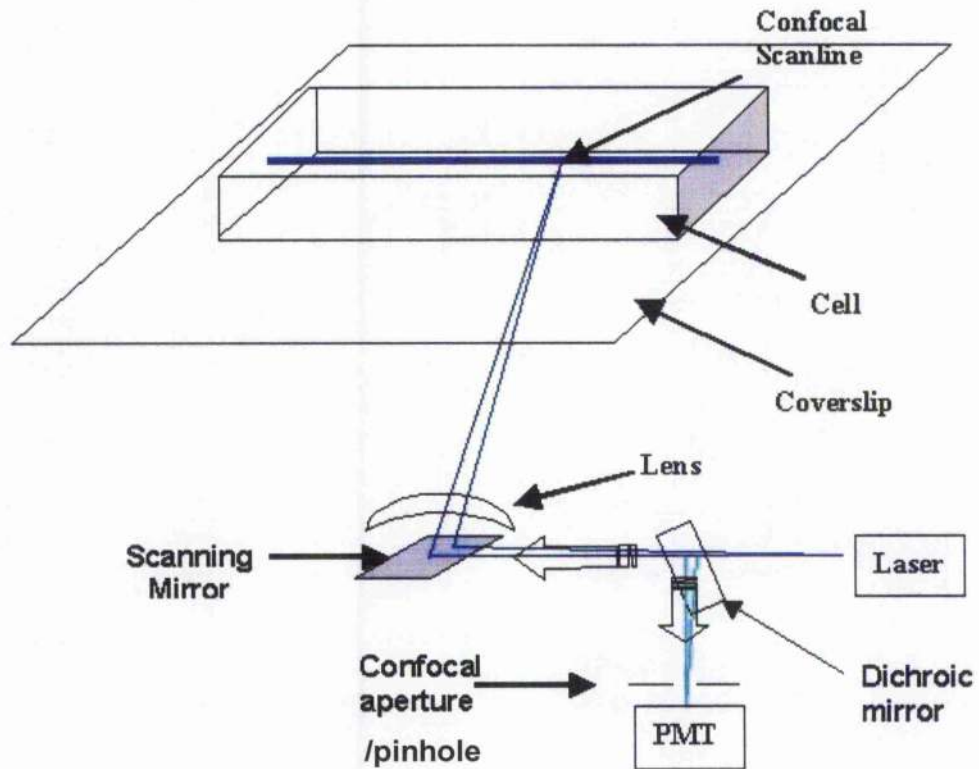
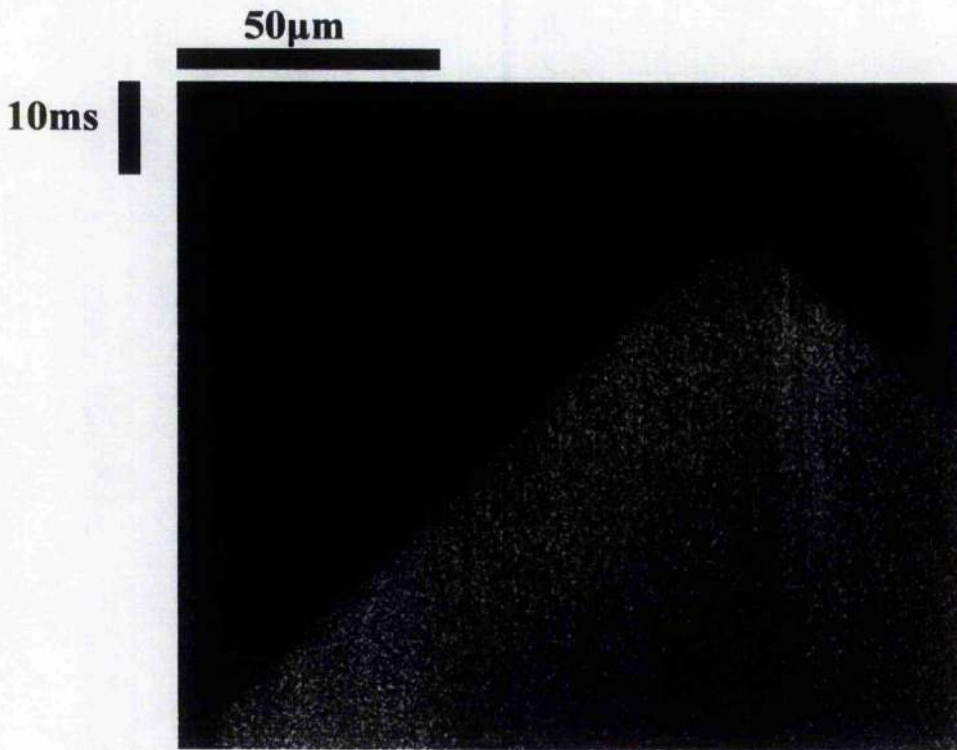


Figure 2-1 Illustration of confocal microscopy.

The cuboid shape is a basic representation of a cardiac myocyte. The blue laser light is focused on a spot inside the cell. It is directed by the scanning mirror along the length of the scanline. The light excites the fluorescent dye to emit green-blue light, which travels down the same light path. The light then reflects off the dichroic mirror and is collected by the Photomultiplier Tube (PMT).

The system allows limited collection of fluorescence from the limited spot the microscope is focused on. All out of focus light falls outside the region of the pinhole and is hence rejected. The degree of confocality can be adjusted by the size of the pinhole (confocal aperture). This method can be employed in a variety of modes.

- 1) **Linescan mode**- in this mode, the scanning mirror displaces the focused laser spot lateral across the field in a line. Then springs back across to the beginning and then repeats the scan. This mode creates “waterfall images” Figure 2-2, where distance is displayed on the x-axis and time is displayed downwards on the y-axis. In this mode it is possible to reach scanning frequencies of 1800 Hz. The standard frequency used for this thesis is 500Hz. Since the  $\text{Ca}^{2+}$  waves have a duration of <1 second, linescan mode is the mainstay for resolving their time-course.
- 2) **Imagescan mode**-In this mode, a thin plane is scanned. The x-y dimensions are specified by the user and the plane can be captured sequentially. This allows the user to visualize whole cells, but has much lower temporal resolution as a result. A 512x512 array is used for this thesis and this can be scanned at ~1Hz.
- 3) **Z-stack mode**-In this mode, the LSCM scans a thin plane, then displaces vertically a specified amount. This allows construction of a 3-D representation of the cell. This is not used in this thesis.



**Figure 2-2** Example of a waterfall plot from the confocal microscope. Time is displaced horizontally; distance displacement is downwards.

#### 2.4.2 CLSM data collection

In all the experiments described in this thesis, the system used was the Bio Rad Radiance 2000 confocal system fitted with a 488nm krypton-argon laser (Bio Rad, Hemel Hempsted, UK). The objective lens used for imaging investigations was the high numerical aperture (NA) Nikon Plan Apochromat 60x/1.2 NA water-immersion lens (Nikon, Surrey, UK). The system zoom was set to 1.4, which normally accommodated one cell width + ~10-20%. The capture rate was set to 500 lines per second (lps) and the system allowed maximum capture of 30000 lines (60 seconds). Confocal aperture iris diameter was set at 1.9 providing an axial (z) resolution of about 0.9 $\mu\text{m}$  and X-Y resolution of about 0.5 $\mu\text{m}$  based on full width half maximal amplitude measurements of images of 0.175 $\mu\text{m}$  fluorescent beads (Molecular probes). Prof. Godfrey Smith carried out these measurements in order

to obtain the resolution of the confocal microscope. The software used to capture the data was Laser Sharp 2000 (Bio Rad).

### **2.4.3 Problems associated with confocal microscopy**

The signal from the CLSM has relatively low signal to noise ratio (SNR). Each pixel is given by integrating for a set period. Hence as the scanning frequency increases, so the integrated signal falls and signal noise levels increase. At the rate used typically in this thesis, the scanning frequency is set to the minimum necessary to allow sufficient temporal resolution for resolving the fast  $[Ca^{2+}]$  changes seen in cardiomyocytes, (500Hz). Even at this rate, the noise level is very high and additional methods need to be employed to extract useful data (See Chapter 3).

Cardiac ventricular myocytes are typically 20 $\mu$ m thick. Optically, this is ideal for CLSM purposes. Above 40 $\mu$ m, it has been shown that a degradation of image contrast occurs, termed spherical aberration (Dempster & Wokosin, 2002).

It has been shown that damage can occur to living cells, on exposure to high intensity light. This is minimized by limiting laser power to 12% (3 MW).

Incidence of laser damage is further decreased by limiting experimental protocols to <5 minutes.

Laser light also causes photo-degradation, (bleaching) of fluorophores. This is also limited by short exposure time and minimal laser power.

Substances such as caffeine cause “quenching” of fluorophore fluorescence. The non-ratiometric nature of the fluorophores means this has to be corrected for, where possible.

[Ca<sup>2+</sup>] is calculated from fluorescence signals after calibration. The fluorescence signal is dependent on fluorophore concentration, so care is taken to ensure this is constant in all solutions. When the cell releases [Ca<sup>2+</sup>], it contracts. This contraction causes transient changes in fluorophore concentration. This causes “contraction artefact”, where [Ca<sup>2+</sup>] estimates are made erroneously higher following cell contraction. This has been tackled in section 2.5.5.

## **2.5 Experimental protocols for [Ca<sup>2+</sup>] measurement in cardiomyocytes.**

### **2.5.1 Introduction to single wavelength Ca<sup>2+</sup> measurement.**

The aim of this thesis is to quantify intracellular Ca<sup>2+</sup> fluxes and recreate these in a physiologically accurate model. This requires carefully calibrated [Ca<sup>2+</sup>] measurements. With the single wavelength measurements taken from the confocal microscope this is technically difficult, with numerous complicating factors influencing it.

Permeabilised cells were used in all experiments. This is beneficial for purposes of Ca<sup>2+</sup> measurement, as prevents changes in intracellular pH, which would alter fluorophore Ca<sup>2+</sup> binding characteristics. All other ion concentrations, as well as ATP and phosphocreatine concentrations are controlled, within physiological limits.

Fluorophore was present at 10µM concentrations in all experiments. This diffused freely into the permeabilised cell and was seen to bind to cellular proteins. This binding has been discussed in detail in numerous papers (Baylor & Hollingworth,

2000;Harkins *et al.*, 1993;Loughrey *et al.*, 2003). As a result, fluorophore concentration inside the cell is elevated (~140%) with respect to the perfusing solution. When the dye binds to certain proteins, their  $K_D$  has been shown to change (Baylor & Hollingworth, 2000). In situ calibration studies (Loughrey *et al.*, 2003) have shown the  $K_D$  of Fluo 3 remains constant over a range of intracellular  $[Ca^{2+}]_i$ . This principle, coupled with measurements of intracellular fluorophore binding was used as a means to convert fluorescence to  $[Ca^{2+}]_i$ .

### 2.5.2 Protocol for production and calibration of Spontaneous $Ca^{2+}$ Waves

For the production of spontaneous  $Ca^{2+}$  waves within permeabilised cells, 0.05R solution was used (see solutions) as a base for all the solutions. The free  $[Ca^{2+}]_i$  was adjusted to  $>250nM$ , as this was determined as the approximate threshold for propagating  $Ca^{2+}$  release events. Where  $Ca^{2+}$  buffered solutions were used, these had composition similar to 0.05R, with ratios of 10mM EGTA:CaEGTA substituting the usual 50 $\mu$ M EGTA. Figure 2-3 shows a typical protocol.

The cell was permeabilised and superfused with 0.05R solution containing 10 $\mu$ M Fluo5F, Cytochalasin d and  $>250nM$   $[Ca^{2+}]_i$ . Perfusion rate was determined to be ~0.5 ml/min. 1 minute post-permeabilisation perfusion was allowed for optimal dye loading and action of cytochalasin d and equilibration of mean cytosolic  $Ca^{2+}$ . After this time, a line within the cell was selected roughly in the centre of the cell, where no nucleus was present. This line was scanned in linescan mode (see confocal section) at 500 Hz for 2 minutes. The bath solution was then switched to one containing 1:1 10 mM EGTA:10 mM CaEGTA (~390nM  $[Ca^{2+}]_o$ ) solution for 1 minute. This allowed estimation of intracellular: extracellular fluorescence ratio (typically 1.4:1) and a measure of the fluorescence value at ~390nM  $[Ca^{2+}]_o$ . Then the solution was switched to a solution with 10 mM EGTA. This allowed a

measurement of  $F_{min}$ . Finally the perfusing solution was switched to 10 mM CaEGTA. This caused hypercontracture of the cell, but allowed verification of free  $[Ca^{2+}]_{bath}$  in the 1:1 solution, by obtaining an accurate measure of extracellular  $F_{max}$ . The protocol was then repeated as necessary, changing both coverslip and cells afterwards.

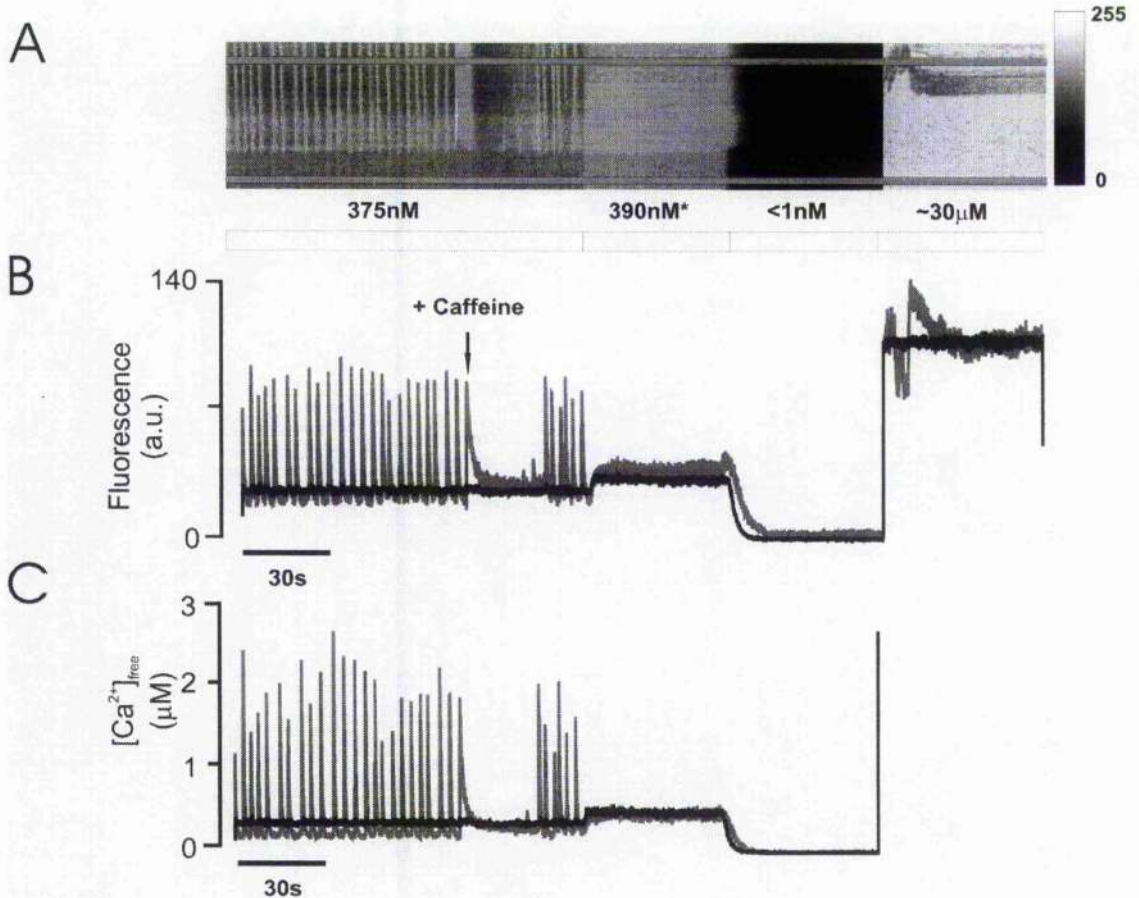


**Figure 2-3** Example of typical protocol for studying  $[Ca^{2+}]$  waves in permeabilised cardiomyocytes from the rabbit.

**A** is a linescan image of the cell during the protocol. This has been rotated so that time increases to the right and distance is displaced vertically. Increases in fluorescence track increases in  $[Ca^{2+}]$ . Two bands are highlighted. These indicate the 20-pixel regions selected for measurement of fluorescence. **B** shows changes in intracellular (grey) and extracellular (black) fluorescence spatially averaged over the 20-pixel bands from **A**. **C** is the resultant  $[Ca^{2+}]_{free}$  trace after calibration.

### 2.5.3 Methods for conversion of fluorescence to $[Ca^{2+}]$

$[Ca^{2+}]_i$  in all solutions were estimated using the React program written by Prof Godfrey Smith, using ligand binding constants for EGTA (Smith & Miller, 1985)

and ATP (Fabiato & Fabiato, 1979); EGTA purity was derived as described elsewhere (Smith & Miller, 1985). Verification and conversion of extracellular fluorescence to  $[Ca^{2+}]_i$  used the following equation.

**Equation 1**

$$Ca_{free}^{2+} = \frac{Kd * F - F_{min}}{F_{max} - F} \quad (\text{Grynkiewicz } et al., 1985)$$

**Where:**

- Fmin** = fluorescence measured in 10E solution.
- Fmax** = fluorescence in 10CaE solution.
- F** = measured fluorescence value.
- K<sub>D</sub>** = dissociation constant of fluorophore.

For intracellular calculations, the following was used.

Fratio = ICF/ECF in 390 buffered  $Ca^{2+}$  solution.

IC Fmin = Fratio \* EC Fmin

The ICFmax =  $(K_D / CaRef + 1.0) * (ICFStd - ICFmin) + ICFmin$

**Where:**

- CaRef** =  $[Ca^{2+}]_i$  in buffered solution (~390nM).
- ICFStd** = Mean Fluorescence recorded in 390nM buffered solution.
- ICFmin** = Mean Fluorescence recorded in <1nM buffered solution.
- ICFmax** = Maximum fluorescence estimated from calculation.

These fmin and fmax values are then inserted into Equation 1 for intracellular estimation of  $[Ca^{2+}]_i$ . This was confirmed when mean intracellular and extracellular  $[Ca^{2+}]_i$  estimations had <40nM differences.

## 2.5.4 Fast switching perfusion system

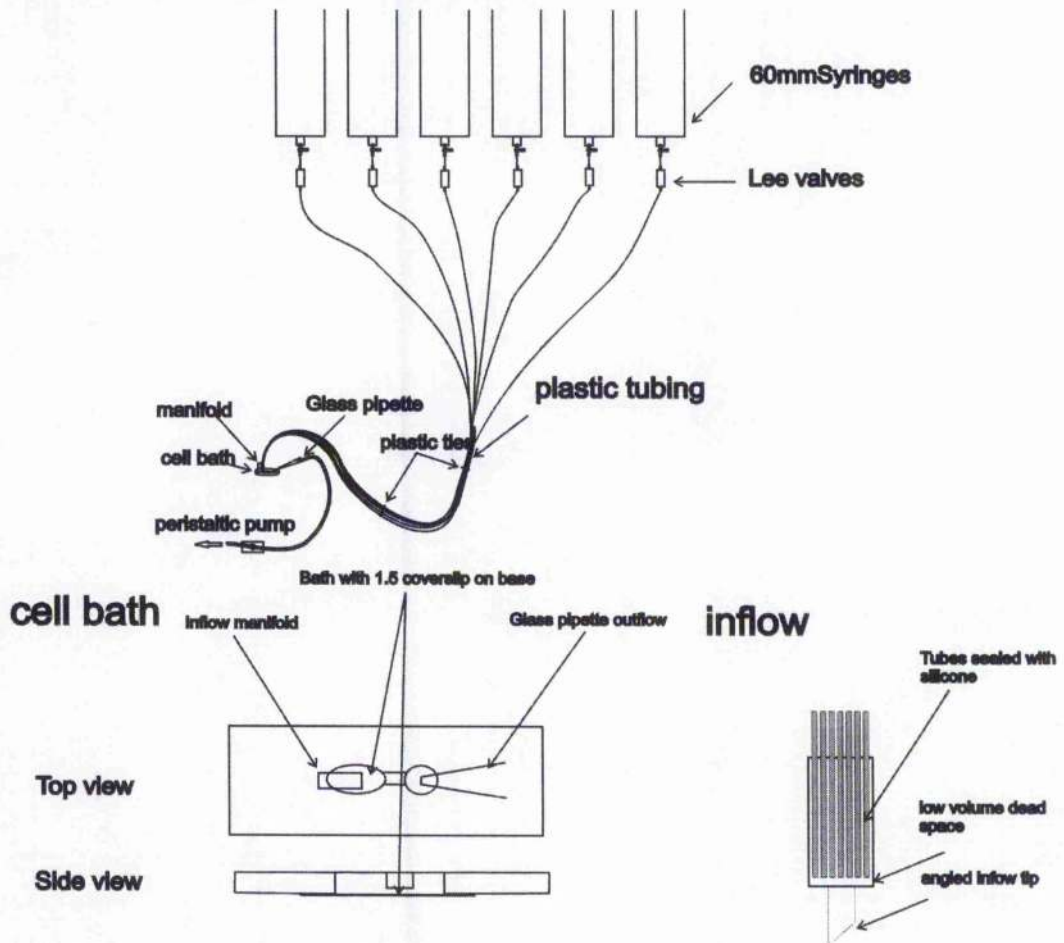


**Figure 2-4** Apparatus for perfusion of isolated cardiomyocytes.

The perfusion system is gravity fed, with perfusion switching accomplished by electrically controlled solenoid valves (Lee, Berks, UK). Thin plastic tubing reduces solution wastage. The cell bath is designed to ensure fast solution changes, whilst minimizing solution wastage. The inflow is designed to allow fast solution changes with minimal dead space. The tip of the inflow is angled to ensure laminar flow across the cell being studied.

The apparatus above was used to allow solution changes within  $<1$ s. The inflow tip was placed almost on top of the cell of study. The height of the syringes were varied to adjust perfusion rate to  $\sim 0.5$ ml/min. The outflow rate was set to be  $\sim$ twice as fast as inflow. Pipette tip position dictated the level of the bath. This was set so that bath volume was  $\sim 200\mu\text{L}$ .

### 2.5.5 Possible problems resolving $[Ca^{2+}]$ at the peak of a $Ca^{2+}$ wave.

#### 2.5.5.1 The problem:

Permeabilised cells bathed in  $\sim 300nM$   $[Ca^{2+}]$  produce  $Ca^{2+}$  waves with systolic peaks transients of  $\sim 2\mu M$  (Loughrey *et al.*, 2003). Other studies published using rat cells yielded similar results, using different  $[Ca^{2+}]$  conversion techniques (Smith & O'Neill, 2001). Preliminary experiments of this thesis, studying  $[Ca^{2+}]$  changes during waves elicited in rat cardiomyocytes yielded spurious estimates of systolic peaks. These were roughly 2-3 times higher than previously seen. Possible reasons for this were investigated.

#### 2.5.5.2 Unsuitable dye?

Initial studies were carried out using Fluo-3. The  $K_D$  of this was measured as  $558 \mu M \pm 15nM$  ( $n=6$ ). If peak  $[Ca^{2+}]_i$  rose above  $2 \mu M$ , the dynamic range of the dye might have been exceeded and as fluorescence came close to  $F_{max}$ , any noise of the signal would cause peak values to appear higher. For this reason a dye was chosen with a higher  $K_D$ , allowing better resolution of peak  $[Ca^{2+}]_i$ . Fluo 5F pentopotassium salt has a reported  $K_D$  of  $2.3\mu M$  (molecular probes, Oregon,).

With the mock intracellular solutions used in this thesis (see solutions section), the  $K_D$  was measured as  $1035 \pm 14nM$  ( $n = 6$ ). The dynamic range of this dye allows ample resolution up to  $3\mu M$  (see Figure 2-5). With fluo 3 the error is 6 times greater with fluo 3 at  $2\mu M$   $[Ca^{2+}]$ . Fluo 5 has only a 3 times increase in error.

When using this dye on rabbit cells, more reliable results were found, but peak  $Ca^{2+}$  values measured in rat cardiomyocytes still proved problematic.

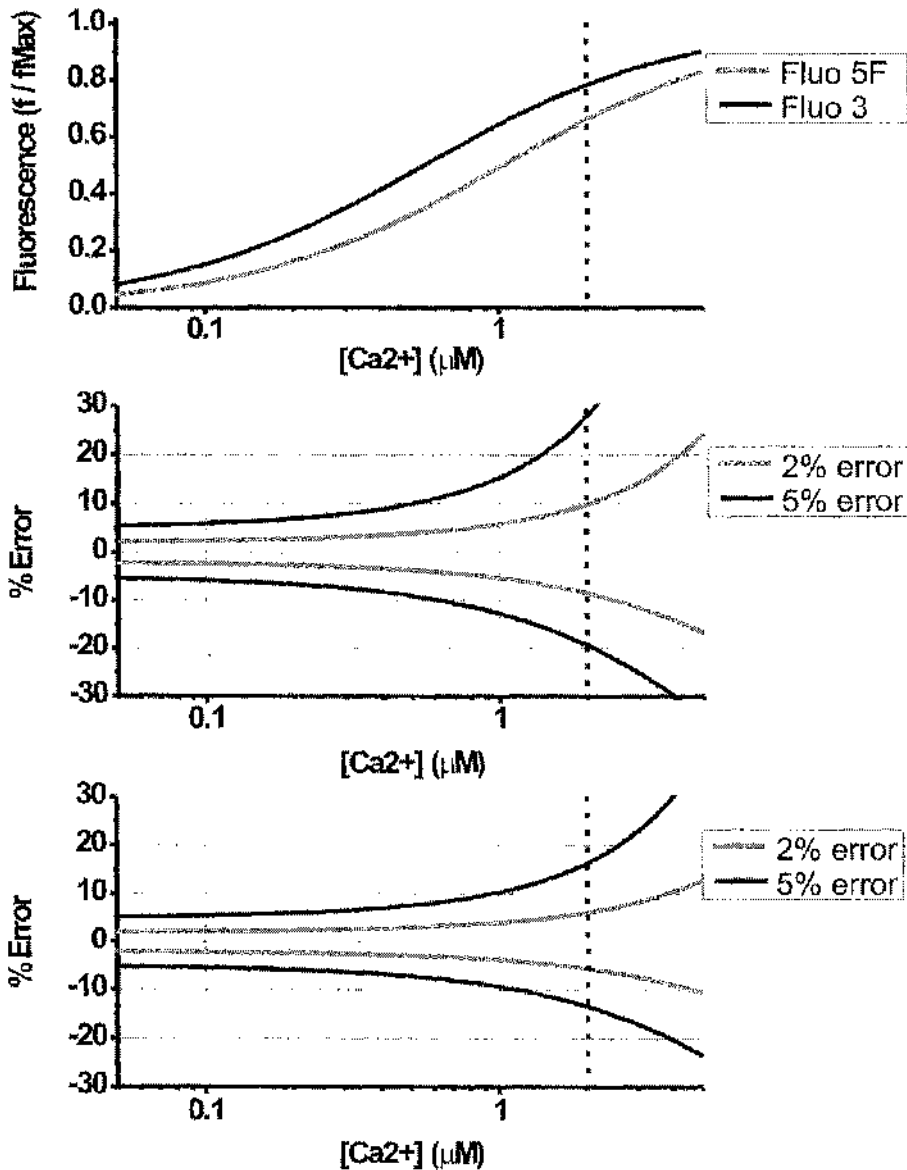


**Figure 2-5** Graphs showing differences in  $Ca^{2+}$  affinities of Fluo 3 and Fluo 5F and the subsequent increases in error above  $1 \mu M$ . Panel A shows the binding curve of Fluo 3 ( $K_D = 0.558$ ) and Fluo 5F ( $K_D = 1.04$ ). The dotted line shows the  $\sim [Ca^{2+}]_i$  at the peak of a typical  $Ca^{2+}$  wave ( $2 \mu M$ ). Panel B shows the effect of increasing  $[Ca^{2+}]_i$  on error at 2 and 5% for Fluo 3. Panel C shows the effect of increasing  $[Ca^{2+}]_i$  on error at 2 and 5% for Fluo 5F.

### 2.5.5.3 Contraction artefact?

From observing the cells during a  $Ca^{2+}$  wave, it was noticed the contraction was more pronounced in rat cells when compared to rabbit. This would possibly lead

to more marked effects of contraction artefact. In order to minimize these effects, known inhibitors of contraction were tested. This is shown below.

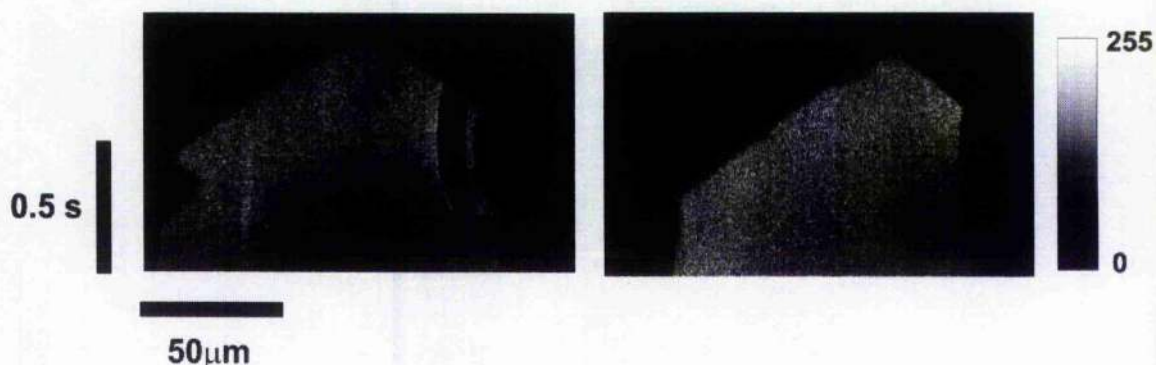


**Figure 2-6** Linescan images of  $\text{Ca}^{2+}$  waves in permeabilised rat (left) and rabbit (right) cardiomyocytes.

The panels on the left show extent of contraction artefact in each species. Contraction is pronounced in the rat.

#### 2.5.5.4 BDM (2,3-butanedione monoxime)

BDM has been shown to inhibit contraction. The agent works as an inhibitor of the myosin ATPase (E.M. Ostap. *et al* 2002). To assess these effects and its effectiveness in limiting contraction, it was studied using the protocol described below.

Cardiomyocytes were permeabilised and perfused with mock intracellular solution (see protocol section). These were then exposed to 5 minutes of BDM and solution containing 300nM  $[\text{Ca}^{2+}]_i$ . Wave frequency, amplitude and contraction were recorded and compared to control values. The results are shown in Figure 2-7.

**Figure 2-7  $\text{Ca}^{2+}$  waves from the rat before and after application of BDM.**

These preliminary experiments showed adverse affects on SR function, which approximately doubled  $\text{Ca}^{2+}$  wave frequency. This result was hypothesised to be attributable to sensitisation of the RyR. Similar effects have been observed previously (Adams *et al.*, 1998;Steele & Smith, 1993). An alternative contraction uncoupler needed to be found.

**2.5.5.5 Cytochalasin D**

This is a known contraction uncoupler, acting through polymerization of actin (Wu *et al.*, 1998). This has also been shown to have adverse effects on cellular processes (Calaghan *et al.*, 2000). The agent was studied replicating the protocol used for BDM. The results are shown in Figure 2-8 below.

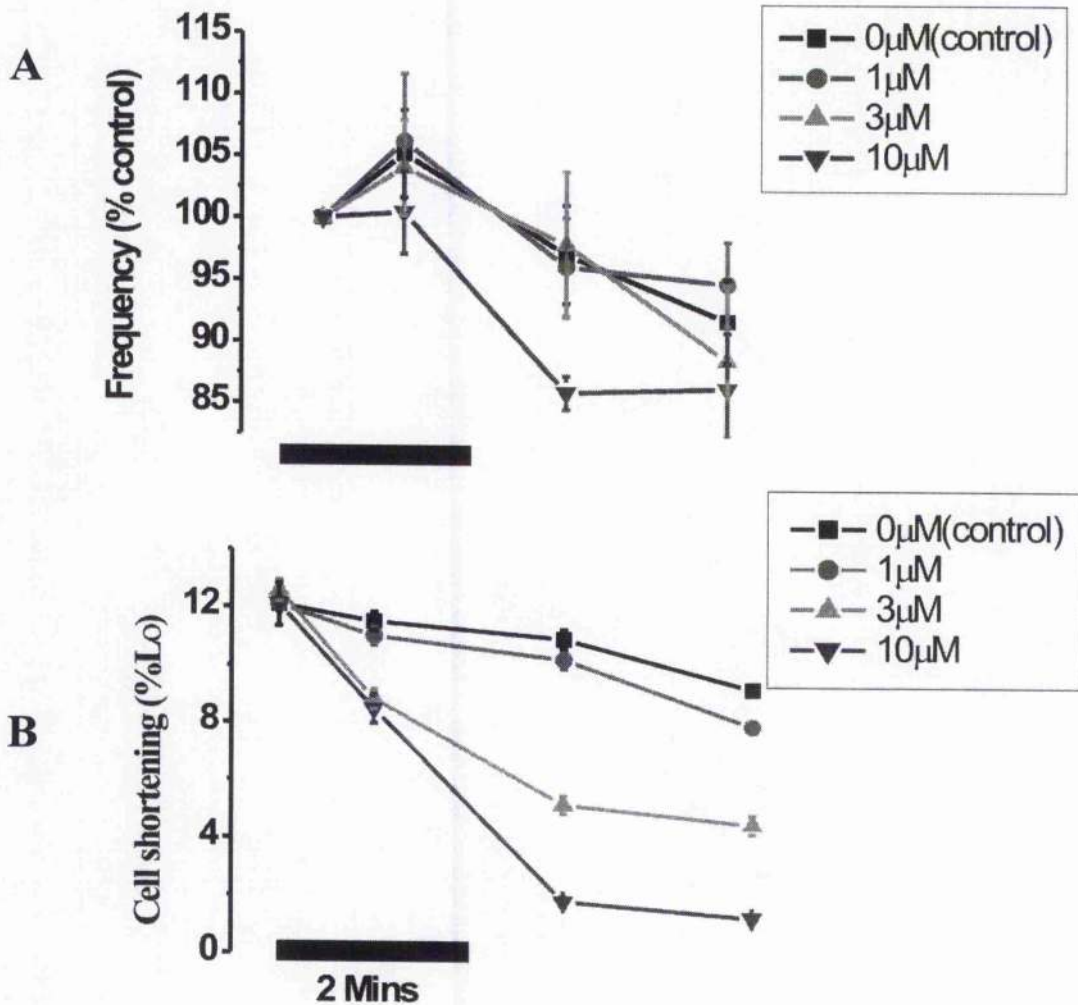


**Figure 2-8** Graphs showing effects of Cytochalasin D on wave frequency and cell shortening.

In Panel A control frequency decreases to  $94 \pm 4\%$ , ( $n=7$ ) of original values. The maximum concentration ( $10\mu\text{M}$ ) decreases to  $86 \pm 6\%$ , ( $n=7$ ) of original values. This represents a significant decrease in frequency (students t-test  $p < 0.05$ ).

Contraction was almost abolished within 3 minutes of perfusion with  $10\mu\text{M}$  cytochalasin D. Frequency was reduced by 8% more than cells without cytochalasin D. This was not significant ( $p > 0.05$   $n=7$ ). This was deemed an acceptable effect given the marked reduction in contraction. Since total abolition of

contraction was necessary to eliminate artefacts, in all subsequent experiments 10 $\mu$ M cytochalasin D was applied for 1 minute prior to experiment and for a further 2 minutes i.e. the typical time for wave experiment protocols.

The use of cytochalasin D, accompanied with the use of Fluo 5F instead of Fluo 3 abolished artefacts due to contraction (see Figure 2-9).

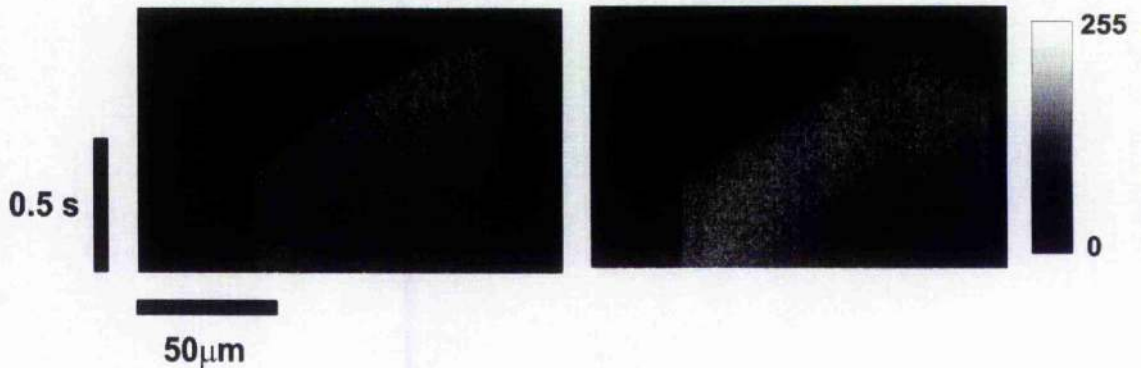


**Figure 2-9** Linescan images of  $\text{Ca}^{2+}$  waves in permeabilised rat (left) and rabbit (right) cardiomyocytes.

The panels show contraction artefact has been abolished.

## **2.6 Measuring the intrinsic $\text{Ca}^{2+}$ buffering capacity of permeabilised cells from the rat.**

### **2.6.1 Introduction**

Previous studies have shown cellular proteins in cardiac ventricular cells bind most of the  $\text{Ca}^{2+}$  released from the sarcoplasmic reticulum (Hove-Madsen & Bers, 1993). In order to quantify SR  $\text{Ca}^{2+}$  release it is first necessary to quantify this intrinsic  $\text{Ca}^{2+}$  buffering capacity. In order to study these proteins in vivo, a method was needed to study changes in  $[\text{Ca}^{2+}]_i$  for added amounts of  $[\text{Ca}^{2+}]_{\text{total}}$ . This has previously been studied using  $[\text{Ca}^{2+}]$  sensitive minielectrodes (Hove-Madsen & Bers, 1993). This method has several drawbacks:

Commercially available versions are available, but can only be used to measure large volumes. For measuring small volumes, it is necessary to synthesise

minielectrodes. This is technically difficult and has the following practical disadvantages:

- (1) The time resolution of electrodes is low (~10s).
- (2) The sensitivity at low  $[Ca^{2+}]$  (~ pCa 7) is limited.

Since it was necessary to measure  $[Ca^{2+}]$  at ~ pCa 7 with relative accuracy, another method was required.

It was decided that fluorescence measurements could be utilised to get obtain better  $Ca^{2+}$  buffering characteristics between pCa 8 and pCa 5.

The Bers study used high concentrations ( $5 \times 10^5$ ) of cells in a small volume (1mL). This precludes the use of cuvette-based measurements, as the high density of cells prevents light passage between emitter and detector. Another method needed to be devised. This is described below.

### **2.6.2 Preparation of cells for buffer capacity measurement**

$2 \times 10^5$  cells were isolated as described previously (2.2.1). These were suspended in Krebs solution containing 1mM EGTA. This decreased  $[Ca^{2+}]$  to < 1nM. These were then hand centrifuged and resuspended in 5mls Krebs containing 50 $\mu$ M EGTA. Cells were resuspended in 0.05R with 10 $\mu$ M Fluo-3 (molecular probes). B-Escin (0.1mg/mL) was then added and the cells were allowed 2 minutes to become permeabilised, after which the cells were hand-centrifuged and the solution was removed. The cells were then resuspended in 1ml of 0.05R solution containing at a cell concentration of  $2 \times 10^6$ /ml.

### **2.6.3 System for studying calcium dynamics on populations of cells**

A Perspex bath (see Figure 2-10) was mounted on a coverslip. A confocal microscope was used to monitor fluorescence changes in a small volume (~5pL). The signal was scanned at 500 Hz and the average of every 50 lines was recorded. The fluorophore containing solution was stirred with a custom-made stainless steel stirrer. This created a cyclone effect, causing cells to circulate around the periphery of the well. Very few cells passed over the centre of the well. This allowed measurement of fluorescence, without the interference of passing cells contaminating the signal.

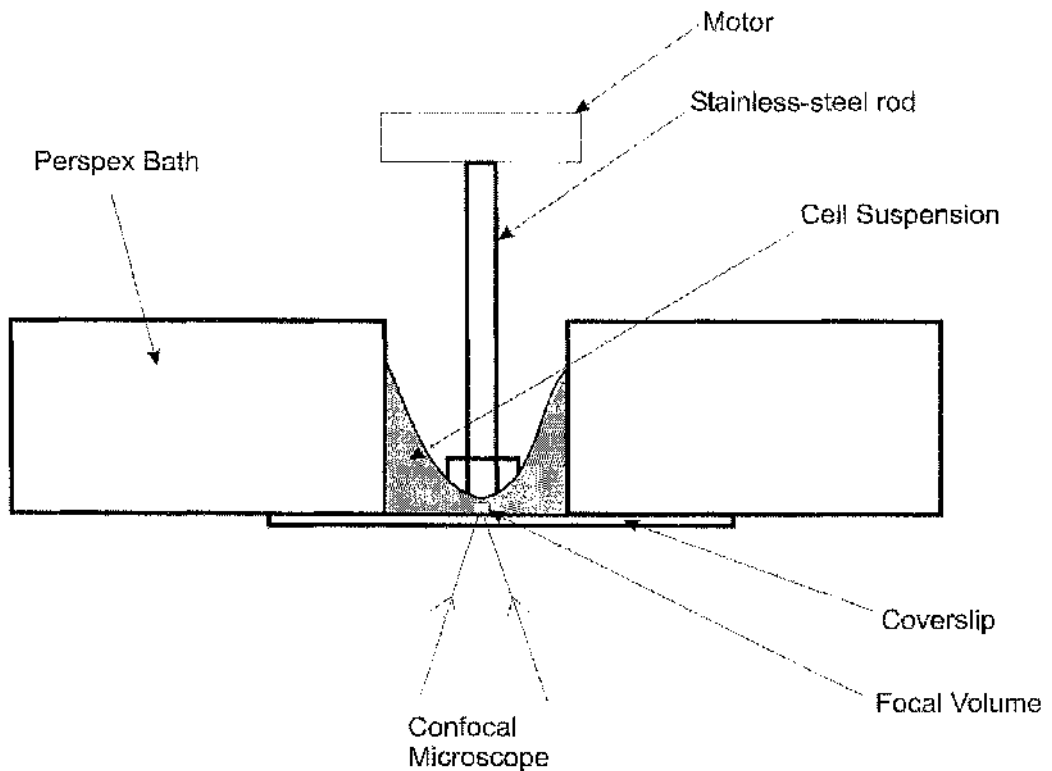


**Figure 2-10** Diagram showing apparatus used for measuring intrinsic cellular  $\text{Ca}^{2+}$  buffering.

The bath accommodates 1mL of cells when the motor is on. The motor ensures fast equilibration of  $\text{Ca}^{2+}$  additions. Inhibitors and  $\text{Ca}^{2+}$  additions are accomplished by pipette to the side of the bath.

### 2.6.4 Protocol for measuring $[Ca^{2+}]$ buffering

1 mL of cell suspension was added to the bath. Inhibitors of SERCA (25  $\mu$ M thapsigargin), and mitochondrial (1  $\mu$ M CCCP, 2  $\mu$ M Oligomycin, 1  $\mu$ M Rotenone)  $Ca^{2+}$  uptake were added and allowed 2 minutes to act. 10  $\mu$ M increments of 2 mM  $CaCl_2$  stock (10  $\mu$ M additions) were added to the bath and changes in fluorescence were recorded on the confocal microscope.

### 2.6.5 Results

Obtaining results from these experiments was problematic. As the highly concentrated cells were stirred and  $Ca^{2+}$  was added, secondary changes in fluorescence were observed. These were hypothetically due to changes in pH and/or other factors being released from the cells. Although the protocol was carried out many times, only one reliable result was obtained. This is shown below.

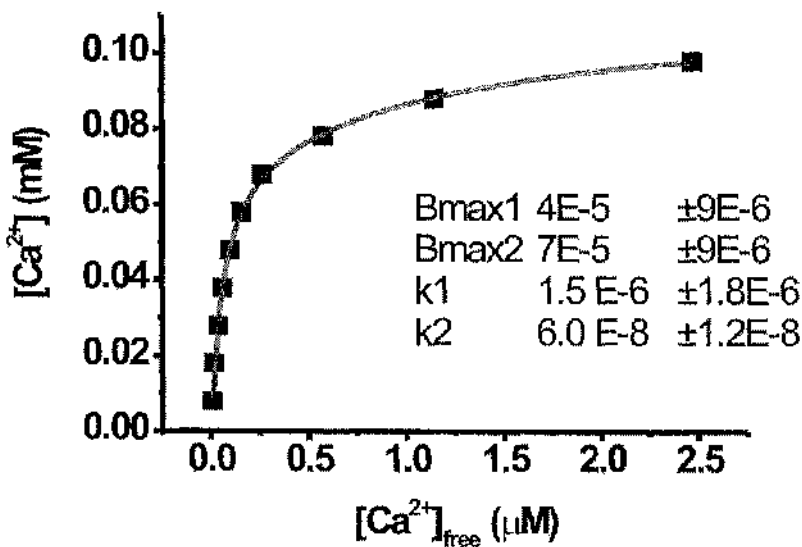


Figure 2-11 Graph showing 2-site binding properties for  $Ca^{2+}$  of permeabilised cardiomyocytes.

Increments of 10  $\mu$ M are shown (■), with line of best fit for a 2-site binding scheme.  $Ca^{2+}$  additions were highly buffered up to 0.5  $\mu$ M free, becoming more modest at higher  $[Ca^{2+}]$ .

The results are similar to previous studies (Hove-Madsen & Bers, 1993; Shannon & Bers, 1997). As only one valid result was attained, values from the previous study (Hove-Madsen & Bers, 1993) were used for future estimations of intrinsic myocyte  $\text{Ca}^{2+}$  buffering characteristics.

**Chapter 3 Computational methods used to analyse wave properties in permeabilised cardiomyocytes.**

### 3.1 Analysing the cardiac $\text{Ca}^{2+}$ release event.

The previous chapter described methods for collection of spontaneously oscillating calcium fluorescence data from cardiac myocytes, and the subsequent conversion of these signals to  $[\text{Ca}^{2+}]_i$ . This section aims to demonstrate how this signal can be deconstructed into the inter-compartmental fluxes taking place within the cell.

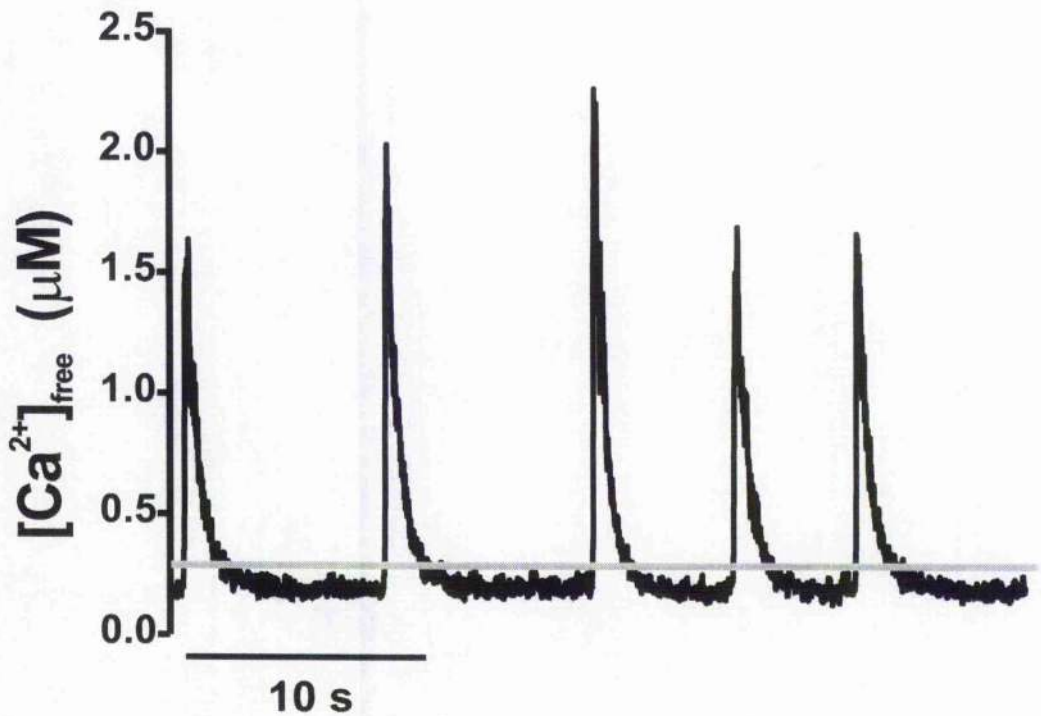


**Figure 3-1** Typical  $[\text{Ca}^{2+}]_i$  trace of  $\text{Ca}^{2+}$  waves from a spontaneously oscillating permeabilised myocyte. Oscillating black line indicates  $\text{Ca}^{2+}$  signal from small intracellular volume. Grey line represents mean of oscillating signal  $[\text{Ca}^{2+}]_i^{mean}$ . Black bar at bottom of figure represents 10-second timescale.

Figure 3-2 depicts the fluxes assumed to contribute to the signal seen in Figure 3-1.

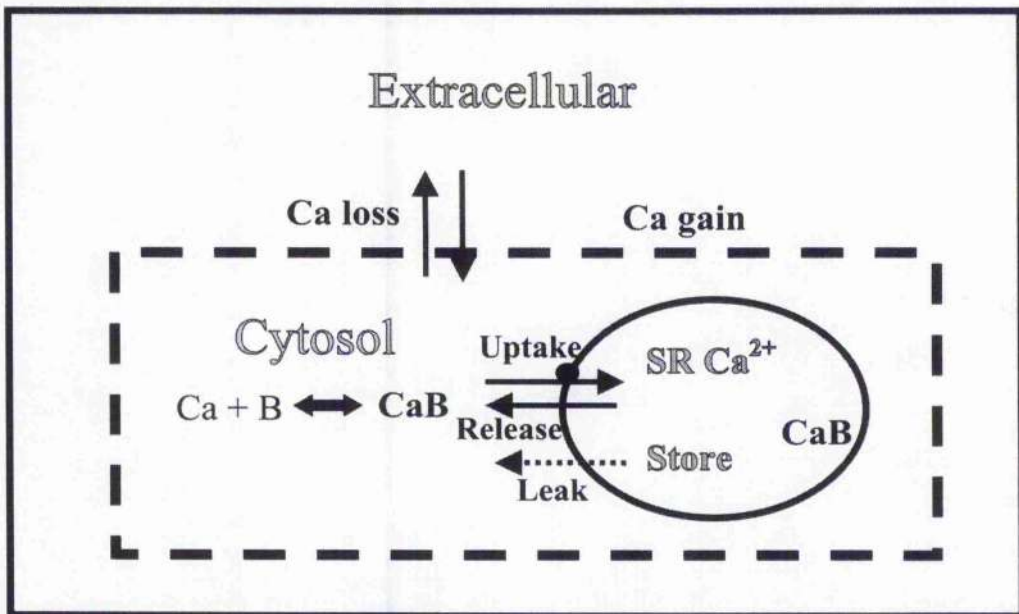


Figure 3-2 Compartmental Flux Diagram.

Scheme of fluxes and buffers comprised in modelling a spontaneous  $\text{Ca}^{2+}$  wave in a permeabilised cardiac myocyte.

Key

<b>B</b>	<b>Cytosolic/vesicular buffers</b>
<b>Ca</b>	<b><math>\text{Ca}^{2+}</math></b>
<b>Uptake</b>	<b>Cytosol — <math>\rightarrow</math> SR flux via SERCA</b>
<b>Release</b>	<b>RyR mediated release</b>
<b>Leak</b>	<b>Efflux pathway for intrinsic SR leak.</b>
<b>Ca loss/gain</b>	<b>Fluxes mediated by Fickian diffusion.</b>

The fluxes shown above were isolated in-turn, for subsequent incorporation into a computational model.

In order to obtain a typical  $\text{Ca}^{2+}$  wave, with minimal signal noise, 5-8 waves were aligned with respect to the midpoint of their upstroke and an average waveform was calculated. An example of this is shown in Figure 3-3 below.

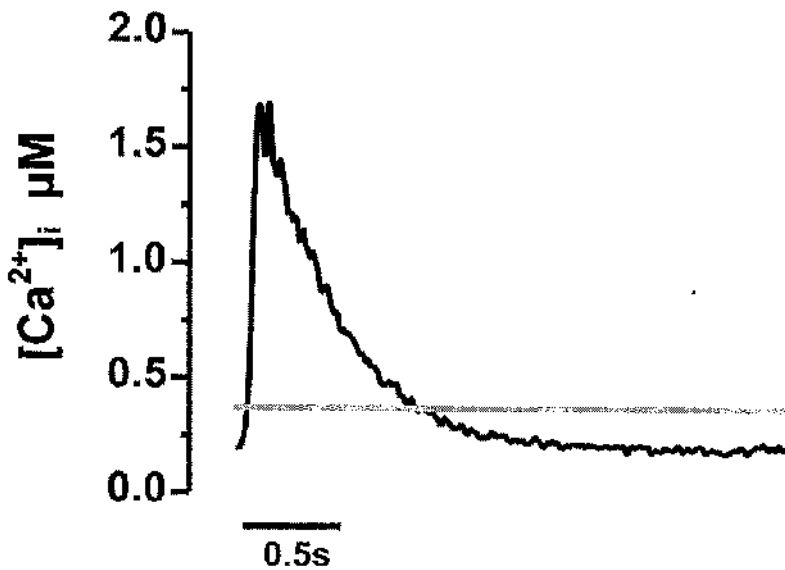


**Figure 3-3** Averaged wave profile from 5 typical  $Ca^{2+}$  waves. Grey line represents mean cytosolic  $[Ca^{2+}]_i$  (320nM).

When the RyR opens, as in a spontaneous release, most  $Ca^{2+}$  entering the cytosol from the SR is bound to cellular proteins, some escapes to the extracellular space by diffusion and the remainder is resequestered into the SR. The trace above is a consequence of all of these processes. In order to assess intracellular flux across the SR membrane, all of these processes must be dealt with in turn (see Figure 3-2).

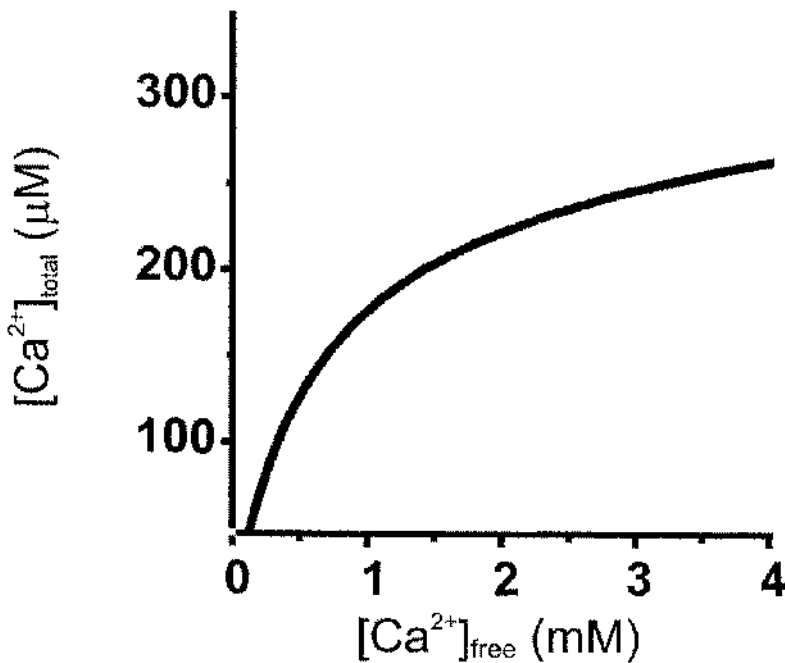
### 3.1.1 Intrinsic Cellular $Ca^{2+}$ Buffering

Attempts to attain a physiological description of intrinsic cellular buffering were described in the previous chapter. Since these proved unsuccessful, a previously published model of intrinsic cellular  $Ca^{2+}$  buffering was used. The model chosen was by Hove-Madsen & Bers, 1993. This is illustrated in Figure 3-4. The equation below shows how cytosolic  $[Ca^{2+}]_{total}$  is derived from a 2-buffer system.

#### Equation 2

$$[Ca]_{Total} = [Ca]_{Free} + \frac{B_{max(1)}}{[1 + (K_{b(1)} / [Ca]_{Free})]} + \frac{B_{max(2)}}{[1 + (K_{b(2)} / [Ca]_{Free})]}$$

,where  $B_{max}$  is the maximum free buffer concentration,  $K_b$  is the buffer dissociation constant, and  $n$  is the Hill coefficient. where  $B_{max(1)}$  and  $B_{max(2)}$  are the maximum free buffer concentrations,  $K_{b(1)}$  and  $K_{b(2)}$  are the dissociation constant for each buffer.



	Bmax	$K_b$
Buffer 1	2.13E-04	4.20E-07
Buffer 2	6.93E-04	7.90E-05

**Figure 3-4 Buffer curve derived from Hove-Madsen & Bers study.**

The figure above shows the resultant buffer curve using Hove-Madsen and Bers' equation. This can be used to convert  $[Ca^{2+}]_i$  to  $[Ca^{2+}]_{total}$  (see Appendix1 for program description). The resultant total cytosolic  $[Ca^{2+}]$  plot is shown in Figure 3-5.

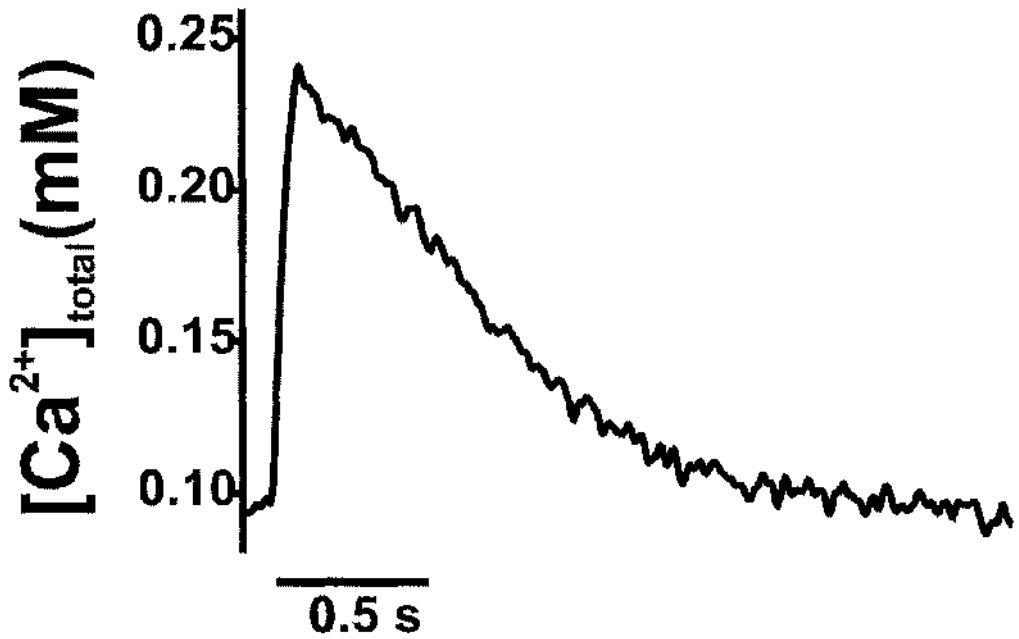


**Figure 3-5** Time course of total cytosolic  $[Ca^{2+}]$  converted from free cytosolic  $[Ca^{2+}]$  from Figure 3-3.

### 3.1.2 $Ca^{2+}$ Diffusion

The experiments discussed in this thesis were all performed on permeabilised cardiomyocytes. Physiological  $Ca^{2+}$  removal processes such as sarcolemmal NCX and Ca-ATPases are short-circuited, efflux and influx is by Fickian diffusion. During the  $Ca^{2+}$  wave, as  $[Ca^{2+}]_i$  exceeds that of the perfusing solution,  $Ca^{2+}$  diffuses out across the sarcolemma.  $Ca^{2+}$  diffuses back into the cell when the intra/extracellular concentration gradient is reversed in the diastolic period. This process can be described by the Fick equation (see below).

#### Equation 3

$$\frac{dCa_{total}}{dt} = k \cdot ([Ca]_i - [Ca]_o)$$

Where:

$$dCa_{total}/dt = \text{flux of } Ca^{2+}$$

$k$  = diffusional constant

This process can be assessed by rapid application of caffeine (10mM) in the presence of thapsigargin (25mM). Caffeine opens the RyR and thapsigargin is used to prevent SERCA uptake affecting the  $Ca^{2+}$  released. This raises intracellular  $Ca^{2+}$  above extracellular and effectively short circuits all SR fluxes and inhibits reuptake. Intracellular  $Ca^{2+}$  decline is therefore purely due to efflux across the surface membrane. This decline is fitted to a polynomial. This is converted to total cytosolic  $[Ca^{2+}]$ , then differentiated. This allows the solution of Equation 3 to derive the diffusion constant ( $k$ ).

For the assumption of Fickian diffusion to be true, a straight-line relationship must occur between diffusional flux ( $dCa_{total}/dt$ ) and the concentration gradient. This was reproducibly found. As shown in Figure 3-6, this was the case in the measurements of  $Ca^{2+}$  from permeabilised cells. The gradient of the line was used to obtain a value of  $k$  shown in Equation 3.

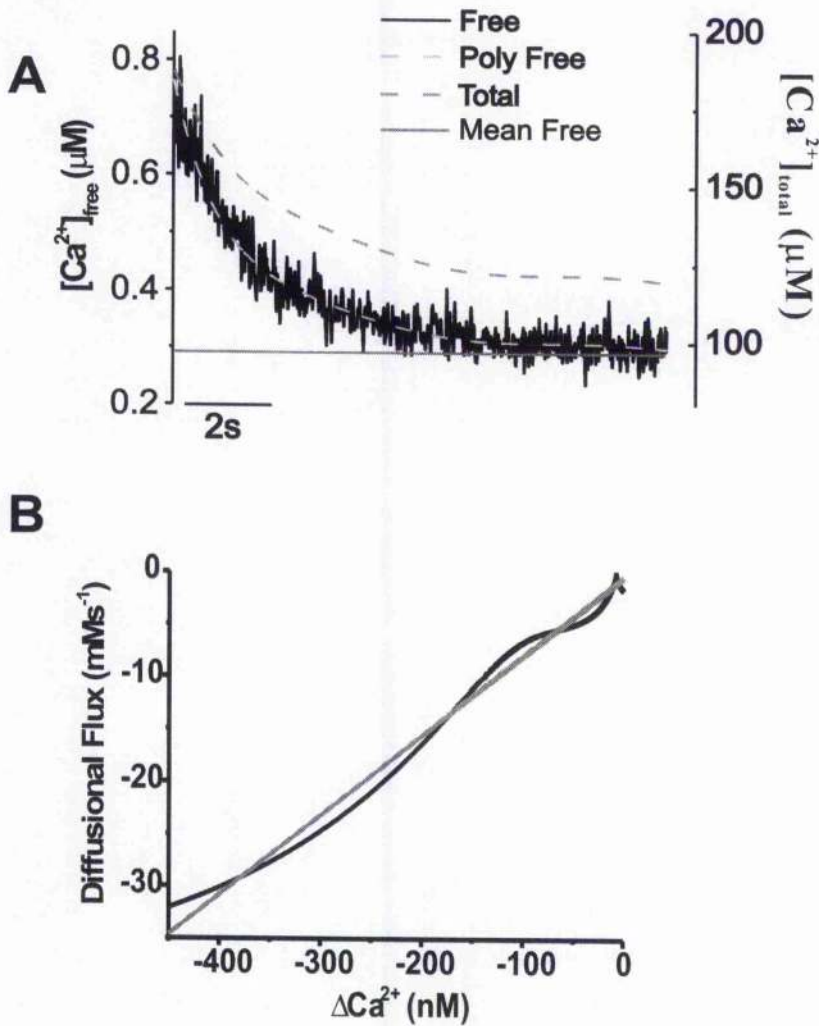


**Figure 3-6** Calculation of diffusion constant ( $k$ ) from decline of caffeine induced  $Ca^{2+}$  release in permeabilised cardiomyocyte.

**A**, plot of  $[Ca^{2+}]$  decline due to diffusion down concentration gradient. Solid grey line =  $[Ca^{2+}]_{bath}$ , solid black line =  $[Ca^{2+}]_i$ , dotted light grey line = polynomial fit of  $[Ca^{2+}]_i$ , dotted dark grey line = total  $[Ca^{2+}]$  converted from dotted light grey line. **B**, diffusional flux rate ( $dCa_{Tot}/dt$ ) vs.  $\Delta [Ca^{2+}]$  (i.e.  $[Ca^{2+}]_i - [Ca^{2+}]_{bath}$ ). Grey line = linear fit.

Typically, the diffusion constant ( $k$ ) was  $\sim 30s^{-1}$ . This was verified on a cell-cell basis (see Appendix for program description).

Once diffusional flux had been calculated over the time course of the wave, it was added to the  $[Ca^{2+}]_{total}$  trace. An example of this is shown Figure 3-7.

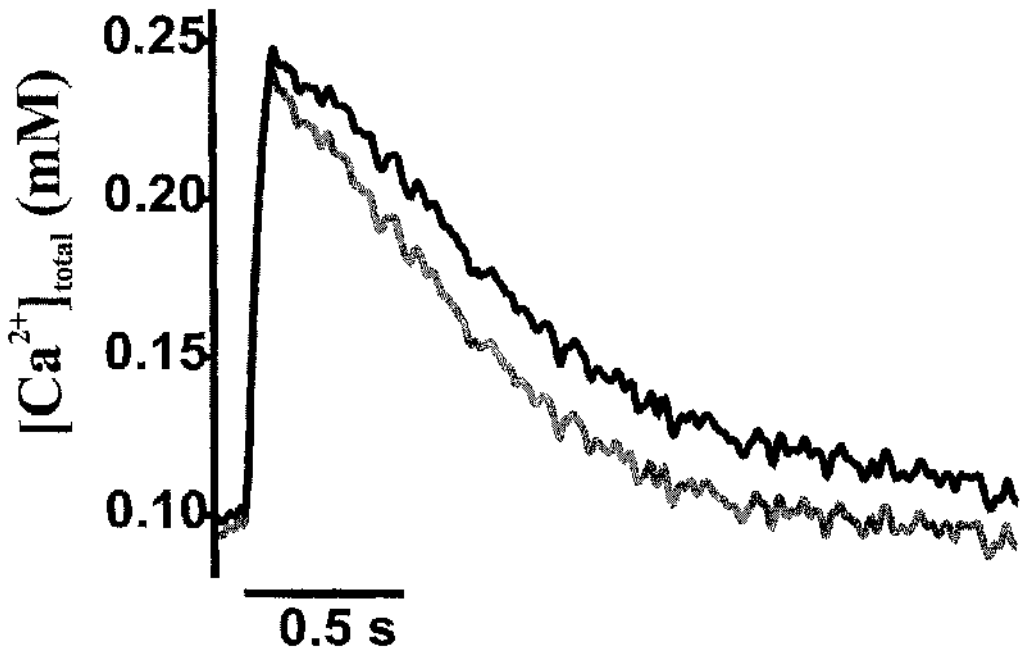


**Figure 3-7** Diffusion added to  $[Ca^{2+}]_{total}$ .  
 Grey line- $[Ca^{2+}]_{total}$  Black line  $[Ca^{2+}]_{total} + [Ca^{2+}]_{diffusion}$ .

The final trace shown in Figure 3-7 depicts the change in  $[Ca^{2+}]_{total}$  as a result of  $Ca^{2+}$  release from the SR. The grey line in Figure 3-7 represents the time-course of changes in  $[Ca^{2+}]_i$  after accounting for cellular buffering and represents the  $Ca^{2+}$  entering/leaving the cytosolic compartment. The black line represents this signal, after diffusional loss/gain to the extracellular compartment has been accounted for. This represents the changes in the cytosolic compartment solely due to  $Ca^{2+}$  release/gain from the SR. Numerically, it represents the integral of the  $Ca^{2+}$  fluxes from the SR. Therefore, to calculate the magnitude of the underlying fluxes, this signal must be differentiated. As shown in Figure 3-9, the first derivative of this relatively noise free signal generated a very noisy signal, from which analysis was difficult. To overcome this problem, the signal was fitted with a series of two polynomials. One polynomial was used to fit the rising phase and region around the peak and the other to fit the remainder of the declining phase. The upstroke, peak and declining phase were then reconstructed and any artefacts resulting from

the joining of the three sections were removed by a cubic-spline interpolation method.

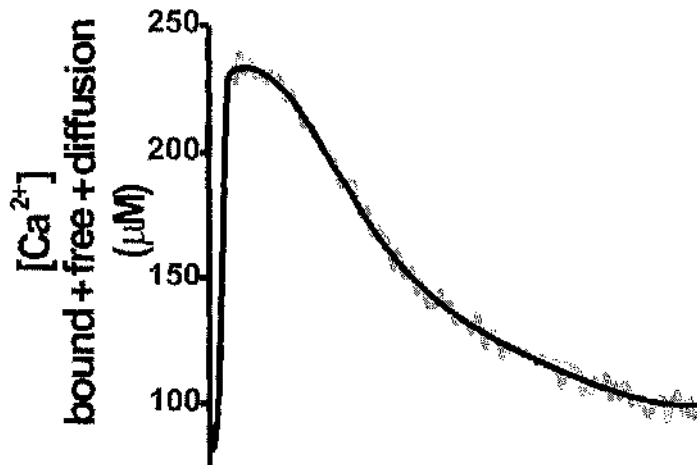


**Figure 3-8 Reconstructed polynomial smoothed trace of SR Ca flux integral. Grey line -unsmoothed trace; Black line 2-polynomial smoothed + original upstroke.**

The derivatives of the smoothed and unsmoothed data are shown in Figure 3-9.

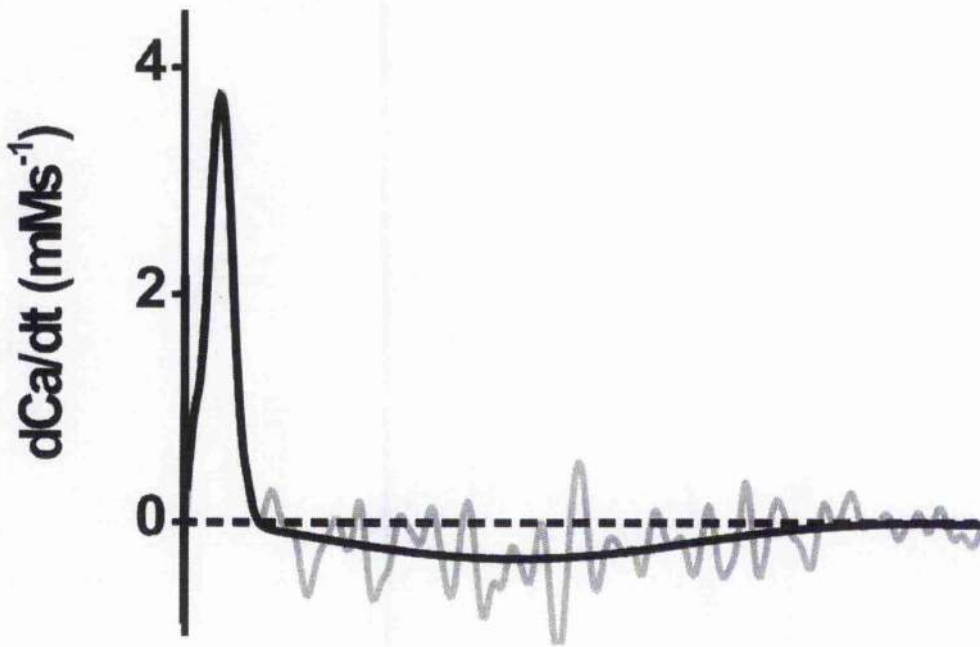


**Figure 3-9** First derivative of polynomial smoothed  $\text{Ca}^{2+}$  wave plot (black). Plot is equivalent to net SR flux. First derivative of unsmoothed data (grey) and zero flux line (dotted) are also shown.

The trace shows a large flux relating to the sharp upstroke, and a more gradual negative flux on the region of the declining phase of the  $\text{Ca}^{2+}$  wave. The initial flux primarily represents the flux through the RyR and the negative phase relates to SERCA uptake. This uptake element can be isolated from the net flux rate by using only the latter part of the wave, when the RyR has closed. See section below.

## 3.1.3 Quantification of SERCA activity

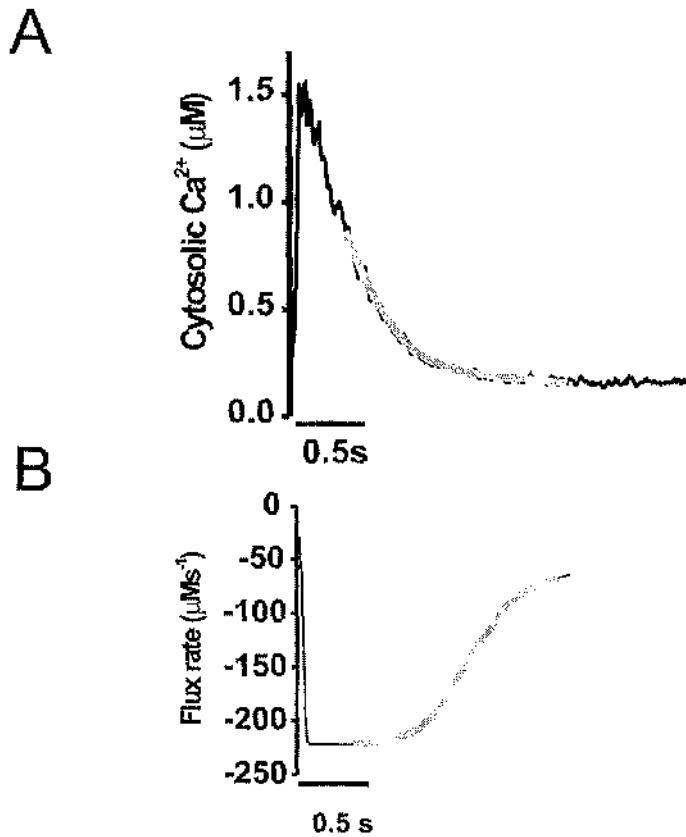


Figure 3-10 Graphs to demonstrate fitting of SERCA activity.

A, Averaged free cytosolic Ca<sup>2+</sup> profile from wave. B, Calculated SERCA flux rate. Grey line in both plots denotes region used to fit SERCA.

A description of SERCA behaviour has been previously described by (Shannon *et al.*, 2000). This contained a forward and reverse pumping mode, with the reverse mode acting to slow net SERCA uptake as the SR became full. The equation derived for this process is shown below.

Equation 4

$$J_{SR} = \frac{V_{max}([Ca^{2+}]_i/K_{mf})^H - V_{max}([Ca^{2+}]_{SR}/K_{mr})^H}{1 + ([Ca^{2+}]_i/K_{mf})^H + ([Ca^{2+}]_{SR}/K_{mr})^H}$$

Where:

$V_{max}$ =Maximal pump rate

$[Ca^{2+}]_i$ =intracellular  $[Ca^{2+}]$

$k_{mf}$ =forward Michaelis-Menten pump constant

$k_{mr}$ = backward Michaelis-Menten pump constant

H=Hill coefficient

$[Ca^{2+}]_{SR}$  =intra-SR  $[Ca^{2+}]$

$K_{mr} = 7000 \times k_{mf}$ .

Fitting was achieved through varying H,  $V_{max}$  and  $k_{mf}$ . Figure 3-10 B shows a typical fitted trace (See appendix for explanation of analysis program).

Equation 4 requires quantification of  $[Ca^{2+}]_{SR}$ . The following method was used for this calculation.

#### 3.1.4 Calculation of $[Ca^{2+}]_{SR}$

In all studies of SR  $Ca^{2+}$  mentioned in this thesis (see following chapter), SR  $Ca^{2+}$  depletion during waves and applications of caffeine were of comparable size. This indicates waves result in total depletion of SR  $Ca^{2+}$ , thus inverting the SR integral trace in Figure 3-8 will yield the total  $[Ca^{2+}]$  in the SR. Using the known binding properties of intra-SR buffers (i.e. calsequestrin), this can be converted to  $[Ca^{2+}]_i$  in the SR. An example trace is shown below.

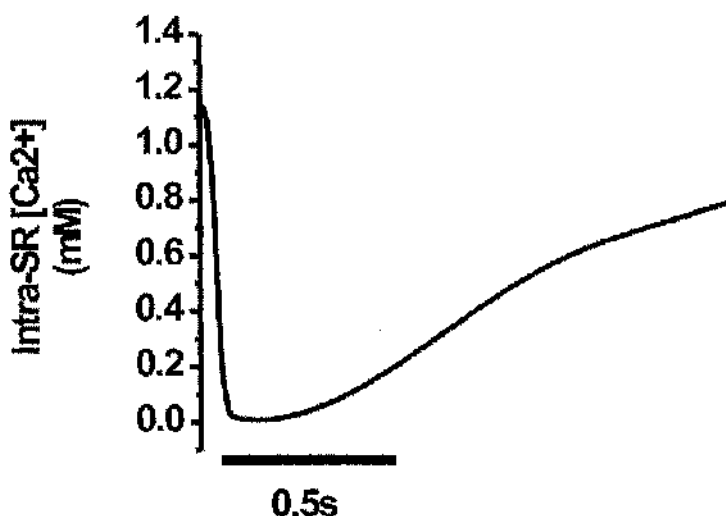
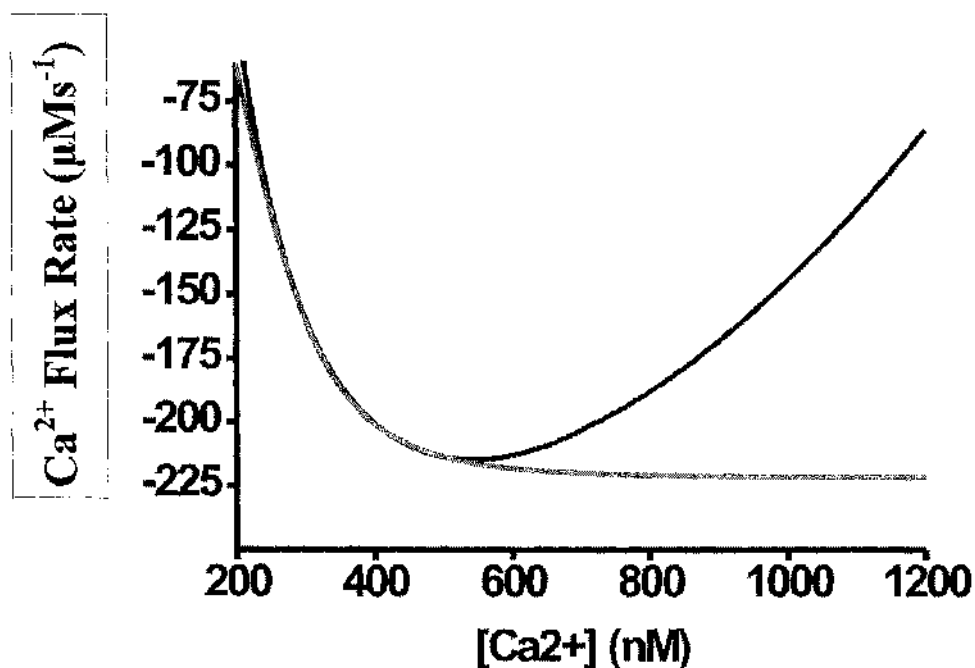


Figure 3-11 Intra-SR  $[Ca^{2+}]_i$  calculated from cytosolic  $[Ca^{2+}]_{total}$ .

The  $Ca^{2+}$  binding characteristics of calsequestrin (CSQ) have been estimated from studies of cardiac myocytes. Its  $K_D$  has been previously shown to be 0.630 mM (Shannon *et al.*, 2002), with a  $B_{max}$  of  $2.7 \pm 0.2$  mM SR or 140  $\mu\text{mol/l}$  cytosol when the volume of the SR has been compensated for (Shannon *et al.*, 2000).

Values for intra-SR  $[Ca^{2+}]$  were converted from units of  $\mu\text{mol/l}$  cytosol to  $\mu\text{M}$  SR by assuming the SR volume is 3.5% of the total cell volume and that 65% of the cell volume is cytosol (Page *et al.*, 1971). The final conversion factor was 18.1 L cytosol/L SR. This information allowed quantification of the  $[Ca^{2+}]_{SR}$  (See appendix for explanation of analysis program).

This quantification of the time-course of  $[Ca^{2+}]_{SR}$  now allows calculation of SERCA  $V_{max}$  and  $K_D$ . This is shown below.



**Figure 3-12** Graph showing calculated net flux from experiment (black line) and SERCA flux (grey line) calculated by fitting the region between 300 and 500 nM  $[Ca^{2+}]$ .

The graph shows the SERCA flux calculated from a region of the flux curve, where RyR release has terminated.  $V_{max}$  and  $K_D$  are calculated and Equation 4 is used to calculate the time-course of SERCA activity. The calculation uses the time-course of two signals ( $Ca^{2+}_i$  and  $Ca^{2+}_{SR}$ ). The graph below illustrates the flux rate-cytosolic  $Ca^{2+}$  relationship for this cell, with  $Ca^{2+}_{SR}$  held at  $1\mu M$ .

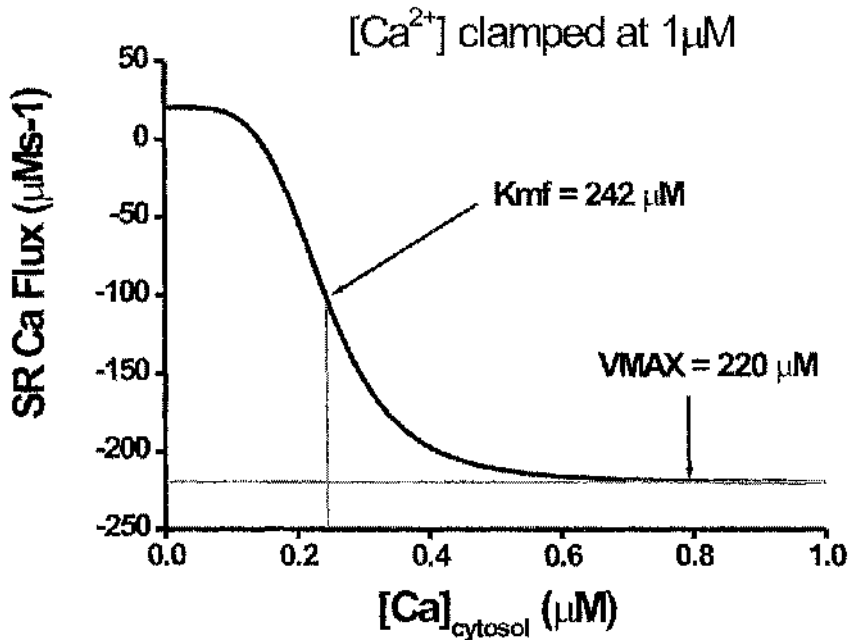


Figure 3-13 SR  $\text{Ca}^{2+}$  flux due to SERCA vs.  $[\text{Ca}^{2+}]_i$  when SR  $\text{Ca}^{2+}$  is clamped at  $1\mu\text{M}$ .  $V_{\text{max}}$  and  $k_m$  used to construct the curve are illustrated.

Figure 3-13 shows the activity- $[\text{Ca}^{2+}]$  plot for the cell shown above at a specific SR  $\text{Ca}^{2+}$ . SR  $\text{Ca}^{2+}$  changes as  $\text{Ca}^{2+}$  is released and resequenced from the SR. This curve will change with varying SR  $\text{Ca}^{2+}$ .

### 3.1.5 Extraction of RyR flux

SERCA flux, calculated using Equation 4, can be subtracted from the net SR flux derived by differentiating the SR flux integral as detailed earlier (See appendix for explanation of analysis program), to yield the Ca efflux component mediated through non-SERCA mechanisms (i.e. RYR channels). The predicted change in SR  $\text{Ca}^{2+}$  efflux during a  $\text{Ca}^{2+}$  wave is shown in Figure 3-14. The transient increase in efflux is attributed to the opening of RyR channels. From this time-course and knowledge of the trans-SR  $\text{Ca}^{2+}$  gradients, the RyR channel permeability can be estimated.

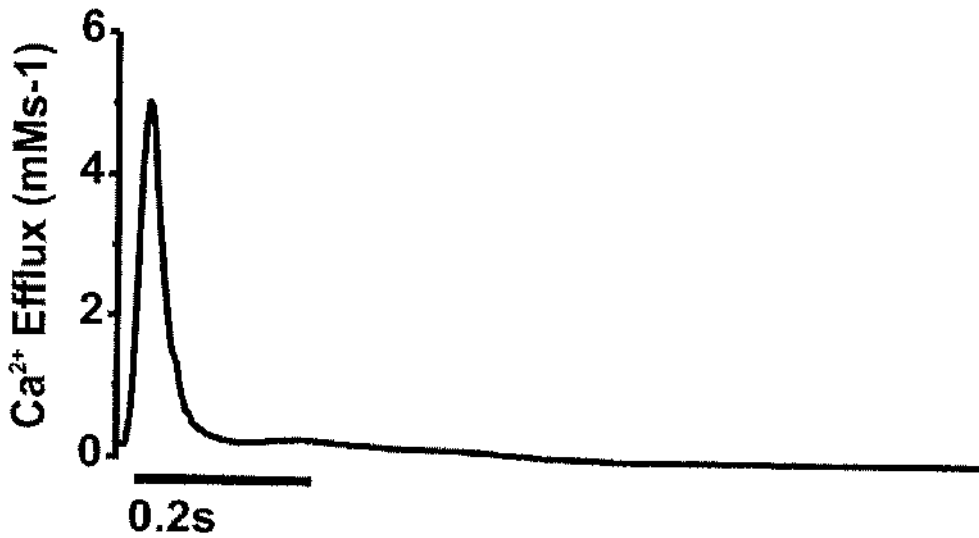


Figure 3-14 Graph of the change in  $Ca^{2+}$  efflux during a wave.

Using the SR-cytosol concentration gradient, permeability can be calculated (see appendix for explanation of analysis program). The equation used to calculate this is shown below.

Equation 5

$$P_{RyR} = \frac{J_{RyR}}{[Ca^{2+}]_{SR} - [Ca^{2+}]_{free}}$$

An example of a typical permeability is shown below.

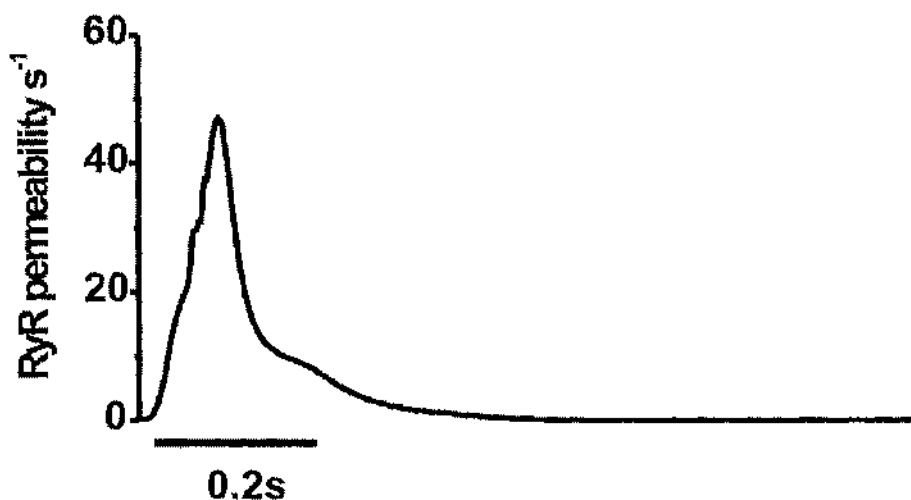


Figure 3-15 Typical RyR permeability calculated from previous RyR flux.

## 3.2 Extraction of wave velocity

### 3.2.1 Introduction

As described previously, the  $\text{Ca}^{2+}$  wave events within cardiomyocytes are recorded using confocal microscopy. This offers the benefit of high temporal (500Hz) and spatial ( $\sim 1\mu\text{m}^3$ ), resolution while sacrificing signal-to-noise ratio. The relatively high level of noise, which is inherent with recordings of low levels of light, prevents accurate quantification of both time-course and position of the waves.

With relatively noise free signals, it would be possible to estimate the position of the wave by finding the midpoint of the rising phase of the wave. With the type of noise typical for confocal measurements (Figure 3-16), both wave velocity and time course cannot be measured without strategies to reduce noise. It is the aim of this section to describe the procedures used to accurately measure the velocity of the  $\text{Ca}^{2+}$  wave and determine the time course of the  $\text{Ca}^{2+}$  wave.

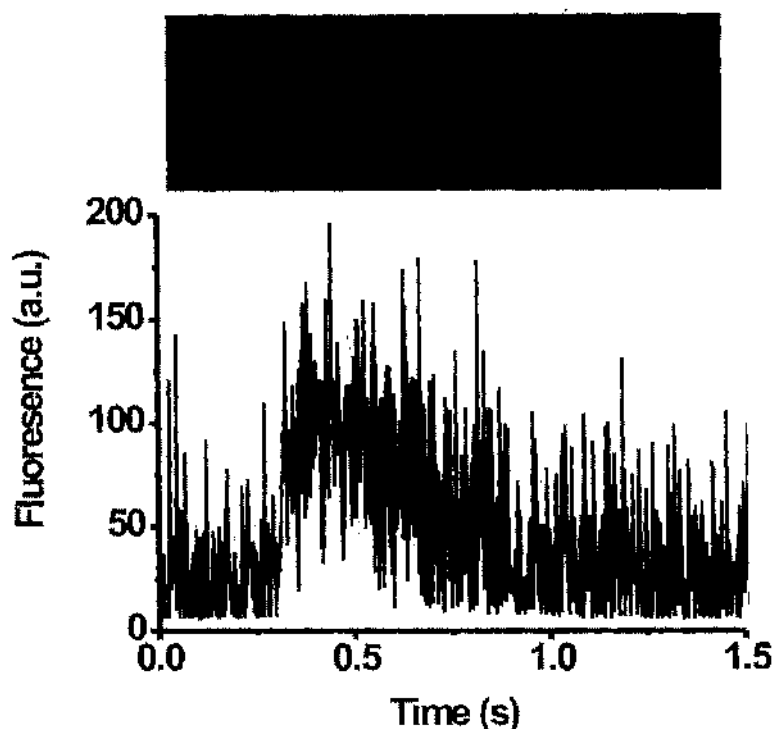


**Figure 3-16 Example of typical  $\text{Ca}^{2+}$  Wave.**

The figure shows a typical linescan image of a  $\text{Ca}^{2+}$  wave (upper) and the change in fluorescence from a one-pixel band with time. The trace has not been averaged or filtered in any way. This demonstrates the high intrinsic noise level relative to signal amplitude.

### 3.2.2 Why measure the velocity of the $\text{Ca}^{2+}$ wave?

The velocity of the  $\text{Ca}^{2+}$  wave is a function of the sensitivity of the CICR mechanisms and the diffusion of  $\text{Ca}^{2+}$  within the preparation. Changes in CICR will reflect changes in wave velocity.

### 3.2.3 Why correct for velocity?

The upstroke of the wave is used to calculate  $\text{Ca}^{2+}$  fluxes across the SR membrane. In order to attain useable data, all noise must be removed from the signal. To this means, as much of the cell is used to construct an averaged, less noisy signal. This averaging of the wave decreases the noise of the signal dramatically, but has adverse effects on the time-course of the wave. This causes temporal "smearing"

with most obvious effect on the upstroke of the wave. This is demonstrated in Figure 3-17 and Table 1.

No. of Pixels Averaged	Noise (% of 1 pixel value)	Max rate of rise (% of 1 pixel value)
1	100	100
2	56.3	84.831
4	29.2	61.461
8	15.2	36.067
10	12.4	28.876
20	6.46	14.494
80	3.31	3.596

**Table 1** Table showing the effect of averaging on the rate of rise of the upstroke of the  $\text{Ca}^{2+}$  wave and % change in noise.

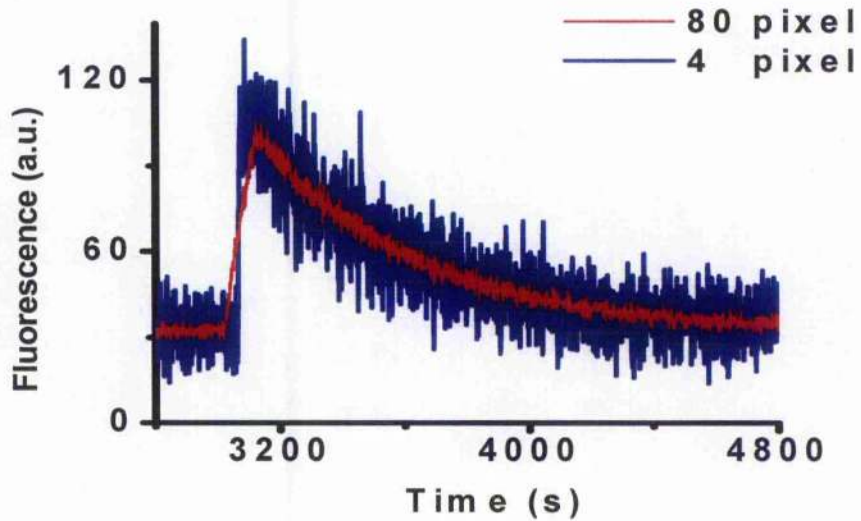


**Figure 3-17** Resultant fluorescence signal from averaged 4-pixel and 80-pixel bands. Note the upstroke of the 80-pixel band is appreciably skewed by the averaging.

The figure and table demonstrate the reduction in noise, but also show the adverse smearing effects. By realigning the wave as in the cross-correlation program, this smearing is avoided and the upstroke remains intact.

### 3.2.4 Signal vs. noise

The confocal system measures light emitted from low concentrations of fluorophore and from very small volumes (~1pL). Typically the scanning interval is 2msec, of which about 1.6ms to collect the signal (0.4 msec is fly-back time). Each line consists of 512 pixels, therefore each pixel is the integrated signal collected in ~3 $\mu$ s (1.6ms/512pixels). The number of photons collected is then expressed in terms as a number between 0 and 255 (8-bit). At this low light level and high sample rate, noise due to statistical fluctuations in light emission/collection becomes more evident. This phenomenon is termed *photon noise*. Photon noise refers to the inherent natural variation of the incident photon flux (<http://www.roperscientific.de/trefsnr.html>).

When measuring light, variation in the signal follows a Poisson distribution.

A Poisson distribution is similar to a Normal or Gaussian distribution with the following exceptions/properties:

A Poisson distribution is for discrete values, not continuous ones.

A Poisson distribution applies only to non-negative quantities--one counts arrivals, not departures.

A Poisson distribution has the property that its variance is equal to its mean:

$$\sigma^2 = \mu.$$

It can therefore be assumed that the histogram of the signal from one pixel over time will be Poisson distributed. For this to be achieved, the signal must first be converted to photons/pixel. Since  $\sigma^2 = \mu$ , the conversion factor from arbitrary fluorescence units to photons can be attained by plotting  $\sigma^2$  vs.  $\mu$  and taking the gradient of the line of best fit. The mean signal amplitude was varied between 20

and 80 using buffered  $\text{Ca}^{2+}$  solutions containing Fluo 3. The mean fluorescence of one pixel by 30000 scanlines (i.e. the duration of a typical experiment) was measured for the various intensities. This is shown in Figure 3-18. The conversion factor was calculated as  $18.1 \pm 0.5$  ( $n=5$ ). This value has consequences for the accuracy of  $\text{Ca}^{2+}$  measurements that will be explained in the later section.

**Figure 3-18 Graph showing change in variance with increasing signal amplitude. The red line shows the line of best fit for this relationship. This yields an estimated conversion factor of  $18.1 \pm 0.5$ .**

It is now possible to use this figure to calculate the number of photons collected per pixel. This could in turn be used to verify the assumption that the histogram of the noise was Poisson distributed.

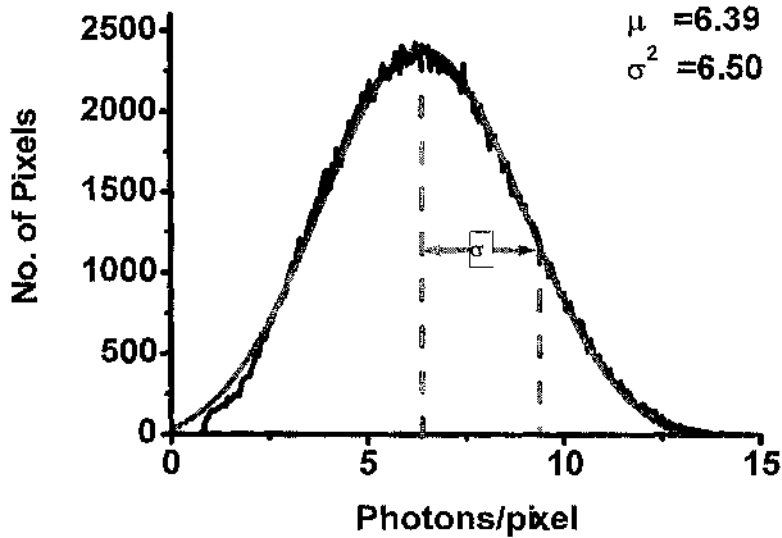


**Figure 3-19 Histogram of pixel intensity.**  
**Histogram shows Poisson distribution as  $\mu$  and  $\sigma^2$  are approximately equal.**

Typically, given the laser power of the system and the concentration of the dye, this equates to between 0.7 and 10 photons/pixel. Given then these low levels of light capture, the signal-to-noise ratio (SNR) is relatively low. This has been measure as between 0.7 (Fmin) and 10 (Fmax) photons/sec. The signal to SNR is typically between 0.8 and 3.1.

There are several ways to increase the SNR:

- 1) Increase fluorophore concentration
- 2) Increase laser power
- 3) Increase collection time

None of these are feasible as increasing fluorophore concentration would have decreased  $[Ca^{2+}]_i$ . This would also make the experiments extremely expensive. Increasing the laser power would induce cellular damage, which could lead to cell death. If the collection time was increased, temporal resolution would be sacrificed

and would impede quantification of the fluxes from the SR. Additional methods must be employed to deal with the SNR.

### 3.2.5 Finding the velocity of a $\text{Ca}^{2+}$ Wave

Several methods are available for estimating the velocity of the wave. By looking at a homogeneous section of wave using, image analysis software (LaserPix, Bio Rad, Hemel Hempstead, UK.), it is possible to estimate the position of the upstroke of the wave. A line can be drawn along the wavefront, where the user estimates the upstroke position (Figure 3-20). The program reports start and end positions of the line in  $\mu\text{m}$  and seconds. These measurements can be used to calculate the gradient of this line, which is equal to the velocity.



**Figure 3-20 Manual estimation of wavefront position using LaserPix program.**

This is the simplest method for finding the velocity of the  $\text{Ca}^{2+}$  wave, but has many disadvantages.

- 1) It is very subjective, with results dependent on the judgment of the individual measuring.
- 2) A long section of fairly constant velocity is need for good estimation.

### **3.2.5.1 Automated (non-subjective) methods for estimating wave velocity**

It is possible to use the midpoint of the rising phase of the wave as a reference point for estimating velocity. However as shown in Figure 3-16 the noise associated with the signal would preclude accurate estimation of the midpoint. The signal would require filtering, but this would also alter the time course of wave. Alternatively signals from adjacent pixels can be averaged to improve SNR. This method has also been tried, but still showed high noise sensitivity. In this thesis, the cross-correlation method previously employed by Cheng et al., (Cheng *et al.*, 1996b) has been used.

### **3.2.6 Cross-correlation method and its use in estimation of $\text{Ca}^{2+}$ wave velocity.**

This method was used as a "noise resistant" method for finding wave position. It is a standard method of estimating the degree to which two series are correlated. The Cheng et al. paper describes how the IDL programming environment was used to find wave position. This shall be summarized, with reference to how the problem was tackled in the case of this study.

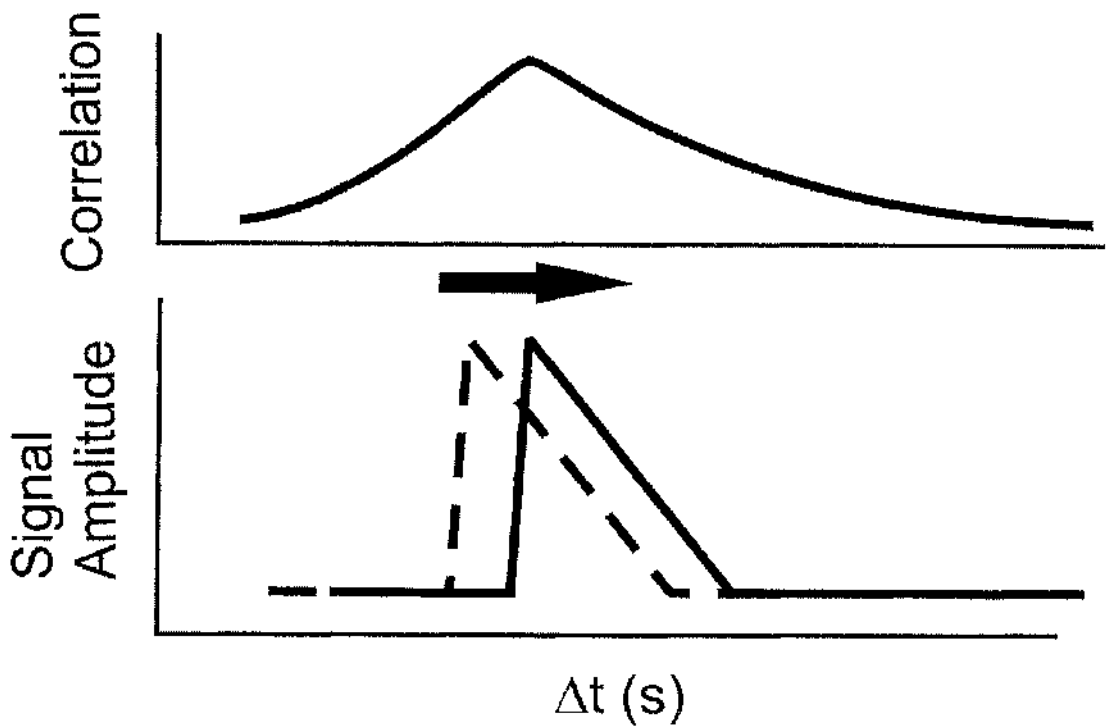


**Figure 3-21** Figure shows correlation result (upper) when dashed shape is moved in x direction (lower).

The method involves taking a section of the trace as a reference waveform and using this as a template for finding waveforms of similar shape. The position (P) of other waves in the wavefront as in the diagram above is given by the maximum of the cross-correlation (R) between the reference waveform (V) and the linescan image at a given line (W).

$$R(x) = \sum_{u=x-xpre}^{n=x+xpost} W(x+u)V(u) \quad \text{Equation 6}$$

Starting at  $xpre$ , (a distance before the wave) and finishing at  $xpost$  (a distance after the wave has occurred), the reference waveform is moved forwards, taking the product of the reference waveform and the linescan image. This gives a value of R,

relating to how similar the reference waveform and the section the waveform has been transposed on. The higher the value of R, the closer the reference waveform is to the waveform on the trace being studied. When R is maximal, the waveforms will be perfectly transposed, hence the wave position can be estimated. The wave velocity is found by plotting the wave position (with time) vs. the pixel resolution of the microscope ( $\sim 0.3\mu\text{m}$  per. pixel) and taking a linear fit. This analysis is only done on waves where sections of approximately constant velocity were observed. It was necessary to interpolate the waveforms to yield 10 times more points, to increase accuracy. This was done by cubic spline interpolation (see Appendix 1). The program was developed using the Borland Delphi programming environment. Various pre-developed components were used to plot data graphically (Rchart, Longinger software), to obtain Linear Fit (Tcurvefit, Longinger software), to read and display images (GraphicEx, Mike Lischke), and to output data to data files (Tdatafile, Francis Burton).

A brief description of how the program (CrossCorr) works is given below, followed by the methods employed to validate it.

### **3.2.7 CrossCorr Program**

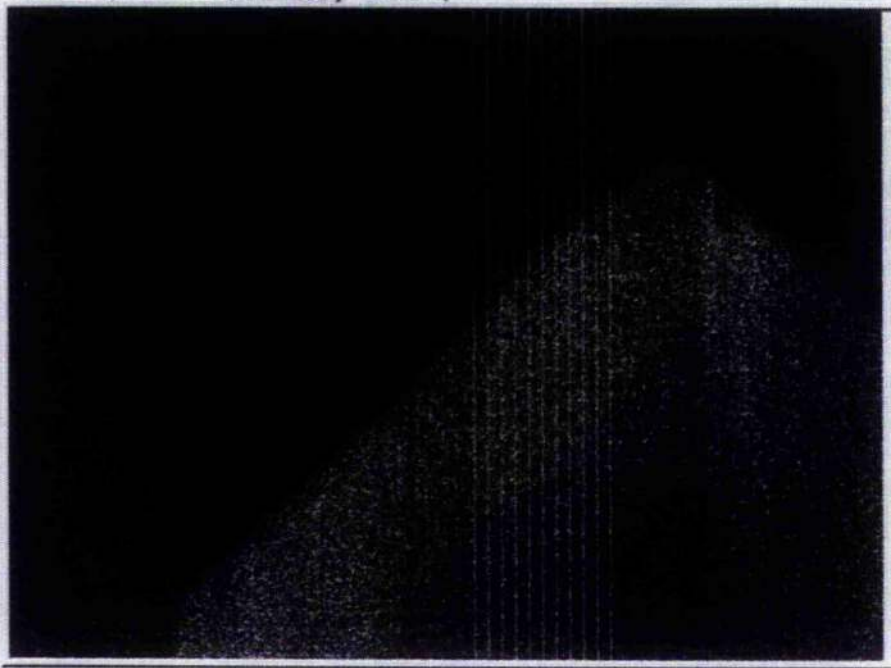
The linescan image is read in from a .TIFF file. The region of interest is selected by placing vertical bands on the image. The position, width and number of these can be varied as required (See Figure 3-22 Panel A). A smooth signal is extracted from the band to the left of the image (in panel A). This is achieved by averaging the fluorescence spatially, for the width of the band and smoothing the data with a lowpass filter temporally. (see filter description in appendix 1). This smooth signal allows the user to count the number of waves in the trace and attain a rough idea of their positioning. This is shown in Figure 3-22 B.

The position of the upstroke of the wave is found by placing a horizontal line, (denoted by the horizontal black line) at around the midpoint of the upstroke of the signal. A number of waves can be looked for at once. If you specify a start (red line), skip (blue line), and end (black line). The program looks for the point at which the fluorescence exceeds the threshold value, between the start and end lines. The program reports the point at which this occurs and skips forward a specified amount (Start+skip). It then begins to look again, until it finds all the waves in the selected section of the trace (between start and end). The program stores this wave position in an array to be indexed later. The black dots above the trace show waves that have been found, and the dot is placed a set number of points behind the wave position (i.e. the time between the red line and the upstroke of the first wave found).

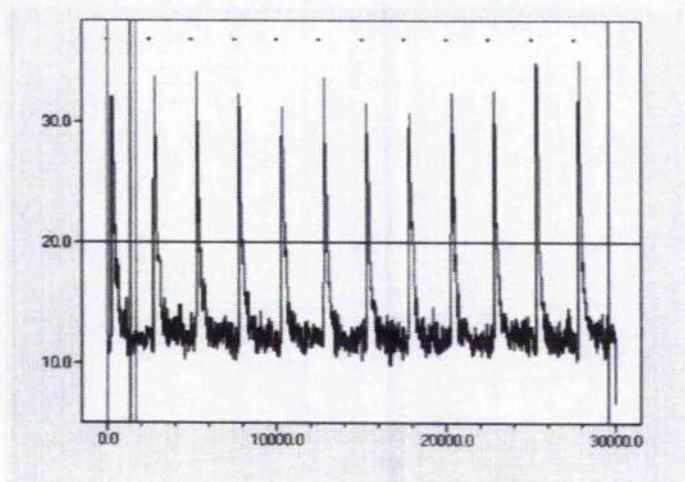
The first wave to be found is then displayed and the user selects a region for the template shape used to find the waves (this data is unfiltered). This region must leave about a 10% margin before and after the region selected for the template (see Figure 3-22 Panel B), to allow for the time between the wave position in the first column and the last column. This template, (Panel C) is read into an array and cross-correlated with the all the rest of the columns. The maximum correlation is reached when the position of the template and the wave being tested are in closest alignment. The template is used to cross correlate with the rest of the bands. Since the time-point of the wave position has been found and the distance between the bands is known, it is possible to roughly calculate the velocity by a linear fit. An average wave shape is then produced by extracting single pixel bands from the tiff file and aligning them, after offsetting for the calculated velocity. This averaged wave has less noise and is used as a more effective template for cross correlation.

This process is iterated a few times. The process usually converges after 3-6 iterations, depending on the noise of the signal. This was then repeated for all the waves that were read in from experiment and the velocities, goodness of fit and the amplitude in  $F/F_0$  of aligned wave were outputted (Panel D).

**A**



**B**



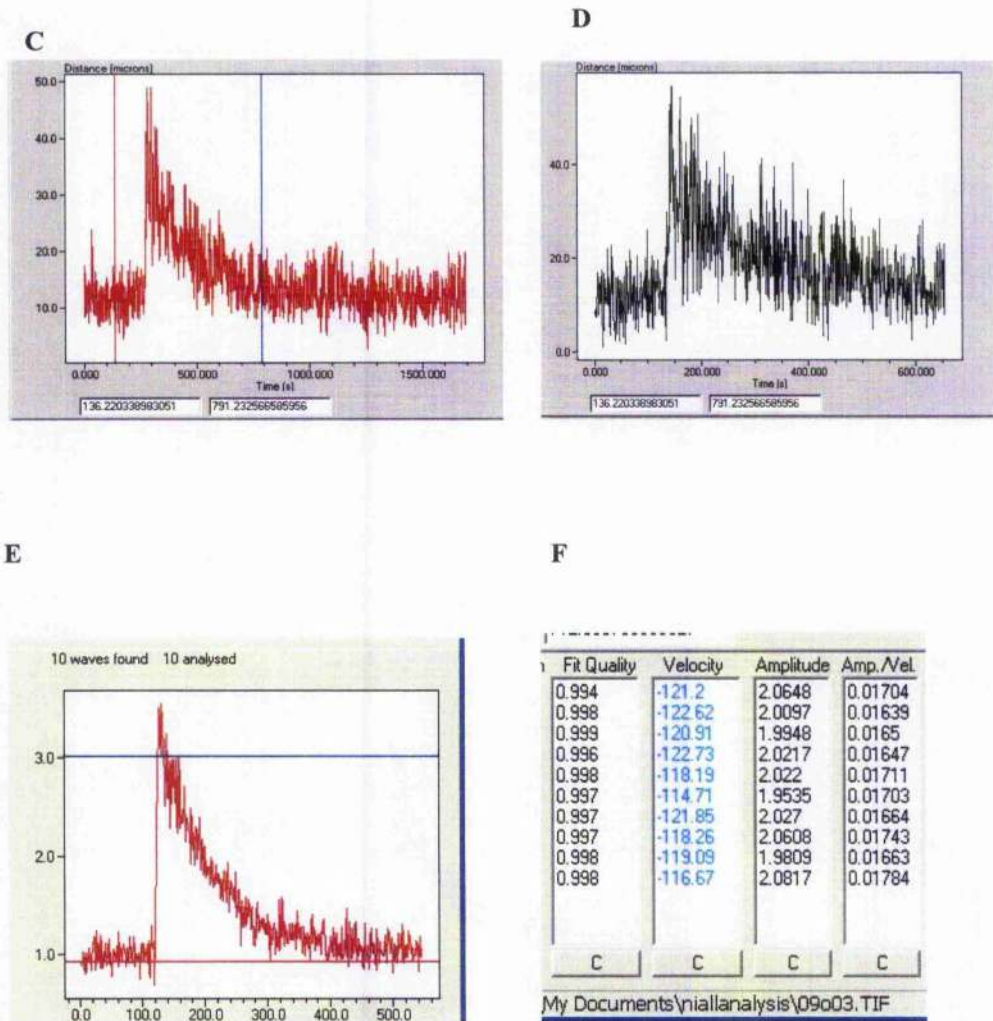


**Figure 3-22 Graphical display from cross correlation program.** Panel A how the region of interest, bandwidth and number of bands are selected from a display superimposed on the image. Panel B shows waves found by the program (Black dots mark the position). Panel C shows the section between the start (red) and stop (green) lines in panel B. Panel D shows the initial template for correlation. Panel E shows the resultant aligned wave after several iterations of the correlation algorithm, after conversion to  $F/F_0$ . The signal still contains high levels of noise, so the trace is filtered using a lowpass filter to obtain better estimates of wave amplitude. The results are outputted as shown in Panel F. The velocity is calculated from a linear fit of wave position and distance from first band. The fit quality of the Linear fit is outputted and waves are rejected if fit quality drops below 0.9. Amplitude is expressed in  $F/F_0$  and Amplitude/Velocity is outputted as a measure of RyR sensitivity.

The program took extensive development and testing, and many thanks go to Dr. Francis Burton, whose nbands program inspired the display and extraction of data from Tiff images. The testing of the program was achieved with the linescan

image generation program (LineSim) written by Dr. John Dempster, see section 3.2.8.

The cross-correlation method was used as a “noise-resistant” method of finding wave position. To verify if this was true and whether an acceptable accuracy level was achieved in analyzing our linescan images, LineSim program was used.

This program generates linescans with variable noise and velocity. How this noise is quantified and subsequently adjusted is discussed in section 3.2.4. Examples of a noisy and noise-free signal are shown in Figure 3-23.

### **3.2.8 Testing the cross-correlation method**

The LineSim program was used in all testing of the CrossCorr program. The program works by firstly constructing a shape analogous to that of a wave. This is represented by a rapid exponential rise, followed by a more gradual exponential fall. A rise time constant of 0.5s and a fall time constant of 0.1s were used in all waves simulations. Unless otherwise stated, wave velocity was set at  $120 \mu\text{ms}^{-1}$ .

The noise for this signal is then added with variance increasing as a function of amplitude. This is repeated for the full width of the image (512 pixels), and the signal is offset by a set amount to replicate a wave of specified velocity. A ratio of peak to resting level of 3 was used in the noise simulations, as shown in Figure 3-16, this is close to that measured experimentally.

The noise level was varied using the LineSim program and the effect on velocity assessed in terms of percentage error.

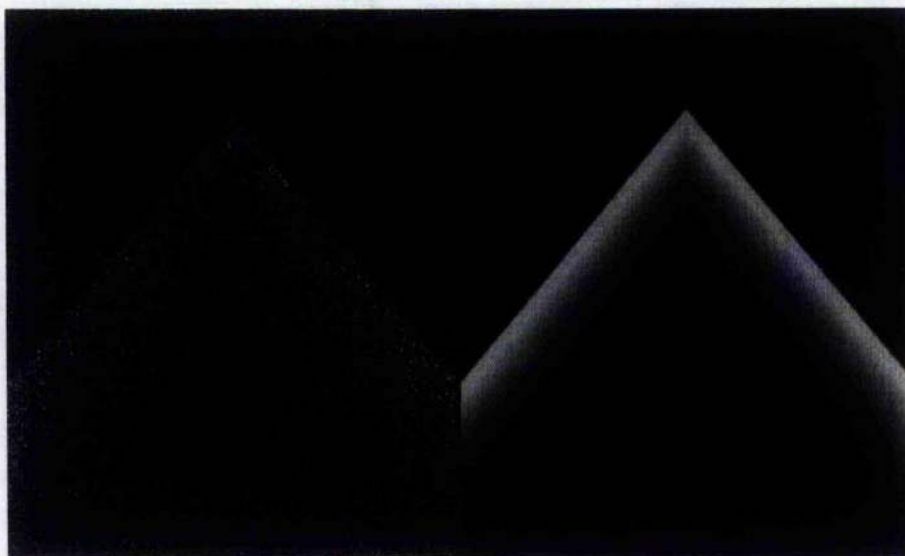


**Figure 3-23** Examples of simulated linescan images with more (left) and less (right) noise.

The minimum number and width of bands was quantified in order to attain this result. The rationale and measurements behind this is detailed below.

### **What proportion of the cell can be used for measurement of velocity?**

In order to minimize error, it would be preferable to take the whole length of the cell for velocity measurement. For practical reasons, this is not possible. A homogeneous region of cell with approximately constant velocity is required for velocity estimation. If this is interrupted, velocity estimation is no longer possible. Various situations arise in the experimental situation which stop a homogeneous wavefront for measurement. The wave initiation site moves from wave to wave. If the initiation site moves into the section used for measurement of velocity, the wave cannot be used. If some of the cell is out of focus, or an organelle is in the field the same is true. A region of  $\sim 1/4$  of the cell or  $\sim 80$  pixels is a practical length to reproducibly measure velocity, as it avoids all of these complications. This is the width covered by each band in Figure 3-22 Panel A.

### 3.2.9 Optimising the program

Two parameters affect the estimate of wave velocity by the cross-correlation method.

Band width

Number of bands

In order to gauge the effectiveness of each of these on the estimation of velocity, both were investigated.

#### 3.2.9.1 Bandwidth

The peak of the cross correlation of reference and test bands gives the position of the wave. If the two signals contain high levels of noise, high variance is observed in the cross-correlation (Table 2) and false peaks can be produced. This yields false estimates of wave velocity. Increasing the number of adjacent bands (bandwidth) used to create and averaged signal decreases the noise substantially and decreases the chance of erroneous correlation peaks (see Figure 3-24).

The effect of this on estimation of wave velocity is described below.

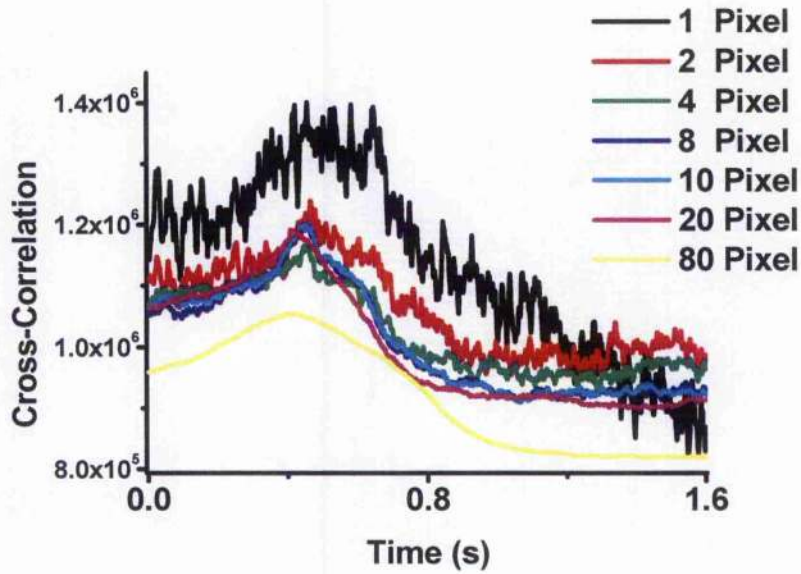


Figure 3-24 Graph showing variability on correlation plots from bands of varying pixel width.

No. of Pixels Averaged	Noise (% of 1 pixel value)	Variance of correlation (% of 1 pixel value)
1	100	100
2	56.3	32
4	29.2	12
8	15.24	3
10	12.4	2
20	6.46	1
80	3.31	0.001

Table 2 Table showing the effect of changing the number of pixels averaged before correlation on both noise and variance of correlation.

Values are expressed as a percentage of one-pixel values. Bands of 8 and above exhibit lower noise and much less variance on their correlations.

Variation is unacceptably high at 1 pixel width. The maximum correlation is obscured by high variability. Analysis on this was done using the same noise level as in the band width study. As mentioned, noise affects the estimate of velocity.

Since increasing the width of the bands decreases the noise and hence should increase accuracy in estimation of velocity. To investigate this further, correlation plots were taken from bands of different width.

Figure 3-24 and Table 2 demonstrate how noise is decreased by increasing the number of adjacent pixels averaged. Noise adversely affects estimation of correlation peak, as false peaks are created due from random variation in the signal. This is particularly evident in the one pixel band correlation plot in Figure 3-24. Table 2 shows how variance falls close to zero when 80 adjacent pixels are averaged. Variance values of 3 or less minimize error on finding the maximum correlation peak.

Quantification of how changing band width affects estimation of velocity was carried out and the results are shown below.

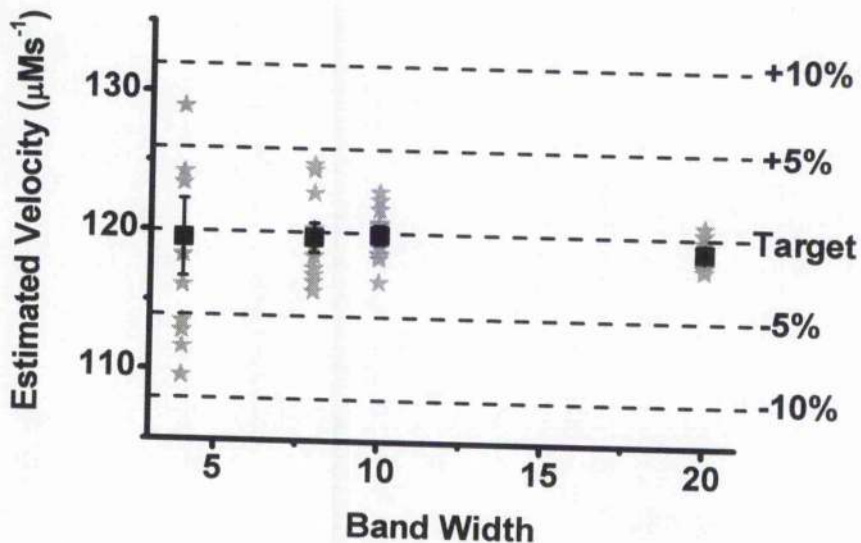


**Figure 3-25** Graph showing the effect of increasing the width of band for averaging fluorescence on the estimated velocity using the correlation program. Black squares represent the mean estimated velocity  $\pm$  S.E.M.. Grey Stars are individual estimates of velocity using the cross-correlation program. Error on estimation of velocity for both 8 and 10 width bands are below 5%. Error was unacceptably high for 1 and 2 width bands, so these are not displayed.

Figure 3-25 shows how band width affects estimation of velocity. Bands of 8 and above exhibit much less noise, less variability of correlation and subsequently have lower error on estimation of velocity. For these reasons, 8-pixel bands was deemed an acceptable level of averaging for the purpose of cross-correlation.

### 3.2.9.2 Number of bands

Once wave positions are estimated, wave velocity is taken as the linear fit of these vs. distance. Increasing the number of bands used in this estimate of velocity increases accuracy.

A range of band numbers from 2-20, each 8 pixels wide were used to find the velocities of simulated waves, with noise levels similar to that of experiment. The results are shown in Figure 3-26.

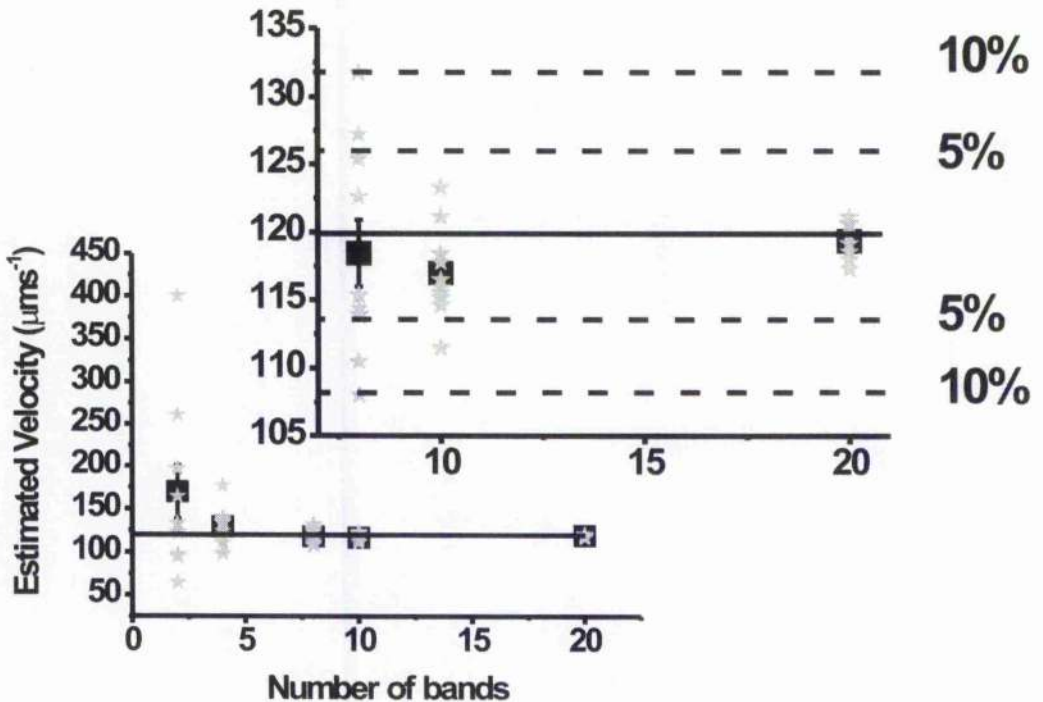


Figure 3-26 Graph showing the effect of increasing number of bands on velocity estimation.

Black squares denote the mean value +/- S.E.M. Black line indicates real velocity stipulated in LineSim program. Inset showing velocity estimates within limited range

**of band number. Error increases exponentially with decreasing number of bands. The range of estimated velocity halves between 8 and 10 bands.**

The graph shows a halving of the range of velocity between 8 and 10 bands. This indicates a high sensitivity when varying the number of bands used in the measurement.

As mentioned, 80 pixels was chosen as the maximum width for estimation of velocity. From the error analysis carried out above, it was possible to show that 10 bands, 8 pixels wide is the optimum combination for minimizing velocity and on average yields <5% error on velocity estimation. For all future measurements of velocity, this will be the combination used.

#### **3.2.10 Effect of noise**

To assess the effect of noise on estimate of velocity, with the chosen width and number of bands, noise levels were varied using the LineSim program. To derive these results, ten simulated waves with the same velocity were created. The noise was varied from ~4 to ~19. The estimate of velocity was carried out on each of the ten simulated waves. The results are plotted in

Figure 3-27.

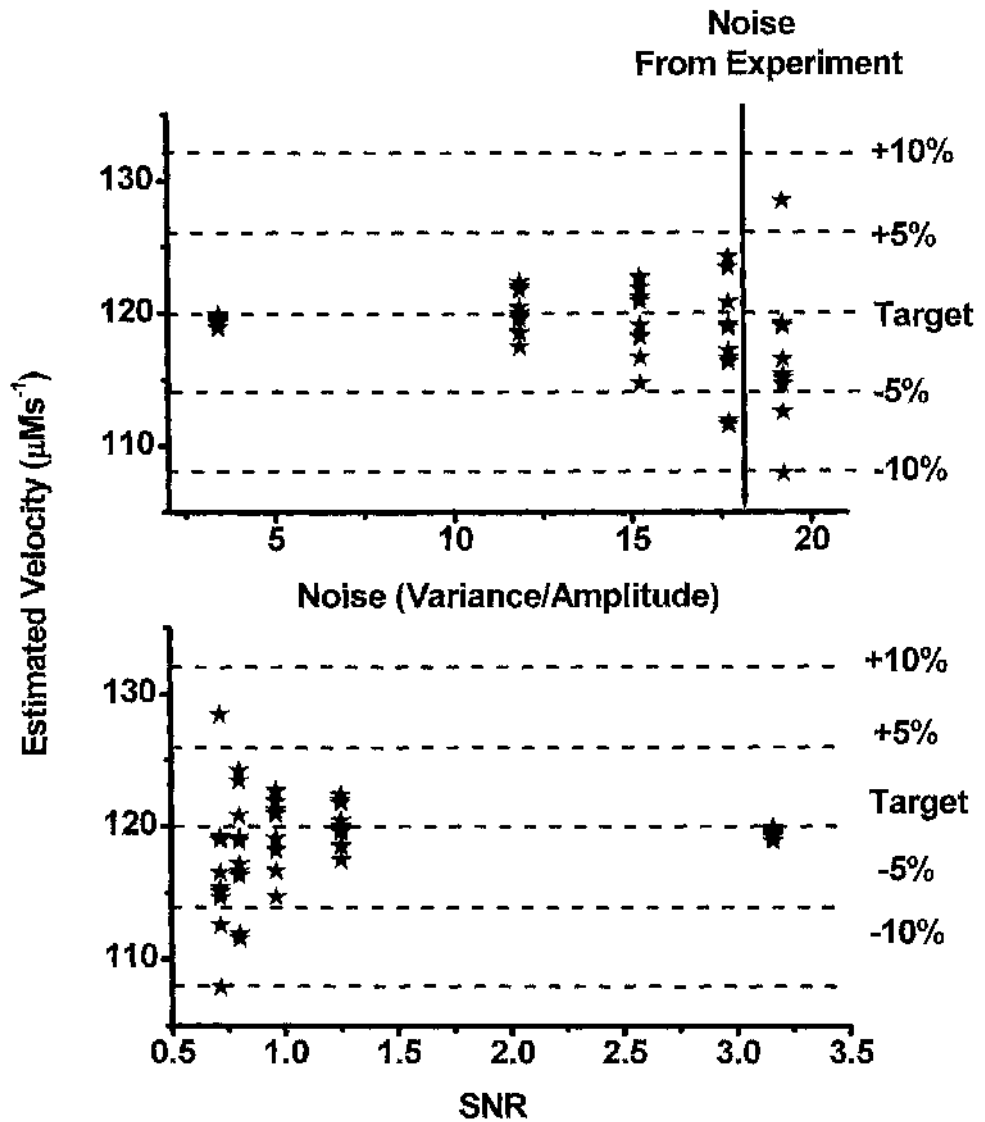


Figure 3-27 Noise dependency of velocity estimation.

Panel A: - Plot of the effect of noise vs. estimated velocity.

Velocity estimation becomes less reliable as noise increases. Black stars indicate individual estimates of velocity. Arrow shows level of noise seen in typically in experiment.

Panel B: - Plot of SNR vs. estimated velocity.

Panel A of

Figure 3-27 shows the estimate of velocity is fairly robust until noise levels become higher than observed experimentally. The method is however not noise resistant.

Panel B demonstrates increasing SNR yields very small gains in velocity estimate above SNR=1. Below SNR=1, velocity estimate reliability decreases dramatically.

With the number and width of bands used in this analysis, most velocity estimates were within 5% of the actual value. This was deemed an acceptable level for experimental measurement.

**Chapter 4 Experimental manipulations used to alter wave characteristics in permeabilised cardiomyocytes.**

## 4.1 Introduction

$\text{Ca}^{2+}$  waves are a phenomenon of CICR induced by overload of the SR. In our experimental preparation,  $\text{Ca}^{2+}$  waves can be studied without the complication of surface membrane processes. This allows resolution of the fluxes involved in SR release and uptake during a  $\text{Ca}^{2+}$  wave (explained in previous chapter). Through this approach it is hoped to use  $\text{Ca}^{2+}$  waves as a tool for quantifying the changes in release and uptake mechanisms under various experimental situations. Subsequent reconstitution of these fluxes into a mathematical model will allow evaluation of current theories of  $\text{Ca}^{2+}$  release from the SR.

In this section,  $\text{Ca}^{2+}$  waves characteristics shall be altered by various means:

1. Increasing mean cytosolic  $\text{Ca}^{2+}$
2. Decreasing RyR sensitivity using tetracaine
3. Decreasing SERCA activity using TBQ

Changes in  $[\text{Ca}^{2+}]_{\text{SR}}$  and parameters of release and uptake shall be quantified to assess the changes observed with each of these alterations.

These shall be used to explain the changes observed in wave frequency, minimum and maximum  $[\text{Ca}^{2+}]_i$ .

## 4.2 Previous work

### 4.2.1 The effect of increased mean $[\text{Ca}^{2+}]_i$ on $\text{Ca}^{2+}$ waves

In the intact cell, increasing stimulation rate will increase diastolic (minimum) and systolic (peak)  $[\text{Ca}^{2+}]_i$  and subsequently  $[\text{Ca}^{2+}]_i^{\text{mean}}$  (Bers, 2002). This also leads to increased loading of the SR.

Increasing stimulation frequency increases  $[Ca^{2+}]_i^{mean}$ . Does  $[Ca^{2+}]_i^{mean}$  dictate spontaneous oscillation?

It has been observed that increasing external  $[Ca^{2+}]$  in intact cells exhibiting spontaneous release will cause increased frequency oscillations (Fabiato & Fabiato, 1972; Stern *et al.*, 1988; Diaz *et al.*, 1997). The Diaz *et al.* study showed both  $Ca^{2+}$  efflux in the wave and SR content did not change. The change in frequency must therefore be independent of SR content (Diaz *et al.*, 1997).

#### 4.2.1.1 Are there different types of $Ca^{2+}$ wave?

Three distinct types of  $Ca^{2+}$  waves were described in a study by Kaneko *et al.* (Kaneko *et al.*, 2000). The study used Langendorff perfused rat hearts and confocal microscopy and found waves with different amplitudes and frequency. Low frequency (0.06 Hz) waves were seen when in intact regions when excitation rate was dropped to <5bpm. These were seen to propagate at  $\sim 80 \mu\text{ms}^{-1}$ . These were termed *sporadic waves*. In cells with higher basal fluorescence, much more frequent waves (0.47 Hz) were observed, propagating at  $\sim 117 \mu\text{ms}^{-1}$ . These were named *Ca<sup>2+</sup>-overloaded waves*. A third class of waves were described, which had very high frequency (2.2 Hz). Propagation velocity ( $\sim 112 \mu\text{ms}^{-1}$ ) was comparable to that observed from the overloaded waves. These were observed in regions damaged by microelectrodes and had basal fluorescence values higher than both sporadic and overloaded waves. These were named *agonal waves*. The study concluded that the different wave types were caused by the  $Ca^{2+}$ -loading state of the cells.

A subsequent study by Loughrey *et al.* (Loughrey *et al.*, 2002) investigated this to characterise various changes in wave parameters over a range of  $[Ca^{2+}]_i^{mean}$ .

Permeabilised rabbit cardiomyocytes were perfused with mock intracellular solutions containing fluorophores (Fluo-3 or Fluo-5) and  $[Ca^{2+}]_i^{mean}$  was varied by changing  $[Ca^{2+}]_{both}^{mean}$ . This study did not find different types of  $Ca^{2+}$  wave, but showed frequency, diastolic (min) and systolic (peak)  $[Ca^{2+}]_i$  were described by linear relationships. Wave frequency was seen to increase linearly over a range of  $[Ca^{2+}]_i^{mean}$  from 0.15 Hz 300nM to ~0.5 Hz at ~900nM. Diastolic (min) and systolic (peak) were seen to increase from 150nM to ~300nM and 2.1 to 2.5  $\mu$ M respectively, over the same range. When wave frequency was explored over a greater  $[Ca^{2+}]_i^{mean}$  range (up to 3.4 $\mu$ M extracellular), the linear relationship continued.

No waves resembling the agonal or sporadic waves of the Kaneko et al. study were observed. This was reconciled by the fact that pH and ATP concentration in the permeabilised experiments could be tightly regulated. Changes in these could alter wave characteristics. This could have occurred in the whole heart study (Kaneko *et al.*, 2000).

#### 4.2.2 The effect of tetracaine on spontaneous release from the SR

Tetracaine is a local anaesthetic, which has been used extensively in the study of E-C coupling. Single channel studies have shown the open probability ( $P_o$ ) of the RyR is decreased by application of tetracaine (Xu *et al.*, 1993b). This has also been demonstrated by inhibition of spontaneous sparks and waves in intact cardiomyocytes (Gyorke *et al.*, 1997; Overend *et al.*, 1997; Smith & O'Neill, 2001). At lower concentrations, it has been shown to potentiate caffeine -induced  $Ca^{2+}$  release by increasing  $[Ca^{2+}]_{SR}$  (Gyorke *et al.*, 1997; Overend *et al.*, 1997; Smith & O'Neill, 2001).

The effect of tetracaine on spontaneous  $\text{Ca}^{2+}$  waves was investigated by Overend et al. (Overend *et al.*, 1997) (Figure 4-1). This study showed effects of tetracaine at  $\geq 50 \mu\text{M}$ . Perfusion of tetracaine initially halted  $\text{Ca}^{2+}$  waves. Spontaneous release was then resumed with decreased frequency and increased amplitude. When tetracaine was removed, a burst of spontaneous activity was observed, followed by a return of frequency to control levels. These results were explained in terms of changes in SR content (Figure 4-2). Tetracaine increased the luminal threshold for release, requiring an initial filling time to reach the new level for release. Once tetracaine was removed, the resultant bursting was caused by a gradual adjustment of threshold back to control levels.

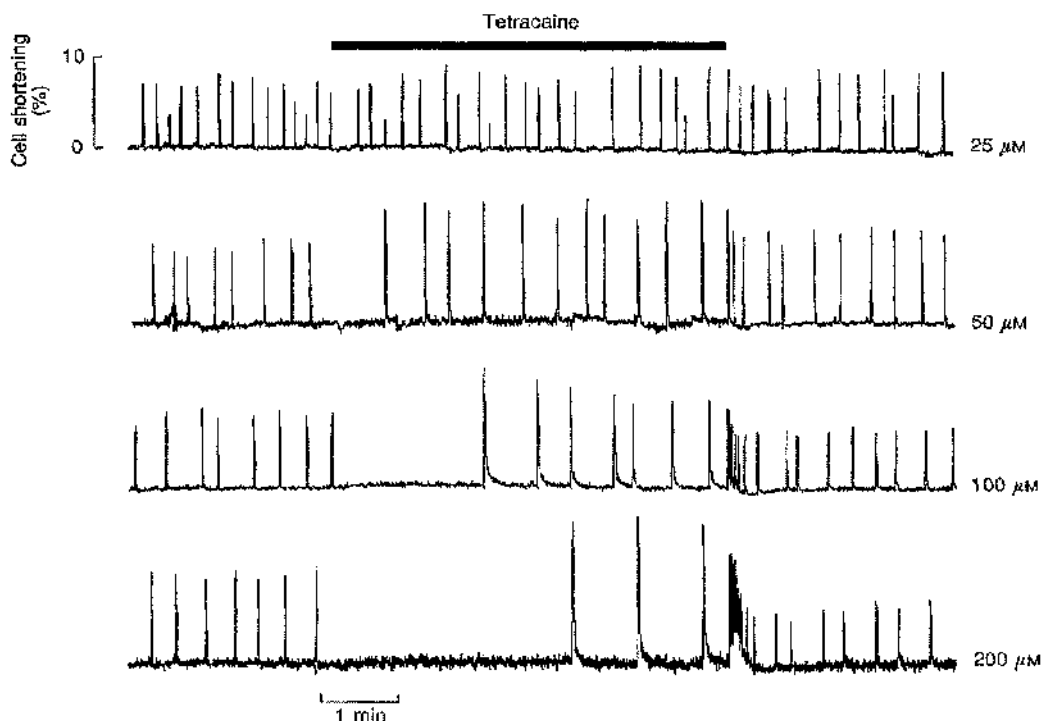


**Figure 4-1.** The effects of tetracaine on spontaneous  $\text{Ca}^{2+}$  waves in intact rat myocytes. Tetracaine of various concentrations (25-200 $\mu\text{M}$ ) was applied for the period shown by the black bar. Traces show cell shortening. (Figure taken from (Overend *et al.*, 1997))

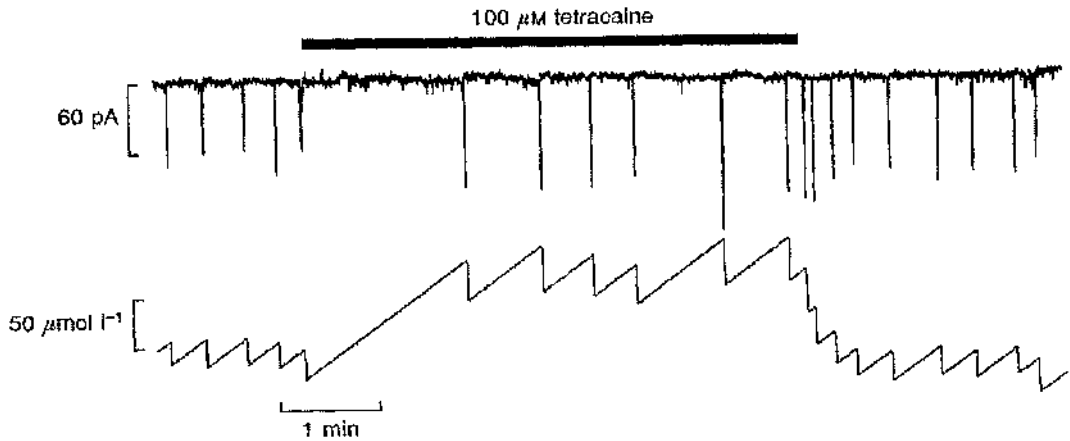


**Figure 4-2** Calculated fluctuations in SR  $\text{Ca}^{2+}$  content during  $\text{Ca}^{2+}$  waves with and without tetracaine ( $100\mu\text{M}$ ).

Membrane current (above) and calculated SR  $\text{Ca}^{2+}$  content (below). Tetracaine ( $100\mu\text{M}$ ) was applied for the period shown. SR  $\text{Ca}^{2+}$  was calculated by integrating current records for the period of each oscillation. (taken from (Overend *et al.*, 1997)).

This data describes a current theory behind the effect of tetracaine on spontaneous release.

#### 4.2.3 The effect of SERCA inhibition on $\text{Ca}^{2+}$ waves

##### 4.2.3.1 Thapsigargin

The effects of inhibiting SERCA on  $\text{Ca}^{2+}$  wave characteristics in rat cardiomyocytes have been previously investigated by Lukyanenko *et al.* (Lukyanenko *et al.*, 1999). This study used thapsigargin ( $10\mu\text{M}$ ) to selectively inhibit SERCA. Thapsigargin is an irreversible, selective inhibitor of SERCA. Inhibition of SERCA is known to deplete the SR of  $\text{Ca}^{2+}$ . This study incubated thapsigargin ( $10\mu\text{M}$ ) for 1 minute prior to experiment. This has been shown to inhibit SR  $\text{Ca}^{2+}$  uptake, but maintain SR  $\text{Ca}^{2+}$  load (Bassani *et al.*, 1993).

$\text{Ca}^{2+}$  waves were initiated by focal application of caffeine ( $10\text{mM}$ ). No differences in wave amplitude or duration (not quantified) were seen, but propagation velocity was seen to increase by 20 %. This increased velocity was attributed to inhibition of SERCA being equivalent to a decrease in cellular  $\text{Ca}^{2+}$  buffering. Changes in

frequency were not studied as the waves were initiated by focal caffeine application instead of occurring spontaneously.

#### 4.2.3.2 2',5'-di(tert-butyl)-1,4-benzohydroquinone

2',5'-di(tert-butyl)-1,4-benzohydroquinone (TBQ) is a reversible inhibitor of SERCA. Its effect on spontaneous  $\text{Ca}^{2+}$  waves has recently been studied (O'Neill *et al.*, 2004). 100 $\mu\text{M}$  TBQ was used to inhibit SERCA in intact rat cardiomyocytes. This inhibition caused little or no change in wave amplitude, but increased wave efflux (amount of  $\text{Ca}^{2+}$  leaving cell during wave) and decreased wave frequency. In contrast to the Lukyanenko *et al.* study, wave velocity decreased. This was explained by a slight decrease in SR content. The time course of the wave was greatly increased, with a time constant of decline to resting levels ~8 times the control value (see Figure 4-3).

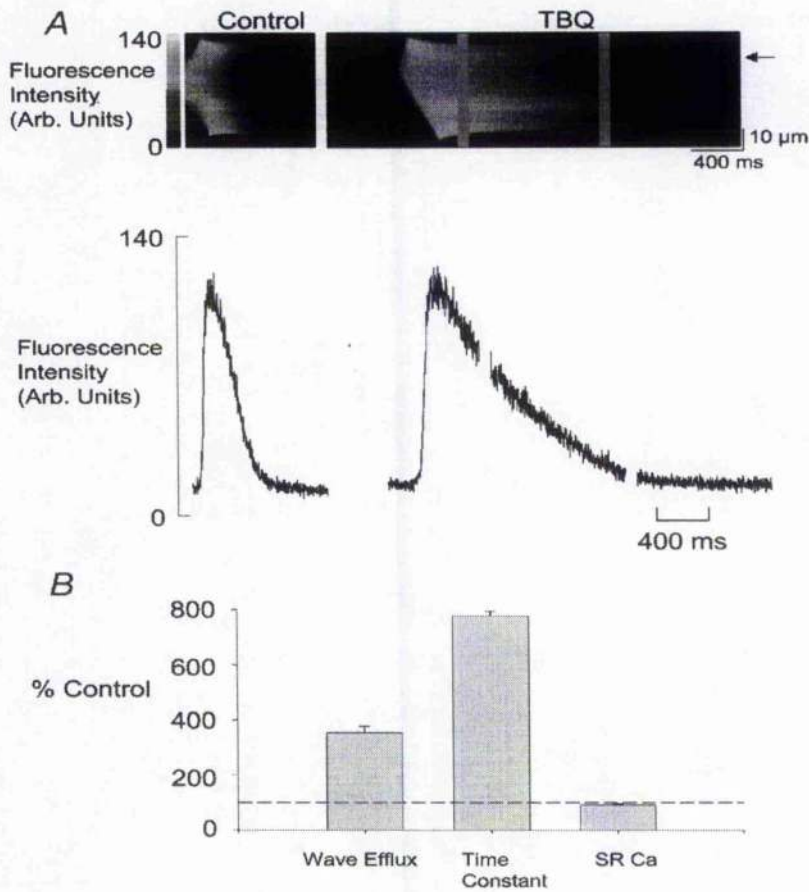


**Figure 4-3** Effect of TBQ on time course of spontaneous wave of  $\text{Ca}^{2+}$  release. **A**, Upper panel- linescan images of  $\text{Ca}^{2+}$  waves in control and TBQ. Lower panel- the  $[\text{Ca}^{2+}]_i$  profile of each wave is shown from the point marked by the arrow. **B**, percentage change of  $\text{Ca}^{2+}$  efflux generated by individual waves, the time constant of recovery of the  $\text{Ca}^{2+}$  transient during a wave and SR  $\text{Ca}^{2+}$  content. The dashed line marks 100% of control. (Figure taken from (O'Neill *et al.*, 2004)).

#### 4.2.3.3 Cyclopiazonic acid (CPA)

This is another agent previously used to inhibit SERCA activity in “skinned” cells exhibiting spontaneous  $\text{Ca}^{2+}$  waves (Kawai *et al.*, 1998). The investigators of the Kawai *et al* study showed a concentration dependent decrease in wave frequency, amplitude and time courses of both rise and decay time of the  $\text{Ca}^{2+}$  release. SR  $\text{Ca}^{2+}$  content was not assessed, nor were effects on velocity.

In this thesis, all three situations shall be explored experimentally and changes in fluxes shall be quantified to aid understanding of the underlying processes involved in spontaneous release.

### 4.3 Experimental results

#### 4.3.1 Cytosolic $\text{Ca}^{2+}$ study

This section shall focus on the changes observed in response to perfusing permeabilised rabbit cells with varying  $[\text{Ca}^{2+}]_{\text{Bath}}$ . Cells were perfused with mock intracellular solution containing  $\sim 300, 600$  and  $900$  nM  $[\text{Ca}^{2+}]_i$  and Fluo5F ( $10\mu\text{M}$ ).  $\text{Ca}^{2+}$  profiles from the resultant spontaneous  $\text{Ca}^{2+}$  release are displayed in Figure 4-4. These signals were recorded using the method described in the General Methods chapter. In a permeabilised cell, perfused with  $[\text{Ca}^{2+}]_{\text{bath}}$  within this range,  $[\text{Ca}^{2+}]_i$  is equilibrated with that of the extracellular perfusate (Loughrey *et al.*, 2002) such that  $[\text{Ca}^{2+}]_i^{\text{mean}}$  is equal to  $[\text{Ca}^{2+}]_{\text{bath}}^{\text{mean}}$ . In the upper panel, at  $300$  nM  $[\text{Ca}^{2+}]_i^{\text{mean}}$  the cell exhibits a spontaneous wave frequency of  $\sim 0.25$  Hz. As  $[\text{Ca}^{2+}]_i^{\text{mean}}$  was increased to  $\sim 600$  nM the frequency increased dramatically to  $\sim 0.8$  Hz and modest increases in systolic (peak)  $[\text{Ca}^{2+}]_i$  were observed. As  $[\text{Ca}^{2+}]_i^{\text{mean}}$  was raised to  $\sim 900$  nM, frequency was seen to increase less noticeably to  $\sim 0.95$  Hz. Systolic (peak)  $[\text{Ca}^{2+}]_i$  also increased more dramatically.

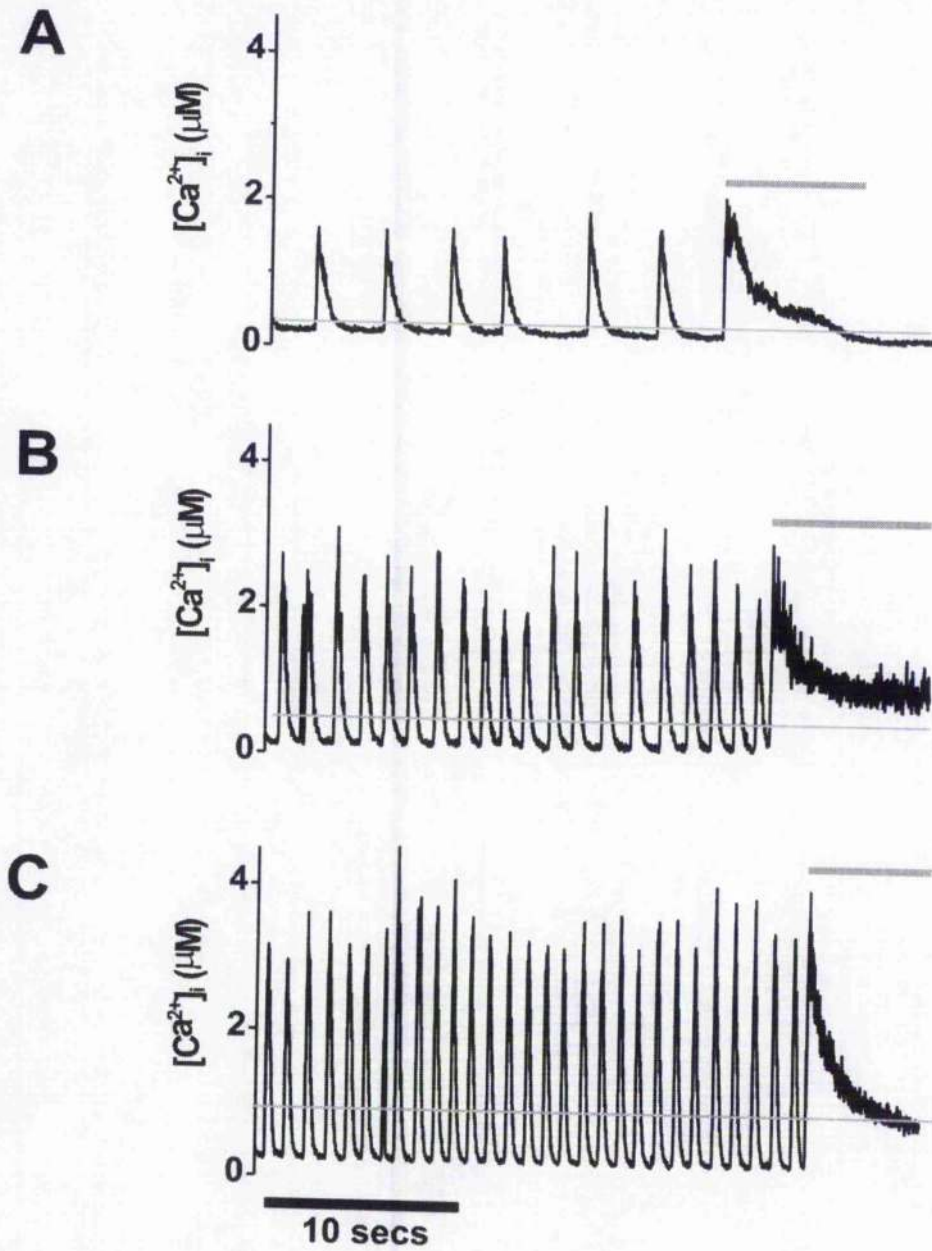


**Figure 4-4**  $\text{Ca}^{2+}$  waves from cardiomyocytes with increasing  $[\text{Ca}^{2+}]_i^{\text{mean}}$ . Panels A, B and C show cells perfused by 0.05R containing 320nM, 600nM and 860nM respectively. Oscillating  $\text{Ca}^{2+}$  signals from  $\text{Ca}^{2+}$  waves (black line) superimposed on mean extracellular signal (grey line). Caffeine (10 mM) was applied by rapid application at the end of each trace (Grey bar). Timescale given by black bar below trace in panel C. Note- cells contract after application of caffeine. This is evident by the final  $[\text{Ca}^{2+}]_i$  after caffeine application being higher than the mean  $[\text{Ca}^{2+}]_i$ .

The mean characteristics of spontaneous  $\text{Ca}^{2+}$  release is summarised in Figure 4-5.

A non-linear increase in systolic (peak)  $[\text{Ca}^{2+}]_i$  was observed as  $[\text{Ca}^{2+}]_i^{\text{mean}}$  was

increased. This showed a modest rise from  $1.70 \pm 0.11$  to  $1.85 \pm 0.08$   $\mu\text{M}$  between  $\sim 300$  and  $\sim 600$  nM, then increased dramatically to  $2.88 \pm 0.10$   $\mu\text{M}$  in the  $\sim 900$  nM mean  $[\text{Ca}^{2+}]_i^{\text{mean}}$ . Diastolic (min)  $[\text{Ca}^{2+}]_i$  increased in a more linear fashion, increasing from  $167 \pm 13$  to  $201 \pm 14$  between  $\sim 300$  to  $600$  nM, and  $261 \pm 12$  nM at  $\sim 900$  nM mean  $[\text{Ca}^{2+}]_i^{\text{mean}}$ . Generally, during the oscillations, minimum diastolic  $[\text{Ca}^{2+}]_i$  was kept well below  $[\text{Ca}^{2+}]_{\text{bath}}$  (See right panel of Figure 4-5). The difference became more pronounced as  $[\text{Ca}^{2+}]_{\text{bath}}$  was increased. Systolic (peak)  $[\text{Ca}^{2+}]_i$  was elevated well above  $[\text{Ca}^{2+}]_{\text{bath}}$  in all three cases, and more markedly at  $900$  nM, where  $[\text{Ca}^{2+}]_i^{\text{mean}}$  was increased by almost  $2\mu\text{M}$  above the  $[\text{Ca}^{2+}]_{\text{bath}}^{\text{mean}}$ .

Wave frequency exhibited a non-linear correlation over the range studied. A sharp increase in frequency was observed between  $300$  and  $600$  nM range, increasing from  $0.23 \pm 0.02$  to  $0.87 \pm 0.04$  Hz. This equates to a  $300\%$  increase. The relationship was seen to level off between  $600$  and  $900$  nM, increasing to  $1.00 \pm 0.02$  Hz. This might indicate a saturation of the uptake and release systems.

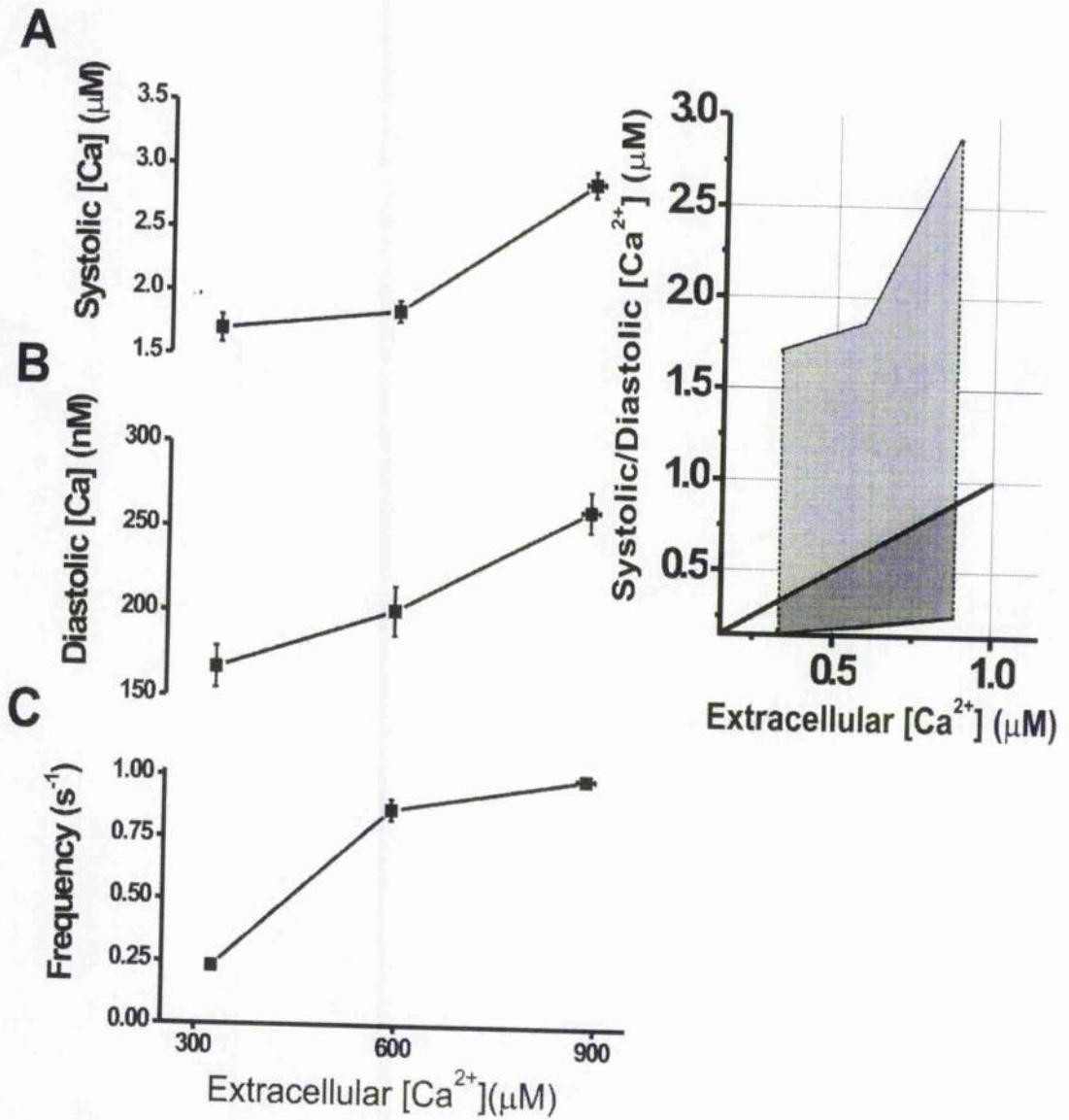


**Figure 4-5** Wave parameters over a range of mean  $[Ca^{2+}]$ . Mean values of systolic (peak)  $[Ca^{2+}]$  (A), minimum diastolic  $[Ca^{2+}]$  (B) and frequency (C) perfused with solutions with free  $[Ca^{2+}]$  of 320nM, 600nM and 860nM. Error bars indicate  $\pm$  S.E.M. Insert panel shows line of unity (Thick black) superimposed on data from A and B. Light grey and dark grey shading represents difference between unity and systolic (peak) and diastolic respectively.

At the end of each trace in Figure 4-4, caffeine (10mM) was rapidly applied. The resultant release was given as an estimate of SR content. In all three traces in Figure 4-4 caffeine effluxes have comparable amplitude to that of the spontaneous release. This is quantified in Figure 4-6. Conversion of free to total  $Ca^{2+}$  bound + free using an intrinsic cellular buffering system described previously (Hove-

Madsen & Bers, 1993). This allows quantification of the efflux of  $\text{Ca}^{2+}$  during both wave and caffeine.  $\text{Ca}^{2+}$  loss due to diffusion over the time of the upstroke of release is minimal in both cases. The upper panel shows no noticeable difference in efflux (denoted by vertical arrows). This efflux can be converted to SR  $[\text{Ca}^{2+}]$  content using the method described in the previous chapter and is analogous to that described by Shannon and Bers (Shannon & Bers, 1997). The bar chart (Figure 4-6 B) shows SR content derived using efflux during a wave and rapid application of caffeine. These were found not significantly different. Using the same method to analyse SR content over the range of  $[\text{Ca}^{2+}]_i^{\text{max}}$  no significant difference was found (Figure 4-6 C). This is at first counterintuitive, as both wave and caffeine amplitude seem to increase over the range. This can be explained better by thinking of the  $\text{Ca}^{2+}$  in terms of total  $\text{Ca}^{2+}$ .

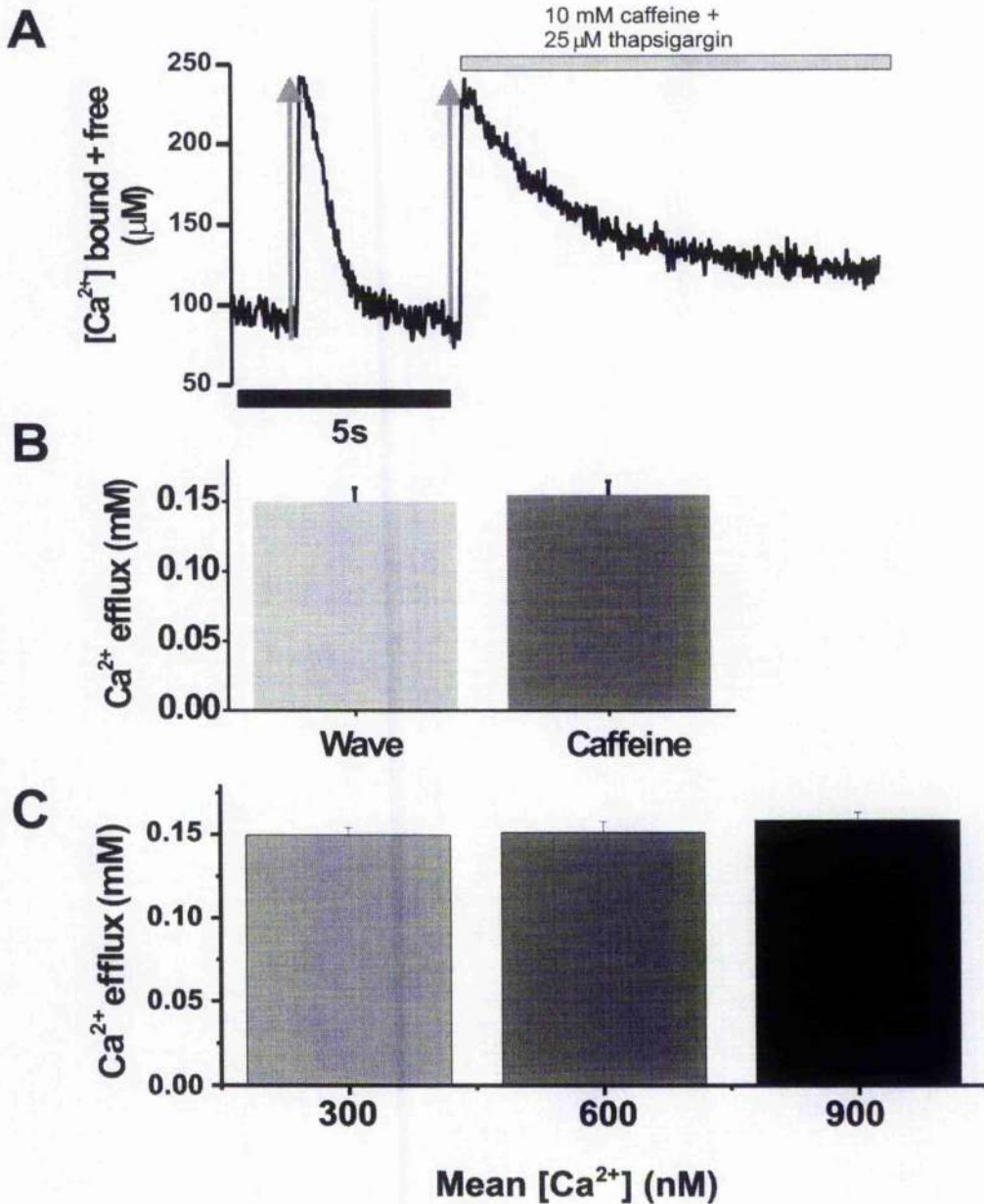


**Figure 4-6** Calcium efflux in waves and SR content over a range of  $[Ca^{2+}]_i^{mean}$ .

**A**, Comparison of spontaneous CICR caused by  $Ca^{2+}$  wave and caffeine (10mM) induced SR release. Thapsigargin (25mM) is included to inhibit  $Ca^{2+}$  uptake via SERCA. Trace has been converted from  $[Ca^{2+}]_i$  to  $[Ca^{2+}]_{total}$ . Grey arrows indicate amplitude of release. **B**, bar chart showing estimation of SR content by efflux at start of  $Ca^{2+}$  wave and caffeine application. **C**, Comparison of SR efflux due to application of caffeine over 300-900nM range. No significant difference was observed ( $p \gg 0.05$ ).

Figure 4-6B shows SR content calculated using efflux during a wave and application of caffeine. SR content as assessed by caffeine was seen not to change

in all three levels of  $[Ca^{2+}]_i^{max}$ . Wave amplitude in terms of  $[Ca^{2+}]_i$  is seen to almost double between 300 and 900nM. How can these results be reconciled?

Figure 4-7 explains the principle behind this discrepancy.

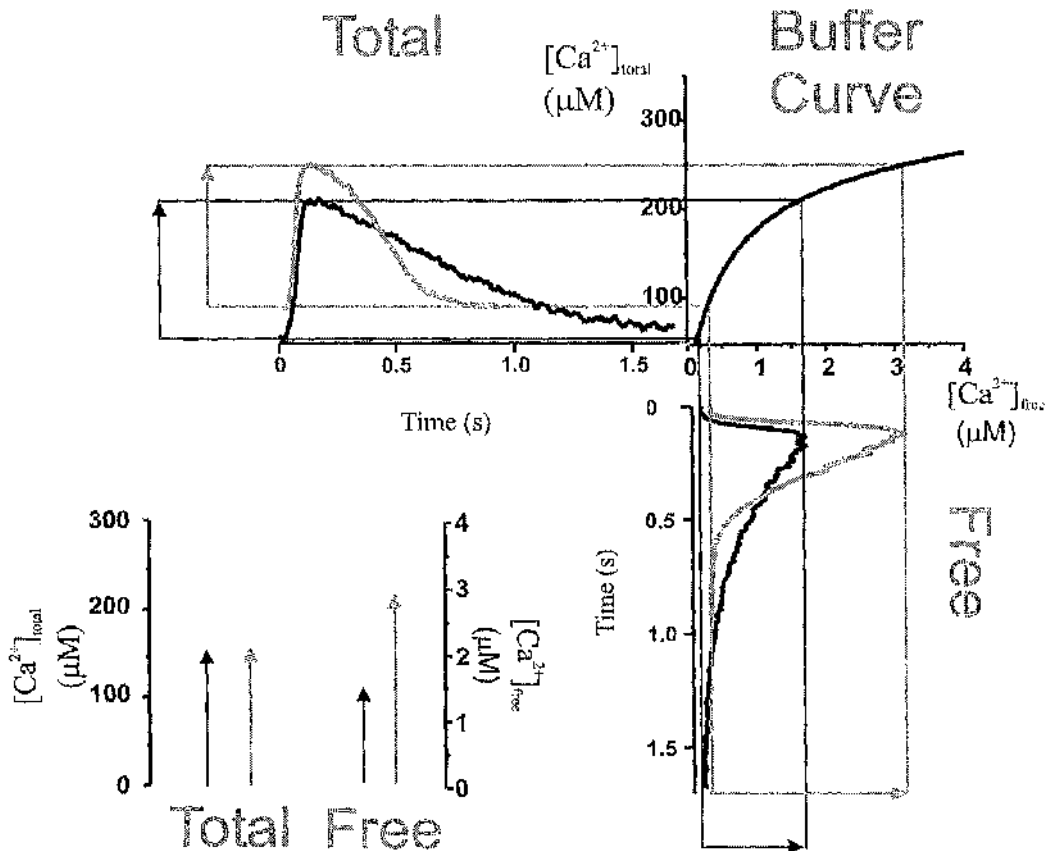


**Figure 4-7** Conversion of free to total bound + free allowing estimation of SR efflux during  $Ca^{2+}$  wave.

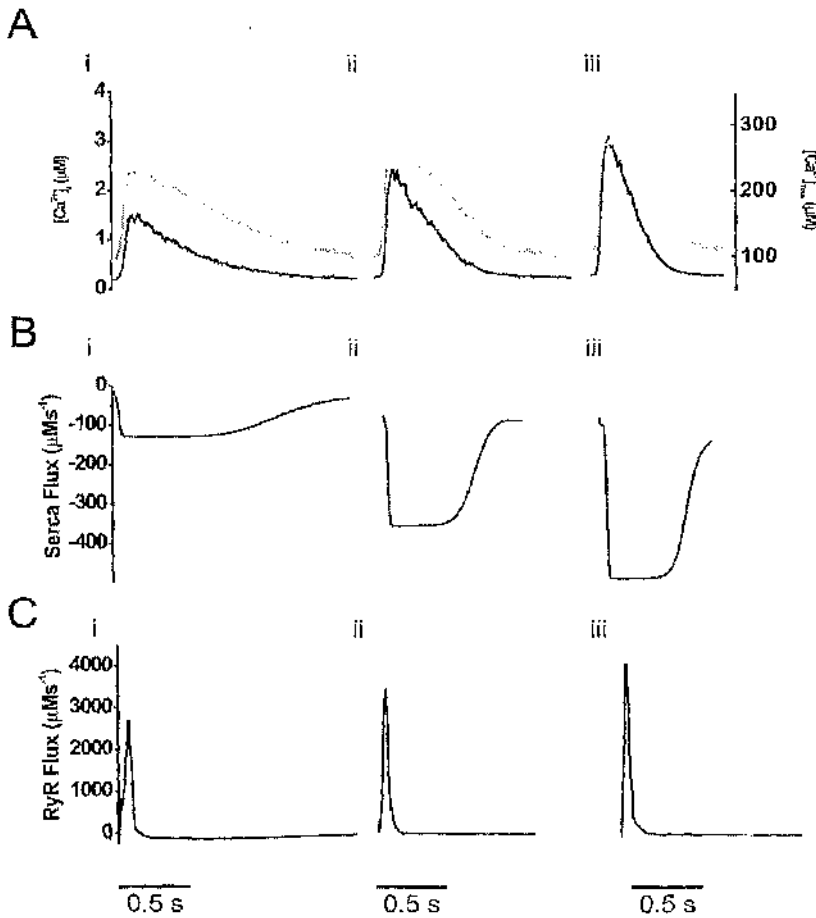
Curve of intrinsic cytosolic buffering (top right) shows conversion of  $[Ca^{2+}]_i$  (horizontal axis) and  $[Ca^{2+}]_{total}$  (vertical axis).

Average transients taken from 5 waves perfused with 310 (black) and 890nM (grey)  $[Ca^{2+}]_i$ . Lines showing maximum and minimum of free (Lower right quadrant) and total (upper left quadrant) for the two transients. Arrows indicate amplitude of transients in terms of  $[Ca^{2+}]_i$  and  $[Ca^{2+}]_{total}$ . Differences in wave amplitude in terms of  $[Ca^{2+}]_i$  and  $[Ca^{2+}]_{total}$  are summarized in the bottom left diagram.

The above figure shows the averaged  $Ca^{2+}$  profile from  $Ca^{2+}$  waves in a cell perfused with mock intracellular solutions containing 310nM and one perfused with 890nM. Wave amplitude in the 890 nM cell is almost twice that of the 310nM

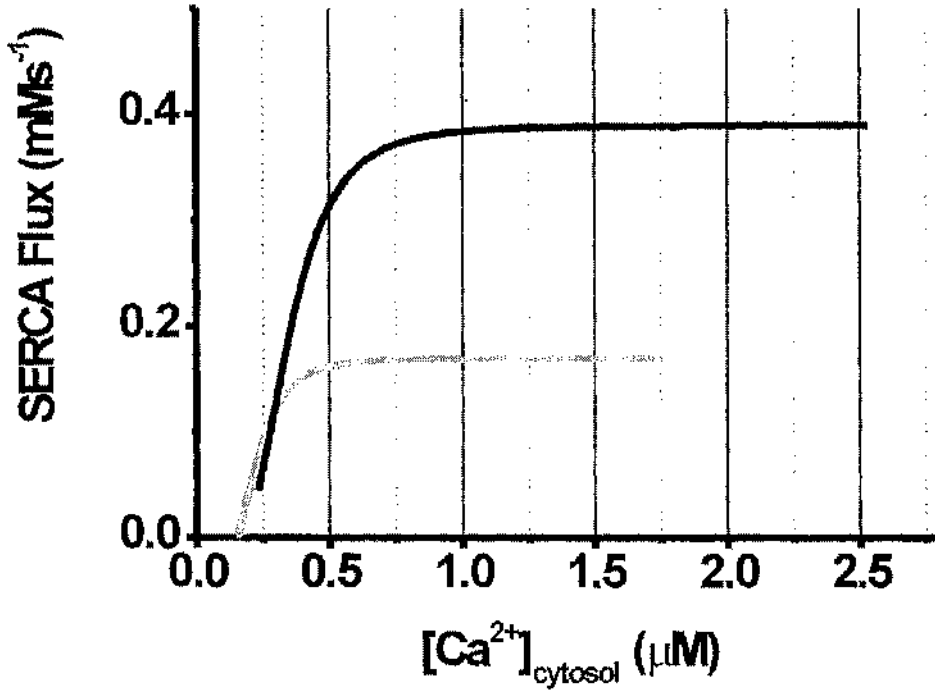
cell. Using a quantification of the cells intrinsic cellular buffer system (Hove-Madsen & Bers, 1993) allows conversion of free to total  $[Ca^{2+}]$ . The small change in minimum diastolic  $[Ca^{2+}]_i$  observed between the two cells translates to a large difference in  $[Ca^{2+}]_{total}$ . Conversely, large differences in systolic (peak)  $[Ca^{2+}]_i$  translate to small differences in  $[Ca^{2+}]_{total}$ . This effectively scales the  $[Ca^{2+}]$  amplitude to  $\sim 154.6\mu M$  and  $157.3\mu M$  for 310 and 890 nM mean  $[Ca^{2+}]_i^{mean}$  cells respectively.

The  $[Ca^{2+}]_{total}$  leaving the SR in each of the three  $[Ca^{2+}]_{bath}$  studied have been quantified. Using the method described in Chapter 3, the  $Ca^{2+}$  fluxes underlying the wave can be quantified. These are shown in Figure 4-8.



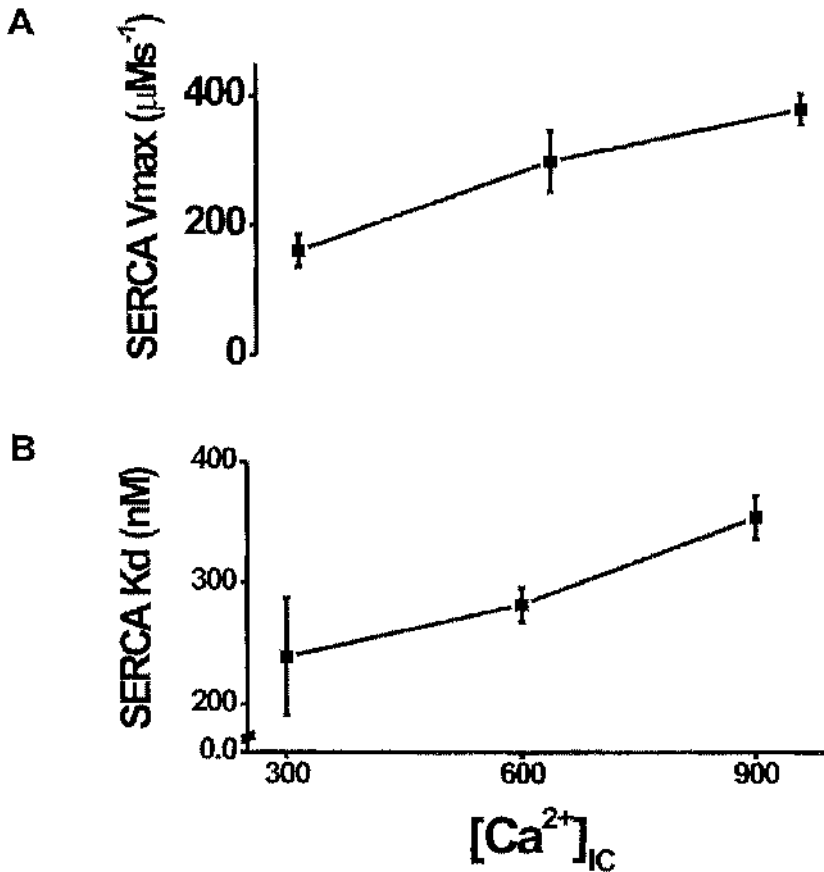
**Figure 4-8** Average  $[Ca^{2+}]_i$  from cells in Figure 4-4, with calculated total  $[Ca^{2+}]$ , and SR fluxes due to SERCA uptake and RyR release. Free external  $[Ca^{2+}]$  in *i*, *ii* and *iii* are 320nM, 600nM and 860nM respectively. *A*, Black line shows average cytosolic signal from 5 consecutive waves. Grey line shows total  $Ca^{2+}$  SR calcium released across the SR (free + bound + diffusion) as described in chapter 3. *B*, Calculated rate of SERCA pump. *C*, Calculated rate of flux through RyRs.

Figure 4-8 shows fluxes from typical cells in the 3  $Ca^{2+}$  conditions studied in this section. As discussed,  $[Ca^{2+}]_i$  amplitudes increase with  $[Ca^{2+}]_i^{mean}$ , whilst  $[Ca^{2+}]_{total}$  have comparable amplitudes. Generally, maximal SERCA flux increased with  $[Ca^{2+}]_i^{mean}$ , whilst the half-maximal duration of SERCA uptake decreased. RyR flux increased moderately over the range of  $[Ca^{2+}]_i^{mean}$ . The plot below shows SERCA  $V_{max}$  vs.  $[Ca^{2+}]_{cytosol}$  for cells bathed in  $\sim 320$  and  $\sim 860$  nM.



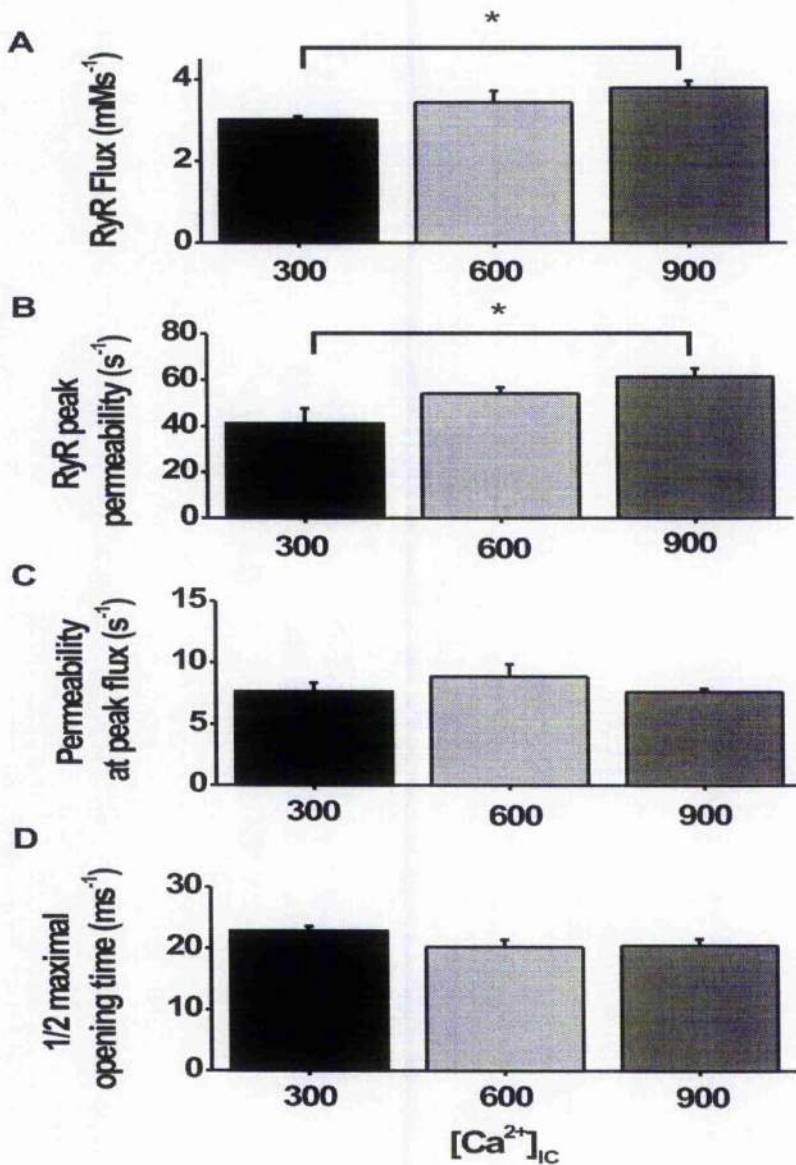
**Figure 4-9** Plot of SERCA flux vs.  $[Ca^{2+}]_{\text{cytosol}}$ . Black line taken from cell bathed in  $\sim 900\text{nM}$   $[Ca^{2+}]$ , grey line taken from cell bathed in  $\sim 300\text{nM}$ .

This illustrates more clearly the relationship between SERCA flux and  $[Ca^{2+}]_i$ . The cell bathed in the higher  $[Ca^{2+}]$  reaches >2-fold higher SERCA flux rates. The 900nM curve is also shifted to the right indicating a higher  $K_D$ . The mean behaviour of SERCA is summarised in the figures below.



**Figure 4-10** Changes in SERCA parameters over a range of  $[Ca^{2+}]_i^{mean}$ . SERCA  $V_{max}$  and  $K_D$  required to obtain best fit of SERCA behaviour based on the reverse mode model (Shannon *et al.*, 2000). Values expressed as mean  $\pm$  S.E.M. ( $n=5$ , 5 & 7 for 300, 600 and 900 nM respectively).

SERCA  $V_{max}$  and  $K_D$  were seen to increase in an approximately linear fashion. In both cases, significant differences were observed between  $\sim 300$  and  $\sim 900$  nM groups. A  $>100\%$  increase in  $V_{max}$  was observed from  $160 \pm 25$  to  $380 \pm 23 \mu Ms^{-1}$  between  $\sim 300$  and  $\sim 900$ .  $K_D$  had a more modest increase from  $239 \pm 48$  at 300 nM  $[Ca^{2+}]_i^{mean}$  to  $354 \pm 18$  nM at 900 nM  $[Ca^{2+}]_i^{mean}$ .



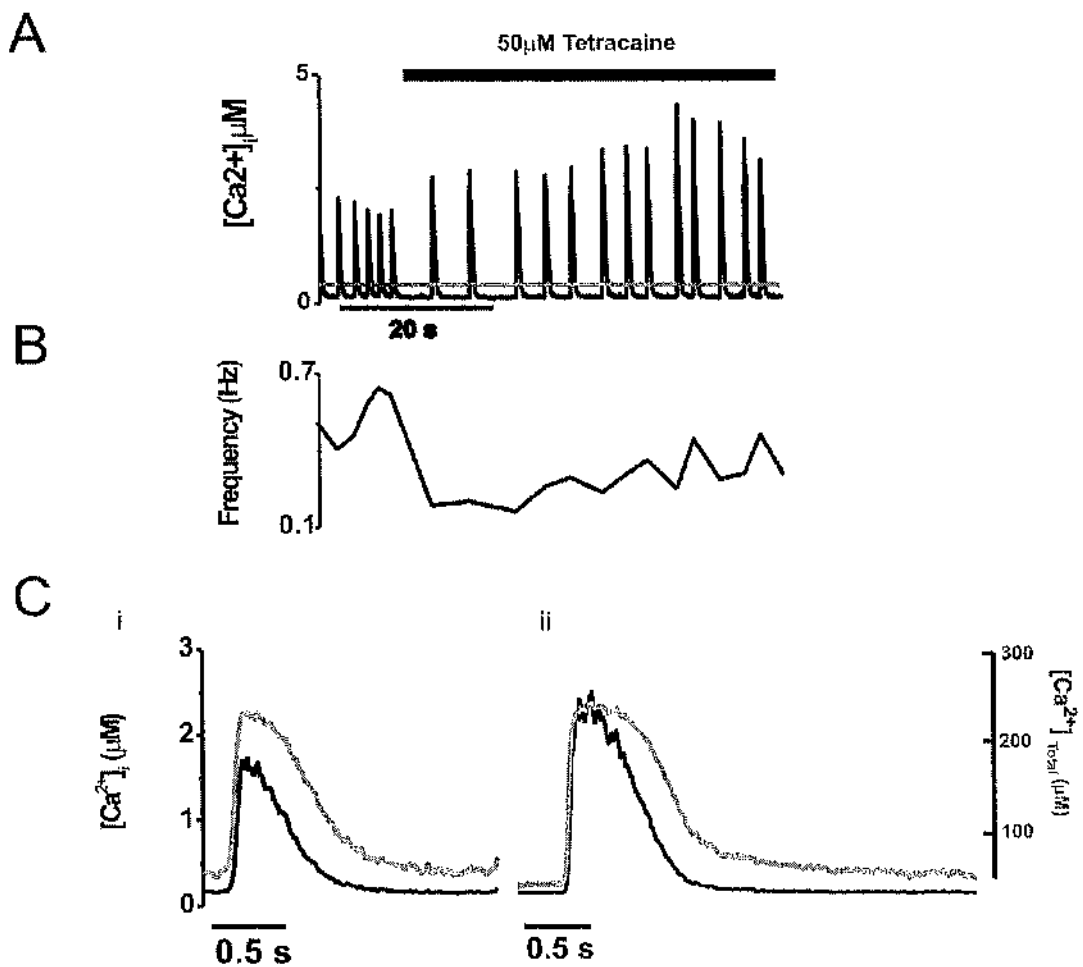
**Figure 4-11** Effect of increasing  $[Ca^{2+}]_i^{mean}$  on RyR opening during a  $Ca^{2+}$  wave. Wave flux rate (A), peak permeability (B), permeability at peak net flux (C) and  $\frac{1}{2}$  maximal RyR opening time (D) over a range of  $[Ca^{2+}]_i^{mean}$ . Mean values are shown  $\pm$  S.E.M. (error bars), significance indicated by \*.

Figure 4-11 depicts changes in RyR opening calculated using the flux derivation method in the previous chapter. RyR Flux was seen to gradually increase with increasing  $[Ca^{2+}]_i^{mean}$ . Significant differences were found between 300 to 900nM, increasing from  $3.01 \pm 0.08$  to  $3.79 \pm 0.17$  mMs<sup>-1</sup>. Peak RyR permeability was also

shown to increase from  $41.1 \pm 6.5$  to  $61.2 \pm 3.6 \text{ s}^{-1}$ . Permeability at the time when peak net flux was used as another measure of permeability. No significant difference was seen over the range of  $[Ca^{2+}]_i^{mean}$ . Half-maximal permeability was observed not to change over the range studied.

### 4.3.2 Tetracaine study

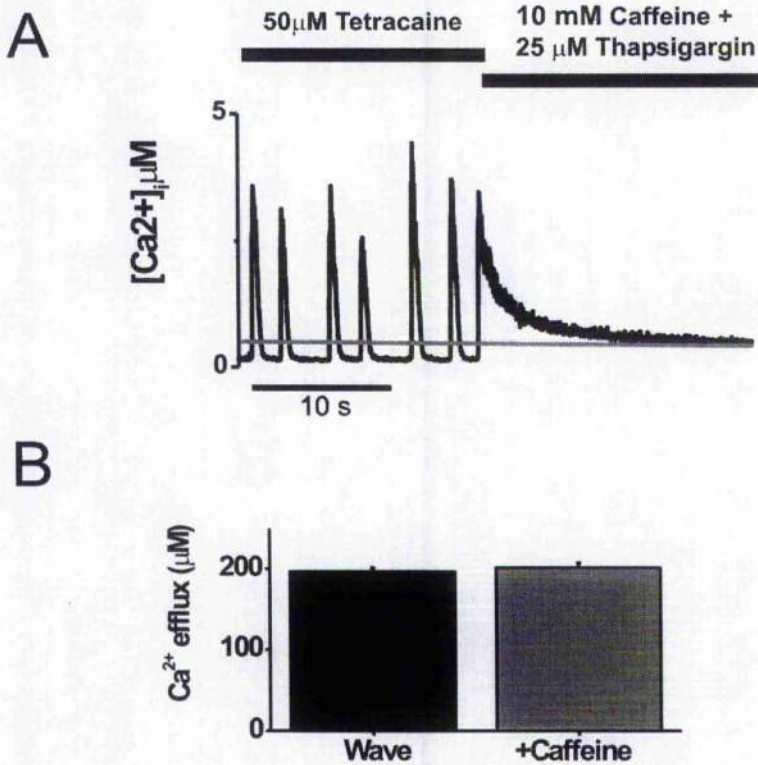
The figure below shows the effect of addition of tetracaine ( $50 \mu\text{M}$ ) on cell oscillatory behaviour.



**Figure 4-12** Effect of tetracaine ( $50 \mu\text{M}$ ) on  $Ca^{2+}$  waves in permeabilised cardiomyocytes from the rabbit.

**A.** Trace shows  $[Ca^{2+}]_i$  from cell perfused with  $0.05\text{R}$ . Black bar denotes period of tetracaine application. Grey line indicates  $[Ca^{2+}]_i^{mean}$ . **B.** Frequency plot of trace **A**, over corresponding timescale. **C.** Average wave profile from control and tetracaine periods of **A**. Black line indicates  $[Ca^{2+}]_i$  and grey line indicates  $[Ca^{2+}]_{total}$ .

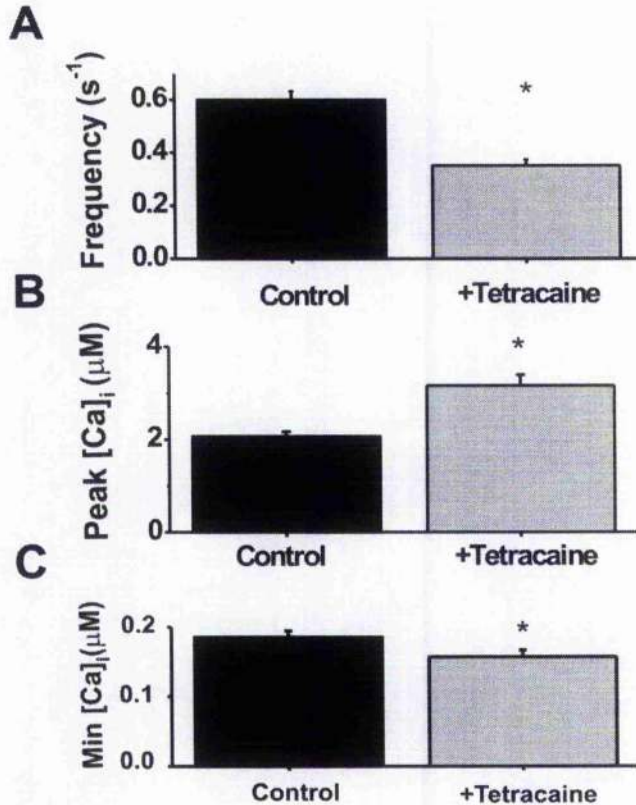
On application of tetracaine, the cell exhibited a dramatic decrease in frequency (see Figure 4-12B). This partially recovered over time, levelling off below that control frequency. Wave amplitude increased after tetracaine addition. Peak  $[Ca^{2+}]_i$  increased dramatically and minimum diastolic  $[Ca^{2+}]_i$  decreased slightly. Conversion to  $[Ca^{2+}]_{total}$  (grey line in Figure 4-12C) highlighted the change in minimum diastolic  $[Ca^{2+}]_i$  and a pronounced change can be observed in minimum  $[Ca^{2+}]_{total}$ .



**Figure 4-13 Comparison of Caffeine and spontaneously evoked transients from after application of tetracaine.**

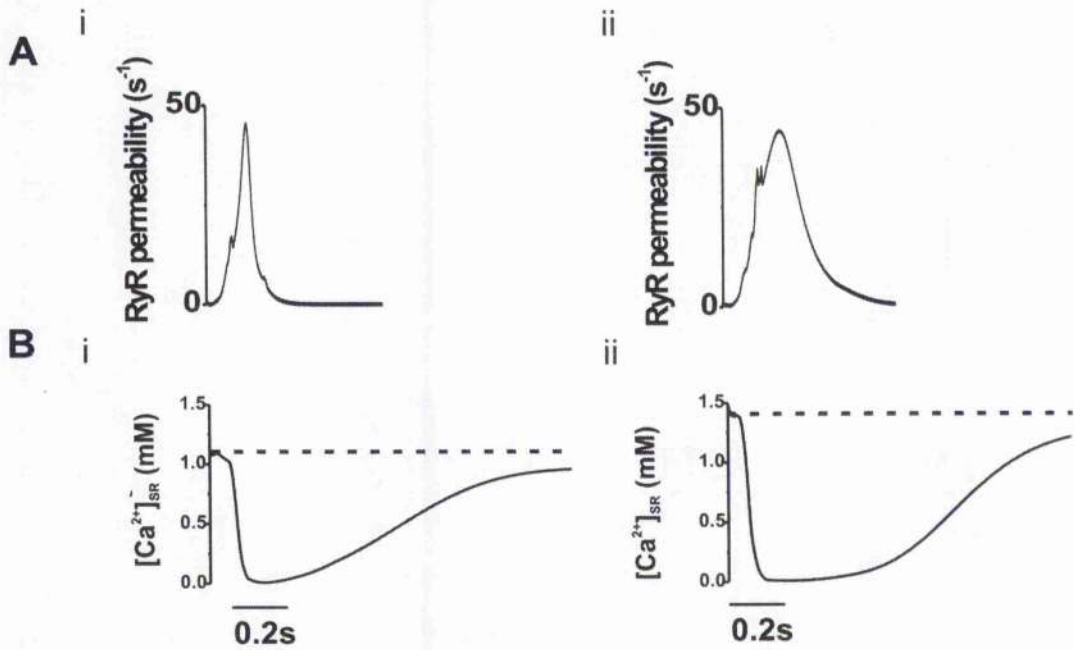
The above figure shows comparison of  $Ca^{2+}$  efflux during a wave and as result of caffeine application when cells ( $n=6$ ) were perfused with tetracaine ( $50\mu$ M). No significant difference was observed. In terms of  $Ca^{2+}$  efflux,  $196\pm 5\ \mu$ M on average left during a wave and  $202\pm 5\ \mu$ M left during a caffeine. This carries forward the

idea that  $\text{Ca}^{2+}$  efflux during a wave is total, i.e. the entire SR  $\text{Ca}^{2+}$  content is released during a wave.



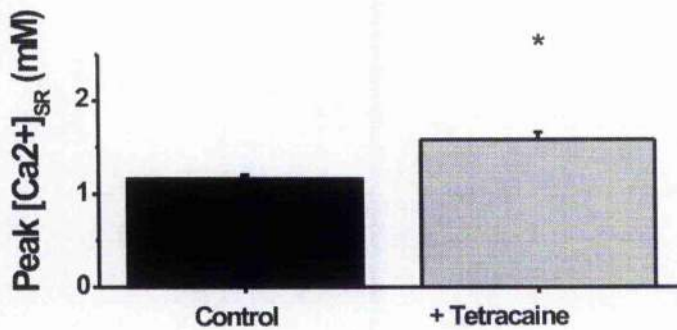
**Figure 4-14 Effect of tetracaine on parameters of spontaneous  $\text{Ca}^{2+}$  waves. Changes in frequency (A), peak  $[\text{Ca}^{2+}]_i$  (B) and minimum  $[\text{Ca}^{2+}]_i$  of  $\text{Ca}^{2+}$  waves under control conditions and after application of tetracaine (50 µM).**

Figure 4-14 summarises the effects of tetracaine (50 µM) on mean  $\text{Ca}^{2+}$  wave characteristics. All values were obtained from cells after a steady state was achieved. Tetracaine caused wave frequency to decrease to ~60% of control value from  $0.598 \pm 0.032$  to  $0.351 \pm 0.021$ . Peak  $[\text{Ca}^{2+}]_i$  from averaged wave profiles increased to ~150% of control rising from  $2.06 \pm 0.11$  µM to  $3.16 \pm 0.24$  µM. Minimum  $[\text{Ca}^{2+}]_i$  was observed to decrease slightly from  $185 \pm 9$  nM to  $157 \pm 10$  nM. All of these changes were found to be significant ( $p < 0.05$ ).



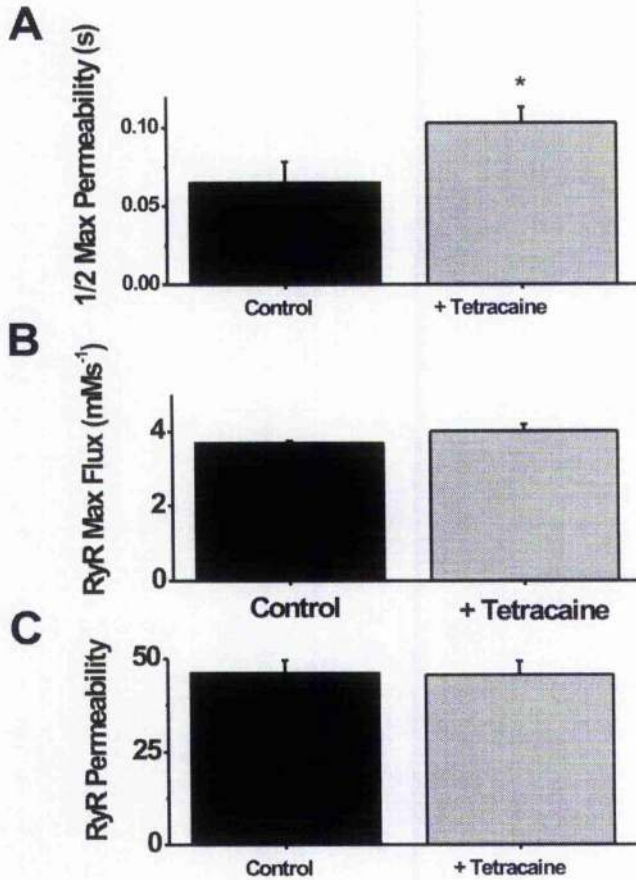
**Figure 4-15** Calculated RyR permeability and SR content before (i) and after (ii) tetracaine (50 $\mu$ M) application. Dotted line in B shows indicates threshold for release.

Figure 4-15 displays typical changes in RyR permeability and  $[Ca^{2+}]_{SR}$ . RyR permeabilities with and without tetracaine have comparable peak values, but prolonged time-course. This prolonged time-course affects  $[Ca^{2+}]_{SR}$ , prolonging the period when the SR is empty. The threshold for release is also higher in the presence of tetracaine. This was due to decreased sensitivity of the RyR.



**Figure 4-16** Effect of tetracaine on SR  $[Ca^{2+}]_i$ .

The maximal  $[Ca^{2+}]_{SR}$  just before release was shown to increase from  $1.16 \pm 0.04$  mM to  $1.58 \pm 0.08$  mM ( $n=6$ ) by the addition of  $50 \mu\text{M}$  tetracaine. This equates to a  $\sim 36\%$  increase. This increase in peak  $[Ca^{2+}]_{SR}$  is consistent with RyR desensitisation, hence luminal  $Ca^{2+}$  threshold for release has been increased.



**Figure 4-17** Changes in RyR opening characteristics after application of tetracaine ( $50 \mu\text{M}$ ).

RyR parameters calculated from  $Ca^{2+}$  waves in control cells (without tetracaine-black) and cells perfused with tetracaine (grey).

The figure above shows the effect of tetracaine on various parameters of the RyR derived from averaged profiles of  $Ca^{2+}$  waves. Half-maximal duration for the transient rise in RyR permeability was significantly increased, from  $65 \pm 14$  ms to  $103 \pm 10$  ms ( $n=6$ ). This suggested that RyR opening was prolonged due to the

action of tetracaine. Peak RyR flux showed a slight increase, although this was not significant. Similarly, no significant difference in maximal RyR permeability was apparent.

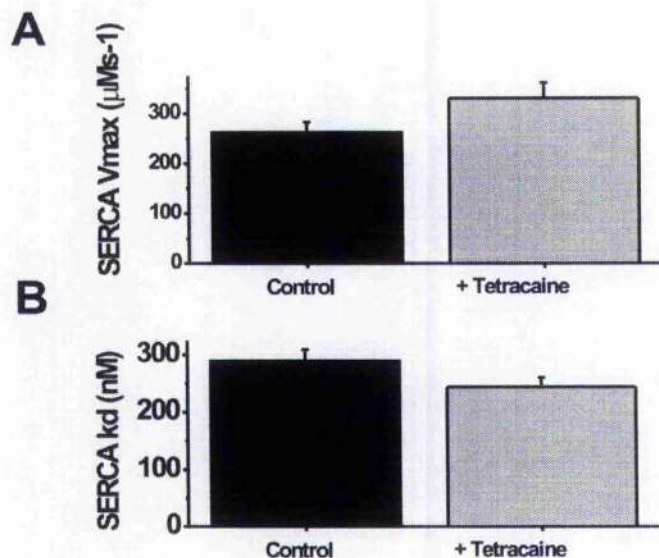


**Figure 4-18 Effect of tetracaine on SERCA Vmax and K<sub>D</sub>.** SERCA Vmax (A) and K<sub>D</sub> measured with and without (control) the presence of tetracaine.

The figure above shows calculated Vmax and K<sub>D</sub> from Ca<sup>2+</sup> waves in control and when perfused with tetracaine. A slight increase in Vmax and a slight decrease in K<sub>D</sub> were seen, but these differences were not significant (n=6). Therefore, no direct effects of tetracaine on SERCA were found.

#### 4.3.3 TBQ study

Figure 4-19 below generally depicts the effect of TBQ (5µM) on Ca<sup>2+</sup> wave amplitude and frequency.

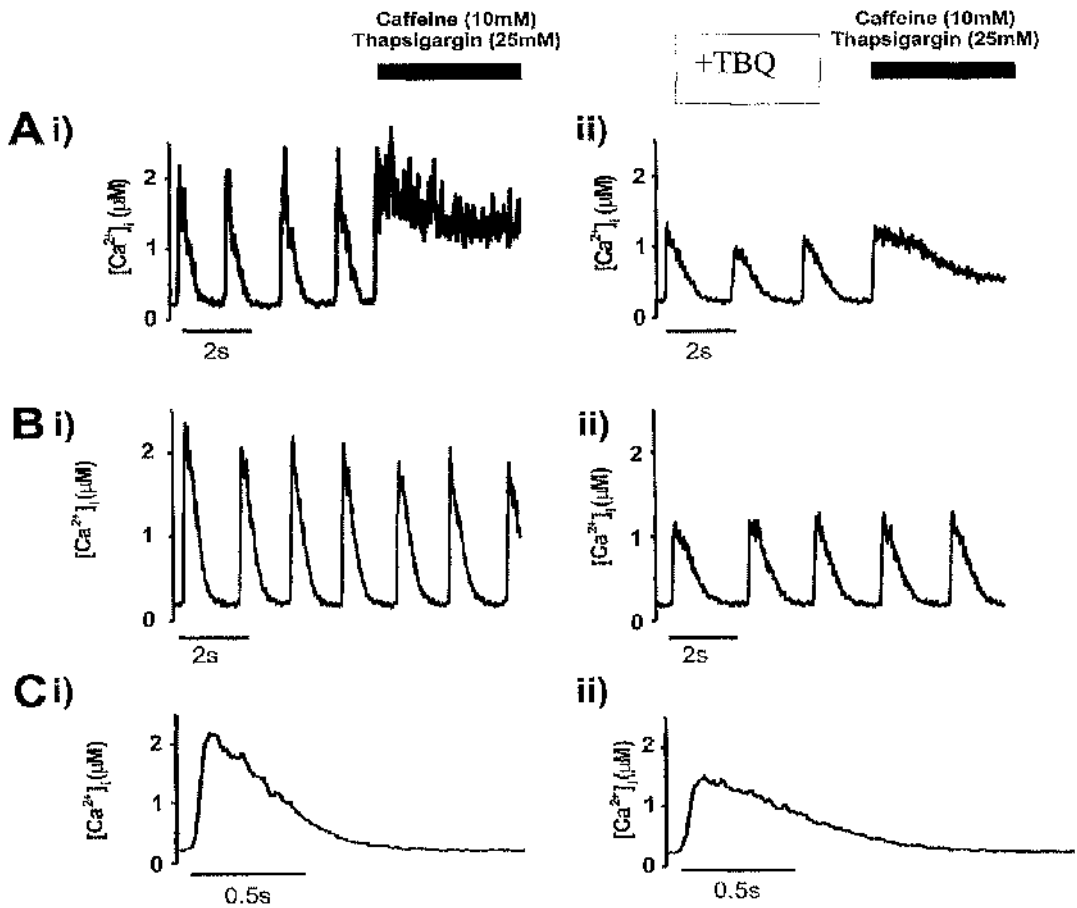


**Figure 4-19** Effect of TBQ on  $Ca^{2+}$  release in  $Ca^{2+}$  waves and caffeine.

**A.**  $Ca^{2+}$  waves shown with caffeine induced release (period shown by black bar). **B.** Typical  $Ca^{2+}$  waves showing amplitude and frequency changes. **C.** Average transient taken from 5 typical waves. Control (i) and cell after ~1 minute TBQ (5 $\mu M$ ) exposure (ii) side by side for comparison.

In general,  $Ca^{2+}$  waves were seen to decrease in amplitude and frequency. Also, rapid application of caffeine (10mM) elicited a smaller response indicating a decreased SR content.

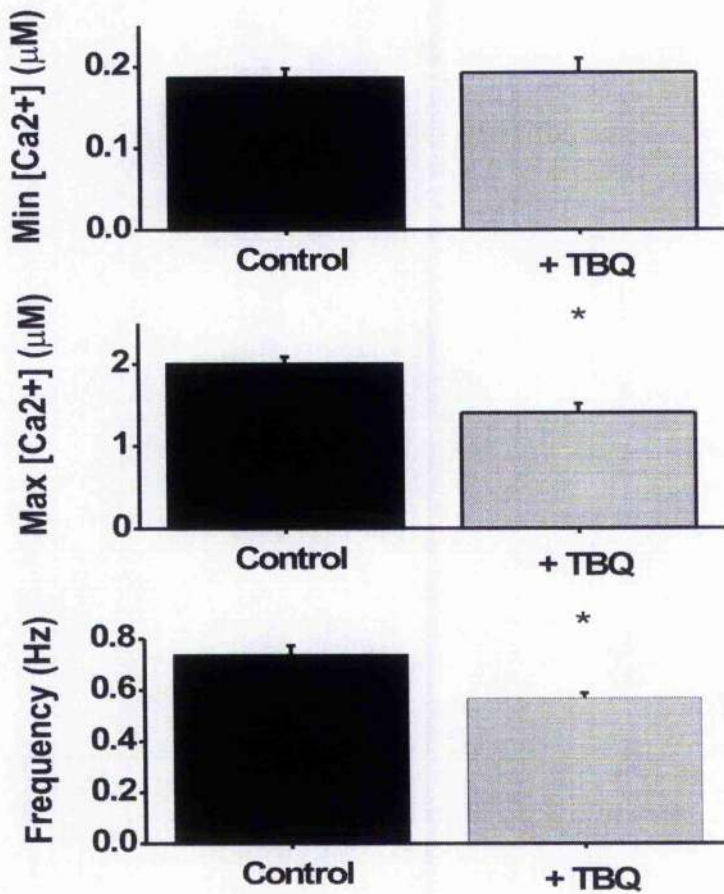


**Figure 4-20** Mean changes in minimum, maximum  $[Ca^{2+}]_i$  and frequency after TBQ application for approx. 1 Minute.

Figure 4-20 shows mean values of minimum and maximum  $[Ca^{2+}]_i$  taken from average transients as shown in Figure 4-19C. Mean wave frequency is also shown. No change was observed in mean minimum  $[Ca^{2+}]_i$ , with values of  $186 \pm 11$  and  $192 \pm 17$  nM for before and after TBQ application. A significant decrease was observed in mean maximum  $[Ca^{2+}]_i$ , decreasing from  $2.00 \pm 0.09$   $\mu$ M to  $1.41 \pm 0.11$   $\mu$ M, possibly confirming the decrease in SR content inferred by the decreased caffeine response in Figure 4-19 Ai. Frequency decreased from  $0.738 \pm 0.034$  to  $0.568 \pm 0.020$  Hz.

Analysis of a typical cell in terms of SR fluxes is shown in Figure 4-21.

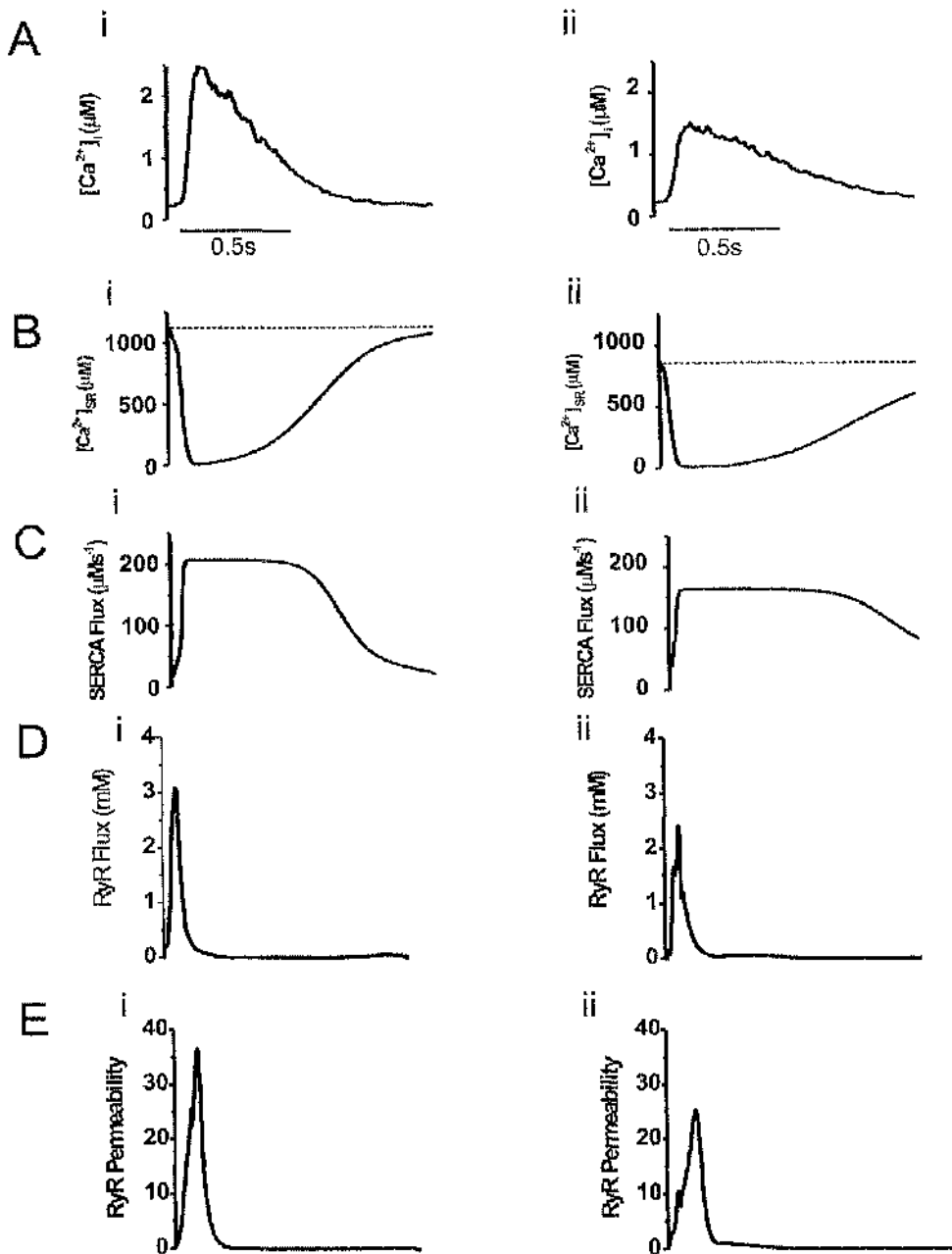


**Figure 4-21** Analysis of changes seen in SR fluxes from control (i) and after application of TBQ (5 μM) (ii).  
**A.-** Mean wave profile (n=5) from a typical before (i) and after (ii) TBQ (5 μM) application. Subsequent graphs show calculated  $[Ca^{2+}]_{SR}$  (B) (dotted line denotes threshold for release in both cases), SERCA flux (C), RyR fluxes (D) and RyR permeability (E), based on data from A.

Generally, a decreased systolic (peak)  $[Ca^{2+}]_i$  was observed in response to 1 minute TBQ application.  $[Ca^{2+}]_{SR}$  also reached lower values, suggesting a decreased SR  $Ca^{2+}$  release threshold. Peak RyR flux rate decreased, but RyR open events were prolonged. Similarly, peak permeability was observed to decrease after TBQ application. These results are summarized in the figures below.

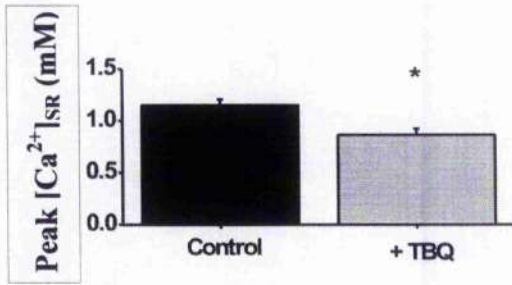


**Figure 4-22 Mean peak  $[Ca^{2+}]_{SR}$  during  $Ca^{2+}$  waves before and after application of TBQ (5 $\mu$ M) (n=5).**

\*Indicates significant difference.

Figure 4-22 show mean peak  $[Ca^{2+}]_{SR}$ . This decreased from  $1.15 \pm 0.06$  mM (n=5) to  $0.86 \pm 0.06$  (n=5) after TBQ exposure.

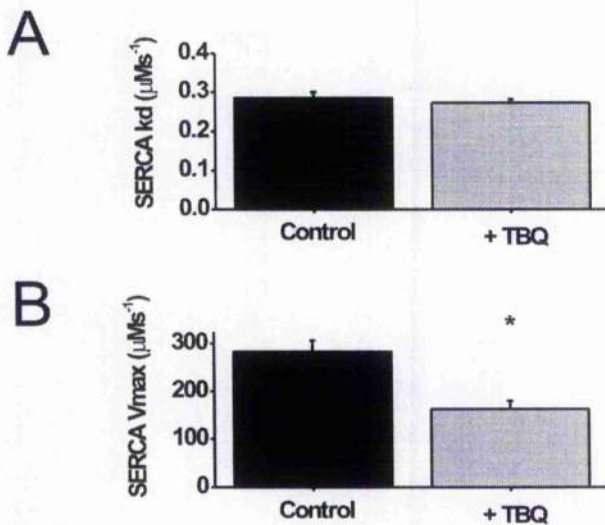


**Figure 4-23 Mean behaviour of SERCA with and without TBQ (5 $\mu$ M). Graphs show mean values of SERCA  $K_D$  (A) and  $V_{max}$  (B) (n=5).**

\*Indicates significant difference.

Changes in SERCA behaviour were seen, most obviously with regards  $V_{max}$ . This decreased from  $282 \pm 24 \mu\text{Ms}^{-1}$  to  $162 \pm 17 \mu\text{Ms}^{-1}$ . No significant changes in SERCA  $K_D$  were observed suggesting TBQ has no effect on SERCA's affinity for  $\text{Ca}^{2+}$ .

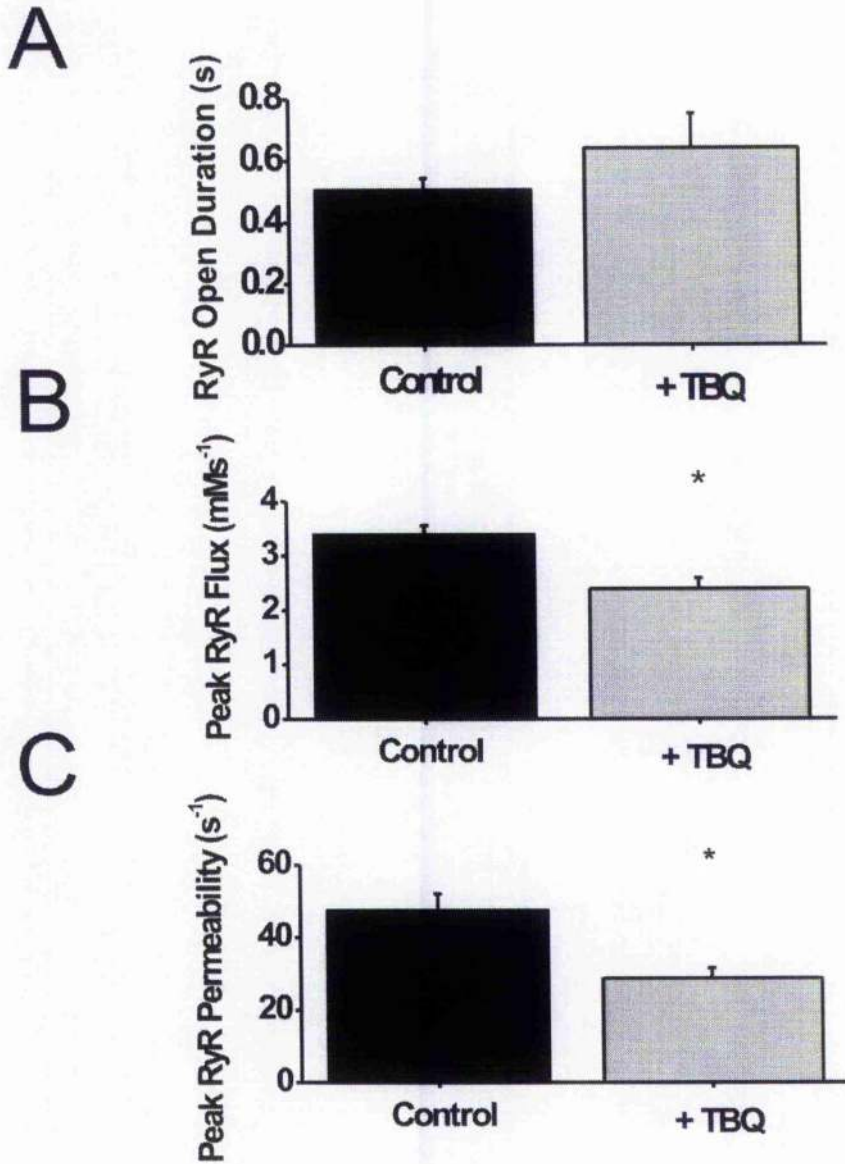


**Figure 4-24 Mean behaviour of RyR with and without TBQ.** Graphs show  $\frac{1}{2}$  maximal RyR open duration (A), Peak RyR Flux (B) and peak RyR permeability (C).

RyR open duration (calculated from time above  $\frac{1}{2}$  maximal permeability) was seen to increase from  $0.506 \pm 0.038$  s to  $0.641 \pm 0.111$  s. Due to high variability in this

parameter, no significant difference was found. Significant differences were observed in both peak RyR flux and peak RyR permeability. Peak RyR flux decreased from  $3.38 \pm 17 \text{ mMs}^{-1}$  to  $2.00 \pm 19 \text{ mMs}^{-1}$ . RyR peak permeability decreased to almost half of control from  $47.4 \pm 4.6 \text{ s}^{-1}$  to  $28.6 \pm 2.7 \text{ s}^{-1}$ .

Previous studies have shown changes in velocity with SERCA inhibition (Lukyanenko *et al.*, 1999; O'Neill *et al.*, 2004). This was tested using the avgwavecorr program. The results are displayed in the figure below.

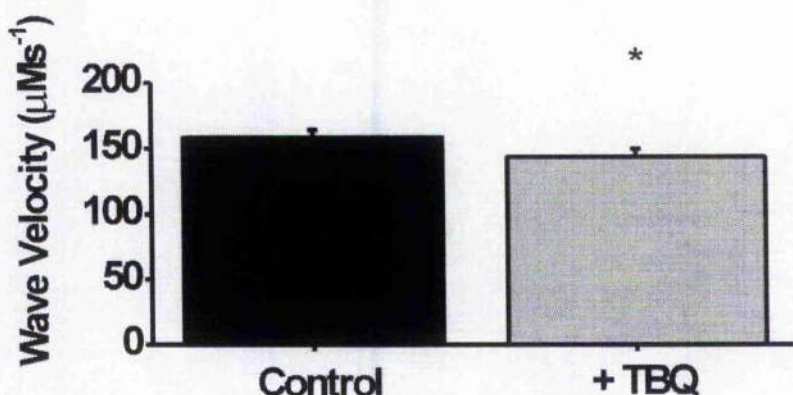


**Figure 4-25** The effect of TBQ on  $\text{Ca}^{2+}$  wave velocity. (\* denotes significant difference at  $P < 0.05$ ).

After TBQ application, wave velocity fell slightly from  $158 \mu\text{m/s}$  to  $143 \mu\text{m/s}$ .

This difference was found to be significant.

## 4.4 Discussion

### 4.4.1 Cytosolic $[\text{Ca}^{2+}]$ study

Over the range of  $[\text{Ca}^{2+}]_i^{\text{mean}}$  investigated in this study, non-linear relationships were found in systolic (peak)  $[\text{Ca}^{2+}]_i$  and oscillation frequency, when plotted

against  $[Ca^{2+}]_i^{mean}$ . Peak  $[Ca^{2+}]_i$  increases were greater between 600- 900nM  $[Ca^{2+}]_i^{mean}$ , and frequency increased most between 300 and 600 nM  $[Ca^{2+}]_i^{mean}$ .

Previous work by Loughrey et al (Loughrey *et al.*, 2002) demonstrated a linear relationship over this range. This was found for the minimum diastolic  $[Ca^{2+}]_i$  parameter, but not for systolic (peak) $[Ca^{2+}]_i$  and frequency. It is possible that by using three limited range values, instead of the more dispersed grouping of  $[Ca^{2+}]_i^{mean}$  used in the Loughrey et al. study, clearer conclusions about these relationships could be drawn.

The Kaneko et al (Kaneko *et al.*, 2000) study mentioned in the introduction to this thesis described 3 distinct types of  $Ca^{2+}$  wave. No such distinctions could be drawn between the waves observed here. Wave properties were seen to vary as a function of the  $[Ca^{2+}]_{bath}$ . No  $Ca^{2+}$  waves conforming to 'agonal' or 'sporadic' waves were observed.

With regard to  $[Ca^{2+}]_{SR}$ , no change was observed over the range of  $[Ca^{2+}]_i^{mean}$  studied. This was in agreement with the previous Diaz et al study (Diaz *et al.*, 1997), where waves occurred with increased frequency when external  $Ca^{2+}$  was raised, but no increase in  $Ca^{2+}$  efflux was observed during the wave.

The absence of changes in  $[Ca^{2+}]_{SR}$  over the range of  $[Ca^{2+}]_i^{mean}$  studied was unexpected, as the cytosolic wave amplitude almost doubled over the range studied. This was reconciled by the description given for Figure 4-7, where it was shown to be as a consequence of the high non-linearity of the cellular buffering system in the  $<1\mu M$  range.

Interestingly,  $\text{Ca}^{2+}$  release during  $\text{Ca}^{2+}$  waves were shown to match that induced by application of caffeine. This led to the conclusion that the SR releases its entire  $\text{Ca}^{2+}$  store during a  $\text{Ca}^{2+}$  wave. This was contrary to previous data collected from whole-cell measurements (Diaz *et al.*, 1997; Overend *et al.*, 1997; Trafford *et al.*, 2000). The use of whole-cell fluorescence/current recordings, as opposed to the localized method used in this study may have lead to this difference in fractional SR release. The SR appears to behave as a series of subcompartments acting more-or-less independently, i.e. the  $\text{Ca}^{2+}$  wave is a propagating release event, with sequential firing of adjacent, but independent release units. Measurement of release should therefore attempt to minimise the temporal smearing which may occur as a result of the out-of-phase release inherent of  $\text{Ca}^{2+}$  waves.

Further analysis of the  $\text{Ca}^{2+}$  wave event allowed elucidation of the fluxes comprising the  $\text{Ca}^{2+}$  wave release event. This allowed quantification of various parameters of the RyR and SERCA. Changes were observed in both sets of fluxes with increased  $[\text{Ca}^{2+}]_i^{\text{mean}}$ .

With regard to the changes in SERCA, the results suggest a significant increase in  $V_{\text{max}}$  and  $K_{\text{D}}$  with increasing  $[\text{Ca}^{2+}]_i^{\text{mean}}$ . At first, this appears contradictory. An increase in activity, but a decrease in affinity. The changes observed between the highest and lowest  $[\text{Ca}^{2+}]_i^{\text{mean}}$  were summarised previously in Figure 4-9.

From the figure, a clear increase in  $V_{\text{max}}$  is observed. The change in  $K_{\text{D}}$ , being more modest is less obvious and as such may have less effect on the  $\text{Ca}^{2+}$  wave properties. The net affect is that SERCA is more active for the majority of the  $\text{Ca}^{2+}$  wave at the higher  $[\text{Ca}^{2+}]_i^{\text{mean}}$ , so  $[\text{Ca}^{2+}]_{\text{cytosol}}$  falls more rapidly from peak to minimum diastolic values and would cause wave frequency to increase. The

observed change in  $K_D$  might contribute to the higher minimum diastolic  $[Ca^{2+}]_i$  found at the higher  $[Ca^{2+}]_i^{mean}$  and would lead to a reduction in frequency.

#### 4.4.1.1 Possible mechanisms for changes in SERCA

Possible mechanisms for the observed increases in SERCA  $K_D$  and  $V_{max}$  could be mediated through phospholamban (PLB) or  $Ca^{2+}$ /calmodulin-dependent kinase (CaMKII) pathways.

Phosphorylation of PLB has been shown to reduce its inhibition of SERCA, thus decreasing  $K_D$ . This is thought to occur as a result of PKA activation of PLB (at the serine 16 site) (Tada & Toyofuku, 1998). If PLB was more phosphorylated at the lower  $[Ca^{2+}]_i^{mean}$ , this would explain the increased  $K_D$ .

CaMKII has been shown to have variable effects on SERCA.

Evidence exists to show CaMKII directly phosphorylates SERCA at the serine 38 site (Xu *et al.*, 1993a). Two more recent studies have found evidence to the contrary of the Xu study. The first, by Odermatt *et al.* (Odermatt *et al.*, 1996) showed no evidence for CaMKII mediated phosphorylation of SERCA, criticising the earlier study for its unphysiological use of  $Ca^{2+}$  free controls. This was reinforced by a more recent study by Rodriguez *et al.* (Rodriguez *et al.*, 2004). This study used an antibody specific to the serine 38 site, finding no significant phosphorylation.

Another study (Mattiuzzi *et al.*, 1994), used a CaMKII inhibitor to assess its effects on SERCA activity or  $K_D$ . The inhibitor (CaMKII I-Pep) caused both  $K_D$  and a  $V_{max}$  to decrease. A subsequent study from the same group found when phospholamban was present, CaMKII facilitated recovery of SERCA uptake during

acidosis (DeSantiago *et al.*, 2004). This was CaMKII activation was concluded to arise as a result of an elevated  $[Ca^{2+}]_i^{mean}$ , which agrees with the present study.

Whilst this area remains controversial, the current study showed  $V_{max}$  and  $K_D$  increase when  $[Ca^{2+}]_i^{mean}$  is raised. This was consistent with the finding by Mattiazzi *et al* where inhibition of CaMKII caused a reduction of  $K_D$  and  $V_{max}$ . The increases in  $V_{max}$  and  $K_D$  found in this thesis may result from stimulation of CaMKII as  $[Ca^{2+}]_i^{mean}$  increases. These hypotheses may be examined experimentally.

#### 4.4.1.2 Testing hypotheses

In order to test if PLB phosphorylation contributed to the shift in  $K_D$ , it would be necessary to repeat the experiments at 300nM and 900nM  $[Ca^{2+}]_i^{mean}$  with an agent to specifically dephosphorylate PLB. One such agent, PP1 (protein phosphatase-1) has been used in this way to effectively maintain PLB in its dephosphorylated state (Berrebi-Bertrand *et al.*, 1998). Once this was added to cells in both  $[Ca^{2+}]_i^{mean}$  conditions, it could be assessed whether the change in  $K_D$  was due to PLB.

It may also be possible to conduct the study on PLB knockout animals, which would identify its importance in this form of SERCA modulation.

In order to test if the changes in  $V_{max}$  and/or  $K_D$  were due to CaMKII activation, a specific CaMKII inhibitor could be used. Previously, Currie *et al* (Currie & Smith, 1999) have used AIP (autocamtide-2-related inhibitory peptide), a highly specific inhibitor of CaMKII to accomplish this. This could be used for  $Ca^{2+}$  wave experiments at 300 and 900nM  $[Ca^{2+}]_i^{mean}$  to see if this abolished the observed changes in  $V_{max}$  and  $K_D$ .

Biochemical studies could also be performed on both phospholamban and SERCA to assess their phosphorylation states.

#### 4.4.1.3 Possible mechanisms for changes in RyR

Peak RyR fluxes and peak permeability was shown to increase with  $[Ca^{2+}]_i^{mean}$ .

This could also be due to phosphorylation of the RyR. The effect of phosphorylation on the RyR is controversial, with many conflicting reports. Some argue RyR is activated by phosphorylation, possibly by CaMKII (Currie *et al.*, 2004; Hain *et al.*, 1995), whilst others show inhibition (Valdivia *et al.*, 1995).

#### 4.4.1.4 Testing hypotheses

Using the CaMKII inhibitor mentioned above, the effect of RyR phosphorylation on its permeability could be assessed using the methods employed in this chapter. CaMKII knockout animals could also be used to assess any changes in RyR permeability taking place.

#### 4.4.2 Tetracaine study

Application of tetracaine had the effect of substantially increasing  $Ca^{2+}$  wave peak systolic and decreasing frequency and minimum diastolic  $[Ca^{2+}]_i$ . This was due to the desensitizing action of tetracaine on the RyR, effectively increasing the threshold required for initiating a  $Ca^{2+}$  wave. The SR threshold was quantified as 36% higher than control levels.

The frequency and amplitude changes have been well documented (Neary *et al.*, 2002; Shannon *et al.*, 2002; Smith & O'Neill, 2001; Lukyanenko *et al.*, 1999; Overend *et al.*, 1997), mirroring the effects described here. What has not been shown before is the gradual increase in frequency and amplitude occurring after tetracaine was applied. This could be explained by changes in SERCA

activity, possibly caused by frequency dependant changes in CaMKII. This frequency dependence has been previously demonstrated by Wehrens et al. (Wehrens *et al.*, 2004). This could increase SERCA  $V_{max}$  and  $K_D$  over this timescale. This result may not have been observed previously due to the very low frequency of oscillation typically observed in intact cells (~2 per minute) as opposed to the ~0.2 to 0.6 Hz used in this study.

The diastolic  $[Ca^{2+}]_i$  was shown to decrease upon application of tetracaine. This is in agreement with a study by Shannon et al (Shannon *et al.*, 2002), which found a decrease in resting  $[Ca^{2+}]_i$  after application and Overend *et al.* (Overend *et al.*, 1997), where no change was found. The change was hypothesised to be due to changes in SR leak. This will be discussed in greater detail in the subsequent chapter.

The other significant change observed after application of tetracaine was an increased  $\frac{1}{2}$ -maximal permeability. This suggests the RyR opening event is more prolonged. This, coupled with the fact that SR efflux from overload and caffeine induced releases were of similar amplitudes consolidated the hypothesis that release in a wave was terminated by SR  $Ca^{2+}$  depletion. RyR peak permeability was unchanged from control values, the RyR mediated SR depletion requires an prolonged period of time to complete.

RyR flux was shown to increase, but the change was found not to be significant. It could be hypothesised that a larger peak flux rate would be expected, since RyR peak permeability remained unchanged, yet SR  $Ca^{2+}$  was increased.

SERCA activity and affinity was found not to change significantly. This suggested tetracaine had no effect on SERCA.

#### 4.4.3 TBQ study

Applying TBQ to the oscillating cardiac cell had most marked effects on  $\text{Ca}^{2+}$  wave frequency and systolic (peak)  $[\text{Ca}^{2+}]_i$ . Diastolic (Min)  $[\text{Ca}^{2+}]_i$  did not change significantly. The decrease in frequency was a direct result of reduced SERCA activity. On average, SERCA  $V_{\text{max}}$  was shown to decrease by 43%, with no changes in  $K_D$ . This reduction in SERCA activity had the secondary consequence of depleting  $[\text{Ca}^{2+}]_{\text{SR}}$ , reducing the SR threshold for spontaneous release by 25%. This explains why mean systolic (peak)  $[\text{Ca}^{2+}]_i$  in the TBQ perfused cells only rose to ~70% of that achieved by the cells without TBQ.

##### 4.4.3.1 Mechanisms for changes in wave amplitude

The changes in wave amplitude found in this study conflict with the recent findings, where wave amplitude remained relatively unchanged by TBQ application on intact cardiomyocytes (O'Neill *et al.*, 2004). Only a slight reduction (8%) of  $[\text{Ca}^{2+}]_{\text{SR}}$  was reported.

The decreased SR release threshold for  $\text{Ca}^{2+}$  waves can be explained in terms of decreased SERCA activity causing a decrease in cytosolic buffering and hence the cytosolic  $\text{Ca}^{2+}$  diffusion coefficient. This reduction in buffering would mean a smaller release would be more likely to trigger a release for an adjacent release unit. A spark, which would normally not be of sufficient amplitude to elicit a propagating release, would do under these conditions of reduced buffering.

Cytosolic diffusion coefficient was not tested in this study.

Another possible mechanism could arise if TBQ's effect did not have a homogenous affect on SERCA throughout the cell. If one region had been less

affected, this would reach the threshold value first, and would act as the effective “pacemaker” for the rest of the cell. The large initial release would elicit a release from the rest of the cell, before the SR had reached the same level of filling. This would result in waves of reduced velocity and amplitude.

Wave velocity was quantified, using the “WaveCorr” program (described earlier). Wave velocity was shown to decrease after TBQ application. This is in agreement with the O’Neill et al study, but in apposition to the results of Lukyanenko et al, where an increase was observed and to those found by Overend et al, where a nonsignificant increase was seen. O’Neill et al proposed the decrease in velocity was due to reduced SR content. The results of the present study indicate a reduction in RyR permeability, which may mean its sensitivity is decreased. This could also account for the decrease in wave velocity.

The increased velocity of the Lukyanenko et al. study was concluded to be due to decreased cytosolic  $[Ca^{2+}]_i$  buffering by SERCA. This was not investigated in the present study.

#### 4.4.3.2 Testing hypotheses

In order to investigate if decreased SR content was the cause of the observed reduction in velocity, it would be necessary to repeat the TBQ experiment, but boost SR content back to threshold levels with an intra-SR buffer, such as citrate. This method has previously been employed by Terentyev et al. (Terentyev *et al.*, 2002). This method may have adverse effects on RyR release. The buffer may reduce  $[Ca^{2+}]_i$  within the SR, which would reduce the concentration gradient and hence the flux rate through the RyR.

Another method that could be used to control for SR content, would be to pharmacologically increase leak from the SR, thus depleting the SR of  $\text{Ca}^{2+}$ . This has been accomplished in a previous study using ionomycin (a  $\text{Ca}^{2+}$  ionophore) (Neary *et al.*, 2002). This was found to decrease oscillation frequency, with no change in amplitude, indicating SR release threshold remained constant. This is not therefore a viable option for the purposes of testing the hypothesis.

Since thapsigargin has previously been shown to deplete the SR in a similar manner to that observed in the present study, it is likely that the effects are solely due to a reduction of SERCA activity.

To verify the changes in SR content are not due to non-specific effects of TBQ on the RyR, TBQ's effects could be assessed using the radioactive RyR binding method (Anderson *et al.*, 1989).

The O'Neill *et al.* study did not quantify SERCA  $V_{\text{max}}$  in the same way as this study, but its activity was purported to decrease by 16%. This was more modest than the 43% observed in this study, even though the concentration used was 20 times less than that used in the O'Neill *et al.* study. Possible reasons for this discrepancy may be due to the fact that permeabilised, rather than intact cells were used here, coupled with the fact that TBQ's effect had mostly equilibrated, with stable SR content and frequency. In the O'Neill *et al.* study it was difficult to assess whether this was the case, as only a few waves occurred before TBQ was removed. This more modest inhibition of the O'Neill study would explain the more modest effects on release threshold and wave frequency.

Two other studies, namely Lukyanenko *et al.* and Overend *et al.* (Lukyanenko *et al.*, 1999; Overend *et al.*, 2001) used thapsigargin to examine the effect of SERCA

inhibition on  $\text{Ca}^{2+}$  wave properties. Both studies showed diminished wave amplitude and frequency, in accordance with the present results. Yet another study (Kawai *et al.*, 1998) used CPA, finding similar results, with the additional observation of an increase in wave rise time.

The current study shows an analogous result. RyR peak permeability decreased after TBQ application. The Kawai *et al* study gave no clear reason for the prolonged rise time and concluded it was probably not due to any reduction in SR content. Possible reasons are: 1. Wave frequency activates similar mechanisms to that observed in the  $[\text{Ca}^{2+}]_i^{\text{mean}}$  study, with lower frequencies affecting activation of kinases such as CaMKII. 2. A functional link between SERCA and RyR exists.

No evidence for either mechanism exists, although biochemical means could be used to assess RyR phosphorylation states in cells before and after TBQ application and specific kinase inhibitors as described before could be used to assess the role of kinases in this behaviour.

The RyR-SERCA link would also be difficult to test and because SERCA is distributed primarily in the longitudinal SR, as opposed to the junctional region, where the RyR is found, this would therefore be improbable.

**Chapter 5  $\text{Ca}^{2+}$  wave model: Construction and comparison  
with experimental results**

### 5.1 Model description

A 1-dimensional, 3-compartment model of  $\text{Ca}^{2+}$  flux was constructed to model the changes in  $[\text{Ca}^{2+}]_i$  observed in  $\text{Ca}^{2+}$  waves in cardiac myocytes incorporated into a model. The figure below shows the fluxes occurring between compartments.

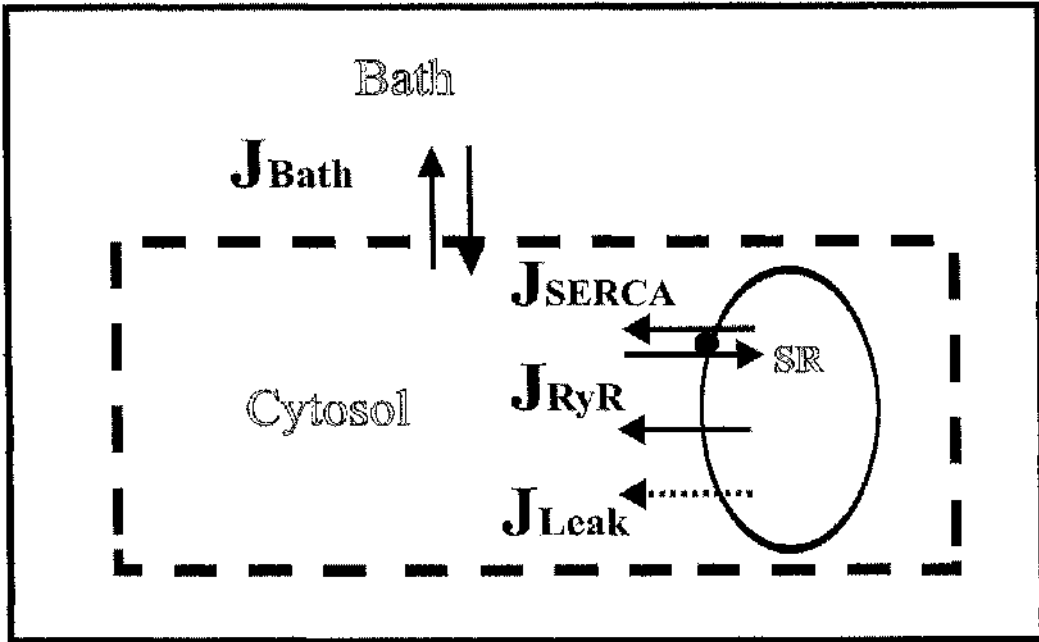


Figure 5-1 Diagram of fluxes occurring between compartments in model.

The equations below describe how these fluxes interact to reproduce the  $\text{Ca}^{2+}$  signals recorded experimentally.

The fluxes affecting the cytosol are represented by:

Equation 7

$${}^{\text{cyt}}\text{Ca}_{t+\Delta t}^{\text{free}} = {}^{\text{cyt}}\text{Ca}_t^{\text{free}} + \Delta\text{Ca}_{\text{free}}$$

Equation 8

$$\Delta\text{Ca}_{\text{free}} = f_{\text{Buff}} (\Delta\text{Ca}_{\text{Total}})$$

**Equation 9**

$$\Delta Ca_{Total} = \frac{{}^{cyt} J_{Net} \bullet \Delta t}{\text{Relative Volume}}$$

**Equation 10**

$${}^{cyt} J_{Net} = J_{RyR} + J_{Leak} + J_{SERCA} + J_{Diff}$$

The time dependence and threshold of  $Ca^{2+}$  release is described by the following equations:

When  $[Ca^{2+}]_{SR} < \text{threshold}$

**Equation 11**

$$J_{RyR} = 0$$

When  $[Ca^{2+}]_{SR} \geq \text{threshold}$ ,

**Equation 12**

$$J_{RyR} = f(t) \bullet (Ca^{2+}_{SR} - Ca^{2+}_i)$$

where  $f(t)$  i.e. the time-course of change in RyR  $Ca^{2+}$  permeability, which is determined by the function shown in Figure 5-2, and is accessed as a lookup table.

Interpolation between time-points is achieved via a cubic spline method.

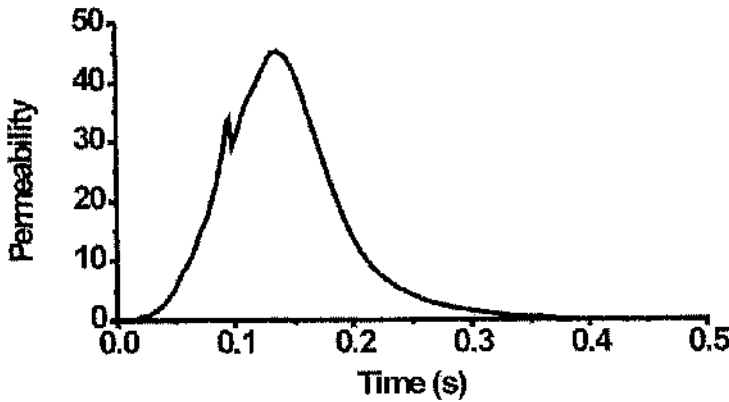


Figure 5-2 Average permeability profile.  
Temporally averaged RyR permeability profile (n-6).

Equation 13

$$J_{leak} = k_{leak} \bullet (Ca^{2+}_{SR} - Ca^{2+}_{cyt})$$

Equation 14

$$J_{Bath} = k_{Diff} \bullet (Ca_{Bath} - Ca_{cyt})$$

For SR compartment,

Equation 15

$$J_{Net}^{SR} = J_{RyR} + J_{SERCA} + J_{leak}$$

Where  $J_{SERCA}$  is always negative and  $J_{RyR}$  is always positive.

Equation 9 is used to calculate the change in total  $Ca^{2+}$  and Equation 8 is used to convert this figure to  $[Ca^{2+}]_{cyt}$ .

The bath compartment has very high relative volume ratio and so  $[Ca^{2+}]_{bath}$  remains constant.

As described earlier, the release event is triggered by  $[Ca^{2+}]_{SR}$  reaching a threshold level. This causes RyR permeability to increase as shown in Figure 5-2

Table 3 below shows relative volumes of compartments. Fluxes between compartments are scaled to these volumes, as described in Equation 9. Relative volumes of cytosol and SR are based on measurements by Page et al. (Page *et al.*, 1971).

**Table 3 Relative volumes of compartments as used in model.**

Compartment	Relative Volume
Cytosol	0.946
SR	0.054
Bath	$\sim \infty$

## 5.2 Program implementation

Simulations were run on a 1000 MHz computer with 128 Mb Ram. Initially, a 1<sup>st</sup>-order Euler method was used to resolve fluxes, which was computationally intensive, with 100nsec time steps required. This typically required ~ 6 hours for 20sec of simulation. To increase efficiency, a 4<sup>th</sup>-order Runge-Kutta method was employed, adapted from code in the Numerical recipes in C book (Press *et al.*, 2002). The equations below describe this method.

### Equation 16

$$\begin{aligned}
 k_1 &= hf(x_n, y_n) \\
 k_2 &= hf\left(x_n + \frac{h}{2}, y_n + \frac{k_1}{2}\right) \\
 k_3 &= hf\left(x_n + \frac{h}{2}, y_n + \frac{k_2}{2}\right) \\
 k_4 &= hf(x_n + h, y_n + k_3) \\
 y_{n+1} &= y_n + \frac{k_1}{6} + \frac{k_2}{3} + \frac{k_3}{3} + \frac{k_4}{6} + O(h^5)
 \end{aligned}$$

(equation from numerical recipes in C)

where:

k= estimate of flux,

y=[Ca<sup>2+</sup>] in the compartment;

h=1,

O=error, which is neglected.

This equation allowed a much larger time step (10µsec) to be employed. This decreased the time for a 20 sec simulation from ~6 hours to ~5 minutes.

At each time step, fluxes were evaluated between each compartment based on the previous [Ca<sup>2+</sup>]<sub>i</sub>. A [Ca<sup>2+</sup>]<sub>total</sub> was calculated from [Ca<sup>2+</sup>]<sub>i</sub> using the binding properties of the buffers in the compartment. The net flux in/out of the compartment was added to this value and a new value of free was calculated.

### 5.2.1 Calculating free from total.

[Ca<sup>2+</sup>]<sub>total</sub> can be calculated using the buffer equation used in Equation 2. A rearrangement of this equation can be used to convert from [Ca<sup>2+</sup>]<sub>total</sub> to [Ca<sup>2+</sup>]<sub>i</sub> when only one buffer is present. The cytosolic compartment in the model contains 4 buffers, namely EGTA, Fluo5F, and 2 buffers representing intrinsic Ca<sup>2+</sup> buffering by the cell (Hove-Madsen & Bers, 1993). This creates the equation shown below, which cannot easily be rearranged in terms of [Ca<sup>2+</sup>]<sub>i</sub>.

**Equation 17**

$$[Ca]_{Total} = [Ca]_{Free} + \frac{B \max_1}{[1 + (Kb_1/[Ca]_{Free})]} + \frac{B \max_2}{[1 + (Kb_2/[Ca]_{Free})]} \\ + \frac{B \max_3}{[1 + (Kb_3/[Ca]_{Free})]} + \frac{B \max_4}{[1 + (Kb_4/[Ca]_{Free})]}$$

The calculation of free from total  $[Ca^{2+}]$  in this case requires an alternative method. This is accomplished by an iterative method (see appendix under the “gsearch” procedure of the model for source code), which uses an initial estimate of  $[Ca^{2+}]_i$ , converts this to  $[Ca^{2+}]_{total}$  and compares the value to the actual total. Each iteration uses the following equation to estimate a new  $[Ca^{2+}]_i$ .

**Equation 18**

$$free_{new} = free_{old} \times \sqrt{\frac{total_{estimate}}{total_{old}}}$$

The estimate of free converges with each successive iteration. Error is calculated as the difference between the estimated total and the actual  $[Ca^{2+}]_{total}$ . The process was repeated until this fell below a set point ( $1 \times 10^{-14}$  M).

Typically, around 10-15 iterations were required in order to accurately estimate  $[Ca^{2+}]_i$ . The number of iterations was cut down to a minimum by using the previous  $[Ca^{2+}]_i$  as the estimate.

### 5.3 Model verification

The model underwent extensive testing to verify its accuracy in replicating experimental data. Firstly, experimental transients were compared to those generated by the simulation. A typical comparison is shown below.

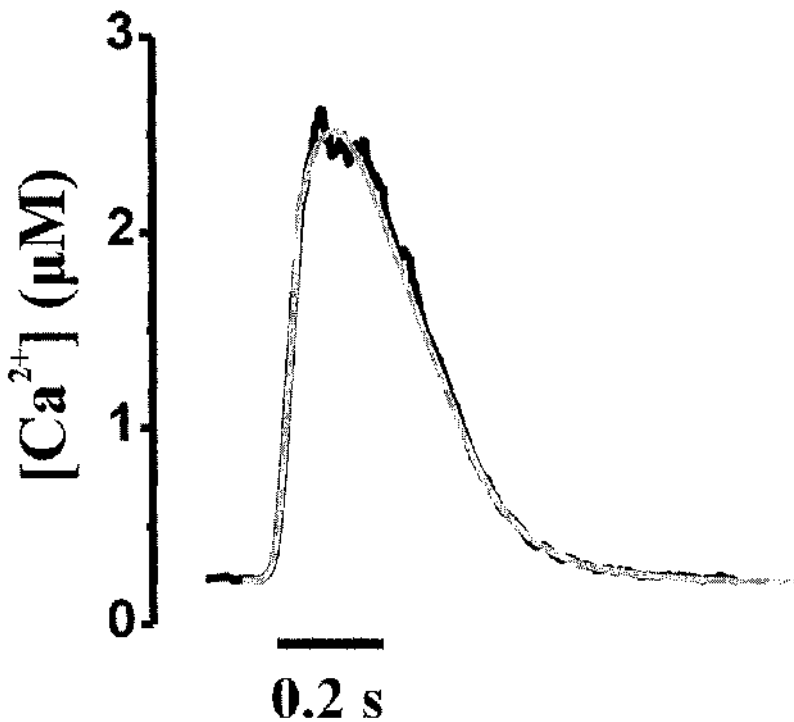


**Figure 5-3 Comparison of modelled and experimental  $[Ca^{2+}]$  profile from wave. Figure shows an averaged  $Ca^{2+}$  profile from 5  $Ca^{2+}$  waves (Black) superimposed on output from the model under similar experimental conditions (grey).**

The experimental and simulated waves show similar time course, peak ( $2.63\mu\text{M}$  vs.  $2.56\mu\text{M}$  for model) and minimum ( $232\text{ nM}$  vs.  $218\text{ nM}$  for model)  $[Ca^{2+}]$ . The frequency of waves from the ccll in Figure 5-3 was  $0.94\text{ Hz}$  in experiment and  $0.96$  in simulation. The model successfully replicated this experimental data.

Results obtained from experiment were used for various parameters in the model. These have errors associated with their measurement. Dependent on the sensitivity of the model to these parameters, small margins of error in any one of these parameters could cause large changes in the results of the model in terms of release frequency, minimum and maximum  $[Ca^{2+}]_i$ . To identify which parameters were most sensitive to error, each was examined in turn and the changes in simulation results were evaluated. These tests are illustrated in the following sections.

## 5.4 Error analysis of model parameters.

Error analysis was carried out by running simulations with typical values from experiment and varying parameters in turn to assess the effect of these changes on simulated results. This allowed assessment of the parameters most sensitive to error. It was also noted that in most cases, the effect of changes in these parameters was larger at higher  $[\text{Ca}^{2+}]_{\text{bath}}$ .

In all cases, the model was run until steady state conditions were achieved. The  $\text{Ca}^{2+}$  wave was analysed in terms of systolic (peak)  $[\text{Ca}^{2+}]$ , diastolic (min)  $[\text{Ca}^{2+}]$  and frequency of the  $\text{Ca}^{2+}$  wave.

### 5.4.1 Diffusion constant

The diffusion constant, as estimated from the decline in  $[\text{Ca}^{2+}]$  observed after caffeine induced  $\text{Ca}^{2+}$  release, was taken from each cell. This was found to be  $30.1 \pm 2.1$  ( $n=15$ ), with no dependency on bath  $[\text{Ca}^{2+}]$ . The graph below shows the effect 10 and 20% error in this parameter had on the simulation results.

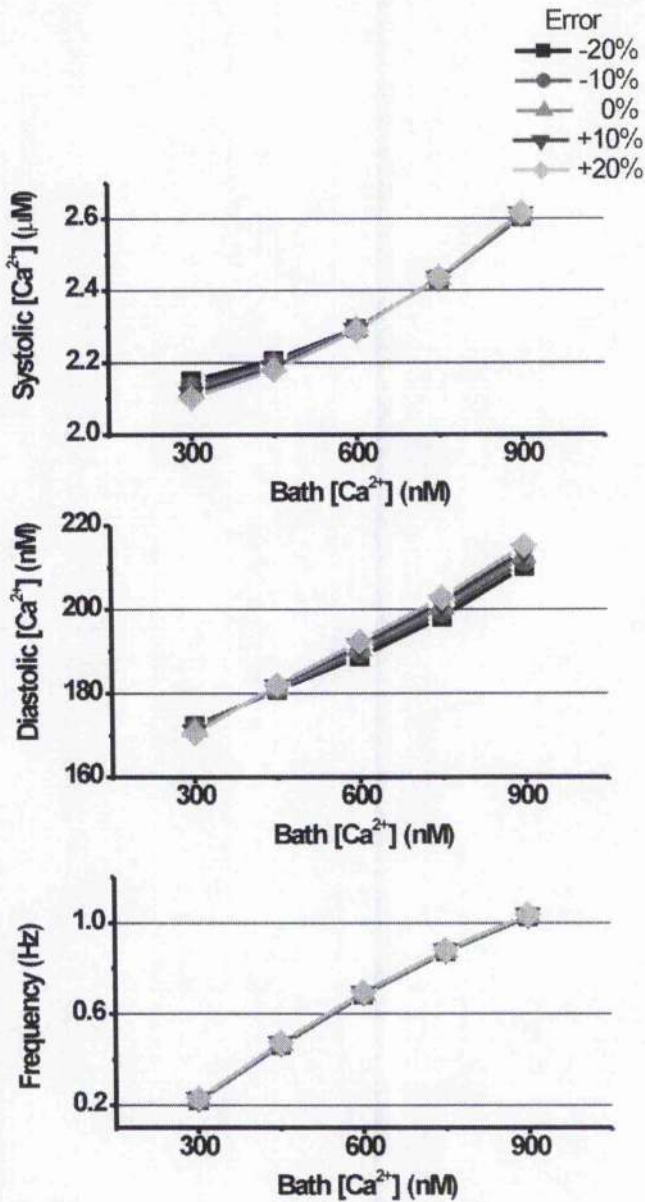


**Figure 5-4 Error analysis of diffusion  $k$  parameter.**  
**Plot of modelled systolic, diastolic and wave frequency over 300 to 900 nM  $[Ca^{2+}]$  range. Lines indicate average experimental diffusion  $k$  (30)  $\pm$  10 and 20 % error.**

Generally, error in diffusion constant ( $k$ ) had minimal effects on all three parameters of the simulated  $Ca^{2+}$  waves. Systolic (peak)  $[Ca^{2+}]$  was more sensitive in the lower range bath  $[Ca^{2+}]$ , with a +20 % error causing an  $\sim$ 1% decrease.

Diastolic  $[Ca^{2+}]$  showed minimal changes as it rose above 600nM, where

increasing diffusion constant by 20% causing an ~1% increase in diastolic  $[Ca^{2+}]_i$ .

Changes in frequency were well below 1% in all cases.

It was hence concluded that the model had low sensitivity to error in diffusion constant.

#### **5.4.2 RyR Permeability**

A typical profile of RyR permeability was loaded into the model and used as a model for release. The amplitude of these showed bath  $Ca^{2+}$  dependent changes (see results chapter). The ramifications of these changes for the model results are shown below.

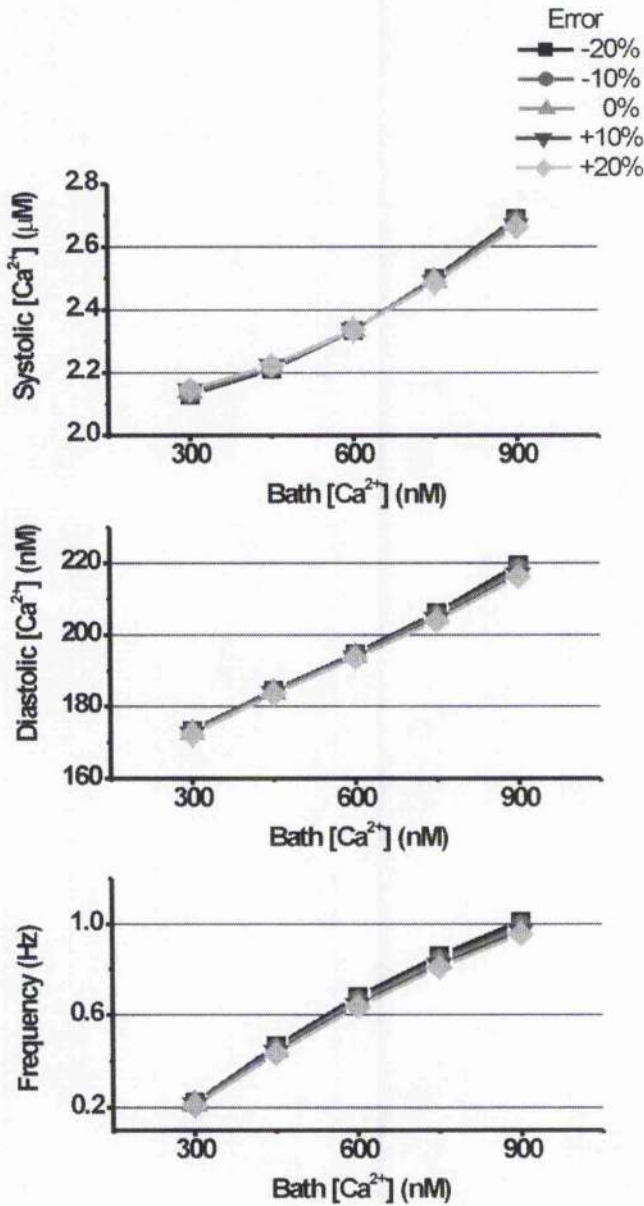


**Figure 5-5 Error analysis of peak RyR permeability profile.** Plot shows modelled data over the 300 to 900 nM [Ca<sup>2+</sup>] range. A representative figure of peak RyR profile (60s<sup>-1</sup>) was used as control. The effect of varying the parameter by +/- 10 and 20% is shown by the symbols in the key.

No major changes occurred in any of the results. Wave frequency was the most sensitive result, with changes becoming more evident as [Ca<sup>2+</sup>]<sub>bath</sub> was increased. At the 900nM [Ca<sup>2+</sup>]<sub>bath</sub>, a ~ 1% increase occurred with +20% error. The model was hence concluded to have low sensitivity to this parameter.

5.4.3 SERCA  $K_D$ 

The figure below shows the effects of error in SERCA  $K_D$  on simulation results.

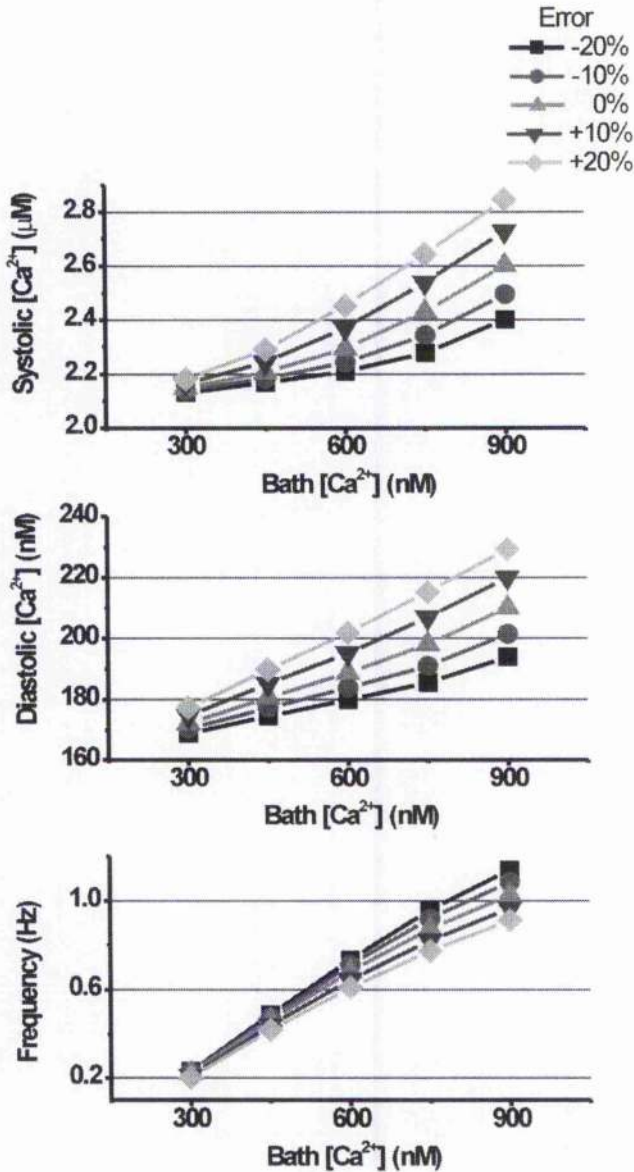


**Figure 5-6 Error analysis of SERCA forward mode  $K_D$ .** Plot shows modelled data over the 300 to 900 nM  $[Ca^{2+}]$  range. A representative figure of  $K_D$  (289nM) was used as control. The effect of varying the parameter by +/- 10 and 20% is shown by the symbols in the key.

Error in SERCA  $K_D$  had a pronounced effect on all three parameters, increasing its effects as  $[Ca^{2+}]_{bath}$  increased. Systolic (peak)  $[Ca^{2+}]$  was shown to increase by

~10% with a +20% error and decrease by ~8% with a -20% error. This effect declined at lower  $[Ca^{2+}]_{bath}$ , with <1% changes at the 300nM  $[Ca^{2+}]_{bath}$ , with 20% error.

Diastolic  $Ca^{2+}$  was also profoundly affected by the error, which again was more evident at the higher  $[Ca^{2+}]_{bath}$ . At 900nM  $[Ca^{2+}]_{bath}$ , with ~9% increase with +20% error. At 600nM, this dropped to ~7% increase and with 300nM, the increase dropped to ~3%, with +20% error.

Frequency was the most sensitive parameter, and a decrease of ~11% from 1.14 to 1.02 with a +20% error in  $K_D$ . At 600nM, a similar decrease was observed, with ~11% decrease seen. At 300nM, this decrease had fallen to 8%.

The behaviour of the model was clearly very sensitive to changes in this parameter, especially at higher  $[Ca^{2+}]_{bath}$ .

#### 5.4.4 SERCA Vmax

The graph below shows the model's sensitivity to error in SERCA Vmax.

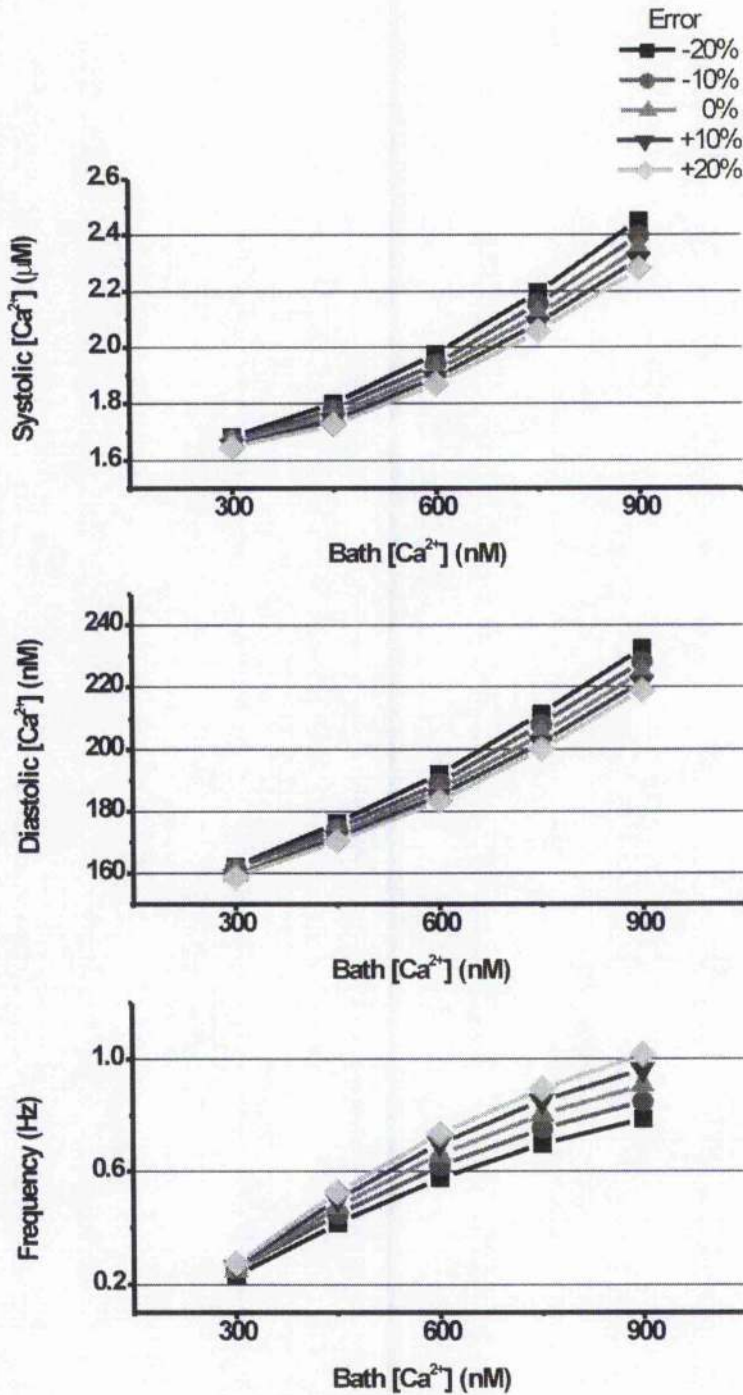


**Figure 5-7 Error analysis of SERCA Vmax.**

Plot shows modelled data over the 300 to 900 nM [Ca<sup>2+</sup>] range. A representative figure of Vmax (260 μM) was used as control. The effect of varying the parameter by +/- 10 and 20% is shown by the symbols in the key in the top left.

Generally, increasing Vmax caused systolic (peak) and diastolic (min) [Ca<sup>2+</sup>] to increase, and frequency to decrease.

Frequency was the most sensitive parameter to changes in  $V_{max}$ , with increased changes observed at the highest  $[Ca^{2+}]_{bath}$ . +20% error caused a 12% increase in frequency at 900nM  $[Ca^{2+}]_{bath}$ . At lower  $[Ca^{2+}]_{bath}$ , the model became gradually less sensitive, with an 8% increase in frequency observed with a +20 error in  $V_{max}$ .

Diastolic  $[Ca^{2+}]$  was much less sensitive to  $V_{max}$  error, with 3% changes observed at the 900  $[Ca^{2+}]_{bath}$ . Its sensitivity decreased with  $[Ca^{2+}]_{bath}$  with <1% changes observed at 300nM  $[Ca^{2+}]_{bath}$ .

The systolic (peak) $[Ca^{2+}]$  parameter showed a comparable sensitivity to  $V_{max}$ , with 3% changes at the 900 nM  $[Ca^{2+}]_{bath}$  with 20% error. This dropped to <1% change at the 300nM value.

#### **5.4.5 SR $Ca^{2+}$ threshold**

The graph below shows model sensitivity to error in threshold.

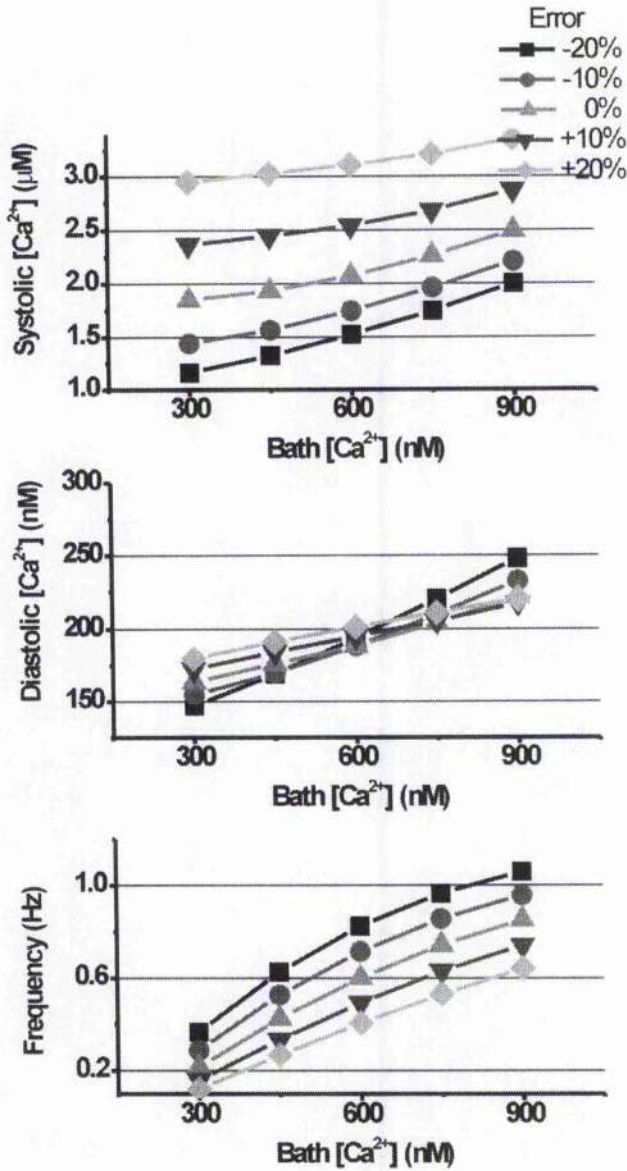


**Figure 5-8** Error analysis of SR  $Ca^{2+}$  threshold for release. Plot shows modelled data over the 300 to 900 nM  $[Ca^{2+}]$  range. A representative figure of threshold (1mM) was used as control. The effect of varying the parameter by  $\pm 10$  and 20% is shown by the symbols in the key.

Of all the variables tested, threshold showed highest sensitivity to error. Error elicited large variations in the systolic (peak) and frequency parameters. Generally, increasing threshold increased systolic (peak)  $[Ca^{2+}]$ , decreased frequency, with increased diastolic  $[Ca^{2+}]$  at lower  $[Ca^{2+}]_{bath}$  and higher diastolic at higher  $[Ca^{2+}]_{bath}$ .

Systolic (peak)  $[Ca^{2+}]$  varied by 24% with a 20% error at 900nM  $[Ca^{2+}]_{bath}$ . At 300nM, relative change increased to 45%, with a  $\pm 20\%$  error, decreasing frequency from 0.22 to 0.12 Hz. Diastolic  $[Ca^{2+}]$  varied by  $\sim 1\%$  at 600nM  $[Ca^{2+}]_{bath}$  with 20% error. At 300nM, a 10 % change in diastolic  $[Ca^{2+}]$  was observed with 20% error. At 900nM  $[Ca^{2+}]_{bath}$ ,  $<1\%$  change was observed with  $+20\%$  error, but a 12% change was observed with  $-20\%$  error.

Systolic (peak)  $[Ca^{2+}]$  varied substantially, with  $+20\%$  error at 900nM  $[Ca^{2+}]_{bath}$  causing an increase from 2.49 to 3.35  $\mu M$ .  $-20\%$  error at this  $[Ca^{2+}]_{bath}$  caused systolic (peak)  $[Ca^{2+}]$  to decrease to 2.00 $\mu M$ . This equated to a  $+34$  and  $-19\%$  change for  $+20$  and  $-20\%$  error respectively. A  $+60\%$  change was caused by  $+20\%$  error in threshold at 300nM and  $-45\%$  change was observed with  $-20\%$  error.

The model showed very high sensitivity to this parameter in terms of systolic (peak)  $[Ca^{2+}]$  and frequency. Diastolic  $[Ca^{2+}]$  was less sensitive to this parameter.

## 5.5 Model Results

### 5.5.1 The effect of changing $[Ca^{2+}]_{bath}$ on parameters of spontaneous release.

The following section illustrates how the model was run, with modulation of SERCA  $V_{max}$ ,  $K_D$  and RyR peak permeability as observed experimentally.

$[Ca^{2+}]_{bath}$  was varied in the 300-900 nM range. Model results are shown with experimental results superimposed for comparison.

#### 5.5.1.1 Model Variables

The model allowed simulations to be run in batches. Typically, these consisted of 5 different  $[Ca^{2+}]_{bath}$  and 5 of another variable, such as threshold, SERCA  $K_D$ , SERCA  $V_{max}$  or diffusion constant.

The model also included an option to incorporate modulation of certain parameters, which were experimentally found to vary with  $[Ca^{2+}]_{bath}$ , primarily SERCA Vmax,  $K_D$  and RyR peak permeability.

Linear fits of all three parameters were taken and used to extrapolate values at any  $[Ca^{2+}]_{bath}$ . These fits and their derived equations are shown below.

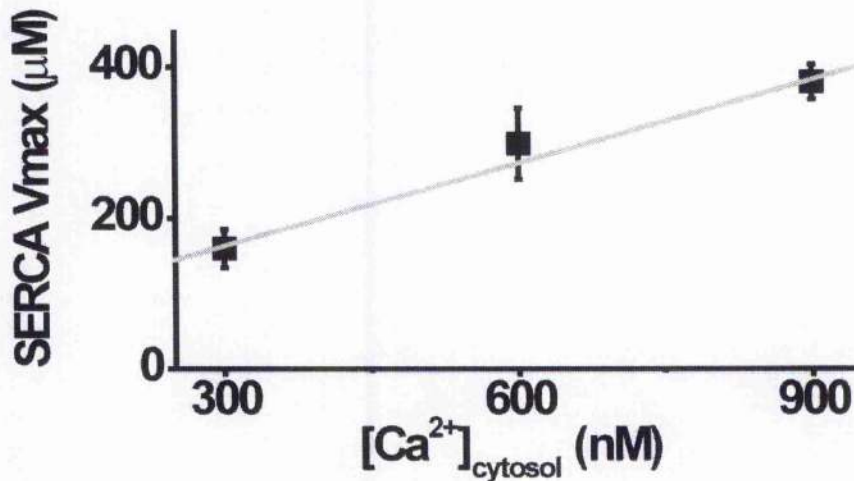


Figure 5-9 Linear fit of SERCA Vmax from experimental results. Grey line represents liner fit (gradient = 0.366, y-intercept=59.9).

Equation 19

$$SERCA \text{ Vmax} = 0.366 \cdot Ca_{cyt} + 59.9$$

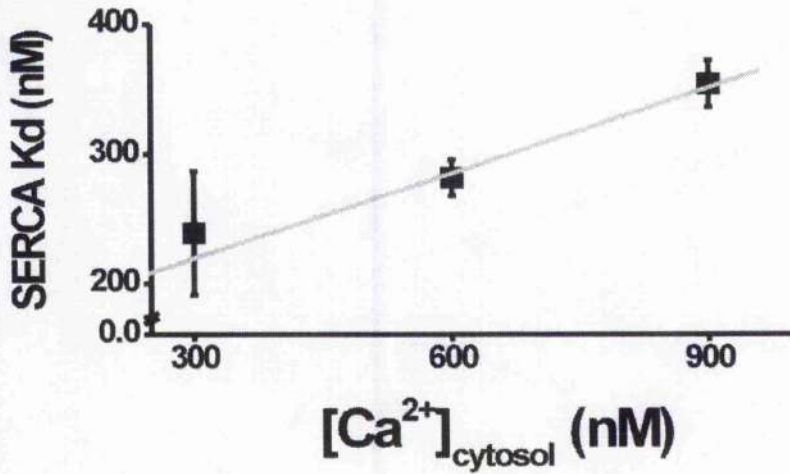


Figure 5-10 Linear fit of SERCA  $K_D$  from experimental results. Grey line represents linear fit (gradient=0.220, y-intercept=153.5).

Equation 20

$$SERCA K_D = 0.220 \cdot Ca_{cyt} + 153.5$$

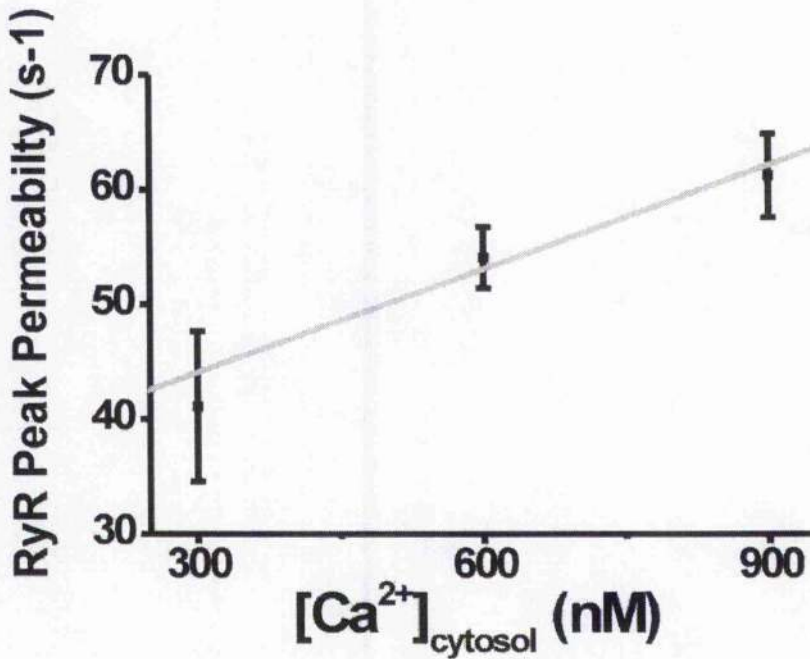


Figure 5-11 Linear fit of RyR peak permeability from experimental results. Grey line indicates linear fit (gradient= 0.0301, y-intercept= 35.1).

**Equation 21**

$$RyR_{Peak} = 0.0301 \cdot Ca_{cyt} + 35.1$$

SERCA Vmax and  $K_D$  were implemented as shown by the equations above. RyR permeability was implemented by normalizing the permeability profile peak to 1 and multiplying the whole profile by the value given by Equation 21.

**5.5.1.2 Model Output**

The figure below shows outputted simulation data for both cytosolic and SR compartments, using the following variables:

**Table 4 Simulation Parameters:**

[Ca <sup>2+</sup> ]Bath	300 nM	900 nM
SERCA Vmax	17.0 $\mu\text{Ms}^{-1}$	39.0 $\mu\text{Ms}^{-1}$
SERCA $K_D$	234 nM	349 nM
RyR <sub>Peak</sub>	44 $\text{s}^{-1}$	62.1 $\text{s}^{-1}$

**Figure 5-12 Plot of changes in [Ca<sup>2+</sup>]<sub>i</sub> from cytosol (upper panel) and SR (lower panel) compartments of model.**

The following plot shows the time-course of changes in Ca<sup>2+</sup> wave amplitude and frequency when [Ca<sup>2+</sup>]<sub>bath</sub> is transiently raised from 300 to 900nM.

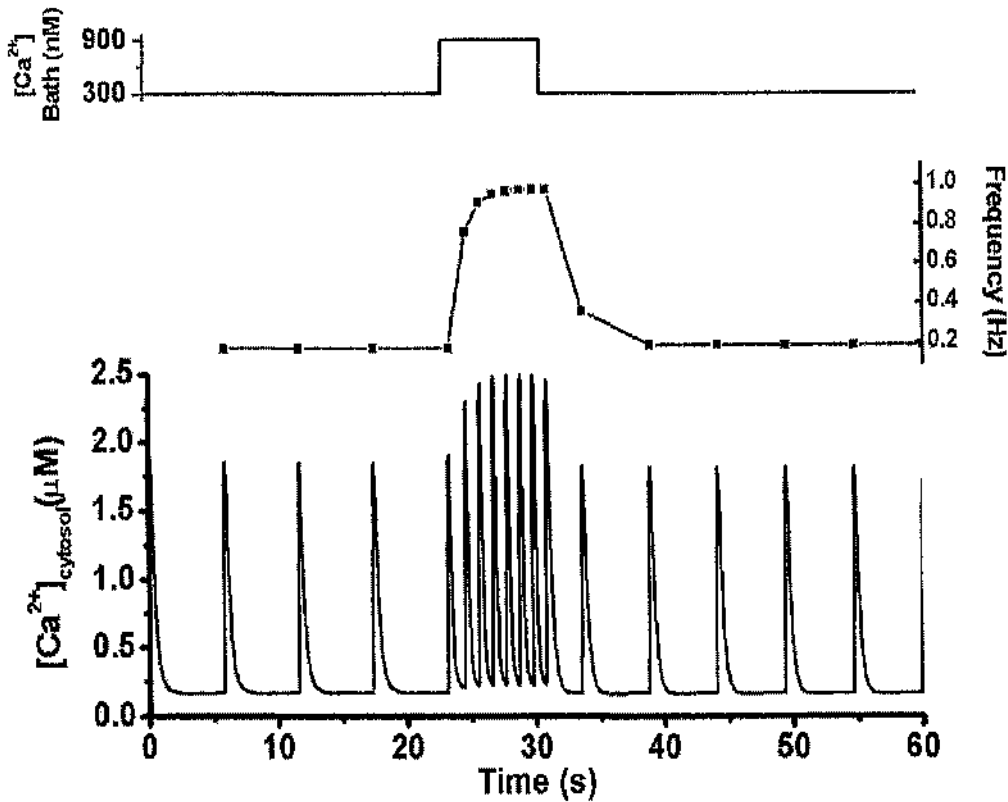


**Figure 5-13** The effect of a transient rise in external  $\text{Ca}^{2+}$  on  $\text{Ca}^{2+}$  release in the model. Time course of changes in Bath  $[\text{Ca}^{2+}]$  (upper), frequency (middle) and  $[\text{Ca}^{2+}]_{\text{cytosol}}$  (lower) are shown.

The above figure shows how the model responds to a rise in  $[\text{Ca}^{2+}]_{\text{bath}}$ . This demonstrates the time-course of equilibration of frequency and amplitude of  $\text{Ca}^{2+}$  release events. Equilibration is accomplished within  $\sim 5\text{s}$  (5 oscillations). Equilibration of frequency and amplitude on reduction of  $[\text{Ca}^{2+}]_{\text{bath}}$  takes approximately the same period. These changes in frequency diastolic and systolic (peak)  $[\text{Ca}^{2+}]$  are quantified further in the following section.

### 5.5.1.3 Steady-state effects over a range of $[\text{Ca}^{2+}]_{\text{bath}}$ .

The graphs below summarize changes in various parameters of  $\text{Ca}^{2+}$  release in the model. Experimental results are superimposed for comparison.

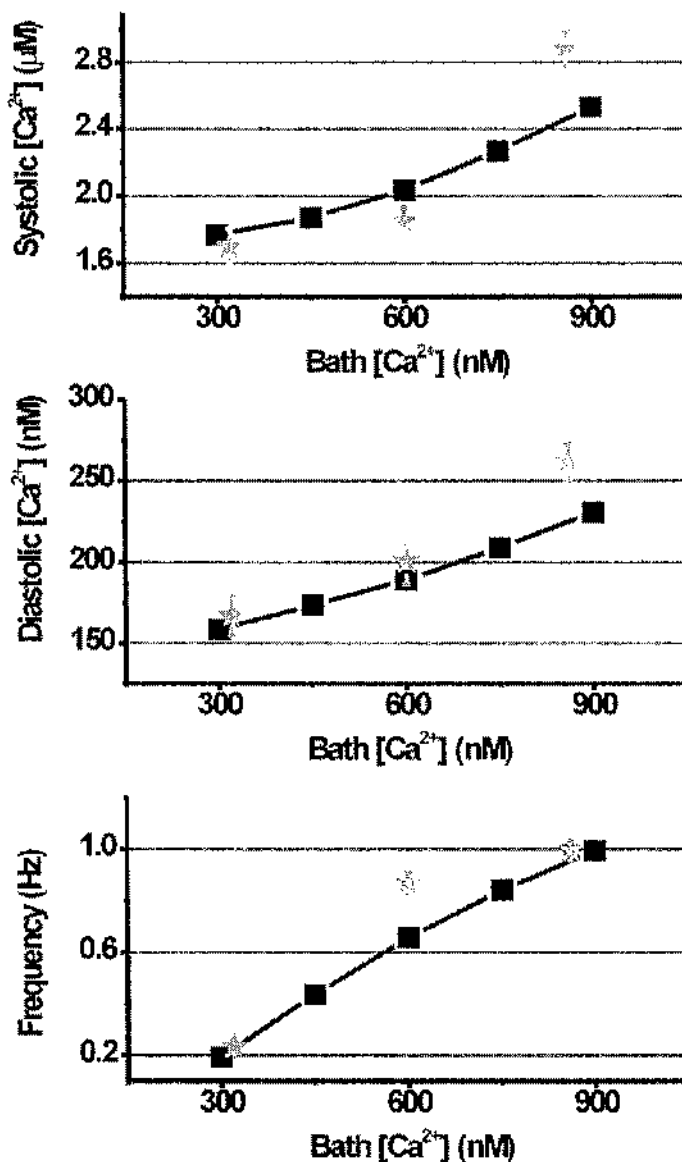


**Figure 5-14** Modelling results over 300 to 900nM bath  $[Ca^{2+}]$  range, with modulation of model variables seen in experiment.

Graphs show changes in systolic (peak) (upper) and diastolic (middle)  $[Ca^{2+}]$  and frequency (lower) over the range of  $[Ca^{2+}]$  studied in experiment. Black line represents modelled data and grey stars are taken from experiment. SERCA  $V_{max}$ ,  $K_D$  and RyR peak permeability were modulated to fit values found experimentally.

Figure 5-14 shows results from simulations in the 300 to 900nM  $[Ca^{2+}]_{bath}$  range.

Generally, systolic (peak)  $[Ca^{2+}]$  increased in over the range, with increments

getting larger as  $[Ca^{2+}]_{bath}$  was raised. Diastolic  $[Ca^{2+}]$  increased in a more linear

fashion, as  $[Ca^{2+}]_{bath}$  increased. Frequency increased dramatically over the range, showing signs of levelling off at the higher  $[Ca^{2+}]_{bath}$ . In general, the model replicated experimental behaviour.

Certain aspects of the experimental data were not accurately predicted by the model. The values of mean systolic (peak) and diastolic  $[Ca^{2+}]$  were higher in experiment than those predicted by the model. The systolic (peak)  $[Ca^{2+}]$  increased in a more non-linear fashion than the model. At 900 nM  $[Ca^{2+}]_{bath}$ , systolic (peak)  $[Ca^{2+}]$  was ~400nM higher than predicted by the model.

Diastolic  $[Ca^{2+}]$  was accurately predicted in the 300 to 600 nM range, but the model underestimated the diastolic  $[Ca^{2+}]$  from experiment at 900 by ~30 nM. This however is well within the range of experimental variability, with several cells having diastolic  $[Ca^{2+}]$  below 240nM at the higher  $[Ca^{2+}]_{bath}$ .

The frequency predicted the 300 and 900 nM experimental values well, but failed to replicate the 600nM  $[Ca^{2+}]_{bath}$  value. The  $[Ca^{2+}]_{bath}$ -frequency relationship was more linear than that observed experimentally.

The graph below shows results of modelling the  $Ca^{2+}$  range with SERCA  $V_{max}$  and  $K_D$  fixed at the values found experimentally at 300 and 900 nM  $[Ca^{2+}]_{bath}$ . Results of the modulated  $V_{max}$  and  $K_D$  are superimposed for comparison.

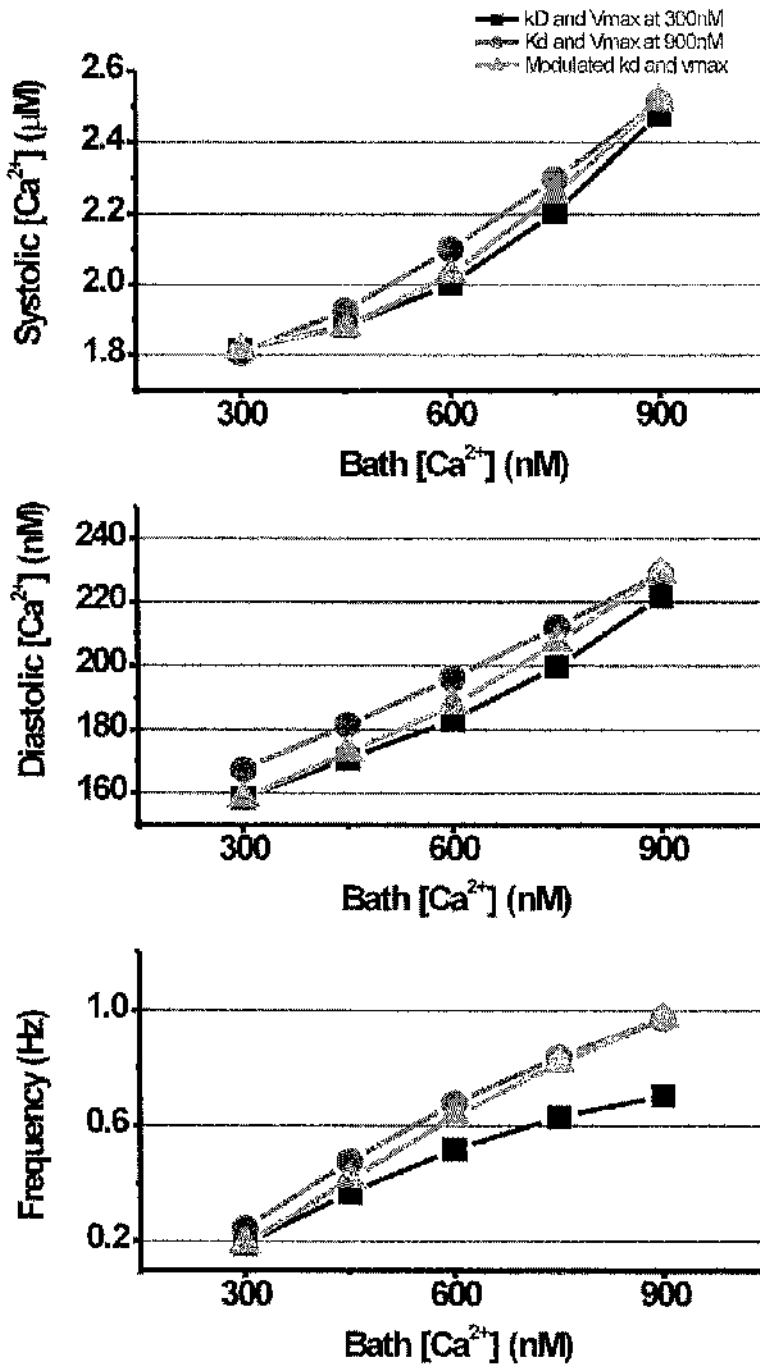


**Figure 5-15** Graph showing simulation results when SERCA  $K_D$  and  $V_{max}$  are changed to the values found experimentally at 300 and 900 nM  $[Ca^{2+}]_{bath}$ . A plot of simulation results when  $V_{max}$  and  $K_D$  are modulated depending on  $[Ca^{2+}]_{bath}$  is also plotted (light grey triangles) for comparison. Changes in model simulated systolic (upper), diastolic (middle) and frequency (lower) results are plotted.

The figure shows the relationship between the three parameters with increasing  $[Ca^{2+}]_{bath}$ , with  $V_{max}$  and  $K_D$  fixed at the values found experimentally at 300 and 900 nM and with a graded modulation based on  $[Ca^{2+}]_{bath}$ .

When the simulation was run with  $V_{max}$  and  $K_D$  set to the 300nM values ( $K_D = 234nM$ ,  $V_{max} = 170\mu m$ ), only slight decreases in systolic (peak) and diastolic  $[Ca^{2+}]$  were observed. The frequency at 900nM only reached 0.70 Hz, as opposed to the 0.97 Hz of the modulated model. This implies that a higher  $V_{max}$  and  $K_D$  is required to replicate the frequency.

When the simulation was run with  $V_{max}$  and  $K_D$  set to the 900nM values, ( $K_D = 349nM$ ,  $V_{max} = 390\mu m$ ), the systolic (peak)- $[Ca^{2+}]_{bath}$  relationship became more linear, with elevated values in the 450-750nM range. Diastolic  $[Ca^{2+}]$  was also more linear and marginally higher, when  $[Ca^{2+}]_{bath}$  was below 900 nM. Changes in frequency were not as marked, although the gap between the modulated plot and that with the 900nM SERCA parameters became more marked at lower  $[Ca^{2+}]_{bath}$ .

### **5.5.2 The effects of tetracaine on parameters of spontaneous waves.**

Previous studies have examined the effects of tetracaine on spontaneous  $Ca^{2+}$  release and interpreted the data in terms of increased threshold for the triggering of  $Ca^{2+}$  release from the SR.

The apparent change in threshold found on application of tetracaine was quantified in the previous chapter. This threshold was used to simulate the effects of tetracaine on parameters of  $Ca^{2+}$  waves. The modelled results are presented below.

### 5.5.2.1 Does the model mimic the behaviour of application and removal of tetracaine?

It has been found experimentally that on application of tetracaine, a quiescent period occurred, before resumption of lower frequency, higher amplitude  $\text{Ca}^{2+}$  waves. When the inhibitor was removed, a “burst” of spontaneous release occurred, followed by a return of  $\text{Ca}^{2+}$  wave frequency and amplitude to control levels. This application and removal of inhibition was simulated in the model, with the following result.

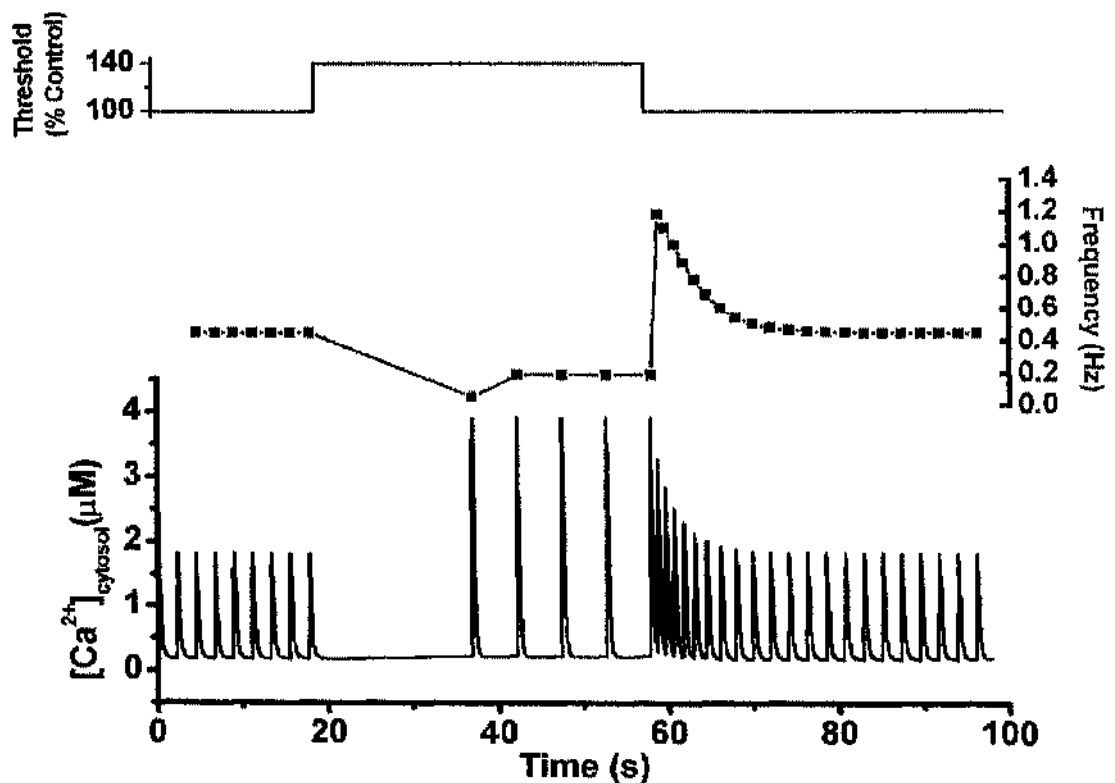


**Figure 5-16** Plot showing changes in cytosolic  $[\text{Ca}^{2+}]$  and frequency when threshold is suddenly increased, then decreased.

This mimics the effects of application and removal of tetracaine on SR release threshold.

Figure 5-16 shows the ability of the model to replicate the phenomena of refractory period and bursting of spontaneous release. Seclusion of release lasted for ~20s after threshold was changed, after which frequency dropped from 0.45 to 0.19 Hz.

This decrease in frequency was accompanied by an increase in amplitude, which was seen to double. On return of threshold to control levels, frequency was initially elevated to 1.2 Hz, with a gradual return to control frequency after 26 seconds. The gradual decrease in frequency was observed with a concomitant decrease in amplitude.

#### 5.5.2.2 Steady state behaviour of increasing threshold

As described above,  $\text{Ca}^{2+}$  wave frequency decreased and amplitude increased on application of tetracaine. The steady state results of the model are plotted below. All of these were taken when equilibration had been achieved. Experimental results are superimposed for comparison.

All simulations were run at  $600 \text{ nM } [\text{Ca}^{2+}]_{\text{bath}}$  and results are expressed as % control (i.e. without tetracaine).

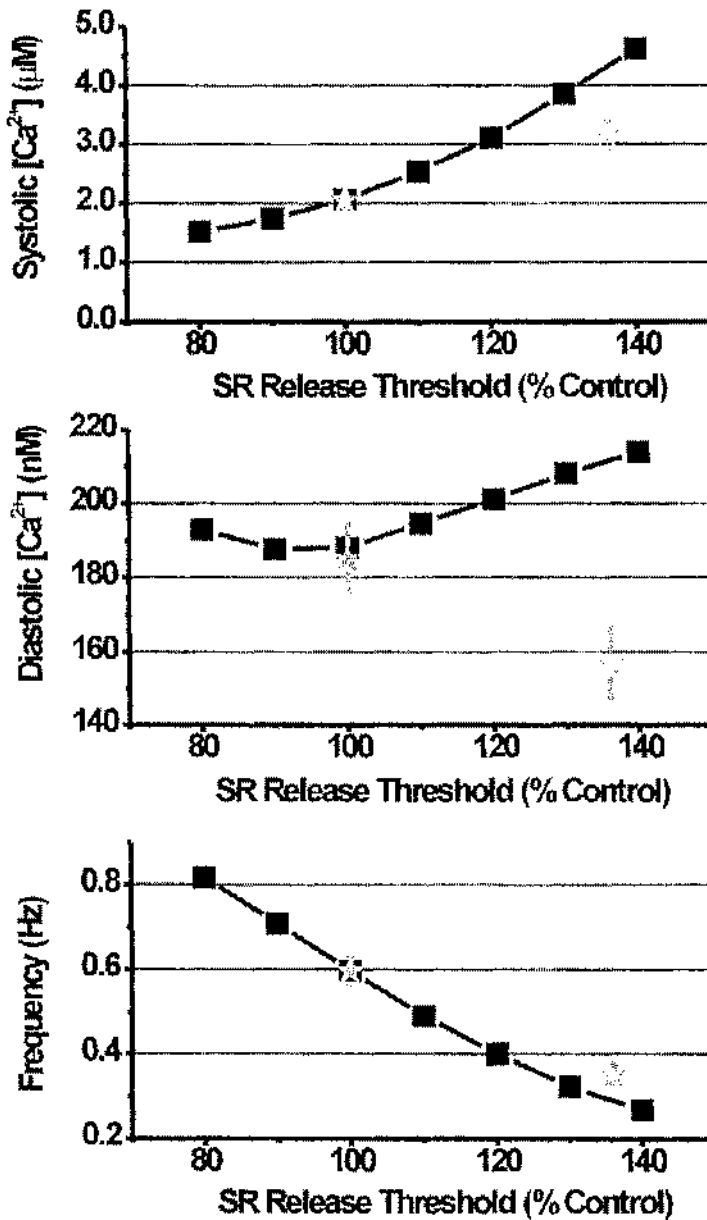


Figure 5-17 Effect of modulating SR release threshold in model to mimic effect on tetracaine ( $50\mu M$ ) on 3 parameters of  $Ca^{2+}$  waves.

Both simulations and experimental data were acquired at  $600nM [Ca^{2+}]_{bath}$ . Grey stars represent mean experimental data with no tetracaine (closed star) and with tetracaine (open star). Error bars indicate S.E.M.

Generally, systolic (peak)  $[Ca^{2+}]$  increased when SR release threshold was increased. Diastolic  $[Ca^{2+}]$  also increased with increasing SR release threshold, but as release threshold was increased further, diastolic  $[Ca^{2+}]$  began to increase again.

Frequency was shown to decrease with increasing release threshold, showing signs of levelling off above 120% control levels. Systolic (peak)  $[Ca^{2+}]$  in the experiment increased, but not to the same extent as predicted by the simulated data. Diastolic  $Ca^{2+}$  in experiment decreased with increased threshold, whilst the model predicted an increase. Frequency was shown to decreased to a similar level as predicted by the model. Experimentally, this fell to 0.351 in the presence of tetracaine (50 $\mu$ M). In the model this fell to 0.291.

### **5.5.3 The effects of TBQ on parameters of spontaneous waves.**

As discussed in Chapter 4, TBQ is a known inhibitor of SERCA and was used to examine the effects of lowered SERCA activity on the Ca wave characteristics. Analysis of the experimental data suggested that TBQ effects were more complex than simply reduced SERCA activity. It appeared that the presence of TBQ decreased SR release threshold by 20% and reduce SERCA  $V_{max}$  by 30% (see section 4.3.3). SERCA  $K_D$  remained unchanged by TBQ. An attempt to replicate these results was carried out using the model.

#### **5.5.3.1 Model behaviour with short-term decreases in $V_{max}$ .**

Generally, the effect of lowering  $V_{max}$  on wave frequency equilibrated after one release cycle. Note: no change in threshold was included in this simulation. The model predicted a reduced wave frequency and a small increase in amplitude.

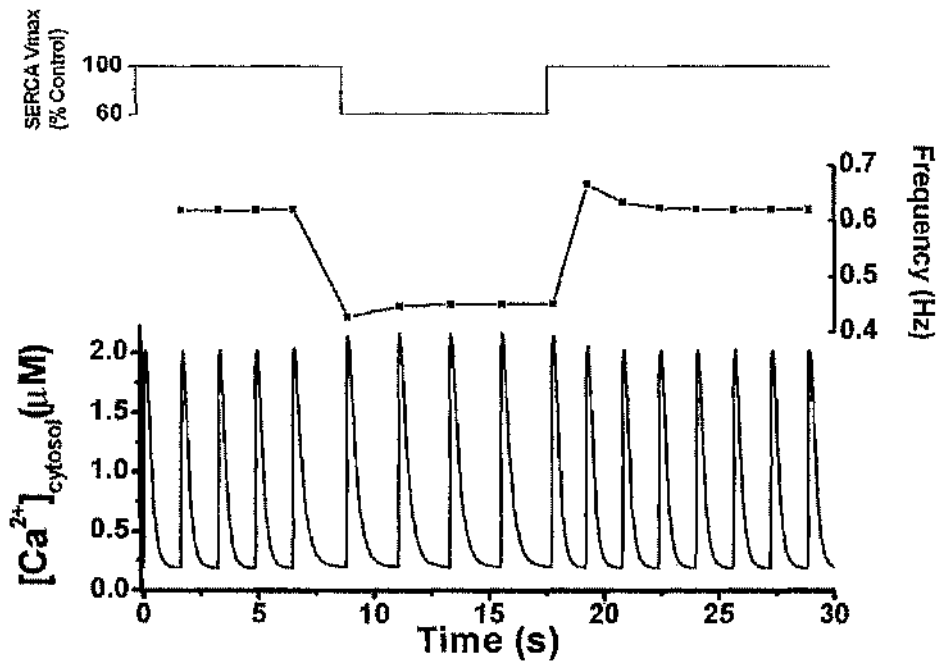


**Figure 5-18** An example of changes observed when  $V_{max}$  is transiently lowered by 40% in the  $Ca^{2+}$  release model.

#### 5.5.3.2 Does the model mimic steady state behaviour of TBQ application?

The results of the simulations used to model the changes observed on application of TBQ are shown in the figure below.

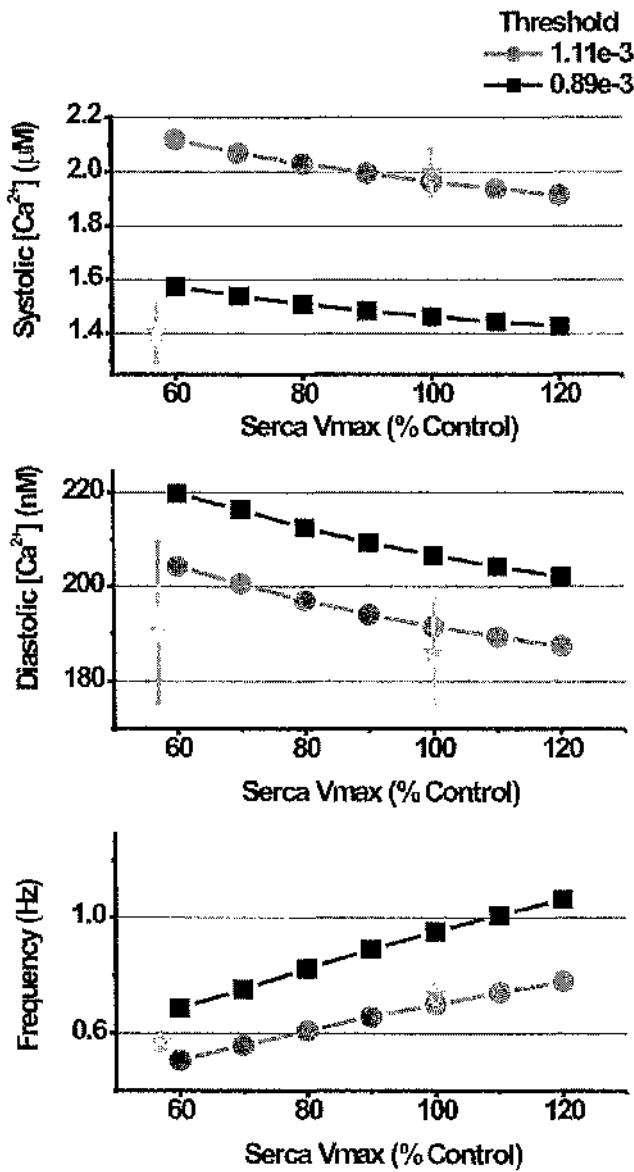


**Figure 5-19** Effect of modulating SERCA Vmax in model to mimic effect on TBQ ( $1\mu\text{M}$ ) on 3 parameters of  $\text{Ca}^{2+}$  waves. Grey stars represent mean experimental data with no tetracaine (closed star) and with tetracaine (open star). Error bars indicate S.E.M.,

The figure shows modelled and experimental data for comparison. The model was run using a range of values of Vmax. As shown in section 4.3.3, systolic (peak)  $[\text{Ca}^{2+}]$  decreased in TBQ. In order to accommodate these changes, SR  $\text{Ca}^{2+}$  release

threshold was lowered to the same extent and results were recorded over the same range of  $V_{max}$  values.

Generally, with a 40% decrease in SERCA  $V_{max}$ , but no decrease in threshold, the model predicted a modest increase in systolic (peak)  $[Ca^{2+}]$ , an increase in diastolic  $Ca^{2+}$  and a modest decrease in frequency (Figure 5-11). Frequency and diastolic  $[Ca^{2+}]$  were in fair agreement with the modelled data in this situation. The decreased systolic (peak)  $[Ca^{2+}]$  from experiment was not replicated with decreased  $V_{max}$  alone.

When the model was run with the lower threshold for release and a 40% reduction in  $V_{max}$ , the systolic (peak)  $Ca^{2+}$  was in better agreement with the experiment, predicting  $1.57\mu M$ , compared to  $1.40 \pm 0.1 \mu M$ . Diastolic  $[Ca^{2+}]$  increased to 192 nM in experiment, after TBQ application. The model rose to 220nM, 15% higher than found experimentally. Error bars on the experimental data indicate experimental variation is high in this parameter. This may be the reason for these differences.

The frequency change observed in experiment was in agreement with the model when only  $V_{max}$  was changed to mimic TBQ. Decreasing the threshold as well caused the model to have an increased frequency. This was 0.68 Hz in the model as compared to the 0.57 Hz value seen experimentally.

## 5.6 Discussion

### 5.6.1 The effects of changing $[Ca^{2+}]_{bath}$ .

The model was capable of predicting most of the general trends of increasing bath  $Ca^{2+}$ . Increasing SERCA  $V_{max}$  and  $K_D$  allowed the model to give reasonable predictions of experimental results over the range of  $[Ca^{2+}]_{bath}$  studied.

Figure 5-15 demonstrates the bath  $\text{Ca}^{2+}$  shows frequency is the most sensitive parameter to these SERCA modulations. The parameters of SERCA at 300nM do not allow prediction of the higher frequencies observed as bath  $\text{Ca}^{2+}$  is raised towards 900nM (~40% lower). Similarly, using the 900nM SERCA parameters caused an overestimation (~30% higher) of the frequency at 300nM. This effect was less obvious in estimation of systolic (peak) and diastolic (min)  $[\text{Ca}^{2+}]$ .

As described in the previous results chapter, the changes in SERCA  $K_D$  and  $V_{\max}$  could be due to phosphorylation mediated changes. CaMKII has also been shown to have effects on the RyR. This could modulate RyR mediated leak in a  $\text{Ca}^{2+}$  /frequency dependent manner. This would have knock-on effects for the measurements of SERCA in this study and hence would affect model behaviour. Further quantification of leak is required before these effects can be assessed.

### 5.6.2 The effects of tetracaine

The primary effect of tetracaine was to inhibit the RyR, increasing the threshold for propagated  $\text{Ca}^{2+}$  release. This was mimicked by increasing the SR release threshold in the model by 36%. It was found that the model replicated the phenomena of application and removal seen experimentally. A quiescent period was observed on application, as well as a period of high frequency waves on removal. The reason for the initial quiescent period was that, when the  $\text{Ca}^{2+}$  wave emptied the SR, the period when SERCA was maximal was relatively short. This allowed SR filling to occur to the level seen at the control threshold.  $[\text{Ca}^{2+}]_i$  then falls to diastolic levels, where uptake would take place at a much lower rate. The 40% of  $[\text{Ca}^{2+}]_{\text{SR}}$  remaining to be filled will do so at a much lower rate, so a prolonged period will be required before threshold is reached. The subsequent

release will be much larger, and cytosolic  $\text{Ca}^{2+}$  will be elevated for a greater period, facilitating more rapid filling, thus the interwave-period will increase. Thus it can be said that the interwave-period is a function of SR threshold and SERCA flux. The bursting phenomenon can be explained through changes in threshold, non-linear buffering. The length of time taken to return to control levels is due to diffusion of  $\text{Ca}^{2+}$  when  $[\text{Ca}^{2+}]$  is above  $[\text{Ca}^{2+}]_{\text{bath}}$ . If the SR release threshold was changed just as the release had initiated, the SR would empty, elevating cytosolic  $\text{Ca}^{2+}$  and activating SERCA uptake to be maximal for a prolonged period (as explained above). The SR will then reach its threshold level before cytosolic  $\text{Ca}^{2+}$  has returned to diastolic levels. When the next release occurs, it will be from an initially higher level, thus the release will be into a region further up the buffer curve (see Figure 4-7) and so the smaller release will cause systolic (peak)  $\text{Ca}^{2+}$  to be raised to slightly below that of the previous release. This will continue until diastolic and  $\text{Ca}^{2+}$  is allowed to fall to control levels. This fall is facilitated by  $\text{Ca}^{2+}$  diffusion out of the cell.

In the steady state, raising SR release threshold by 40% caused increases in systolic (peak)  $[\text{Ca}^{2+}]$  and diastolic (min)  $[\text{Ca}^{2+}]$ , whilst wave frequency decreased.

The decrease in frequency predicted by the model was comparable, if slightly below that found experimentally. Increases in systolic (peak) were observed in both model and experiment, although the model underestimated the mean experimental value. Most stark differences were found in diastolic  $[\text{Ca}^{2+}]$ , with the model predicting a slight increase, contrasting the significant decrease found experimentally.

This difference highlights a possibly crucial inaccuracy in the model. As described in the previous chapter, diastolic  $\text{Ca}^{2+}$  has been previously shown to fall on

application of tetracaine (1mM) (Shannon *et al.*, 2002). It was proposed, the fall was as a consequence of decreased RyR mediated leak. The leak constant value ( $k$ ) used in the model was taken from previous estimations and fitted with the forward and reverse model of SERCA (Shannon *et al.*, 2000). This value originated from measurements carried out on myocytes where the SR was depleted of  $\text{Ca}^{2+}$ . A more recent measurement by the same group described much higher values of leak  $k$ . This theory is still controversial, but basically describes a nonlinear leak  $k$ , which increases as SR  $[\text{Ca}^{2+}]$  increases (Shannon *et al.*, 2002). This was proposed to be mediated by increases in  $\text{Ca}^{2+}$  spark activity. It is possible that if this sparking activity were to be inhibited, diastolic  $\text{Ca}^{2+}$  spark activity would be inhibited, thus decreasing diastolic  $[\text{Ca}^{2+}]$ . This theory can be tested using the existing model. Since the leak value was possibly underestimated, the effect of raising the value was investigated. The figure below illustrates the result.

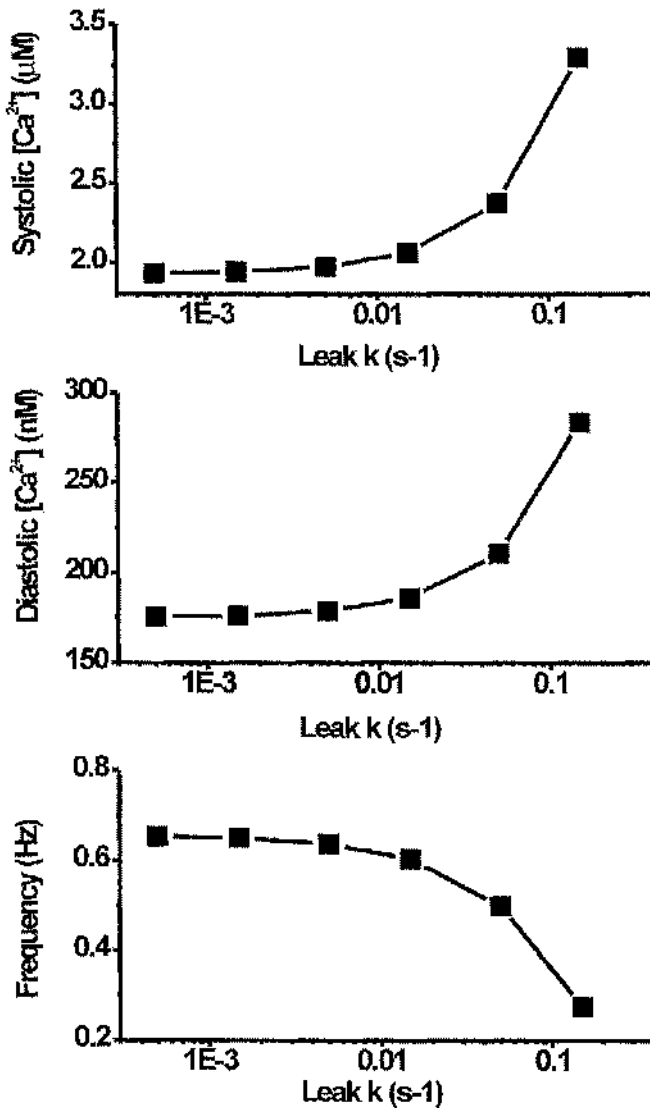
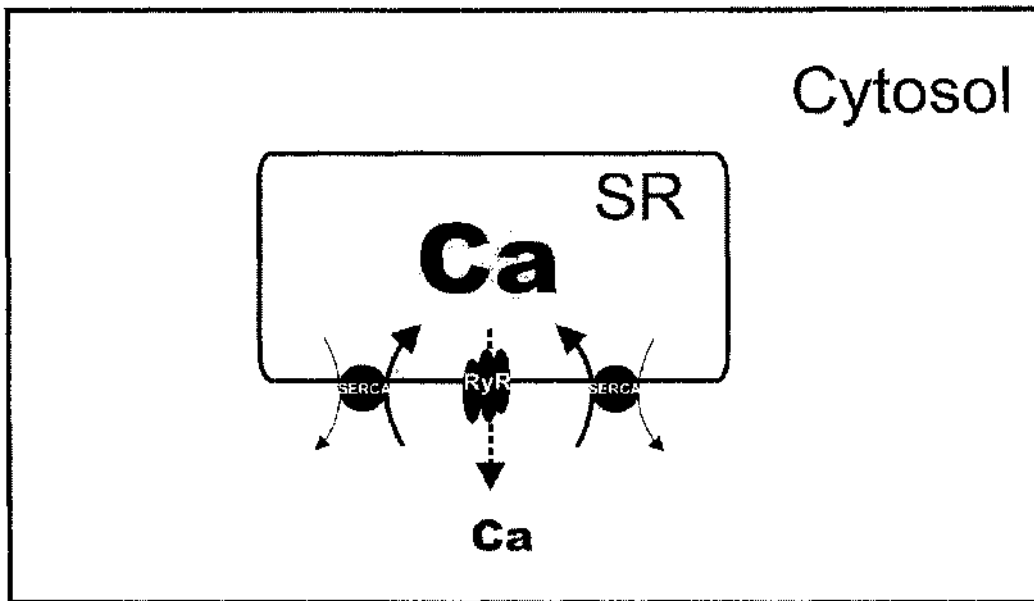


Figure 5-20 Plots of changes in wave systolic (peak)  $Ca^{2+}$ , diastolic (min)  $Ca^{2+}$  and frequency with increases in leak k in the model.

No obvious effects of leak k on model results were observed in any of the parameters until leak k was raised above  $0.005 \text{ s}^{-1}$ . Both systolic (peak) and diastolic (min)  $[Ca^{2+}]$  were increased with higher leak k, whilst frequency was decreased.

The effect of leak on  $Ca^{2+}$  uptake and hence diastolic  $Ca^{2+}$  is discussed below.



**Figure 5-21** Diagram of  $\text{Ca}^{2+}$  leak effects on  $\text{Ca}^{2+}$  uptake.

The diagram above describes how leak and uptake interact. RyR mediated SR leak works to short-circuit SERCA  $\text{Ca}^{2+}$  uptake. This effect would become more evident as  $[\text{Ca}^{2+}]_{\text{SR}}$  and hence the trans-SR concentration gradient increased. As the SR filled, SERCA would become less effective at resequestering  $\text{Ca}^{2+}$  from the cytosol.

This process would increase refilling time and reduce SERCA's ability to lower diastolic  $[\text{Ca}^{2+}]$ , hence the lower frequency and increased diastolic (min)  $[\text{Ca}^{2+}]$  seen in Figure 5-20. The higher systolic (peak)  $[\text{Ca}^{2+}]$  is explained by the buffer curve principle described in Figure 4-7.

In order to cause the  $\sim 30\text{nM}$  change in diastolic  $\text{Ca}^{2+}$  observed experimentally, using the diastolic-leak relationship of Figure 5-20, it could be postulated that leak is actually  $\sim 100$  times greater than initially proposed.

If the model were modified to include this much higher leak rate, it may predict the behaviour seen experimentally. Increasing SR content and decreasing RyR leak  $k$  would be used to simulate tetracaine application.

Leak was not measured in this study, but could be measured using methods similar those of the (Bassani & Bers, 1995) study, but using permeabilised cells.

Thapsigargin (25 $\mu$ M) could be applied to cells perfused with a solution containing  $\sim$ 200 nM  $[Ca^{2+}]_i$ . This is just below the threshold for  $Ca^{2+}$  waves.  $[Ca^{2+}]_{SR}$  could be assessed using rapid application of caffeine (10mM) at 2-minute intervals, to assess the time dependence of the depletion. This could then be used to back calculate a leak  $k$  at each time point. The effect of agents which change SR content or RyR sensitivity, such as TBQ and tetracaine on this leak could also be assessed.

If the leak flux was discovered to be higher, reanalysis of data would be necessary to reassess SERCA  $K_D$  and  $V_{max}$ . Figure 5-15 shows the effect of increasing leak  $k$  on SERCA  $V_{max}$  and  $K_D$  quantified using the CellFlux analysis program.

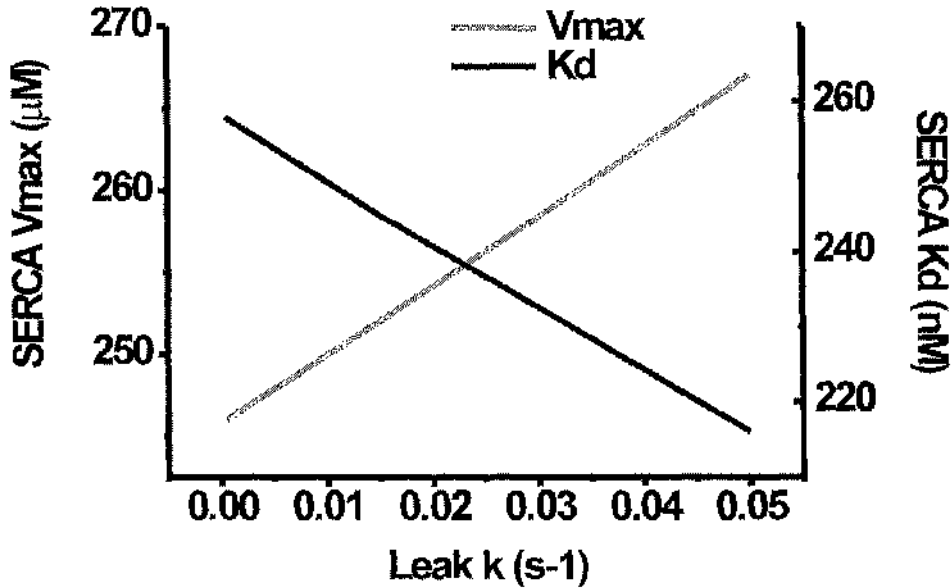


Figure 5-22 Effect of varying leak  $k$  parameter in estimation of  $V_{max}$  and  $K_D$  using the CellFlux program.

Linear increases are observed in fitted SERCA  $V_{max}$  (since leak is subtracted from the net SR flux before  $V_{max}$  is calculated). Linear decreases in  $K_D$  are also observed. If leak  $k$  was assessed to be higher than that previously reported by Shannon et al, large changes in derived SERCA  $V_{max}$  and  $K_D$  would be required. Since the model was previously shown to be sensitive to changes in  $V_{max}$  and  $K_D$  (section 5.4.3), this would cause large changes in model behaviour.

If a subsequent measure of leak  $k$  is found to be higher than that used in this study, all experimentally derived values of SERCA  $V_{max}$  and  $K_D$  could be affected. This may explain some of the changes in SERCA observed in section 4.3.1.

An attempt to model the hypothetical changes in leak  $k$  and adjusted SERCA  $K_D$  and  $V_{max}$ , which might occur during application of tetracaine is shown below.

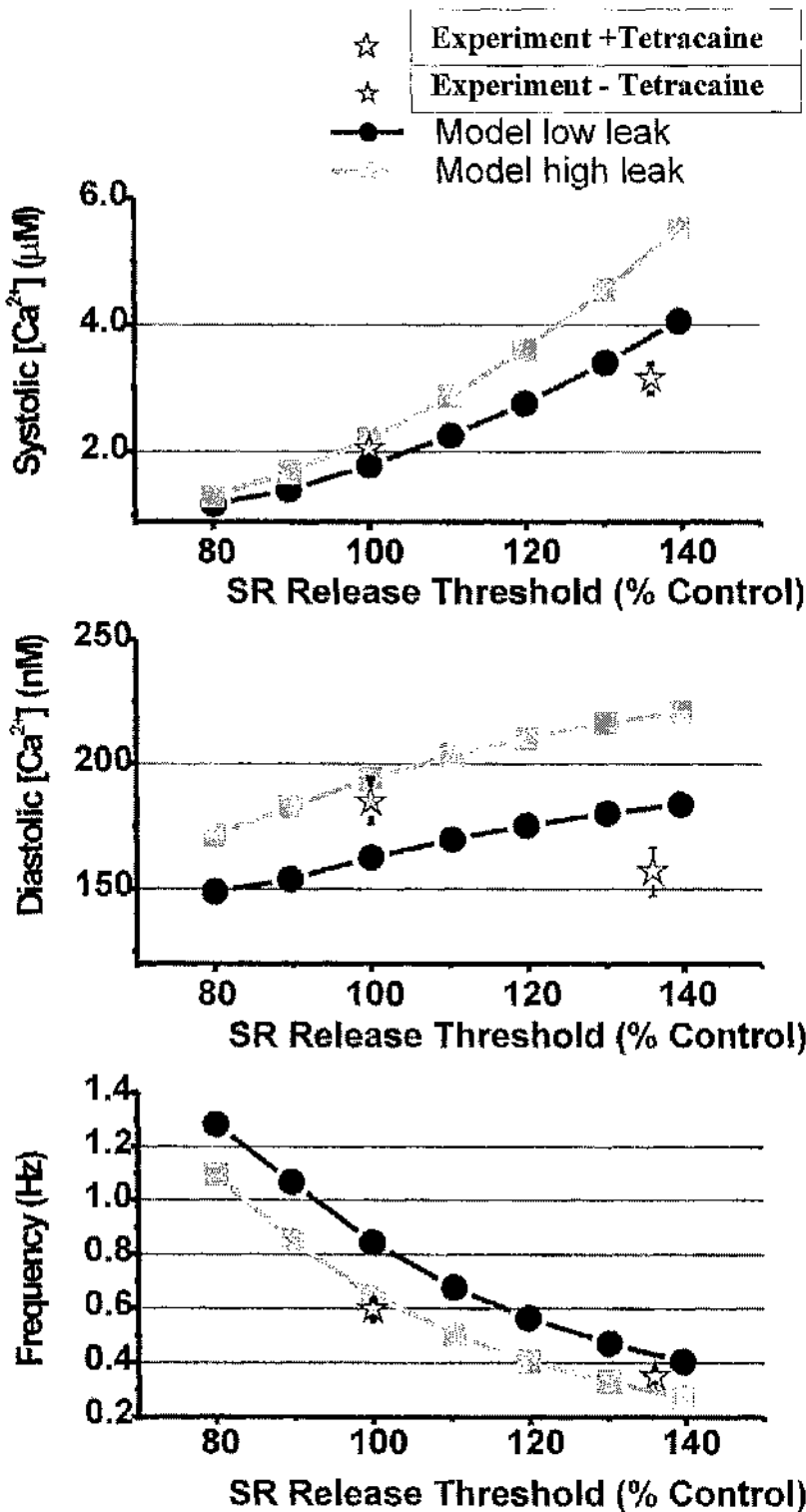


Figure 5-23 Hypothetical simulation of tetracaine's effect on SR leak and threshold. Modelled results of systolic (peak), diastolic (min) and frequency are shown with experimental results over a range of threshold values superimposed.

The grey line in Figure 5-23, depicts modelled results with a high leak  $k$  value ( $0.12\text{s}^{-1}$ ) and compensatory adjustments in SERCA  $V_{\text{max}}$  and  $K_{\text{D}}$ . At the control value (100%), the model adequately predicts all three parameters. The black line mimics the effect of threshold changes on parameters of  $\text{Ca}^{2+}$  waves when leak is inhibited. When leak  $k$  is reduced in the model (as shown by the black line in the figure), to mimic the hypothesised effect of tetracaine on RyR mediated leak, diastolic (min) and systolic (max) values are reduced, but remain higher than the results of the experimental study. This indicates leak may currently be incorrectly represented in the model.

### 5.6.3 The effects of TBQ

The effect of TBQ on SERCA was quantified in the previous chapter as a 43% reduction in activity, with no significant effect on affinity. This decrease in SERCA activity was found to be accompanied by a reduced threshold for propagated release. These combined effects resulted in a decrease in systolic (peak)  $\text{Ca}^{2+}$ , no change in diastolic  $\text{Ca}^{2+}$  and caused frequency to decrease.

The model was run for both control and TBQ threshold for a range of SERCA  $V_{\text{max}}$ 's. The decreased threshold yielded a better prediction of systolic (peak)  $[\text{Ca}^{2+}]$  with a 40% reduction in  $V_{\text{max}}$ , but predicted diastolic (min) and frequency less effectively.

#### 5.6.3.1 Model prediction of diastolic $\text{Ca}^{2+}$

The model predicted diastolic  $[\text{Ca}^{2+}]$  to increase, when SR release threshold and SERCA  $V_{\text{max}}$  were decreased to mimic experimental values. The model's overestimation in diastolic  $[\text{Ca}^{2+}]$  may be due to an inadequate description of leak (see page 177 and 178 for effects). Inclusion of this modified leak would lower leak flux, due to the lower SR content. This would decrease diastolic  $\text{Ca}^{2+}$  as a

lower SR content would create a lower leak flux and may serve to lower diastolic  $\text{Ca}^{2+}$  to the levels seen experimentally. The lower uptake coupled with the lower leak flux would have the net effect of keeping diastolic  $[\text{Ca}^{2+}]$  the same.

#### 5.6.3.2 Model prediction of frequency

The model predicted a frequency slightly above observed experimentally. If the leak were modelled as described above, SERCA would be more effective at filling the SR and frequency would increase. This increased frequency would allow better prediction of experimental results.

**Chapter 6**  
**General Discussion**

The primary aim of this study was to discover the magnitude and time course of the fluxes involved in the  $\text{Ca}^{2+}$  wave and reconstitute these into a model, which may be used to predict experimental results.

This thesis presents the development of experimental methods and analysis programs, which allow quantification of the inter-compartmental fluxes and their time-course within the  $\text{Ca}^{2+}$  wave. These methods allowed the  $\text{Ca}^{2+}$  wave to be used as a tool for investigating the  $\text{Ca}^{2+}$  sensitivity of the release and uptake process that control intracellular  $[\text{Ca}^{2+}]$  in heart muscle.

These methods yielded some new experimental results, providing insight into the events underlying the  $\text{Ca}^{2+}$  wave release event.

No significant difference was found between the initial  $\text{Ca}^{2+}$  efflux induced by application of caffeine and the initial  $\text{Ca}^{2+}$  released during a  $\text{Ca}^{2+}$  wave. This is in contrast to previous results (Overend *et al.*, 1997; Smith & O'Neill, 2001) and suggests that depletion is a factor in termination of  $\text{Ca}^{2+}$  release during a wave.

$\text{Ca}^{2+}$  waves were studied over a range of  $[\text{Ca}^{2+}]_{\text{bath}}$ . Interestingly,  $[\text{Ca}^{2+}]_{\text{SR}}$  was found not to change as  $[\text{Ca}^{2+}]_{\text{bath}}$  was raised from ~300 to 900 nM. This was unexpected, as  $\text{Ca}^{2+}$  wave amplitude increased over this range. The increase in amplitude was the consequence of the non-linear intrinsic cellular  $\text{Ca}^{2+}$  buffering system.

Non-linear relationships were found in wave frequency, minimum and maximum  $[\text{Ca}^{2+}]$ . This revises the linear relationships in these parameters found previously (Loughrey *et al.*, 2002). No evidence was found of the agonal or sporadic waves previously reported by the Kaneko *et al.* (2000) study at high intracellular  $[\text{Ca}^{2+}]$ .

SERCA  $K_D$  and  $V_{max}$  were both found to increase when  $[Ca^{2+}]_{bath}$  was raised.

This has not been reported before and suggests long-term control over the characteristics of SERCA by mean intracellular  $[Ca^{2+}]$ . More work is required to better quantify RyR mediated  $Ca^{2+}$  leak before firm conclusions can be drawn about these findings.

The effects of tetracaine on  $Ca^{2+}$  wave behaviour were also studied. Waves were found to increase in amplitude and decrease in frequency after application, agreeing with the results of previous studies (Gyorke *et al.*, 1997; Overend *et al.*, 1997; Smith & O'Neill, 2001). It was concluded that that this was primarily due to an increased threshold for propagated spontaneous release, subsequent to a desensitisation of the RyR.

The effect of SERCA inhibition on  $Ca^{2+}$  wave properties was also studied. This was accomplished by addition of TBQ. This had the effect of both reducing wave frequency and amplitude. The reduced amplitude was found to be due to a depletion of  $[Ca^{2+}]_{SR}$  release threshold. This reduction was more pronounced than that previously reported by the 2004 O'Neill *et al.* study, even though higher concentrations were used. This may have been due to the permeabilised cell preparation used in the present study. In agreement with the O'Neill study, a slight decrease in velocity was observed.

The construction of a viable 3-compartment model of spontaneous  $Ca^{2+}$  release was the primary aim of this thesis. The current model was able to accurately reproduce the changes in wave characteristics observed over the range of  $[Ca^{2+}]_{bath}$  studied. It was also able to predict the frequency changes observed when either tetracaine or TBQ were applied, but was less successful at predicting minimum  $[Ca^{2+}]_i$  between waves. The incomplete predictions of the model suggest that the actions of these

agents may be more complex than initially predicted. The model was then used to predict additional action of the drugs, which requires further experimentation to predict. The quiescent and bursting behaviour observed on application and removal of tetracaine were successfully reproduced by the model. This led to a better understanding of what causes these phenomena. It was concluded that the quiescent period was caused by the prolonged period of time when the SR needs to fill to the new release threshold, when cytosolic  $\text{Ca}^{2+}$  and hence SERCA uptake rate is at its lowest. The bursting effect is a phenomenon resulting from the non-linear  $\text{Ca}^{2+}$  buffering system into which the SR store releases.

Overall the modelling and experimental data have clarified many hypotheses surrounding the  $\text{Ca}^{2+}$  wave event. Further work will be needed to clarify some aspects of the model, such as better characterisation of the cytosolic and intra-SR buffering systems, as well as quantification of the RyR mediated SR  $\text{Ca}^{2+}$  leak.

Studies to characterise changes in  $\text{Ca}^{2+}$  velocity should be possible, if the model were expanded to include 2, or 3 spatial dimensions. This will hopefully be completed in the future.

**Chapter 7**  
**Appendices**

## Appendix A Description of WaveModel Program

### 7.1 Description of WaveModel Program

#### 7.1.1 Purpose of program

- To mimic fluxes involved in spontaneously active SR in cardio myocytes
- To display changes in  $[Ca^{2+}]$  in the cytosolic and SR compartments of the model.
- To allow importing of experimentally derived RyR flux profile from experiment
- To allow altering of parameters to observe changes in frequency and minimum and maximum cytosolic  $[Ca^{2+}]$ .

#### How to use:

#### 7.1.2 Setting up simulation variables.

Certain variables are set to default values. These are:  $Dx$  set to  $1 \times 10^{-5}$ , buffering parameters of EGTA, Fluo5, intrinsic cellular buffers (B1 & B2), and SR buffering (CSQ) are set to default values from published results. Leak is set to 0.00047 as described in the (Shannon *et al.*, 2000) paper.

$Ca^{2+}$  Bath is a value representing  $[Ca^{2+}]$  in the solution perfusing the permeabilised cell. This was limited to a range of 300 – 900 nM in all experiments. This could be increased if desired.

$[Ca^{2+}]$  Cyt (initial cytosolic  $[Ca^{2+}]$ ) should be in the 100 to 300 nM range.  $[Ca^{2+}]$  Lum (initial SR  $[Ca^{2+}]$ ) is reset to just below the value entered as a release threshold. This causes a release to occur just after the simulation is started. Free  $Ca^{2+}$  error is the value for the iterative method used to estimate free  $Ca^{2+}$ . This is

set to  $1 \times 10^{-12}$ . SERCA Hillf (the hill coefficient for SERCA) is normally set to 4.

Time taken is the time in seconds it has taken for the simulation to run.

The user can import SERCA parameters from a cell analysed by the “CellFlux” program by clicking “File..Load Sim Conditions” and selecting a file exported from the program, usually called “profilestats.dat”. SERCA  $V_{max}$ ,  $K_D$  and hill coefficient are set to that of the analysed cell.

SERCA and RyR profile maximum can be set to be modulated with  $[Ca^{2+}]$  bath by clicking the Yes box in the SERCA or RyR section of the modulated group.

The user can use the program to run one simulation, a batch of simulations over a range of one variable, or a batch of simulation over the ranges of two variables.

These batches record results and compartmental  $[Ca^{2+}]$  changes and output them to a specified folder. This is described below.

### **7.1.3 To run a single simulation**

Set up the simulation variables as desired.

Click “run single simulation” button.

The user is asked “Do you want to load RyR profile?”.

Click yes and browse to the file containing the RyR permeability profile from experiment.

The file is loaded and displayed in the “RyR Profile Loader” tab in red and a profile interpolated by the cubic spline method is calculated for each dx and displayed in blue (see Figure 7-2).

The simulation then begins and calculates  $[Ca^{2+}]$  in the SR and cytosol points for each dx. Points for every 0.002s are outputted to the grid at the bottom left of the window and graphs are plotted in the various tabs. A box is shown displaying the progress of the simulation.

The program makes a sound when the simulation is complete and the time taken for the simulation to run is shown in the parameter box labelled "time taken".

#### **7.1.4 To run a batch of simulations for a range of one variable**

Set up the variables as described above.

Select the simulation variable from the box labelled "Multi-Sim Mode".

Click the button labelled "Run Multiple Sims".

The user will be prompted to select the number of simulations to run in a batch "How many sims do you want to run?" is displayed. Enter the number required in the box provided.

A box appears, where the selected number of variables should be inputted.

Click "Ok" button when finished.

A directory browse box then appears and the user selects the folder where the simulation results should be outputted.

Click "Ok" button

The batch operation begins and a box appears displaying the simulation number running and its progress.

The data entered into the data sheet at the bottom left is exported to the folder as a .csv file for each simulation. Oscillation frequency, maximum and minimum  $Ca^{2+}$  are also exported as .txt files for each simulation.

### **7.1.5 To run a batch of simulations for a range of two variables**

The process is similar to that described above, only the user selects one of the variables in the multi-sim box and one of the variables in the multiple variable box, then clicks the “Run Multi for 2 vars” button.

The user then enters the number of simulations required for the variable entered in the “Multiple Variable” box and then enters the values required.

Then the user enters the number of simulations required for the variable entered in the “Multi-Sim Mode” box and then enters the values required.

The user then uses the supplied directory browse box to select a folder for the outputted files.

The simulation then begins and places folders labelled as selected multiple variable and its value.

The outputted files from the “multi-sim mode” variable are then placed in these folders.

### **7.1.6 Exploring the output**

Once a simulation is run, its outputted fluxes are displayed in graphs on the tabs within the program interface. These graphs can be examined after the program has stopped. These should look similar to outputs of Figure 7-3 to Figure 7-8. A zoom utility can be used to drag a box on all plots. This is accomplished by selecting the “on” in the Zoom mode box and dragging around the selection of interest.

The bounds of the zoomed selection then dictate the new bounds of the plot. This can be reversed by clicking the rescale to show all” button.

Results of frequency,  $[Ca^{2+}]$  max and min recorded from the last complete oscillation of the simulation are displayed in boxes on the “RyR profile loader tab”.

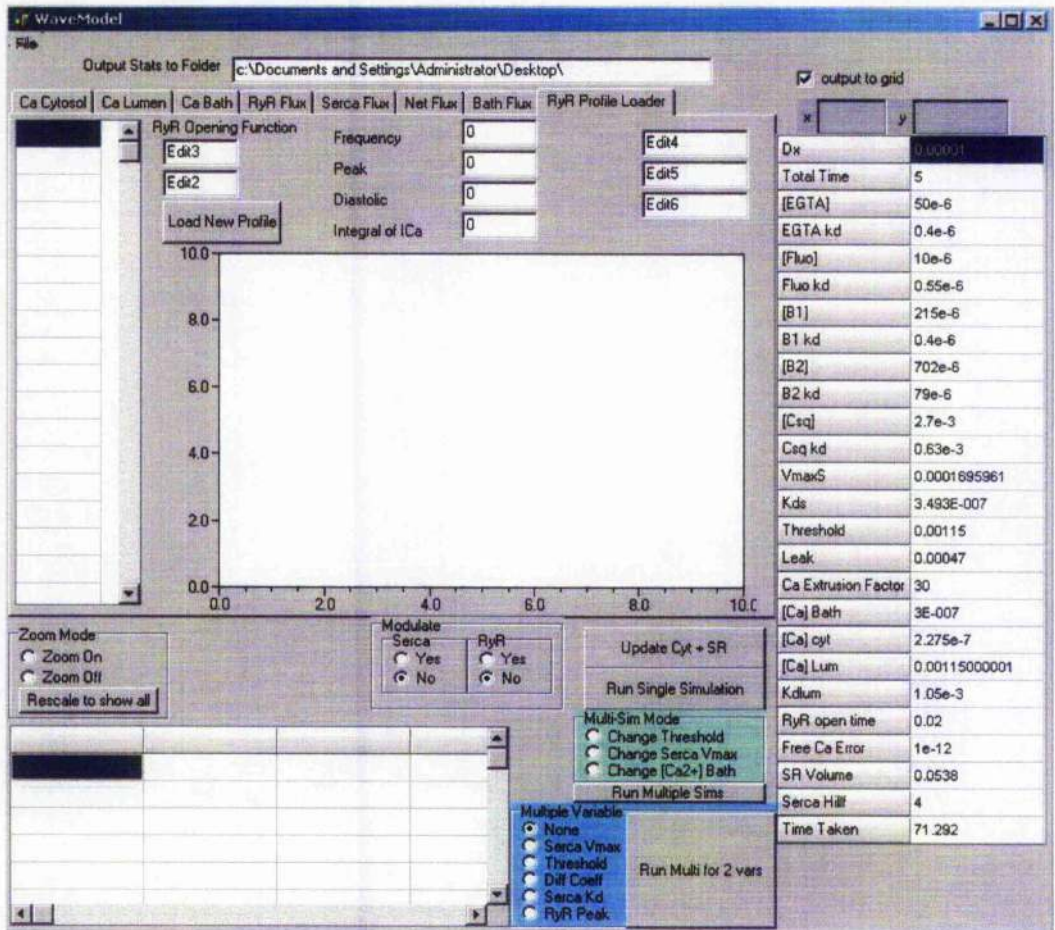


Figure 7-1 Screenshot of program when first initialised.

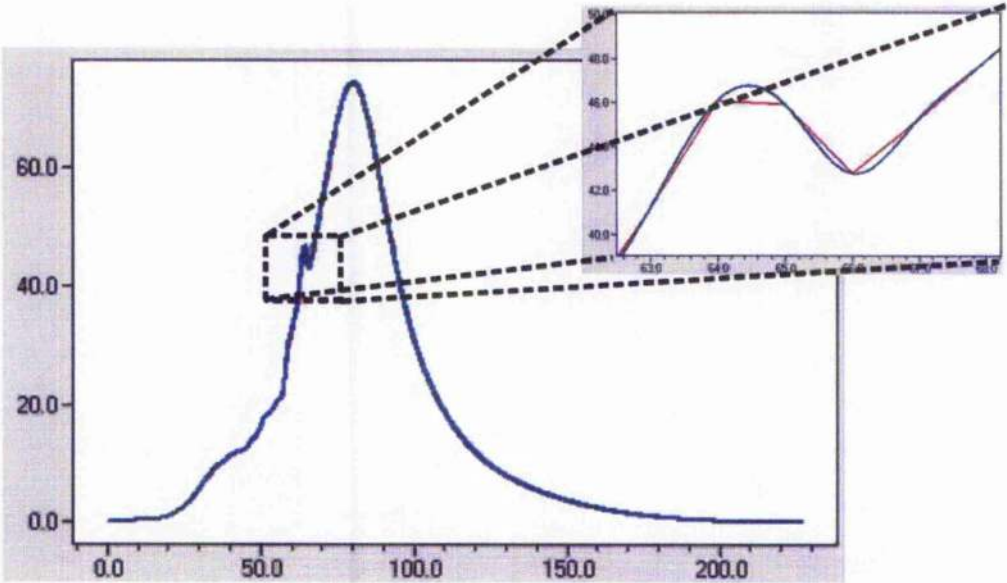


Figure 7-2 Screenshot showing imported RyR permeability profile (red) and cubic-interpolation of plot (blue).  
Zoomed section shows interpolated data in more detail.

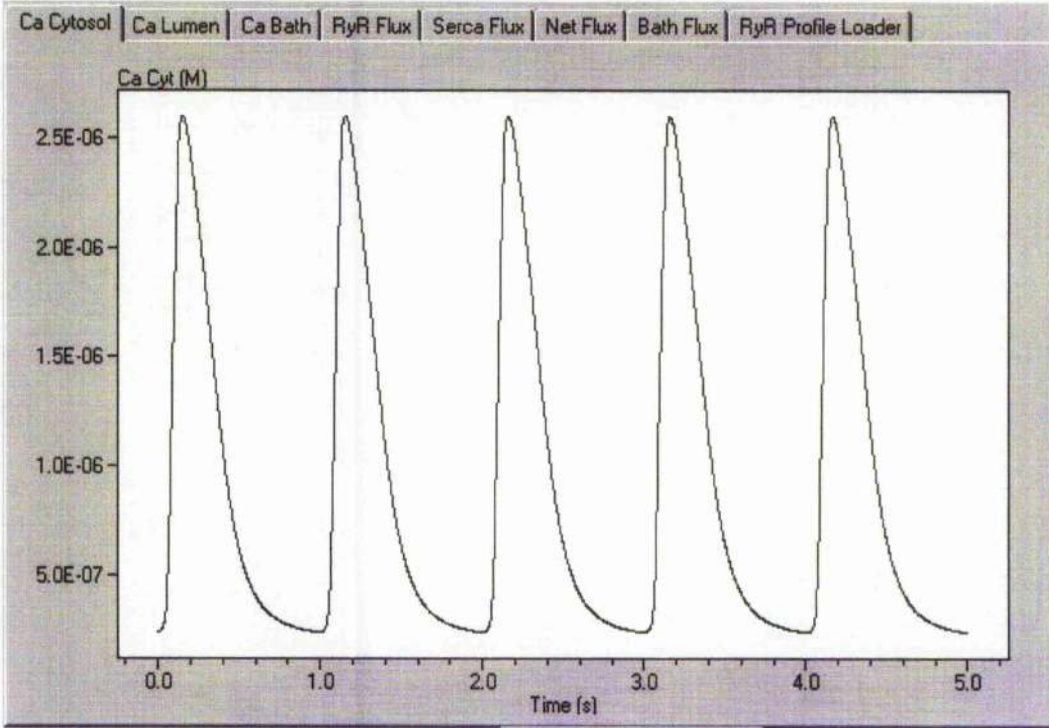


Figure 7-3 Screenshot of Ca Cytosol plot

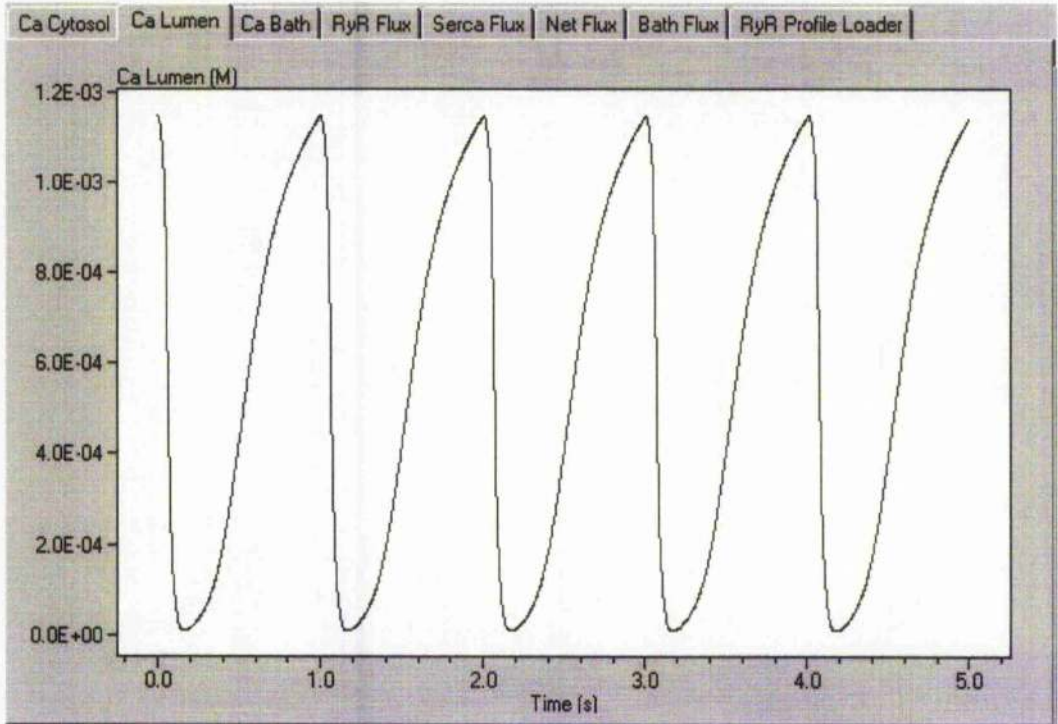


Figure 7-4 Screenshot of Ca Lumen plot (i.e. SR  $[Ca^{2+}]$ )

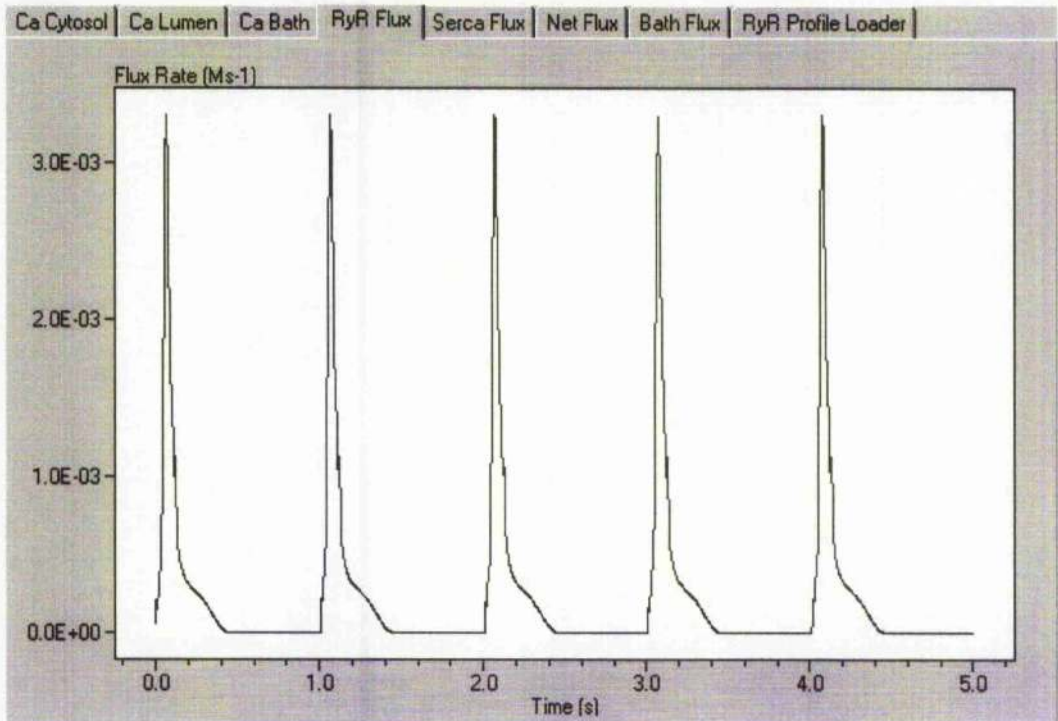


Figure 7-5 Screenshot of RyR flux plot

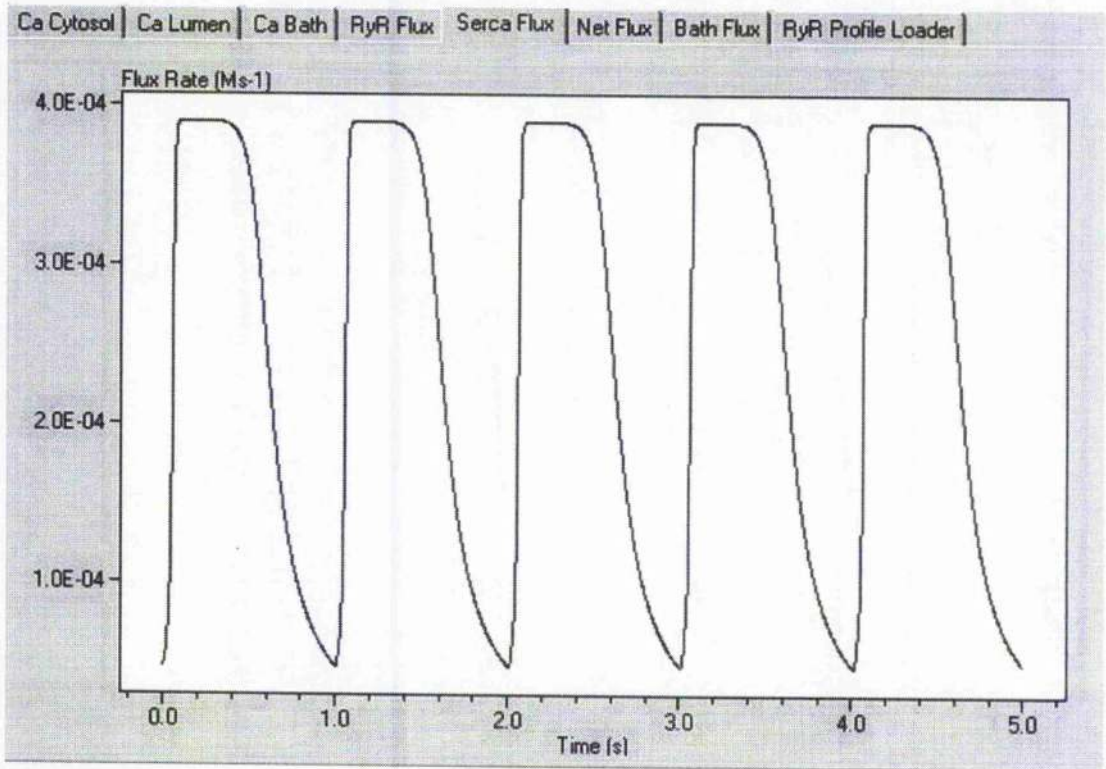


Figure 7-6 Screenshot of SERCA Flux plot

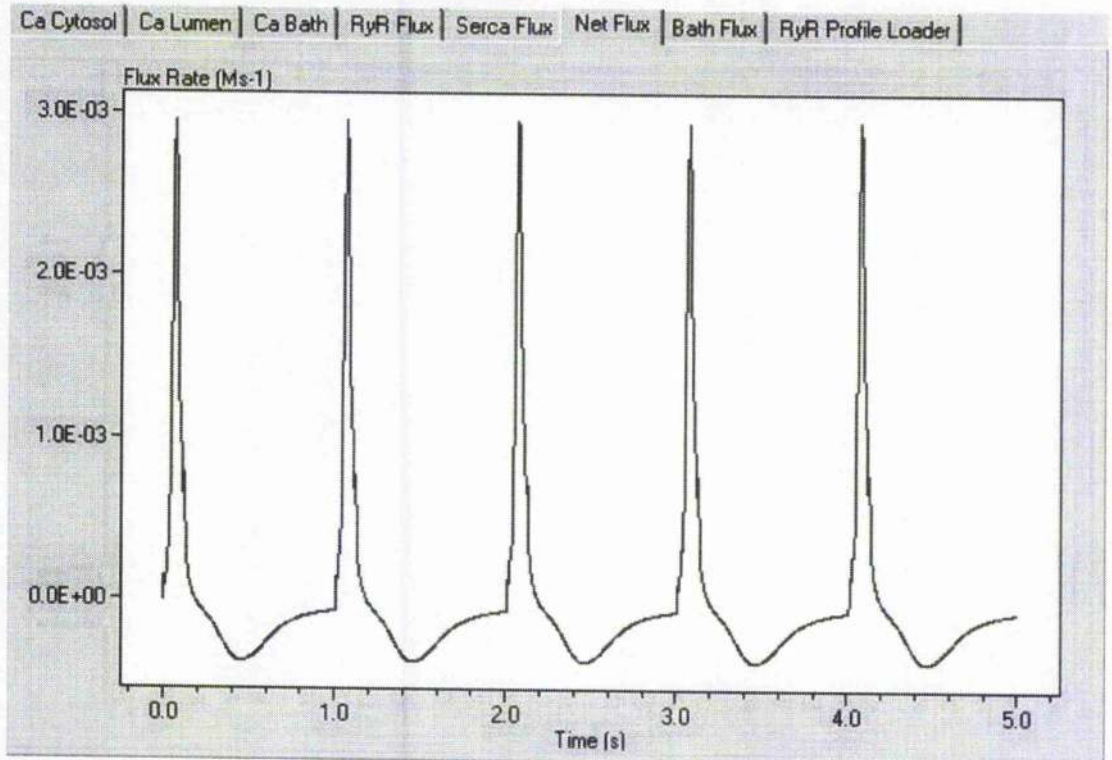


Figure 7-7 Screenshot of Net Flux plot (i.e.) net flux between SR and cytosol compartments.

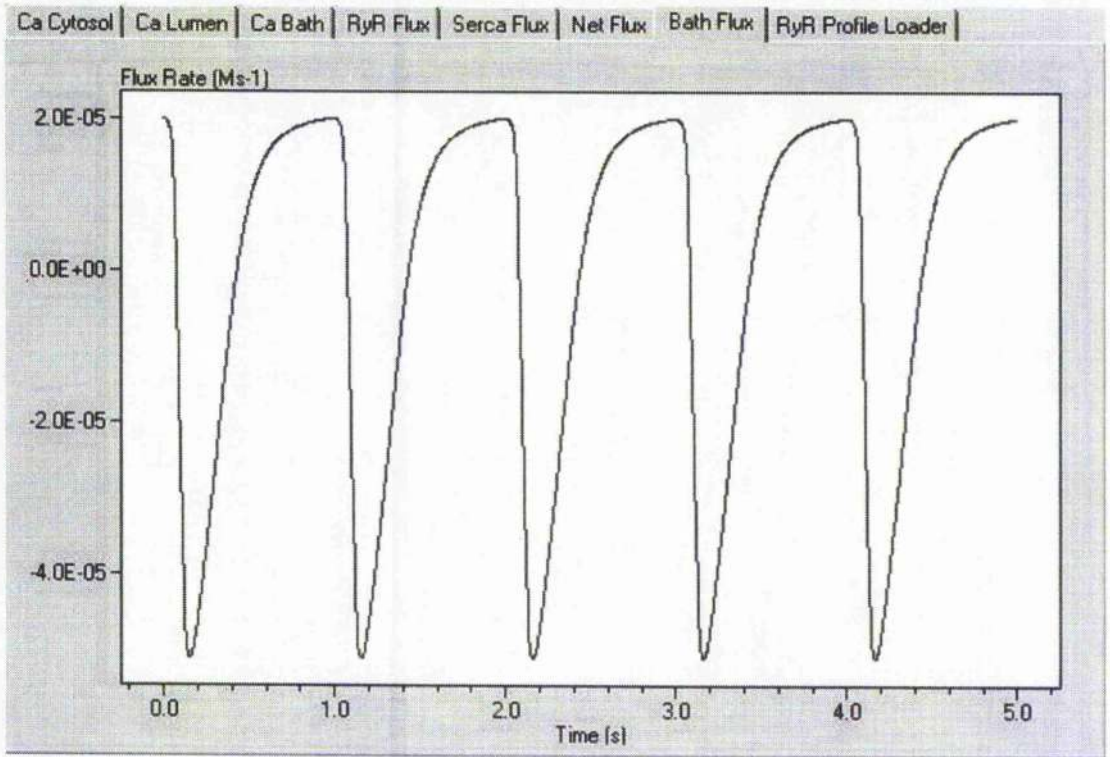


Figure 7-8 Screenshot of Bath Flux

## Appendix B

### 7.2 Description of Flo2Ca program

#### 7.2.1 Purpose of program

To import and filter and convert fluorescence to  $\text{Ca}^{2+}$ .

To obtain an average  $\text{Ca}^{2+}$  transient.

To convert  $[\text{Ca}^{2+}]_{\text{free}}$  to  $[\text{Ca}^{2+}]_{\text{total}}$ .

To add diffusional flux to average  $[\text{Ca}^{2+}]_{\text{total}}$  trace.

To obtain parameters from experiment such as mean  $[\text{Ca}^{2+}]$ , wave frequency and amplitude.

#### 7.2.2 How to use:

##### 7.2.2.1 Import and filter data

Click File...Open (shortcut F1)

Select datafile containing intracellular trace (IC)

Select datafile containing extracellular trace (BG)

Figure 1 shows the imported data (IC-red, BG-black).

Click filter...Glowpass (shortcut F2). Input 0.03 for IC and 0.01 for BG filter strength.

Figure 2 shows filtered trace.

##### 7.2.2.2 Convert fluorescence to $\text{Ca}^{2+}$

Double click at beginning and end of region of trace with stable Fmax signal (usually within last 30000 linescans of trace).

Arrange red and black lines so their bounds include the standard  $\text{Ca}^{2+}$  (~375nM) and low  $\text{Ca}^{2+}$  (~ 0.1nM) 10E buffered solutions (see Figure 2).

Click button labelled "Calculate Std  $\text{Ca}^{2+}$ ".

Enter calculated value in box labelled "std Ca" on left of window.

Click "Calculate  $\text{Ca}^{2+}$ " button.

The program subtracts intrinsic cellular fluorescence entered in boxes labelled ICBG and ECBG boxes (normally 5 and 4 respectively). These values are subtracted from the whole traces. Then "Fratio" is calculated. This is the ratio of fluorescence from inside and outside the cell (usually~1.4). Fmin is taken from the section between the black lines in Figure 3.

Intracellular Fmin and Fmax are calculated as follows:

**Equation 22**

$$\text{ICFmin} = \text{ECFmax} \bullet \text{Fratio.}$$

**Equation 23**

$$\text{ICFmax} = \text{ECFmax} \bullet \text{Fratio.}$$

Fluorescence is then converted to  $[\text{Ca}^{2+}]$  as follows:

**Equation 24**

$$[\text{Ca}^{2+}]_i = (F - \text{FMin}) / (\text{Fmax} - F) \bullet K_D$$

where F= fluorescence minus intrinsic fluorescence

$K_D$  =dissociation constant of fluorophore (e.g. 1.035 $\mu\text{M}$  for Fluo 5F).

Select tab labelled "Calcium".

Output should appear as in Figure 3.

$[Ca^{2+}]_i$  (red) and  $[Ca^{2+}]_e$  (black) are displayed, as are running averages of  $[Ca^{2+}]_i$  (blue) and  $[Ca^{2+}]_e$  (green), sampled every 5000 linescans.

Rescale plot by either changing values in boxes at bottom left labelled rescale or moving cursors, then click "calculate  $Ca^{2+}$ " again.  $[Ca^{2+}]_i^{mean}$  and  $[Ca^{2+}]_e^{mean}$  are given in boxes below the graph pane, labelled "ICAV" and "BGAV" in the middle. The difference between the two is given in the box labelled "diff". If this is  $<50nM$ , the Fratio is correct, otherwise move cursors to more stable region on STD  $Ca^{2+}$  section of trace.

#### 7.2.2.3 To obtain an average $Ca^{2+}$ transient.

Move average  $Ca^{2+}$  cursors to section of  $\sim 5$  waves of similar amplitude.

Click "SET 4 AVG" button in top right of window.

Fluorescence trace of selected region is shown as in Figure 4.

Place the blue cursor at the start of the first wave.

Position red cursor just after the first wave and around the midpoint of the wave amplitude.

Place the black cursor at the start of the second wave.

Place the green cursor at the end of the section.

The program starts at the blue cursor, and looks forward for the time when the trace rises above the horizontal red line. This marks the position of the first wave. The time between the black line and the attained position of the first wave is stored as a value called "pretrig".

The program skips forward to where the red vertical line is and starts looking for the next wave. It repeats this process, finding waves and adding them to a storage

array, then takes the average waveform by dividing that array by the number of waves found. The averaged fluorescence trace is then converted to  $[Ca^{2+}]_{free}$  and then to  $[Ca^{2+}]_{total}$ .

Diffusional flux is added using the value inputted in the box at the top right, labelled specified diffusion coefficient. The following equation is used:

**Equation 25**

$$\frac{dCa_{total}}{dt} = k.([Ca]_i - [Ca]_o)$$

therefore,

$$dCa_{total} = k.([Ca]_i - [Ca]_o).dt$$

Where:

$dCa_{total}/dt$  = rate of flux

k = diffusional flux constant

dt = time interval

Wave frequency and amplitude in terms of free and total  $[Ca^{2+}]$  is reported.

Figures 5 and 6 show examples of these calculated traces.

#### 7.2.2.4 Adjusting for caffeine quench

Application of caffeine causes a decrease in fluorophore emission, known as quench. Figure 7 shows an example of this. Caffeine quench has a time course dependent on perfusion rate. Quench is adjusted for by applying an exponential decline to the quenched trace. The result of this is shown in figure 8. Once this quench is adjusted for, fluorescence is converted to  $[Ca^{2+}]$ . Time course for

adjusting the quench is varied using the vertical blue cursors shown in figure 7.

The amplitude of the exponential is adjusted by moving the horizontal red cursor to the level of the unquenched extracellular (black) trace and the horizontal blue cursor to the level of the quenched trace. Time constant for the exponential is inputted in the box to the left of the window labelled T1. Click “quench...adjust for quench” from the menu.

#### 7.2.2.5 Exporting and printing data

Average free and total  $\text{Ca}^{2+}$  data and .BMP images are exported from the program by clicking “File...export” on the menu.

Label the plots using the boxes in the bottom right with the date, cell no. and protocol. Print by selecting “File... Print”.

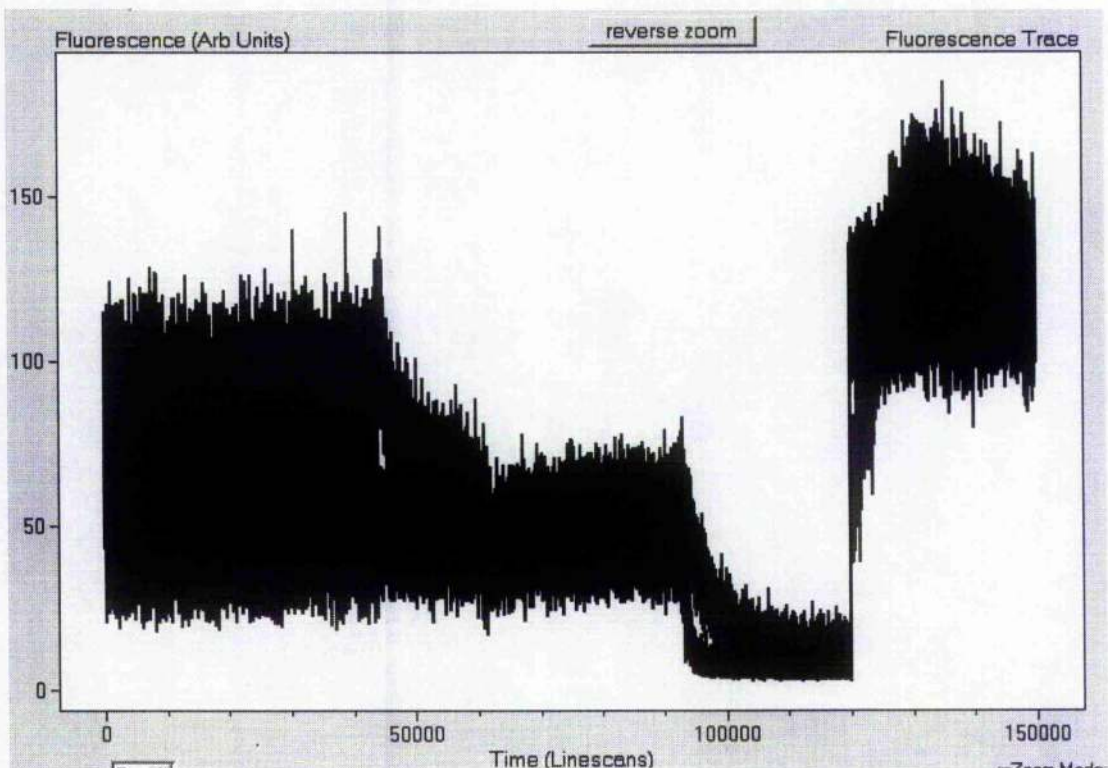


**Figure 7-9** Imported intracellular and extracellular fluorescence trace from typical protocol.

Red line- intracellular (IC) trace, Black line- extracellular (EC) trace.

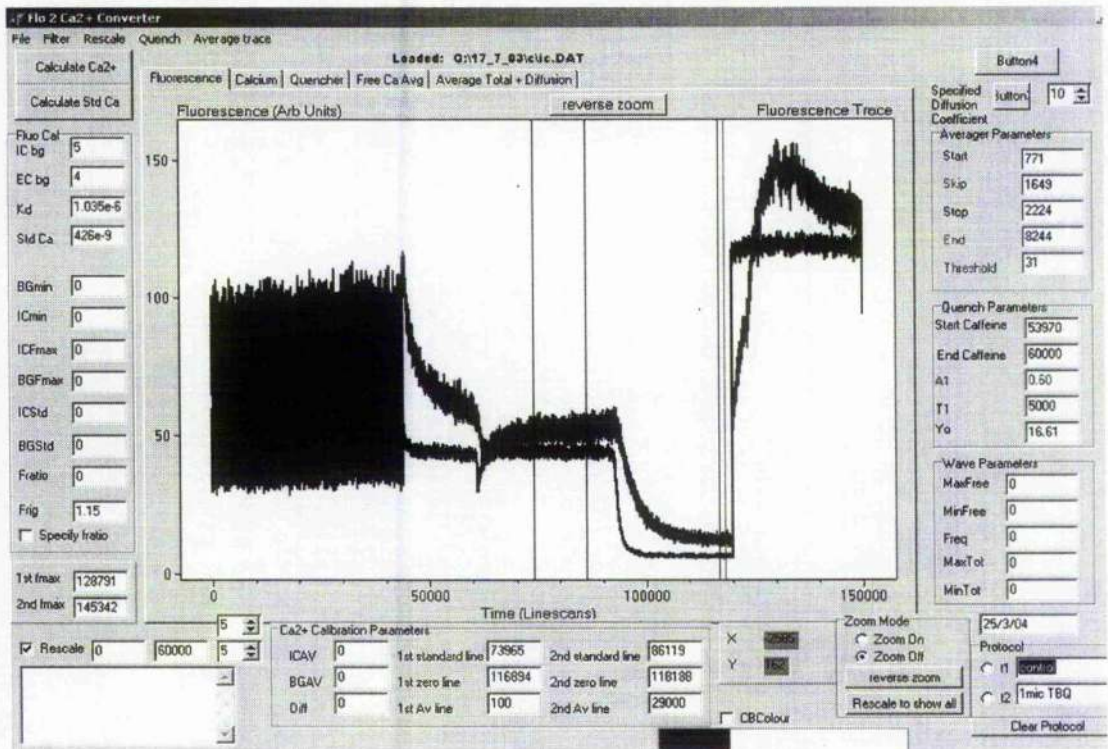


Figure 7-10 Imported traces after applying filter.

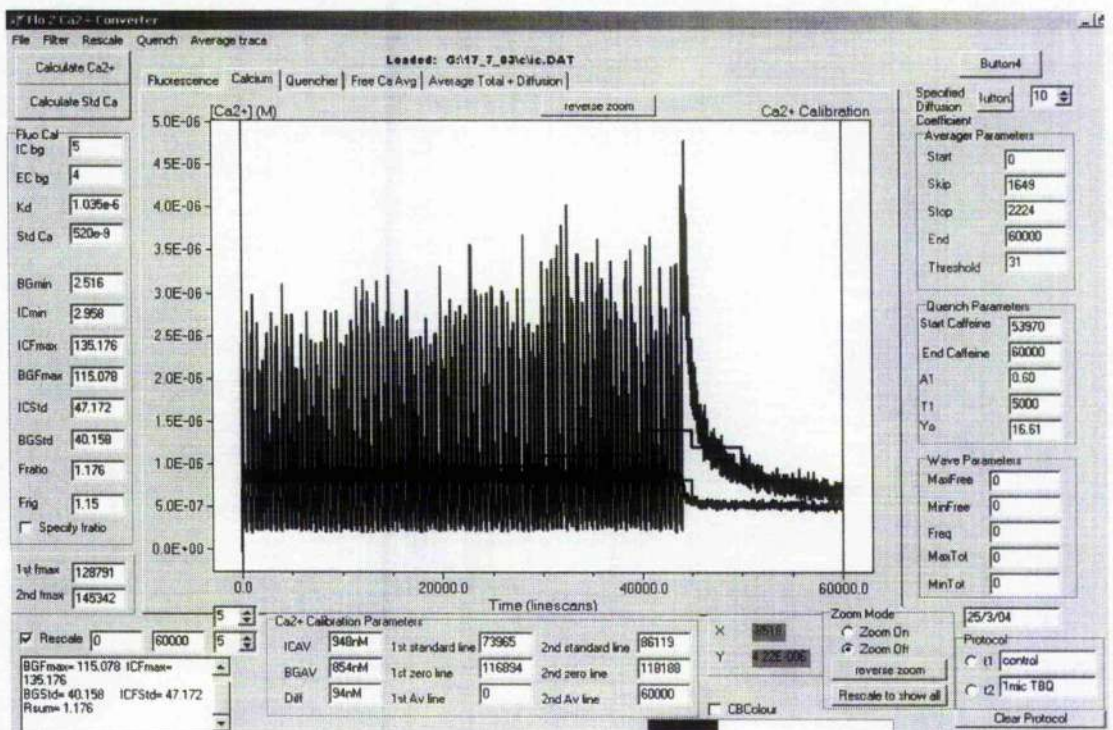


Figure 7-11 Resultant [Ca<sup>2+</sup>] trace after conversion of fluorescence.

Red line- IC  $[Ca^{2+}]$ , Black line- EC  $[Ca^{2+}]$ , Blue line- mean IC  $[Ca^{2+}]$  per 500 linescans, Green line- mean EC  $[Ca^{2+}]$  per 5000 linescans.

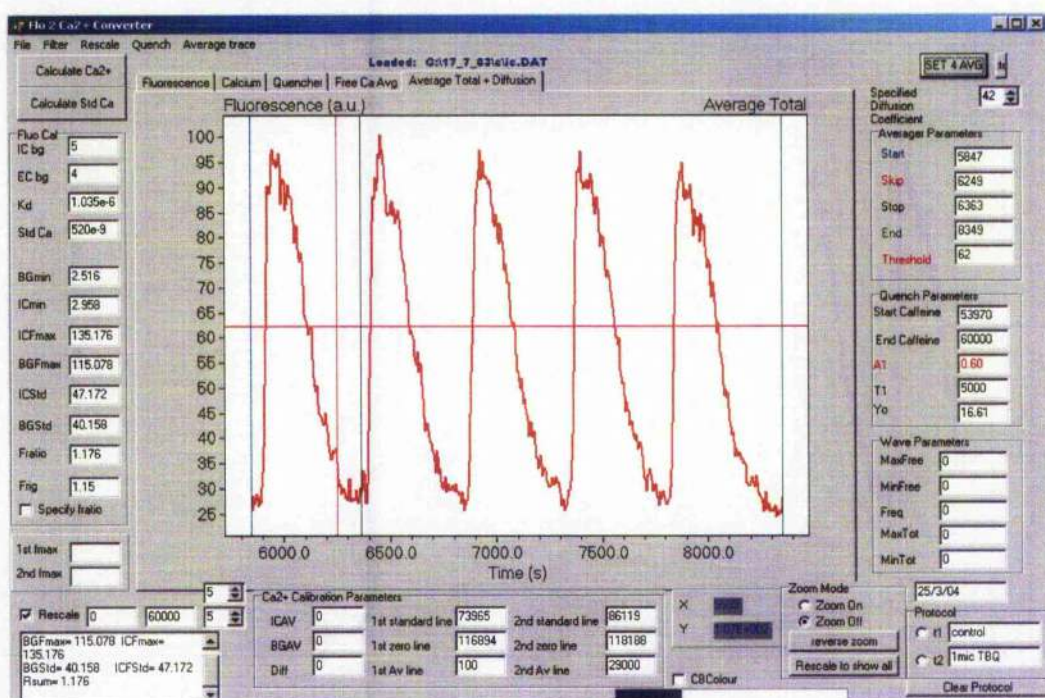


Figure 7-12 Screen used to select waves for averaging. Blue line- Start, Red vertical line- skip, Red horizontal line- threshold, Black line- Stop, and Green line- end.

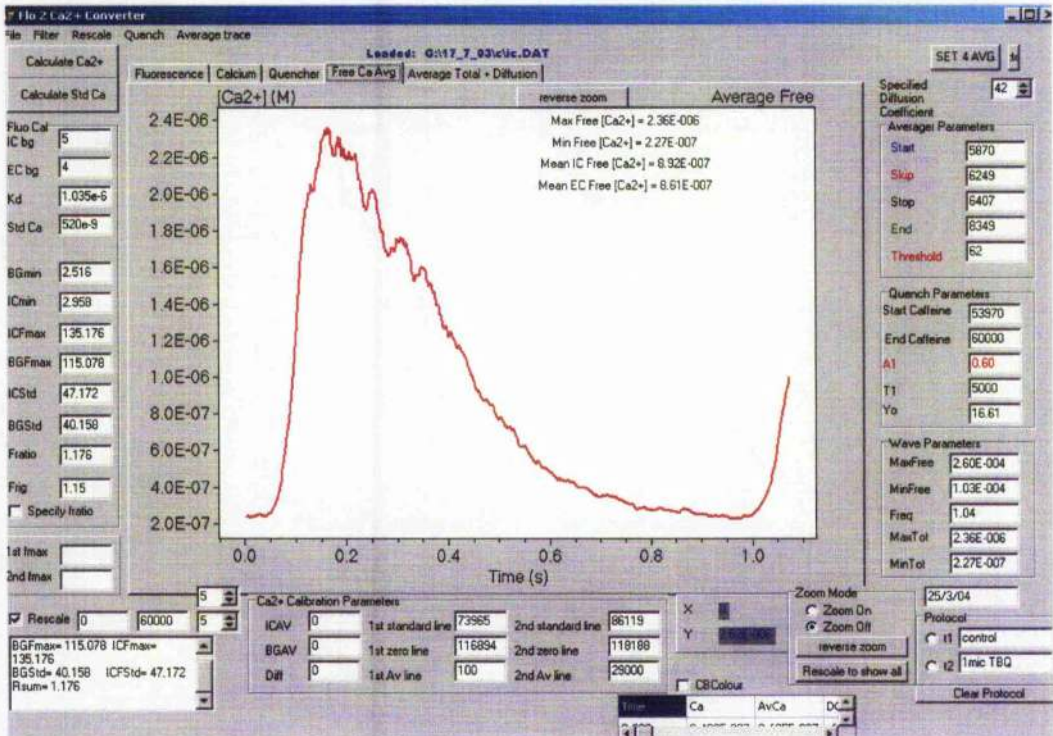


Figure 7-13 Average  $[Ca^{2+}]_i$  transient from region selected in figure 4. Max and Min  $[Ca^{2+}]_i$  and mean IC and EC  $[Ca^{2+}]_i$  are displayed in the top right of the plot.

## Appendix C

### 7.3 Description of PolySmooth program

#### 7.3.1 Purpose of program

- To import  $\text{Ca}^{2+}$  signals from Experiment
- To use polynomial smoothing to remove noise, yet retain time course of wave.
- Calculate first derivative of smoothed traces
- Export Data

**How to use:**

#### 7.3.2 Import data

Click "File..Open"

Select "TcAvg.dat" datafile outputted from Flo2Ca program.

Click "Total  $\text{Ca}^{2+}$ " tab on graphical display.

The display should appear as shown below.

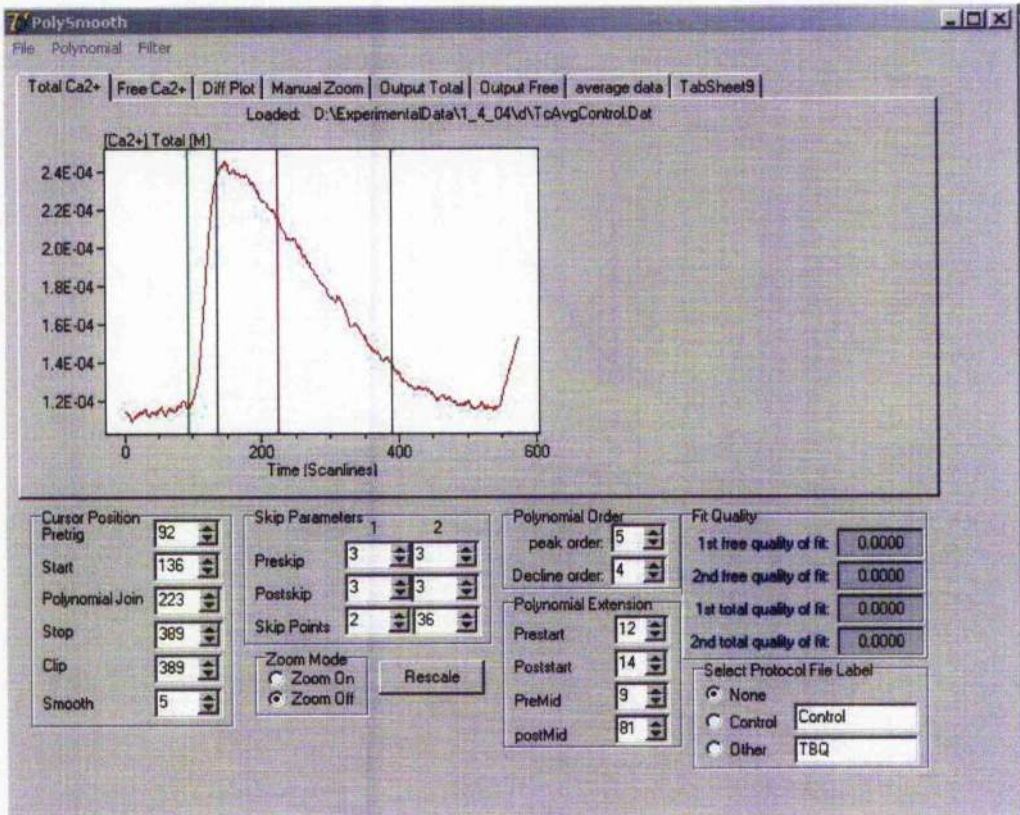


Figure 7-14 Screenshot of program after importing data.

### 7.3.3 Polynomial smooth

Position cursors as follows

Green (Pretrig)-move to start of upstroke

Blue (Start)-Move to end of upstroke, where noise starts to become apparent.

Black-(Stop)-Move to end of declining phase, where Ca<sup>2+</sup> returns to resting values.

Red (Polynomial Join)-move to 1/2 way between start and stop.

Cursors can also be moved by changing values in boxes within the “cursor position” panel.

Increase polynomial order so fit quality is  $>0.95$ . If fit quality is less than 0, then decrease polynomial order until fit quality  $>0$  and move polynomial join cursor until better fit is obtained.

As cursors move, the polynomial is automatically re-evaluated.

#### **7.3.4 Polynomial extension**

This increases the amount of data available to the polynomial fitting routine and enables the use of higher polynomial orders, hence producing a better fit-quality.

Typically around the peak, the polynomial needs 2-5 points before the polynomial (prestart) and  $\sim 20$  points after the end of the first polynomial (PostMid).

The second polynomial typically requires  $\sim 20$ -50 points before the joining point (PreMid).

#### **7.3.5 Joining Polynomials.**

Two joining points occur within the smoothing. The first occurs between the original upstroke and the first polynomial. The second join is between the 2 polynomials. Joining is accomplished by using the cubic spline interpolation method. In the program, this is represented by skip parameters. A spline is fitted from  $n$  points before and after the joint, where  $\text{skip}$ . An example of this is shown below.

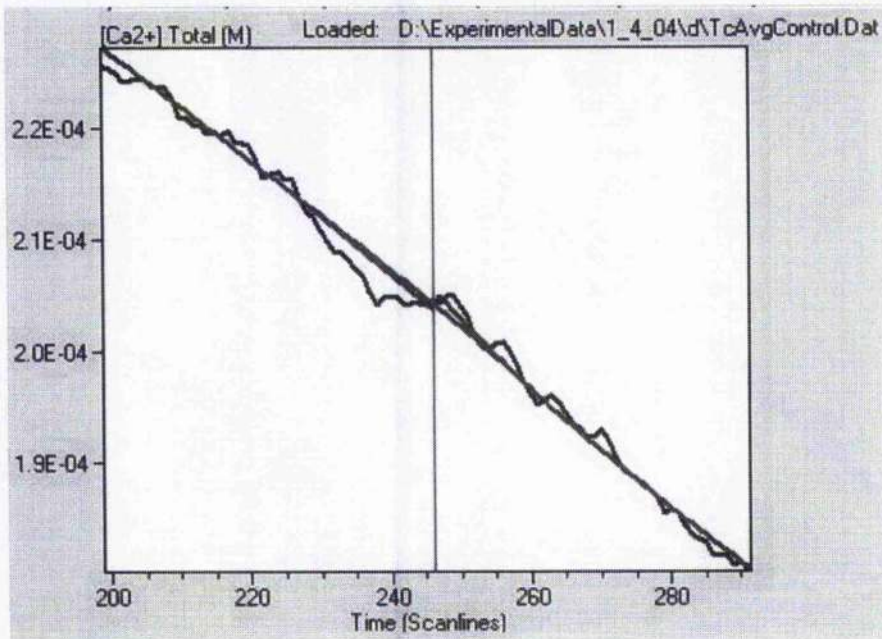


**Figure 7-15** Example of cubic spline fitted to span region of two joining polynomials. Black line-[Ca<sup>2+</sup>]total from experiment, red data line- two polynomials, green line cubic spline, red horizontal line-cursor indicating joining point of polynomials.

An example of the first derivative before and after this joining method has been applied are shown in the following two figures.

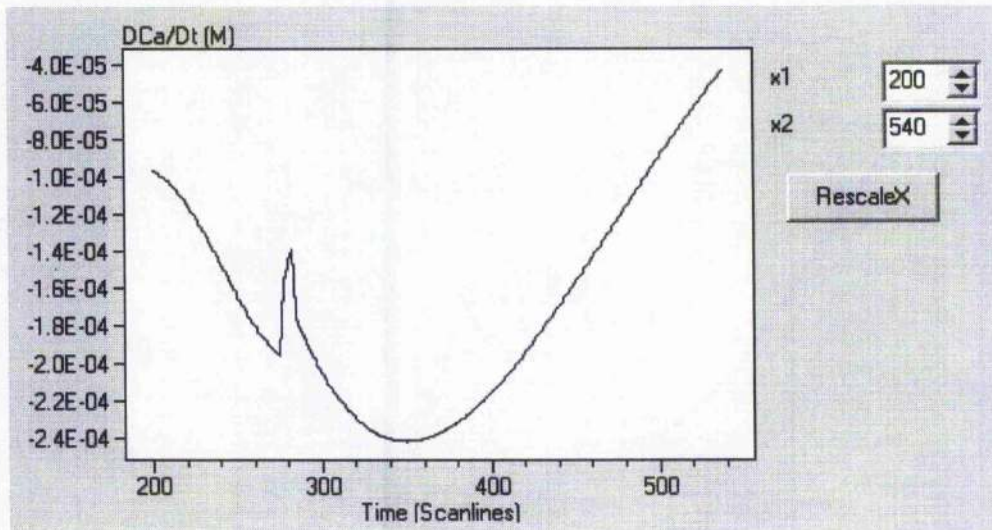


**Figure 7-16** First derivative before joining method was applied.

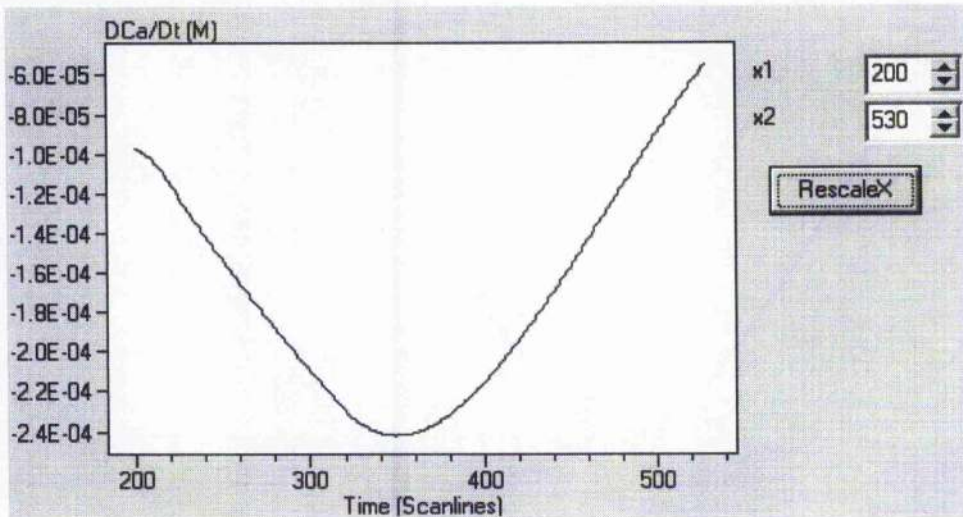


**Figure 7-17 Plot of first derivative after joining method has been applied.**

The joining method is only applied to the region between the peak and the point of maximum negative flux. The latter part of the trace is later used for SERCA parameter fitting. This section should remain unaffected by the joining method.

### 7.3.6 Calculating the first derivative.

This is automatically calculated at the same time as the polynomial. A central difference method was used to find the first derivative. First derivatives of polynomial smoothed free and total  $[Ca^{2+}]$  traces were placed in arrays. Any artefact in first derivatives can be highlighted by viewing "DiffPlot" and "Manual Zoom" Tabs.

The "DiffPlot" tab displays the first derivative vs.  $[Ca^{2+}]_i$ . The "clip" and "pretrig" parameters should be adjusted so noise at the start and end of traces is minimal. An Example trace is shown in the figure below.

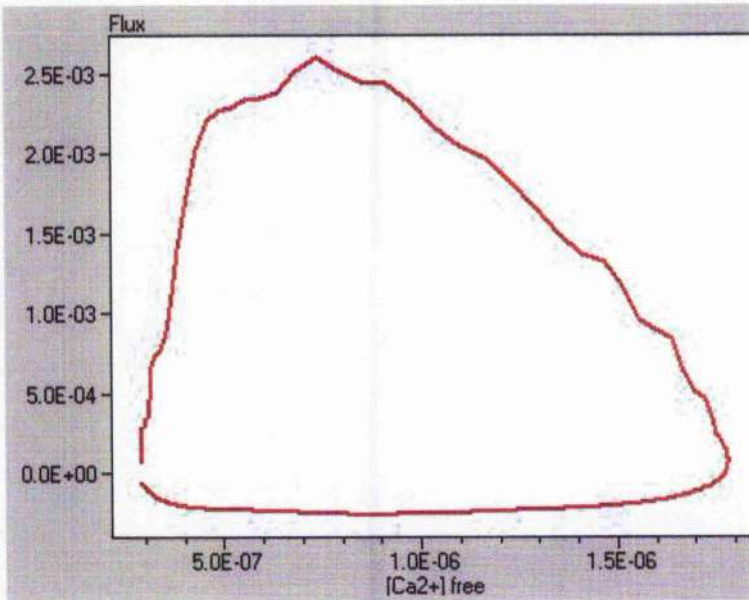


Figure 7-18 Plot of flux rate vs.  $[Ca^{2+}]$ , after polynomial smoothing.

### 7.3.7 Exporting Data

Click "File..Export" . Data is exported as .dat text file, nominally called 'Bell.dat'.

### 7.3.8 Possible artefacts of method.

Without the joining method, glitches are evident, where the transition between two sections occur.

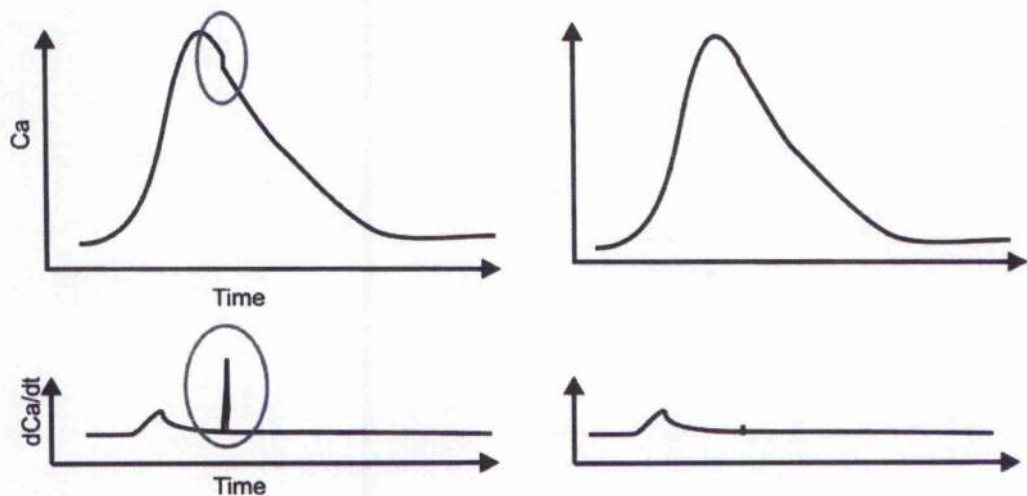


Figure 7-19 Examples of glitches in the  $Ca^{2+}$  and  $dCa/dt$

To remove this artefact,  $n$  points before and after are skipped with the intervening points are interpolated based on points before and after the skipped region. This method can introduce artefacts if the sections to be joined are much different from each other. Ideally, the sections should have a minimal artefact, but the peak and minimum flux rate should remain unaffected.

This can be checked on the "Manual Zoom" tab of the program. Set the bounds to around the region of the join of interest. The window plots the first derivative between these bounds. Any discontinuities in the first derivative will be highlighted by irregularities in the plot.

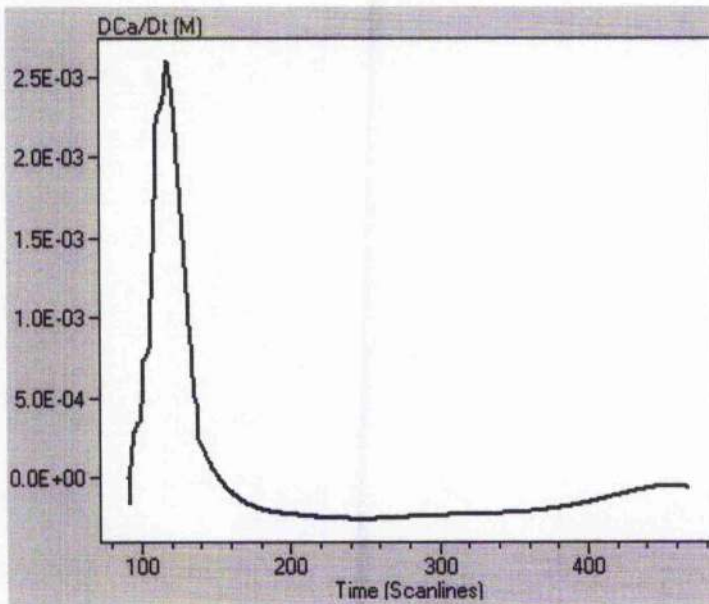


Figure 7-20 Plot of first derivative vs. time from manual zoom tab.

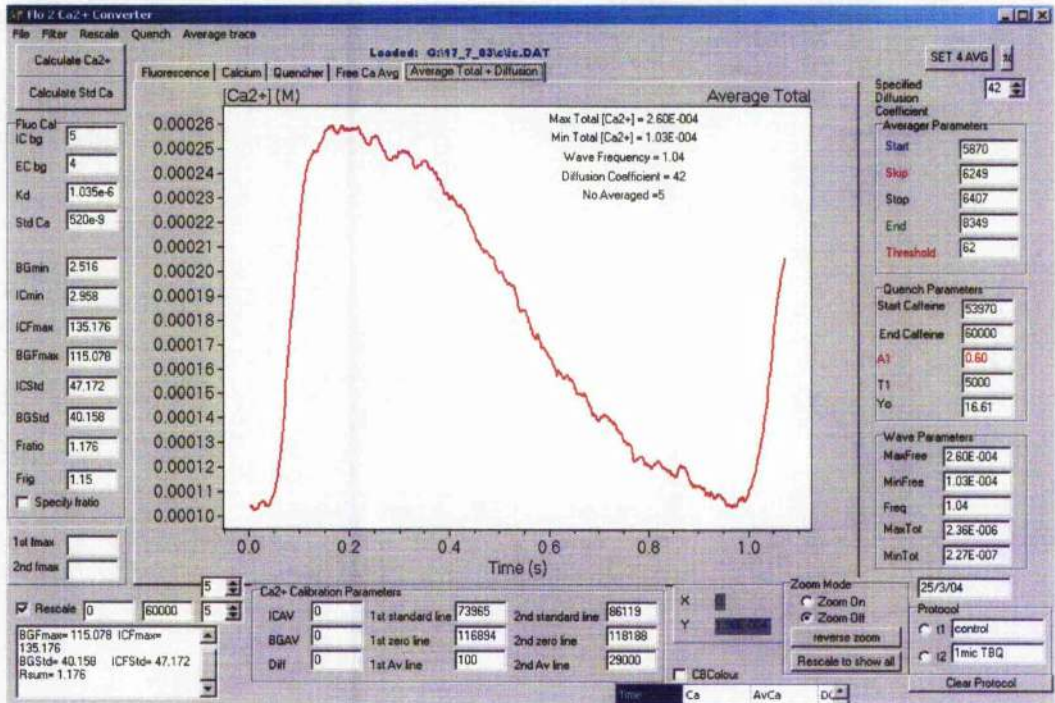


Figure 7-21 Average [Ca<sup>2+</sup>]total calculated fro previous figure. Maximum [Ca<sup>2+</sup>]total, minimum [Ca<sup>2+</sup>]total, wave frequency, diffusion coefficient and no. of waves averaged are displayed in the top right of the plot.

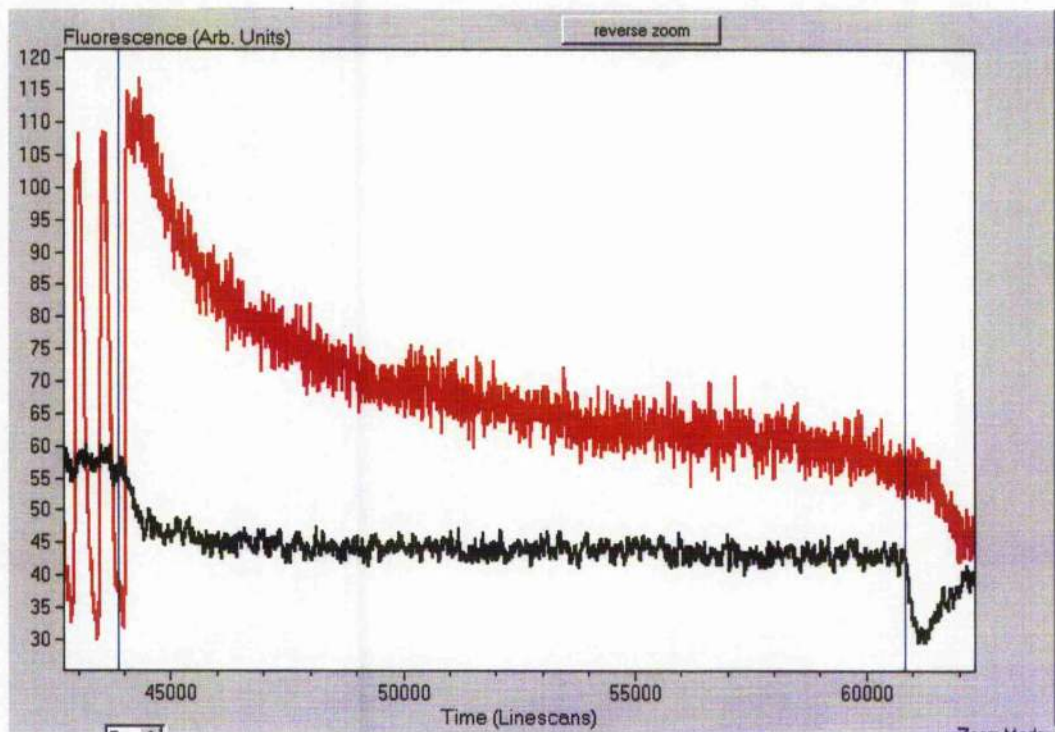


Figure 7-22 Plot shows section where caffeine was applied.

Quench due to caffeine is evident on lower EC fluorescence trace. Red line shows IC fluorescence, black line shows EC fluorescence.

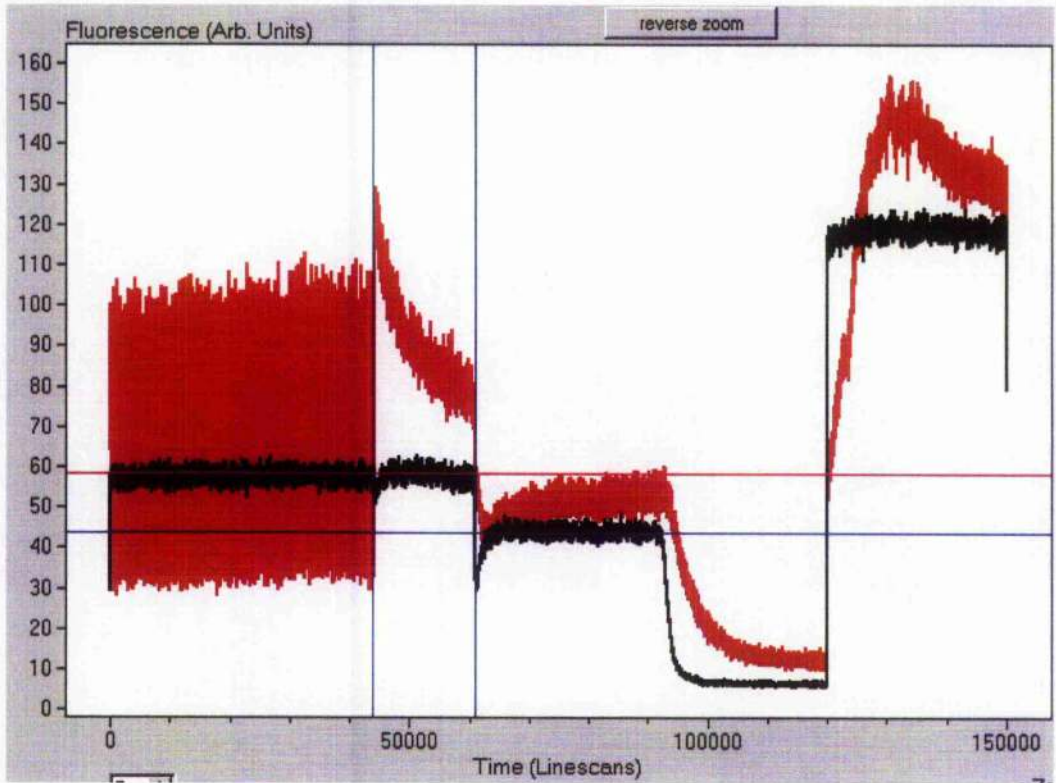


Figure 7-23 Adjusted trace, after allowing for quench. Plot shows fluorescence after adjustment for quench.

## **Appendix D Computational methods used to analyse wave properties in permeabilised cardiomyocytes.**

### **7.4 Description of CellFlux program**

#### **7.4.1 Purpose of program**

- To import  $\text{Ca}^{2+}$  signals from PolySmooth program (see description).
- Calculate SR  $[\text{Ca}^{2+}]$  based on imported  $\text{Ca}^{2+}$  fluxes and existing estimations of calsequestrin buffering properties.
- Use existing models of fluxes to quantify leak and SERCA fluxes.
- Extract RyR flux and calculate RyR permeability.

**How to use:**

#### **7.4.2 Importing data**

Click "File..Open".

Select file exported from PolySmooth program (e.g. TCAVG.dat). Trace should appear as shown below.

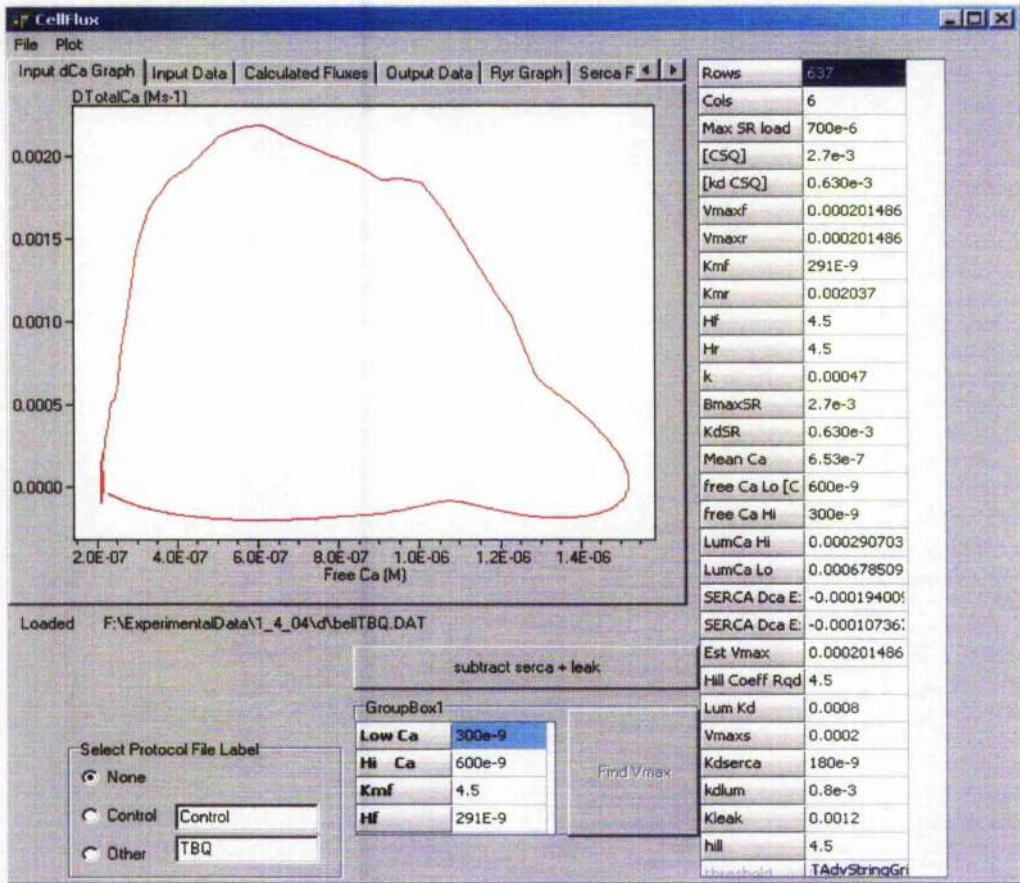


Figure 7-24 Screenshot of plot displayed after inputting data from PolySmooth program.

Plot shows rate of  $[\text{Ca}^{2+}]_{\text{total}}$  change plotted against free  $[\text{Ca}^{2+}]$ .

#### 7.4.3 Calculating SR $[\text{Ca}^{2+}]$

Click “subtract SERCA +Leak” button. This initialises the calculation of SERCA and leak fluxes. SR  $[\text{Ca}^{2+}]$  is calculated as described earlier.  $[\text{CSQ}]$  and  $K_D$  CSQ are used as  $B_{\text{max}}$  and  $K_D$  for conversion to free  $[\text{Ca}^{2+}]$ . The intra-SR  $\rightarrow$  cytosol  $[\text{Ca}^{2+}]$  gradient and the leak constant  $k$  are used to calculate leak as described earlier. SERCA activity is calculated.

#### 7.4.4 Fitting parameters of SERCA

SERCA is fitted manually by varying  $k_{\text{mf}}$  (forward mode  $K_D$  of SERCA) and  $H_f$  (forward mode hill coefficient of SERCA).  $K_{\text{mr}}$  is calculated as 7000 times  $K_{\text{mf}}$ .

$V_{maxf}$  (forward mode SERCA) is calculated from the flux rate from experiment at a set  $[Ca^{2+}]_i$  (usually ~550-600nM).  $V_{maxr}$  and  $H_r$  are equal to the forward mode values. These parameters are based on an existing model of SERCA (Shannon *et al.*, 2000). Leak is calculated and subtracted from net flux.

Enter cytosolic  $[Ca^{2+}]_i$  values over which to study SERCA activity (typically 250 and  $600 \times 10^{-9}$  M for low  $Ca^{2+}$  and Hi  $Ca^{2+}$  respectively) should be studied.

Click the "Find  $V_{max}$ " button.

This calculates a  $V_{max}$  based on the flux rate at the time when cytosolic  $Ca^{2+}$  falls to the value supplied in the Hi  $Ca^{2+}$  box. A calculation based on the  $k_{mf}$  and  $H_f$  supplied is carried out using the Shannon *et al.* SERCA equation when solved for  $V_{max}$  as shown below.

$$V_{max} = \frac{(netflux - leak) \times (1 + [Ca^{2+}]_{cyt} / k_{mf})^{h_f} + ([Ca^{2+}]_{SR} / k_{mr})^{h_r}}{([Ca^{2+}]_{cyt} / k_{mf})^{h_f}}$$

This calculated  $V_{max}$ , along with the  $H_f$  and  $k_{mf}$  supplied by the user is then used to calculate SERCA pump rates, given the cytosolic  $[Ca^{2+}]$  and SR  $[Ca^{2+}]$  at each point from experiment. This is plotted as pump rate vs. cytosolic  $[Ca^{2+}]$  (red line in figure below). The user varies  $K_{mf}$  and  $H_f$ , then presses the "find  $V_{max}$ " button to display the newly calculated plot. As  $K_{mf}$  is increased, the blue, calculated rate line moves up. Increasing  $H_f$  increases the curvature of the blue line. These are varied until red and blue lines are in close agreement. This indicates a good prediction of SERCA parameters. See example below.

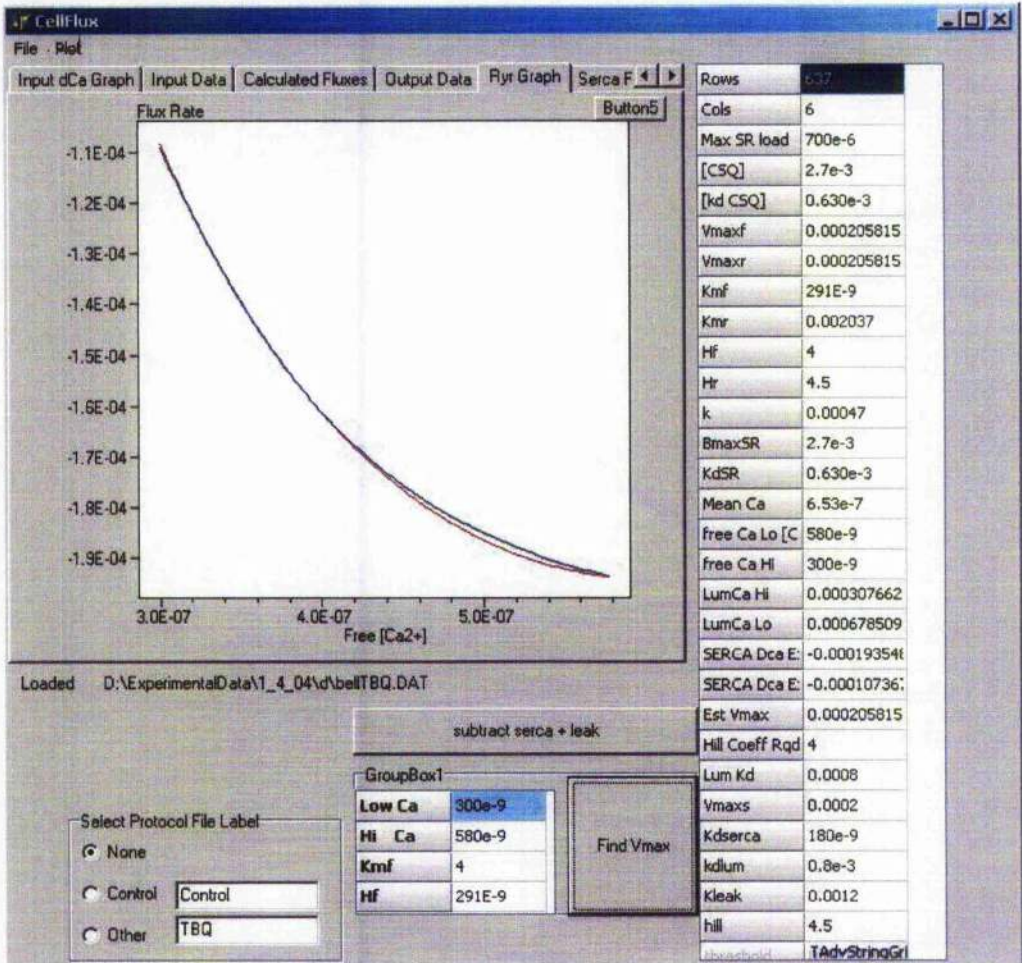
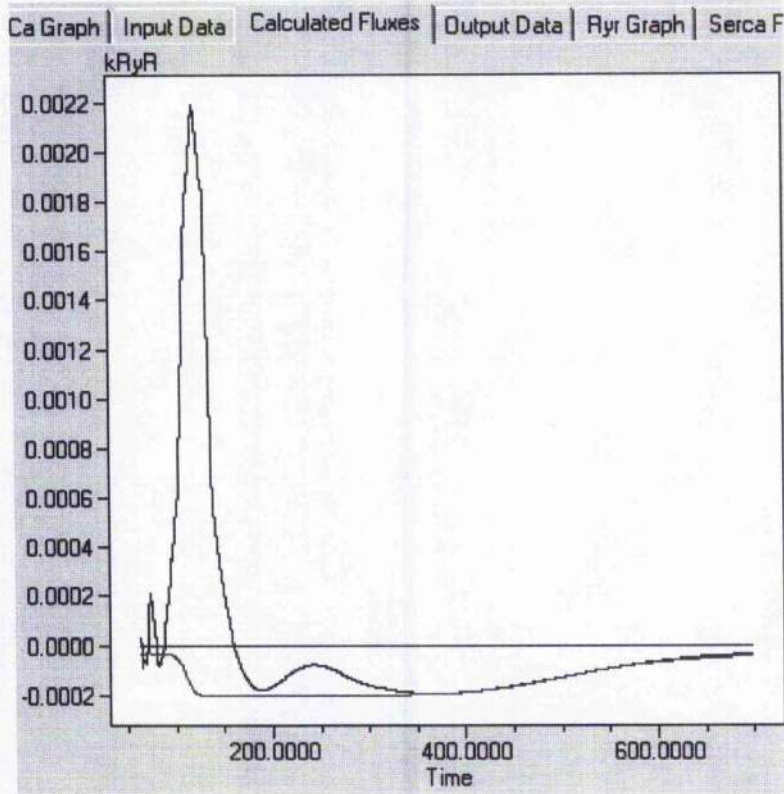


Figure 7-25 Screenshot showing experimental flux (red line) and calculated flux (blue line), plotted against cytosolic [Ca<sup>2+</sup>].

#### 7.4.5 Calculating RyR flux rate.

Once SERCA and leak fluxes have been calculated, both are subtracted from the imported SR net flux rate. This is accomplished by pressing the “subtract serca + leak button”. These fluxes are plotted against time in the figure below.



**Figure 7-26** Plot showing goodness of fit of experimental (black) and calculated (red) fluxes.  
Leak is also plotted (blue line).

#### 7.4.6 Calculating permeability

Once RyR flux rate has been calculated, SR-cytosol  $[Ca^{2+}]$  gradient is used to calculate permeability. Using the equation below.

$$\text{Flux rate} = K \times ([Ca^{2+}]_{\text{cytosol}} - [Ca^{2+}]_{\text{SR}})$$

A typical result is shown below.

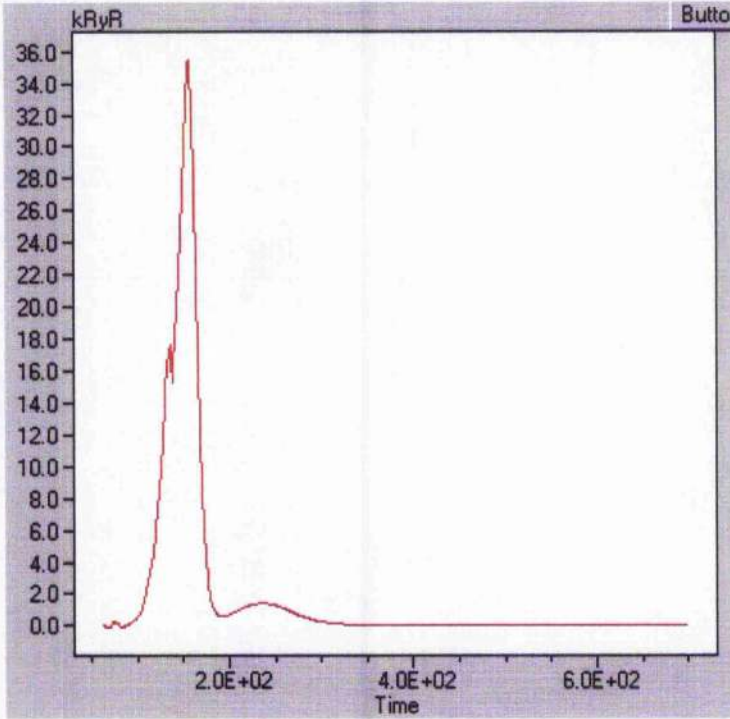


Figure 7-27 RyR permeability constant profile.

#### 7.4.7 Exporting data and results.

The data and SERCA parameters used for the fitting are exported as data files (Entitled ryrprofile.dat and ryrprofilestats.dat).

## References

- Adams, W., Trafford, A. W., & Eisner, D. A. (1998). 2,3-Butanedione monoxime (BDM) decreases sarcoplasmic reticulum Ca content by stimulating Ca release in isolated rat ventricular myocytes. *Pflugers Arch.* **436**, 776-781.
- Allen, D. G. & Blinks, J. R. (1978). Calcium transients in aequorin-injected frog cardiac muscle. *Nature* **273**, 509-513.
- Allen, D. G., Eisner, D. A., Smith, G. L., & Valdeolmillos, M. The effects of timing of a calcium oscillation on the subsequent systolic Ca<sup>2+</sup> transients in isolated ferret ventricular muscle. Proceedings of the Physiological Society 376. 1985.  
Ref Type: Abstract
- Anderson, K., Lai, F. A., Liu, Q. Y., Rousseau, E., Erickson, H. P., & Meissner, G. (1989). Structural and functional characterization of the purified cardiac ryanodine receptor-Ca<sup>2+</sup> release channel complex. *J.Biol.Chem.* **264**, 1329-1335.
- Asahi, M., McKenna, E., Kurzydowski, K., Tada, M., & MacLennan, D. H. (2000). Physical interactions between phospholamban and sarco(endo)plasmic reticulum Ca<sup>2+</sup>-ATPases are dissociated by elevated Ca<sup>2+</sup>, but not by phospholamban phosphorylation, vanadate, or thapsigargin, and are enhanced by ATP. *J.Biol.Chem.* **275**, 15034-15038.
- Backx, P. H., de Tombe, P. P., Van Deen, J. H., Mulder, B. J., & ter Keurs, H. E. (1989). A model of propagating calcium-induced calcium release mediated by calcium diffusion. *J.Gen.Physiol* **93**, 963-977.
- BANGHAM, A. D., HORNE, R. W., GLAUERT, A. M., DINGLE, J. T., & LUCY, J. A. (1962). Action of saponin on biological cell membranes. *Nature* **196**, 952-955.
- Barceñas-Ruiz, L. & Wier, W. G. (1987). Voltage dependence of intracellular [Ca<sup>2+</sup>]<sub>i</sub> transients in guinea pig ventricular myocytes. *Circ.Res.* **61**, 148-154.
- Bassani, J. W., Bassani, R. A., & Bers, D. M. (1993). Twitch-dependent SR Ca accumulation and release in rabbit ventricular myocytes. *Am.J.Physiol* **265**, C533-C540.
- Bassani, R. A. & Bers, D. M. (1995). Rate of diastolic Ca release from the sarcoplasmic reticulum of intact rabbit and rat ventricular myocytes. *Biophys.J.* **68**, 2015-2022.
- Baylor, S. M. & Hollingworth, S. (2000). Measurement and Interpretation of Cytoplasmic. *News Physiol Sci.* **15**, 19-26.

- Beard, N. A., Sakowska, M. M., Dulhunty, A. F., & Laver, D. R. (2002). Calsequestrin is an inhibitor of skeletal muscle ryanodine receptor calcium release channels. *Biophys.J.* **82**, 310-320.
- Berrebi-Bertrand, I., Brument-Larignon, N., Camelin, J. C., Quiniou, M. J., & Bril, A. (1998). Relationship between biochemical and functional effects of protein phosphatase 1 inhibitors in rabbit cardiac skinned fibers. *J.Mol.Cell Cardiol.* **30**, 1945-1954.
- Berridge, M. J., Lipp, P., & Bootman, M. D. (2000). The versatility and universality of calcium signalling. *Nat.Rev.Mol.Cell Biol.* **1**, 11-21.
- Bers, D. M. (2002). Cardiac excitation-contraction coupling. *Nature* **415**, 198-205.
- Beuckelmann, D. J. & Wier, W. G. (1988). Mechanism of release of calcium from sarcoplasmic reticulum of guinea-pig cardiac cells. *J.Physiol* **405**, 233-255.
- Brandl, C. J., Green, N. M., Korczak, B., & MacLennan, D. H. (1986). Two Ca<sup>2+</sup> ATPase genes: homologies and mechanistic implications of deduced amino acid sequences. *Cell* **44**, 597-607.
- Calaghan, S. C., White, E., Bedut, S., & Le Guennec, J. Y. (2000). Cytochalasin D reduces Ca<sup>2+</sup> sensitivity and maximum tension via interactions with myofilaments in skinned rat cardiac myocytes. *J.Physiol* **529 Pt 2**, 405-411.
- Campbell, K. P., Knudson, C. M., Imagawa, T., Leung, A. T., Sutko, J. L., Kahl, S. D., Raab, C. R., & Madson, L. (1987). Identification and characterization of the high affinity [<sup>3</sup>H]ryanodine receptor of the junctional sarcoplasmic reticulum Ca<sup>2+</sup> release channel. *J.Biol.Chem.* **262**, 6460-6463.
- Capogrossi, M. C., Kort, A. A., Spurgeon, H. A., & Lakatta, E. G. (1986). Single adult rabbit and rat cardiac myocytes retain the Ca<sup>2+</sup>- and species-dependent systolic and diastolic contractile properties of intact muscle. *J.Gen.Physiol* **88**, 589-613.
- Chen, S. R., Li, X., Ebisawa, K., & Zhang, L. (1997). Functional characterization of the recombinant type 3 Ca<sup>2+</sup> release channel (ryanodine receptor) expressed in HEK293 cells. *J.Biol.Chem.* **272**, 24234-24246.
- Cheng, H., Lederer, M. R., Lederer, W. J., & Cannell, M. B. (1996b). Calcium sparks and [Ca<sup>2+</sup>]<sub>i</sub> waves in cardiac myocytes. *American Journal of Physiology* **270**, C148-C159.
- Cheng, H., Lederer, M. R., Lederer, W. J., & Cannell, M. B. (1996a). Calcium sparks and [Ca<sup>2+</sup>]<sub>i</sub> waves in cardiac myocytes. *Am.J.Physiol* **270**, C148-C159.

- Cheng, H., Lederer, M. R., Xiao, R. P., Gomez, A. M., Zhou, Y. Y., Ziman, B., Spurgeon, H., Lakatta, E. G., & Lederer, W. J. (1996c). Excitation-contraction coupling in heart: new insights from Ca<sup>2+</sup> sparks. *Cell Calcium* **20**, 129-140.
- Cheng, H., Lederer, W. J., & Cannell, M. B. (1993). Calcium sparks: elementary events underlying excitation-contraction coupling in heart muscle. *Science* **262**, 740-744.
- Cleemann, L. & Morad, M. (1991). Role of Ca<sup>2+</sup> channel in cardiac excitation-contraction coupling in the rat: evidence from Ca<sup>2+</sup> transients and contraction. *J.Physiol* **432**, 283-312.
- Copello, J. A., Barg, S., Onoue, H., & Fleischer, S. (1997). Heterogeneity of Ca<sup>2+</sup> gating of skeletal muscle and cardiac ryanodine receptors. *Biophys.J.* **73**, 141-156.
- Currie, S., Loughrey, C. M., Craig, M. A., & Smith, G. L. (2004). Calcium/calmodulin-dependent protein kinase II $\delta$  associates with the ryanodine receptor complex and regulates channel function in rabbit heart. *Biochem.J.* **377**, 357-366.
- Currie, S. & Smith, G. L. (1999). Enhanced phosphorylation of phospholamban and downregulation of sarco/endoplasmic reticulum Ca<sup>2+</sup> ATPase type 2 (SERCA 2) in cardiac sarcoplasmic reticulum from rabbits with heart failure. *Cardiovasc.Res.* **41**, 135-146.
- Dempster, J. & Wokosin, D. (2002). Fluorescence imaging systems: A quick overview of the technology. *Physiology News* **48**, 12-14.
- DeSantiago, J., Maier, L. S., & Bers, D. M. (2004). Phospholamban is required for CaMKII-dependent recovery of Ca transients and SR Ca reuptake during acidosis in cardiac myocytes. *J.Mol.Cell Cardiol.* **36**, 67-74.
- Diaz, M. E., Trafford, A. W., O'Neill, S. C., & Eisner, D. A. (1997). Measurement of sarcoplasmic reticulum Ca<sup>2+</sup> content and sarcolemmal Ca<sup>2+</sup> fluxes in isolated rat ventricular myocytes during spontaneous Ca<sup>2+</sup> release. *J.Physiol* **501** ( Pt 1), 3-16.
- Elliot, E. A Quantitative assessment of permeabilisation in cardiac myocytes. 2002. Ref Type: Thesis/Dissertation
- Endo, M., Tanaka, M., & Ogawa, Y. (1970). Calcium induced release of calcium from the sarcoplasmic reticulum of skinned skeletal muscle fibres. *Nature* **228**, 34-36.
- Escande-Geraud, M. L., Rols, M. P., Dupont, M. A., Gas, N., & Teissie, J. (1988). Reversible plasma membrane ultrastructural changes correlated with electropermeabilization in Chinese hamster ovary cells. *Biochim.Biophys.Acta* **939**, 247-259.

Fabiato, A. (1983). Calcium-induced release of calcium from the cardiac sarcoplasmic reticulum. *Am.J.Physiol* **245**, C1-14.

Fabiato, A. (1985a). Rapid ionic modifications during the aequorin-detected calcium transient in a skinned canine cardiac Purkinje cell. *J.Gen.Physiol* **85**, 189-246.

Fabiato, A. (1985b). Simulated calcium current can both cause calcium loading in and trigger calcium release from the sarcoplasmic reticulum of a skinned canine cardiac Purkinje cell. *J.Gen.Physiol* **85**, 291-320.

Fabiato, A. (1985c). Time and calcium dependence of activation and inactivation of calcium-induced release of calcium from the sarcoplasmic reticulum of a skinned canine cardiac Purkinje cell. *J.Gen.Physiol* **85**, 247-289.

Fabiato, A. & Fabiato, F. (1972). Excitation-contraction coupling of isolated cardiac fibers with disrupted or closed sarcolemmas. Calcium-dependent cyclic and tonic contractions. *Circ.Res.* **31**, 293-307.

Fabiato, A. & Fabiato, F. (1975). Contractions induced by a calcium-triggered release of calcium from the sarcoplasmic reticulum of single skinned cardiac cells. *J.Physiol* **249**, 469-495.

Fabiato, A. & Fabiato, F. (1979). Calculator programs for computing the composition of the solutions containing multiple metals and ligands used for experiments in skinned muscle cells. *J.Physiol (Paris)* **75**, 463-505.

Ferrier, G. R. (1976). The effects of tension on acetylcholinesterase-induced transient depolarizations and aftercontractions in canine myocardial and Purkinje tissues. *Circ.Res.* **38**, 156-162.

Ferrier, G. R. & Howlett, S. E. (1995). Contractions in guinea-pig ventricular myocytes triggered by a calcium-release mechanism separate from  $\text{Na}^+$  and L-currents. *J.Physiol* **484 (Pt 1)**, 107-122.

Fill, M. & Coronado, R. (1988). Ryanodine receptor channel of sarcoplasmic reticulum. *Trends Neurosci.* **11**, 453-457.

Fleischer, S., Ogunbunmi, E. M., Dixon, M. C., & Fleer, E. A. (1985). Localization of  $\text{Ca}^{2+}$  release channels with ryanodine in junctional terminal cisternae of sarcoplasmic reticulum of fast skeletal muscle. *Proc Natl.Acad.Sci.U.S.A* **82**, 7256-7259.

Ford, L. E. & Podolsky, R. J. (1970). Regenerative calcium release within muscle cells. *Science* **167**, 58-59.

- Franzini-Armstrong, C., Protasi, F., & Ramesh, V. (1999a). Shape, Size and Distribution of  $\text{Ca}^{2+}$  Release Units and Couplons in Skeletal and Cardiac Muscles. *Biophysical Journal* **77**, 1528-1539.
- Franzini-Armstrong, C., Protasi, F., & Ramesh, V. (1999b). Shape, size, and distribution of calcium release units and couplons in skeletal and cardiac muscles. *Biophys.J.* **77**, 1528-1539.
- Grynkiewicz, G., Poenie, M., & Tsien, R. Y. (1985). A new generation of  $\text{Ca}^{2+}$  indicators with greatly improved fluorescence properties. *J.Biol.Chem.* **260**, 3440-3450.
- Gyorke, I. & Gyorke, S. (1998). Regulation of the cardiac ryanodine receptor channel by luminal  $\text{Ca}^{2+}$  involves luminal  $\text{Ca}^{2+}$  sensing sites. *Biophys.J.* **75**, 2801-2810.
- Gyorke, I., Hester, N., Jones, L. R., & Gyorke, S. (2004). The role of calsequestrin, triadin, and junctin in conferring cardiac ryanodine receptor responsiveness to luminal calcium. *Biophys.J.* **86**, 2121-2128.
- Gyorke, S. & Fill, M. (1993). Ryanodine receptor adaptation: control mechanism of  $\text{Ca}^{2+}$ -induced  $\text{Ca}^{2+}$  release in heart. *Science* **260**, 807-809.
- Gyorke, S., Lukyanenko, V., & Gyorke, I. (1997). Dual effects of tetracaine on spontaneous calcium release in rat ventricular myocytes. *J.Physiol* **500** ( Pt 2), 297-309.
- Hain, J., Onoue, H., Mayrleitner, M., Fleischer, S., & Schindler, H. (1995). Phosphorylation modulates the function of the calcium release channel of sarcoplasmic reticulum from cardiac muscle. *J.Biol.Chem.* **270**, 2074-2081.
- Harkins, A. B., Kurebayashi, N., & Baylor, S. M. (1993). Resting myoplasmic free calcium in frog skeletal muscle fibers estimated with fluo-3. *Biophys.J.* **65**, 865-881.
- Hove-Madsen, J., & Bers, D. M. (1993). Passive Ca buffering and SR Ca uptake in permeabilized rabbit ventricular myocytes. *Am.J.Physiol* **264**, C677-C686.
- Ikemoto, N., Ronjat, M., Mészáros, L. G., & Koshita, M. (1989). Postulated role of calsequestrin in the regulation of calcium release from sarcoplasmic reticulum. *Biochemistry* **28**, 6764-6771.
- Izu, L. T., Wier, W. G., & Balke, C. W. (2001). Evolution of cardiac calcium waves from stochastic calcium sparks. *Biophys.J.* **80**, 103-120.
- Jeyakumar, L. H., Copello, J. A., O'Malley, A. M., Wu, G. M., Grassucci, R., Wagenknecht, T., & Fleischer, S. (1998). Purification and characterization of ryanodine receptor 3 from mammalian tissue. *J.Biol.Chem.* **273**, 16011-16020.

- Kaneko, T., Tanaka, H., Oyamada, M., Kawata, S., & Takamatsu, T. (2000). Three distinct types of  $\text{Ca}^{2+}$  waves in Langendorff-perfused rat heart revealed by real-time confocal microscopy. *Circ.Res.* **86**, 1093-1099.
- Kass, R. S., Lederer, W. J., Tsien, R. W., & Weingart, R. (1978). Role of calcium ions in transient inward currents and aftercontractions induced by strophanthidin in cardiac Purkinje fibres. *J.Physiol* **281**, 187-208.
- Kawai, M., Hussain, M., & Orchard, C. H. (1998).  $\text{Cs}^+$  inhibits spontaneous  $\text{Ca}^{2+}$  release from sarcoplasmic reticulum of skinned cardiac myocytes. *Am.J.Physiol* **275**, H422-H430.
- Keizer, J. & Smith, G. D. (1998). Spark-to-wave transition: saltatory transmission of calcium waves in cardiac myocytes. *Biophys.Chem.* **72**, 87-100.
- Kort, A. A., Capogrossi, M. C., & Lakatta, E. G. (1985). Frequency, amplitude, and propagation velocity of spontaneous  $\text{Ca}^{++}$ -dependent contractile waves in intact adult rat cardiac muscle and isolated myocytes. *Circ.Res.* **57**, 844-855.
- Kort, A. A. & Lakatta, E. G. (1984). Calcium-dependent mechanical oscillations occur spontaneously in unstimulated mammalian cardiac tissues. *Circ.Res.* **54**, 396-404.
- Kort, A. A. & Lakatta, E. G. (1988a). Bimodal effect of stimulation on light fluctuation transients monitoring spontaneous sarcoplasmic reticulum calcium release in rat cardiac muscle. *Circ.Res.* **63**, 960-968.
- Kort, A. A. & Lakatta, E. G. (1988b). Spontaneous sarcoplasmic reticulum calcium release in rat and rabbit cardiac muscle: relation to transient and rested-state twitch tension. *Circ.Res.* **63**, 969-979.
- Lappe, D. L. & Lakatta, E. G. (1980). Intensity fluctuation spectroscopy monitors contractile activation in "resting" cardiac muscle. *Science* **207**, 1369-1371.
- Launikonis, B. S. & Stephenson, D. G. (1999). Effects of beta-escin and saponin on the transverse-tubular system and sarcoplasmic reticulum membranes of rat and toad skeletal muscle. *Pflugers Arch.* **437**, 955-965.
- Laver, D. R. & Lamb, G. D. (1998). Inactivation of  $\text{Ca}^{2+}$  release channels (ryanodine receptors RyR1 and RyR2) with rapid steps in  $[\text{Ca}^{2+}]$  and voltage. *Biophys.J.* **74**, 2352-2364.
- Laver, D. R., Roden, L. D., Ahern, G. P., Eager, K. R., Junankar, P. R., & Dulhunty, A. F. (1995). Cytoplasmic  $\text{Ca}^{2+}$  inhibits the ryanodine receptor from cardiac muscle. *J.Membr.Biol.* **147**, 7-22.

- Leberer, E., Timms, B. G., Campbell, K. P., & MacLennan, D. H. (1990). Purification, calcium binding properties, and ultrastructural localization of the 53,000- and 160,000 (sarcalumenin)-dalton glycoproteins of the sarcoplasmic reticulum. *J.Biol.Chem.* **265**, 10118-10124.
- Lederer, W. J. & Tsien, R. W. (1976). Transient inward current underlying arrhythmogenic effects of cardiotonic steroids in Purkinje fibres. *J.Physiol* **263**, 73-100.
- Lipp, P. & Niggli, E. (1993). Microscopic spiral waves reveal positive feedback in subcellular calcium signaling. *Biophys.J.* **65**, 2272-2276.
- Liu, Z., Zhang, J., Li, P., Chen, S. R., & Wagenknecht, T. (2002). Three-dimensional reconstruction of the recombinant type 2 ryanodine receptor and localization of its divergent region 1. *J.Biol.Chem.* **277**, 46712-46719.
- London, B. & Krueger, J. W. (1986). Contraction in voltage-clamped, internally perfused single heart cells. *J.Gen.Physiol* **88**, 475-505.
- Loughrey, C. M., MacEachern, K. E., Cooper, J., & Smith, G. L. (2003). Measurement of the dissociation constant of Fluo-3 for Ca<sup>2+</sup> in isolated rabbit cardiomyocytes using Ca<sup>2+</sup> wave characteristics. *Cell Calcium* **34**, 1-9.
- Loughrey, C. M., MacEachern, K. E., Neary, P., & Smith, G. L. (2002). The relationship between intracellular [Ca<sup>2+</sup>] and Ca<sup>2+</sup> wave characteristics in permeabilised cardiomyocytes from the rabbit. *J.Physiol* **543**, 859-870.
- Lukyanenko, V., Gyorke, I., & Gyorke, S. (1996). Regulation of calcium release by calcium inside the sarcoplasmic reticulum in ventricular myocytes. *Pflugers Arch.* **432**, 1047-1054.
- Lukyanenko, V., Subramanian, S., Gyorke, I., Wiesner, T. F., & Gyorke, S. (1999). The role of luminal Ca<sup>2+</sup> in the generation of Ca<sup>2+</sup> waves in rat ventricular myocytes. *J.Physiol* **518 (Pt 1)**, 173-186.
- Lukyanenko, V., Wiesner, T. F., & Gyorke, S. (1998). Termination of Ca<sup>2+</sup> release during Ca<sup>2+</sup> sparks in rat ventricular myocytes. *J.Physiol* **507 (Pt 3)**, 667-677.
- Marco, L. A. & Nastuk, W. L. (1968). Sarcomeric oscillations in frog skeletal muscle fibers. *Science* **161**, 1357-1358.
- Marx, S. O., Ondrias, K., & Marks, A. R. (1998). Coupled gating between individual skeletal muscle Ca<sup>2+</sup> release channels (ryanodine receptors). *Science* **281**, 818-821.

- Mattiazzi, A., Hove-Madsen, L., & Bers, D. M. (1994). Protein kinase inhibitors reduce SR Ca transport in permeabilized cardiac myocytes. *Am.J.Physiol* **267**, H812-H820.
- McDonald, T. F., Pelzer, S., Trautwein, W., & Pelzer, D. J. (1994). Regulation and modulation of calcium channels in cardiac, skeletal, and smooth muscle cells. *Physiol Rev.* **74**, 365-507.
- Mejia-Alvarez, R., Kettlun, C., Rios, E., Stern, M., & Fill, M. (1999). Unitary Ca<sup>2+</sup> current through cardiac ryanodine receptor channels under quasi-physiological ionic conditions. *J.Gen.Physiol* **113**, 177-186.
- Minta, A., Kao, J. P., & Tsien, R. Y. (1989). Fluorescent indicators for cytosolic calcium based on rhodamine and fluorescein chromophores. *J.Biol.Chem.* **264**, 8171-8178.
- Murayama, T., Oba, T., Katayama, E., Oyamada, H., Oguchi, K., Kobayashi, M., Otsuka, K., & Ogawa, Y. (1999). Further characterization of the type 3 ryanodine receptor (RyR3) purified from rabbit diaphragm. *J.Biol.Chem.* **274**, 17297-17308.
- Natori, R. (1954). Repeated contraction and conduction observed in isolated myofibrils. *Jikeikai Med.J.* **2**, 1-5.
- Neary, P., Duncan, A. M., Cobbe, S. M., & Smith, G. L. (2002). Assessment of sarcoplasmic reticulum Ca<sup>2+</sup> flux pathways in cardiomyocytes from rabbits with infarct-induced left-ventricular dysfunction. *Pflugers Arch.* **444**, 360-371.
- Niggli, E. (1999). Localized intracellular calcium signaling in muscle: calcium sparks and calcium quarks. *Annu.Rev.Physiol* **61**, 311-335.
- Niggli, E. & Lederer, W. J. (1990). Voltage-independent calcium release in heart muscle. *Science* **250**, 565-568.
- Nuss, H. B. & Houser, S. R. (1992). Sodium-calcium exchange-mediated contractions in feline ventricular myocytes. *Am.J.Physiol* **263**, H1161-H1169.
- O'Neill, S. C., Miller, L., Hinch, R., & Eisner, D. A. (2004). Interplay between SERCA and sarcolemmal Ca<sup>2+</sup> efflux pathways controls spontaneous release of Ca<sup>2+</sup> from the sarcoplasmic reticulum in rat ventricular myocytes. *J.Physiol* **559**, 121-128.
- Odermatt, A., Kurzydowski, K., & MacLennan, D. H. (1996). The v<sub>max</sub> of the Ca<sup>2+</sup>-ATPase of cardiac sarcoplasmic reticulum (SERCA2a) is not altered by Ca<sup>2+</sup>/calmodulin-dependent phosphorylation or by interaction with phospholamban. *J.Biol.Chem.* **271**, 14206-14213.

- Orchard, C. H., Eisner, D. A., & Allen, D. G. (1983). Oscillations of intracellular  $\text{Ca}^{2+}$  in mammalian cardiac muscle. *Nature* **304**, 735-738.
- Orchard, C. H., Houser, S. R., Kort, A. A., Bahinski, A., Capogrossi, M. C., & Lakatta, E. G. (1987). Acidosis facilitates spontaneous sarcoplasmic reticulum  $\text{Ca}^{2+}$  release in rat myocardium. *J.Gen.Physiol* **90**, 145-165.
- Orchard, C. H., Smith, G. L., & Steele, D. S. (1998). Effects of cytosolic  $\text{Ca}^{2+}$  on the  $\text{Ca}^{2+}$  content of the sarcoplasmic reticulum in saponin-permeabilized rat ventricular trabeculae. *Pflugers Arch.* **435**, 555-563.
- Overend, C. L., Eisner, D. A., & O'Neill, S. C. (1997). The effect of tetracaine on spontaneous  $\text{Ca}^{2+}$  release and sarcoplasmic reticulum calcium content in rat ventricular myocytes. *J.Physiol* **502** ( Pt 3), 471-479.
- Overend, C. L., Eisner, D. A., & O'Neill, S. C. (2001). Altered cardiac sarcoplasmic reticulum function of intact myocytes of rat ventricle during metabolic inhibition. *Circ.Res.* **88**, 181-187.
- Page, E., McCallister, L. P., & Power, B. (1971). Stereological measurements of cardiac ultrastructures implicated in excitation-contraction coupling. *Proc.Natl.Acad.Sci.U.S.A* **68**, 1465-1466.
- Press, W. H., Teukolsky, S. A., Vetterling, W. T., & Flannery, B. P. (2002). *Numerical Recipes in C : The Art of Scientific Computing*; 2nd Edition. ed. Cambridge University Press..
- REITER, M. (1962). [The origin of "postcontractions" in the myocardium under the influence of calcium and digitalis glycosides in relation to the frequency of stimulation]. *Naunyn Schmiedebergs Arch.Exp.Pathol.Pharmakol.* **242**, 497-507.
- Rodriguez, P., Jackson, W. A., & Colyer, J. (2004). Critical evaluation of cardiac  $\text{Ca}^{2+}$ -ATPase phosphorylation on serine 38 using a phosphorylation site-specific antibody. *J.Biol.Chem.* **279**, 17111-17119.
- Satoh, H., Blatter, L. A., & Bers, D. M. (1997). Effects of  $[\text{Ca}^{2+}]_i$ , SR  $\text{Ca}^{2+}$  load, and rest on  $\text{Ca}^{2+}$  spark frequency in ventricular myocytes. *Am.J.Physiol* **272**, H657-H668.
- Sham, J. S., Song, L. S., Chen, Y., Deng, L. H., Stern, M. D., Lakatta, E. G., & Cheng, H. (1998). Termination of  $\text{Ca}^{2+}$  release by a local inactivation of ryanodine receptors in cardiac myocytes. *Proc.Natl.Acad.Sci.U.S.A* **95**, 15096-15101.
- Shannon, T. R. & Bers, D. M. (1997). Assessment of intra-SR free  $[\text{Ca}]$  and buffering in rat heart. *Biophys.J.* **73**, 1524-1531.

- Shannon, T. R., Ginsburg, K. S., & Bers, D. M. (2000). Reverse mode of the sarcoplasmic reticulum calcium pump and load-dependent cytosolic calcium decline in voltage-clamped cardiac ventricular myocytes. *Biophys.J.* **78**, 322-333.
- Shannon, T. R., Ginsburg, K. S., & Bers, D. M. (2002). Quantitative assessment of the SR Ca<sup>2+</sup> leak-load relationship. *Circ.Res.* **91**, 594-600.
- Shannon, T. R., Guo, T., & Bers, D. M. (2003). Ca<sup>2+</sup> Scraps: Local Depletions of Free [Ca<sup>2+</sup>] in Cardiac Sarcoplasmic Reticulum During Contractions Leave Substantial Ca<sup>2+</sup> Reserve. *Circulation Research* **93**, 40.
- Sipido, K. R., Carmeliet, E., & Van de, W. F. (1998). T-type Ca<sup>2+</sup> current as a trigger for Ca<sup>2+</sup> release from the sarcoplasmic reticulum in guinea-pig ventricular myocytes. *J.Physiol* **508** ( Pt 2), 439-451.
- Sipido, K. R., Maes, M., & Van de, W. F. (1997). Low efficiency of Ca<sup>2+</sup> entry through the Na(+)-Ca<sup>2+</sup> exchanger as trigger for Ca<sup>2+</sup> release from the sarcoplasmic reticulum. A comparison between L-type Ca<sup>2+</sup> current and reverse-mode Na(+)-Ca<sup>2+</sup> exchange. *Circ.Res.* **81**, 1034-1044.
- Sitsapesan, R. & Williams, A. J. (1997). Regulation of current flow through ryanodine receptors by luminal Ca<sup>2+</sup>. *J.Membr.Biol.* **159**, 179-185.
- Smith, G. D. (1996). Analytical steady-state solution to the rapid buffering approximation near an open Ca<sup>2+</sup> channel. *Biophys.J.* **71**, 3064-3072.
- Smith, G. L. & Miller, D. J. (1985). Potentiometric measurements of stoichiometric and apparent affinity constants of EGTA for protons and divalent ions including calcium. *Biochim.Biophys.Acta* **839**, 287-299.
- Smith, G. L. & O'Neill, S. C. (2001). A comparison of the effects of ATP and tetracaine on spontaneous Ca(2+) release from rat permeabilised cardiac myocytes. *J.Physiol* **534**, 37-47.
- Soeller, C. & Cannell, M. B. (2002). Estimation of the sarcoplasmic reticulum Ca<sup>2+</sup> release flux underlying Ca<sup>2+</sup> sparks. *Biophys.J.* **82**, 2396-2414.
- Steele, D. S. & Smith, G. L. (1993). Effects of 2,3-butanedione monoxime on sarcoplasmic reticulum of saponin-treated rat cardiac muscle. *Am.J.Physiol* **265**, H1493-H1500.
- Stern, M. D. (1992). Theory of excitation-contraction coupling in cardiac muscle. *Biophysical Journal* **63**, 497-517.

- Stern, M. D., Capogrossi, M. C., & Lakatta, E. G. (1988). Spontaneous calcium release from the sarcoplasmic reticulum in myocardial cells: mechanisms and consequences. *Cell Calcium* **9**, 247-256.
- Stern, M. D., Kort, A. A., Bhatnagar, G. M., & Lakatta, E. G. (1983). Scattered-light intensity fluctuations in diastolic rat cardiac muscle caused by spontaneous  $\text{Ca}^{++}$ -dependent cellular mechanical oscillations. *J.Gen.Physiol* **82**, 119-153.
- Stern, M. D., Weisman, H. F., Renlund, D. G., Gerstenblith, G., Hano, O., Blank, P. S., & Lakatta, E. G. (1989). Laser backscatter studies of intracellular  $\text{Ca}^{2+}$  oscillations in isolated hearts. *Am.J.Physiol* **257**, H665-H673.
- Subramanian, S., Viatchenko-Karpinski, S., Lukyanenko, V., Gyorke, S., & Wiesner, T. F. (2001). Underlying mechanisms of symmetric calcium wave propagation in rat ventricular myocytes. *Biophys.J.* **80**, 1-11.
- Sutko, J. L., Thompson, L. J., Kort, A. A., & Lakatta, E. G. (1986). Comparison of effects of ryanodine and caffeine on rat ventricular myocardium. *Am.J.Physiol* **250**, H786-H795.
- Tada, M. & Katz, A. M. (1982). Phosphorylation of the sarcoplasmic reticulum and sarcolemma. *Annu.Rev.Physiol* **44**, 401-423.
- Tada, M. & Toyofuku, T. (1998). Molecular regulation of phospholamban function and expression. *Trends Cardiovasc.Med.* **8**, 330-340.
- Takahashi, T. (1942). On the mechanism of muscle shortening. A study by high speed cinematograph of muscle contractile movement under the influence of quinine chloride. *J.Physiol.Soc.Japan* **7**, 659-662.
- Takamatsu, T. & Wier, W. G. (1990). Calcium waves in mammalian heart: quantification of origin, magnitude, waveform, and velocity. *FASEB J.* **4**, 1519-1525.
- Terentyev, D., Viatchenko-Karpinski, S., Valdivia, H. H., Escobar, A. L., & Gyorke, S. (2002). Luminal  $\text{Ca}^{2+}$  controls termination and refractory behavior of  $\text{Ca}^{2+}$ -induced  $\text{Ca}^{2+}$  release in cardiac myocytes. *Circ.Res.* **91**, 414-420.
- Trafford, A. W. & Eisner, D. A. (2003). No role for a voltage sensitive release mechanism in cardiac muscle. *J.Mol.Cell Cardiol.* **35**, 145-151.
- Trafford, A. W., Lipp, P., O'Neill, S. C., Niggli, E., & Eisner, D. A. (1995). Propagating calcium waves initiated by local caffeine application in rat ventricular myocytes. *J.Physiol* **489** ( Pt 2), 319-326.

- Trafford, A. W., Sibbring, G. C., Diaz, M. E., & Eisner, D. A. (2000). The effects of low concentrations of caffeine on spontaneous Ca release in isolated rat ventricular myocytes. *Cell Calcium* **28**, 269-276.
- Tsien, R. Y., Rink, T. J., & Poenie, M. (1985). Measurement of cytosolic free Ca<sup>2+</sup> in individual small cells using fluorescence microscopy with dual excitation wavelengths. *Cell Calcium* **6**, 145-157.
- Valdeolmillos, M., O'Neill, S. C., Smith, G. L., & Eisner, D. A. (1989). Calcium-induced calcium release activates contraction in intact cardiac cells. *Pflugers Arch.* **413**, 676-678.
- Valdivia, H. H., Kaplan, J. H., Ellis-Davies, G. C., & Lederer, W. J. (1995). Rapid adaptation of cardiac ryanodine receptors: modulation by Mg<sup>2+</sup> and phosphorylation. *Science* **267**, 1997-2000.
- Vassort, G. & Alvarez, J. (1994). Cardiac T-type calcium current: pharmacology and roles in cardiac tissues. *J.Cardiovasc.Electrophysiol.* **5**, 376-393.
- Volders, P. G., Kulcsar, A., Vos, M. A., Sipido, K. R., Wellens, H. J., Iazzara, R., & Szabo, B. (1997). Similarities between early and delayed afterdepolarizations induced by isoproterenol in canine ventricular myocytes. *Cardiovasc.Res.* **34**, 348-359.
- Walford, G. D., Gerstenblith, G., & Lakatta, E. G. (1984). Effect of sodium on calcium-dependent force in unstimulated rat cardiac muscle. *Am.J.Physiol* **246**, H222-H231.
- Wehrens, X. H., Lehnart, S. E., Reiken, S. R., & Marks, A. R. (2004). Ca<sup>2+</sup>/Calmodulin-Dependent Protein Kinase II Phosphorylation Regulates the Cardiac Ryanodine Receptor. *Circ.Res.*
- Weiss, R. G., Gerstenblith, G., & Lakatta, E. G. (1990). Calcium oscillations index the extent of calcium loading and predict functional recovery during reperfusion in rat myocardium. *J.Clin.Invest* **85**, 757-765.
- Wier, W. G. (1979). Intracellular calcium transients accompanying contraction of mammalian muscle. *Fed Proc* **38**, 1389.
- Wier, W. G., Cannell, M. B., Berlin, J. R., Marban, E., & Lederer, W. J. (1987). Cellular and subcellular heterogeneity of [Ca<sup>2+</sup>]<sub>i</sub> in single heart cells revealed by fura-2. *Science* **235**, 325-328.
- Williams, D. A., Delbridge, L. M., Cody, S. H., Harris, P. J., & Morgan, T. O. (1992). Spontaneous and propagated calcium release in isolated cardiac myocytes viewed by confocal microscopy. *Am.J.Physiol* **262**, C731-C742.

Wu, J., Biermann, M., Rubart, M., & Zipes, D. P. (1998). Cytochalasin D as excitation-contraction uncoupler for optically mapping action potentials in wedges of ventricular myocardium. *J.Cardiovasc.Electrophysiol.* **9**, 1336-1347.

Xu, A., Hawkins, C., & Narayanan, N. (1993a). Phosphorylation and activation of the Ca(2+)-pumping ATPase of cardiac sarcoplasmic reticulum by Ca2+/calmodulin-dependent protein kinase. *J.Biol.Chem.* **268**, 8394-8397.

Xu, L., Jones, R., & Meissner, G. (1993b). Effects of local anesthetics on single channel behavior of skeletal muscle calcium release channel. *J.Gen.Physiol* **101**, 207-233.

